Finite-Range Regularisation of Chiral Effective Field Theory

Ross D. Young

Supervisors: A/Prof. D. B. Leinweber and Prof. A. W. Thomas

Special Research Centre for the
Subatomic Structure of Matter
and
Department of Physics,
University of Adelaide,
Australia

October 2004

Abstract

Modern calculations of quantum chromodynamics (QCD) in lattice gauge theory are restricted to the simulation of quark masses which are significantly heavier than those observed in nature. In order to compare with experiment, an extrapolation of lattice QCD results is required. A low-energy effective field theory (EFT), chiral perturbation theory (χPT), provides an optimal framework for studying the quark-mass variation of hadron properties. Established as a rigorous expansion about the limit of vanishing quark-masses, convergence of the EFT at the scale of masses explored in lattice QCD is not guaranteed.

Working with various regularisation schemes, a quantitative analysis is performed to investigate the convergence properties of the quark-mass expansion. The traditional formulation of χPT, defined by a minimal subtraction renormalisation scheme, is found to have a limited range of applicability. An alternative scheme, namely finite-range regularisation (FRR), displays significantly enhanced convergence properties. Consequently, the use of FRR permits the reliable extrapolation of modern lattice simulation results to the physical regime.

The study of the quark-mass dependence of nucleon properties in quenched lattice QCD provides valuable insight into the structure of the nucleon. Application of finite-range regularisation reveals a phenomenological link between quenched QCD and the physical theory. This work offers an improved understanding of the dynamical role of the pion field in baryon spectroscopy and electromagnetic structure.

Statement of Originality

This work contains no material which has been accepted for the award of any other degree or diploma in any university or other tertiary institution and, to the best of my knowledge and belief, contains no material previously published or written by another person, except where due reference has been made in the text.

I give consent to this copy of my thesis, when deposited in the University Library, being available for loan and photocopying.

17 JUNE 2005

Acknowledgements

Firstly, I wish to thank my supervisors, Derek Leinweber and Tony Thomas, for their continued assistance, support, encouragement, enthusiasm, friendship and everything else a graduate student could wish from their supervisors.

The assistance and contributions of Stewart Wright made my transition into the graduate program an effortless one. I offer a special thanks to Ian Cloet and Alex Kalloniatis for providing invaluable feedback on sections of this Thesis.

The atmosphere provided at the CSSM has been tremendous. I thank everyone I have been fortunate enough to share the workplace with. James and Will, let's go get jugs of Coopers.

There is no way that I would have done all of this without something to do when not sitting at the computer. For all the good times and hilarity that we have had, thanks to Tim, Dean, Paul, Heath, Rich, Fady and everyone else.

To Thomas, my strength comes from you, well done and thanks. Mum and Dad, you know that you're the best, thank you so much for everything.

And Amy-Victoria — thank you for offering the future.

Contents

1

Introduction

Quantum chromodynamics (QCD) is the fundamental quantum field theory which governs the strong-interaction force in nature. The interactions of all subatomic particles, such as protons, neutrons, pions etc., are governed by this theory. At high-energies, QCD provides an excellent description of the dynamics of electron–proton scattering experiments. In the low-energy domain, the quarks and gluons of QCD are manifest as the constituents of hadrons. Developing a dynamical description of this manifestation is one of the ultimate ambitions of hadronic physics. This problem presents a tremendous challenge, where perturbative techniques of quantum field theory are unable to account for the highly nontrivial structure of the QCD vacuum.

A rigorous method for extracting the low-energy properties of QCD, where traditional perturbative techniques fail, is delivered by lattice gauge theory. Calculations in lattice QCD are limited by computational approximations, necessary for the efficient simulation of the theory on today's computers. One significant restriction is the use of quark-masses an order of magnitude larger than those in nature, with typical simulations having quark-masses of the order 50 MeV and above, compared to the physical value of about 5 MeV. This requires an extrapolation in quark-mass to complete the scientific process of comparing theory with experiment. It is this extrapolation problem which is the principal focus of this research.

An introduction to the theory of QCD is described in Chapter 2. Particular emphasis is given to the formulation of QCD in lattice gauge theory and some of the practical aspects of modern simulations. With an evident restriction to unphysically large quark-masses, an outline of the issues in chiral extrapolation is provided. In particular, the extrapolation problem is complicated by the dynamic structure of the nucleon. Some empirical observations of the physical nucleon are addressed to highlight this intrinsic complexity.

These nontrivial characteristics of the nucleon are a consequence of spontaneously broken phase of chiral symmetry in the QCD vacuum. The elementary concepts of chiral symmetry and spontaneous symmetry breaking are described in Section 3.1. This leads to the subsequent development of an effective field theory (EFT) of low-energy QCD, which encompasses the imposed symmetry constraints. This nonperturbative approach to QCD, an alternative to an ex-

pansion in small coupling constant, chiral perturbation theory (χPT) defines a systematic expansion in both momentum scale and quark mass.

As for any physical description in quantum field theory, infinities arising from self-interactions must be regularised and renormalised to make the theory meaningful. This two step procedure is discussed in detail in Section 3.3, where the traditionally implemented minimal subtraction regularisation scheme is introduced. Whereas this scheme is ideal for elementary particles, general physical arguments suggest that the applicability will become more restrictive when working with effective fields of finite structure. This leads to the construction of a regularisation scheme which embodies this extended nature of the fields. Characterised by the suppression of the ultraviolet behaviour of loop integrals, this scheme is referred to as finite-range regularisation (FRR). The implementation of this procedure is given and the mathematical equivalence to minimal subtraction is demonstrated.

Before attempting chiral extrapolation based upon χPT, it is important to understand the effective range of the expansion about vanishing quark-mass. The convergence properties of the quark-mass expansion of the nucleon mass are the primary focus of Chapter 4. The combination of the physical observable, lattice simulation results and χPT enables estimates of the quark-mass dependence of the nucleon mass over a wide range of mass scale. Near the chiral limit, all regularisation schemes are mathematically indistinguishable. As the quark masses are increased, differences in the truncation of the chiral series become apparent. To the order of the calculation, it is observed that minimal subtraction regularisation, or equivalently dimensional regularisation (DR), exhibits a much narrower range of convergence, compared to the alternative offered by FRR.

When using a chiral series based upon DR, the maximum accessible pion mass[1], within the scope of the EFT, is found to be of the order $m_\pi^2 < 0.4\,\mathrm{GeV}^2$. On the other hand, the chiral expansions offered by FRR provide enhanced convergence properties, applying up to $m_\pi^2 \sim 0.8\,\mathrm{GeV}^2$.

For the application to lattice QCD, the actual problem of interest reverses the role of the initial investigation. Instead of analysing the expansion about the chiral limit, the converse issue of *extrapolation* is distinguished by the determination of the chiral series in the *absence of low quark-mass data.* The described regularisation schemes are applied to the extrapolation of lattice simulation results in Chapter 5. The results of FRR are profound, with the extrapolated nucleon mass displaying a systematic accuracy of two parts in one thousand. Stability with respect to truncation of the chiral series is also discovered, with

[1] As described in Chapter 3, a consequence of chiral symmetry is that the square of the pion mass is proportional to the quark mass, $m_\pi^2 \propto m_q$. Throughout, the pion mass and quark mass are therefore used interchangeably as a measure of deviation from the chiral limit.

an observed difference of less than one percent between the leading-order result and that at next-to-leading order. Neglecting the discretisation artifacts of the lattice formalism, the conclusions produce a solution to the chiral extrapolation problem.

The determination of the nucleon mass, based upon the successful union of lattice gauge theory and this modern implementation of χPT, represents the most rigorous nonperturbative calculation of this fundamental observable in QCD.

Upon completion of the investigation of QCD, the focus of this Thesis is redirected to the study of a modification of QCD commonly implemented in lattice simulations. In particular, the quenched approximation of QCD can offer valuable insight into the chiral behaviour of hadron properties. Quenched QCD is a modification of standard QCD, defined by the absence of dynamical quark loops in the vacuum. This modification induces an alteration of the low-energy effective theory, the main features of which are discussed in Chapter 6. Two differing techniques, for the calculation of nonanalytic contributions to hadron properties, are illustrated.

With the modified chiral behaviour, an investigation of the quark-mass dependence of baryon masses in quenched QCD is presented in Chapter 7. The improved convergence properties of the EFT formulated with FRR are exploited. The adoption of FRR leads to a remarkable, somewhat unexpected, result. Although no rigorous connection between QCD and its quenched analogue can be given, it is found that accounting for the modified chiral interactions can describe the primary differences in the observed baryon masses. This phenomenological link is demonstrated to extract physical masses of the nucleon and Delta baryons, from a purely quenched simulation. This discovery provides an enhanced understanding of the role of chiral physics in baryon structure, and subsequently assists an improved description of the origin of the physical baryon spectrum.

Beyond the description of the mass of the nucleon, further information on internal structure of the nucleon is provided by its response to the electromagnetic field. The charge and current distributions of the nucleon are characterised by the electromagnetic form factors. Revealing the nature of this structure is one of the elementary objectives of lattice QCD. The restriction to the simulation of relatively large quark masses means that a significant portion of this dynamical structure is absent. In Chapter 8, the chiral behaviour of the proton magnetic moment is investigated. This analysis considers the extrapolation method for both quenched and physical simulations of QCD. The chiral unquenching procedure, as discovered in the baryon mass analysis, is successfully applied to provide improved estimates of the physical moment. The pion cloud is observed to

describe almost one third of the physical proton magnetic moment, highlighting the dynamical nature of QCD — beyond the static constituent quark picture.

A summary and concluding remarks of the work presented in this Thesis are presented in Chapter 9.

2

QCD is Nonperturbative

The building blocks of atomic nuclei are protons and neutrons, generically referred to as nucleons. Understanding the structure of the nucleus has challenged physicists since Rutherford's discovery in 1911 of a *small,* positive-charge core to the atom. In 1932 Chadwick confirmed the existence of the neutron, the neutral-charge partner to the proton. The force binding these constituents to the nucleus is *strong*, much stronger than the familiar Coulomb force.

Today, the strong binding force is understood as the residual interaction of the complex substructure of individual nucleons. Nucleons themselves are comprised of a system of quarks and gluons whose dynamics are governed by the quantum gauge theory, QCD. QCD is the fundamental theory of all strong interaction physics — from high energy particle collisions and the decay of heavy nuclei to the properties of matter under extreme conditions, such as at the core of a neutron star.

Although the theory of QCD can be written down in a compact form, understanding the physical dynamics presents a tremendous theoretical challenge. To date, rigorous testing of QCD against experiment is restricted to the domain of high-energy scattering. The low-energy nature of QCD has shown a much stronger resistance to theoretical development. We focus our attention on the low-energy structure of QCD, in particular the properties of the nucleon at rest. Lattice QCD has proven to be the most successful method for studying QCD in the low-energy regime.

After giving an introduction to QCD, in this Chapter we outline the lattice regularisation of quantum field theory and the simulation of QCD. Computation costs restrict simulations to quark masses much larger than those observed in nature. We address the necessity to extrapolate results in quark mass to compare with physical observables. We highlight some of the early research into performing extrapolations which are consistent with known properties of QCD.

Central to the chiral extrapolation problem are the strong coupling of the nucleon to the light pseudoscalar pion. We highlight some phenomenological aspects of the pion-cloud structure of the nucleon.

2.1 An Outline of QCD

In the Standard Model, hadrons are composite objects comprised of a complex substructure of quarks and gluons. Hadrons are classified into two subgroups, mesons and baryons, which are bosons and fermions respectively. To date, all known hadrons can be described in terms of a simple underlying quark structure. Mesons are quark-antiquark ($q\bar{q}$) pairs and baryons are three-quark (qqq) systems. Recently, there has been extensive interest in the possible discovery of a pentaquark baryon ($qqqq\bar{q}$) [N$^+$03, S$^+$03].

The underlying theory describing the interactions of quarks is quantum chromodynamics. QCD is a gauge field theory built on the premise of invariance under local gauge transformations of $SU(3)_{\text{colour}}$. Each quark carries an internal quantum number, one of three possible colours. The gauge bosons of the theory are the eight gluon fields lying in the adjoint representation of the gauge group.

The QCD Lagrangian, in naive form, can be summarised as

$$\mathcal{L}_{\text{QCD}} = \sum_q \bar{\psi}_q^i (i\gamma^\mu D_\mu^{ij} - \delta^{ij} m_q)\psi_q^j - \frac{1}{4} F_{\mu\nu}^{(a)} F^{(a)\mu\nu} , \tag{2.1}$$

with

$$F_{\mu\nu}^{(a)} = \partial_\mu A_\nu^a - \partial_\nu A_\mu^a - g_s f_{abc} A_\mu^b A_\nu^c , \tag{2.2}$$

and

$$D_\mu^{ij} = \delta^{ij}\partial_\nu + i g_s \frac{1}{2} \lambda_a^{ij} A_\mu^a , \tag{2.3}$$

with 3 colours, i; 6 flavours, q; and 8 gluon fields, a.

The non-Abelian nature of the theory means that the gluons couple to themselves. This causes the vacuum to become highly nontrivial as the coupling becomes strong. At high energy, the coupling becomes weak, vanishing in the limit of infinite momentum transfer. This property is referred to as asymptotic freedom.

The experimental observation of asymptotic freedom and the existence of point-like constituents in hadronic matter, is of fundamental importance to the foundation of QCD in the Standard Model.

2.2 Lattice Quantum Field Theory

At low energies, perturbative methods are unable to account for large scale fluctuations of the vacuum. QCD calculations therefore require nonperturbative techniques. Only with continued theoretical developments will the low-energy domain be tested with experimental rigour.

Lattice gauge theory provides the only calculable definition of the path integral in the nonperturbative regime. The lattice formulation was first proposed by Wilson in 1974 [Wil74]. QCD Green functions, defined via the path integral, are calculated on a lattice-discretised, Euclidean space-time. There are numerous review articles on the modern implementation of lattice gauge theory, those of Richards [Ric99], Di Pierro [DP00] and McNeile [McN03] have been particularly useful.

The primary focus of this Thesis is the study of the nucleon mass in QCD. As an example calculation, we outline some of the principal components in the calculation of the nucleon mass in lattice QCD.

Ground-state masses are calculated by the determination of the large Euclidean time behaviour of two-point correlation functions, calculated in coordinate space,

$$\tilde{C}_N(x) = \langle \Omega | \chi_N(x) \overline{\chi}_N(0) | \Omega \rangle \,, \tag{2.4}$$

where χ_N is a spinor interpolating field carrying the quantum numbers of the nucleon, Ω denotes the QCD vacuum. The source and sink of the nucleon field are located at 0 and $x = (t, \vec{x})$, respectively.

This correlation function is defined through the path integral by

$$\langle \Omega | \chi_N(x) \overline{\chi}_N(0) | \Omega \rangle = \int \mathcal{D}A_\mu \mathcal{D}\overline{\psi} \mathcal{D}\psi \, \chi_N(x) \overline{\chi}_N(0) e^{-S_{\mathrm{E}}^{\mathrm{QCD}}[A_\mu, \psi, \overline{\psi}]} \,. \tag{2.5}$$

To explain how this is calculated within the lattice formalism, we first consider the evaluation of a correlation function, $\mathcal{O}$, which does not depend explicitly on the fermion fields, such as

$$\langle \Omega | \mathcal{O} | \Omega \rangle = \int \mathcal{D}U \mathcal{D}\overline{q} \mathcal{D}q \, \mathcal{O}[U] e^{-S_{\mathrm{E}}^{\mathrm{LQCD}}[U, q, \overline{q}]} \,. \tag{2.6}$$

The continuum fields have been replaced by their lattice-discretised analogues and appropriate lattice action. The lattice fermion fields, q and $\overline{q}$, lie on the lattice sites, with gauge symmetry preserved by the covariant link variables U. These link variables encompass the gluon fields.

There has been a tremendous effort towards creation of improved formulations of the lattice QCD action and we return to address these issues below. Whatever our choice of lattice action, we separate the purely gauge component and the fermion component by[1]

$$S^{\mathrm{LQCD}}[U, q, \overline{q}] = S^G[U] + S^F[U, q, \overline{q}] \,, \tag{2.7}$$

[1] From here we drop the subscript E and assume a Euclidean space-time implicitly.

where the fermion part can be written as

$$S^F[U,q,\overline{q}] = \sum_{x,y} \overline{q}(x) M(x,y;U) q(y) \tag{2.8}$$

and M is the fermion matrix. In Eq. (2.6), we can now perform the integral over the fermion fields explicitly

$$\langle \Omega | \mathcal{O} | \Omega \rangle = \int \mathcal{D}U \, \mathcal{O}[U] \det M(U) \, e^{-S^G[U]} . \tag{2.9}$$

Computation of this integral may still seem a formidable task. We have an integration over 8 colours of gauge field for every link on the lattice. With a typical lattice volume $16^3_{\text{space}} \times 32_{\text{time}}$, this gives a total integration over a 10^6 dimensional parameter space. Fortunately, Monte Carlo integration techniques are able to make this problem computationally tractable.

Since we are working in Euclidean space we have a positive-definite action and hence the factor

$$\det M(U) \, e^{-S^G[U]} , \tag{2.10}$$

can be treated as a probabilistic weight. The functional integral can be approximated by an ensemble average of gauge configurations

$$\langle \Omega | \mathcal{O} | \Omega \rangle = \frac{1}{N} \sum_{\{U_i\}} \mathcal{O}[U_i] , \tag{2.11}$$

where N gauge configurations, U_i, have been *randomly* generated based on the acceptance probability of the weight function, Eq. (2.10).

Evaluation of the fermion determinant is a nonlocal operation and hence dramatically slows down the process of generating an ensemble of gauge configurations. To save time, lattice simulations have often made the crude approximation of setting the determinant to unity. This is known as the quenched approximation and corresponds to performing calculations on a purely gluonic gauge field. The physical implications of quenching are discussed in Chapters 6 and 7.

For the nucleon two-point correlation function, Eq. (2.5), we need to deal with explicit fermion fields. It turns out that the same set of gauge configurations can be used to perform the functional integration over gauge fields. The explicit inclusion of the fermions requires a Wick contraction and the relevant quark propagators must be calculated explicitly for each gauge configuration.

To be more explicit, we define the nucleon interpolating field

$$\chi_N(x) = \epsilon_{abc} \left(u_a^T(x) C \gamma_5 d_b(x) \right) u_c(x) , \tag{2.12}$$

where *abc* denote the colour labels and the spinor multiplication remains implicit. C is the charge conjugation matrix. For each gauge configuration, U_i, the quark propagators are evaluated

$$S_f^{ab}(x,y) = \langle \Omega_i | q_f^a(x) \overline{q}_f^b(y) | \Omega_i \rangle \,, \tag{2.13}$$

where f denotes the quark flavour. Propagators are typically calculated from a fixed source point, y, to every point on the lattice, x, by inversion of the fermion matrix. Being limited to iterative solution methods, this causes calculation of the quark propagator, to every site on the lattice, for every configuration to be computationally intensive.

Performing the appropriate Wick contractions we can express the two-point correlation function of the nucleon as

$$\begin{aligned}\langle \Omega | \chi_N(x) \overline{\chi}_N(0) | \Omega \rangle = \\ \frac{1}{N} \sum_{\{U_i\}} \epsilon_{abc} \epsilon_{a'b'c'} \Big\{ \mathrm{tr} \left[S_u^{aa'}(x,0) \right] \mathrm{tr} \left[\tilde{C} S_d^{bb'}(x,0) \tilde{C}^{-1} S_u^{cc'}(x,0) \right] \\ + \mathrm{tr} \left[S_u^{aa'}(x,0) \tilde{C} S_d^{bb'}(x,0) \tilde{C}^{-1} S_u^{cc'}(x,0) \right] \Big\} \,,\end{aligned} \tag{2.14}$$

where the traces are over Dirac space and we use the shorthand notation $\tilde{C} = C\gamma_5$.

With the correlation functions at hand, the low-lying mass states are now readily accessible. The coordinate-space correlation function, $\tilde{C}_N(x)$, is decomposed into its Fourier modes in momentum space

$$C_N(t,\vec{p}) = \sum_{\vec{x}} e^{i\vec{p}.\vec{x}} \langle \Omega | \chi_N(x) \overline{\chi}_N(0) | \Omega \rangle \,, \tag{2.15}$$

and inserting a complete set of mass eigenstates, α, with momenta $\vec{q}$ gives

$$C_N(t,\vec{p}) = \sum_{\alpha,\vec{q}} \sum_{\vec{x}} e^{-i\vec{p}.\vec{x}} \langle \Omega | \chi_N(x) | \alpha(\vec{q}) \rangle \langle \alpha(\vec{q}) | \overline{\chi}_N(0) | \Omega \rangle \,, \tag{2.16}$$

$$= \sum_{\alpha,\vec{q}} \sum_{\vec{x}} e^{-i\vec{p}.\vec{x}} \langle \Omega | e^{-i\hat{q}.x} \chi_N(0) e^{+i\hat{q}.x} | \alpha(\vec{q}) \rangle \langle \alpha(\vec{q}) | \overline{\chi}_N(0) | \Omega \rangle \,, \tag{2.17}$$

$$= \sum_{\alpha,\vec{q}} \sum_{\vec{x}} e^{-i(\vec{p}-\vec{q}).\vec{x}} e^{-E_\alpha t} \langle \Omega | \chi_N(0) | \alpha(\vec{q}) \rangle \langle \alpha(\vec{q}) | \overline{\chi}_N(0) | \Omega \rangle \,, \tag{2.18}$$

$$= \sum_{\alpha,\vec{q}} \delta(\vec{p}-\vec{q}) e^{-E_\alpha t} \langle \Omega | \chi_N(0) | \alpha(\vec{q}) \rangle \langle \alpha(\vec{q}) | \overline{\chi}_N(0) | \Omega \rangle \,, \tag{2.19}$$

$$= \sum_{\alpha} e^{-E_\alpha(\vec{p})t} \langle \Omega | \chi_N(0) | \alpha(\vec{p}) \rangle \langle \alpha(\vec{p}) | \overline{\chi}_N(0) | \Omega \rangle \,. \tag{2.20}$$

Since we are only considering the mass extraction we can just consider the zero momentum component of our field

$$C_N(t) \equiv C_N(t, \vec{p} = 0) = \sum_\alpha e^{-M_\alpha t} \lambda_\alpha \bar{\lambda}_\alpha \,. \tag{2.21}$$

We see that the energy, $E_\alpha(\vec{p})$, has now been replaced by the rest mass, M_α, and for convenience we have defined the notation

$$\lambda_\alpha = \langle \Omega | \chi_N(0) | \alpha(\vec{0}) \rangle \,, \quad \bar{\lambda}_\alpha = \langle \alpha(\vec{0}) | \overline{\chi}_N(0) | \Omega \rangle \,. \tag{2.22}$$

In the case where we use point sources and sinks these two equations are complex conjugates, $\bar{\lambda}_\alpha = \lambda_\alpha^*$. When the interpolating fields are smeared in the spatial direction, this simplification is no longer valid and we employ the bar notation to remain generic. Smearing is a common technique used in lattice simulations, which acts to reduce high-momentum modes and hence increase overlap with the ground-state wave-functions.

The large time behaviour of C_N will be dominated by the lowest-lying mass states, with all excited states being suppressed by the exponential. For extraction of the mass, we define the effective mass

$$M_{\text{eff}} = \log \left(\frac{C_N(t)}{C_N(t+1)} \right) \,, \tag{2.23}$$

which for large times, $t \to \infty$, gives the lowest-lying mass, M_0. The effective mass is typically plotted as a function of the time and once a plateau is observed, it is clear that the ground-state has been isolated.

The final step in the extraction of the nucleon mass, m_N, is to convert the lattice measurement to physical units. All calculations are computed in dimensionless lattice units, such that the simulated nucleon mass is given by $a\, m_N$, with a the physical lattice spacing.

Determination of the scale in lattice QCD is an important step for the comparison with physical observables. For studying the quark mass variation of hadron properties and in particular, the chiral extrapolation problem, it is essential that the scale-determination procedure is insensitive to chiral physics. This ensures that we do not contaminate the very physics that we are attempting to investigate.

We identify the Sommer scale [Som94] for QCD [EHK98a] as the ideal method for setting the scale for the present application. The Sommer scale is extracted from the static quark potential at an intermediate distance scale. Considering the QCD flux tube as a string model, the large distance behaviour of the potential in pure gauge theory is described by

$$V(r) = V_0 + \sigma r - \frac{e}{r} \,. \tag{2.24}$$

In pure gauge theory, or quenched simulations, the string tension σ is a well defined quantity and therefore the large distance behaviour can be used to determine the scale. In a dynamical simulation the sea quarks permit string-breaking and a modified procedure is therefore required. Sommer proposed defining the scale by the static quark force at an intermediate scale r_0 by

$$r_0^2 V'(r_0) = c\,, \tag{2.25}$$

with c set to a dimensionless constant. Typical values of the parameters, c and r_0, are set by phenomenological models of heavy quark potentials. These show the least model dependence at a distance scale near $r_0 = 0.5\,\text{fm}$, which corresponds to $c = 1.65$. This then sets the physical lattice spacing, a, and allows us to convert the extracted lattice mass to dimensional units.

With this rigorous formulation of the QCD path integral through lattice regularisation, QCD observables can be evaluated. In performing calculations, one must be careful to deal with all approximations in a systematic fashion. The immediately apparent approximations are those associated with the discretisation of space-time — both the finite cutoff scale, a, and the finite volume of the lattice, V. The physical theory is obtained in the limits $a \to 0$ and $V \to \infty$. These issues are beyond the scope of this Thesis, and most of the time we will assume lattice results represent the continuum, infinite-volume theory.

The other major limitation of modern lattice simulations is the restriction to the domain of heavy quarks. Producing results for light, dynamical quarks is computationally expensive. Simulation time increases rapidly as the lattice volume is enlarged. The physical volume of the lattice must be large enough to contain the longest-ranging quantum fluctuations. The spatial extent of these fluctuations is characterised by the Compton wavelength ($\lambda_C = 2\pi/m$) of the lightest excitation. As the pion is the lightest degree of freedom in QCD, accurate simulation requires a physical length of $L \gtrsim \lambda_C^\pi$, or equivalently, satisfy the dimensionless measure $m_\pi L \gtrsim 2\pi$. For a physical pion mass simulation, this requires $L \sim 9\,\text{fm}$.

In addition to the volume constraints, the implementation of fermion actions on a discrete space-time causes increased computational complexity, as the chiral regime is approached. There are various formulations of lattice fermions which attempt to improve access to light quark simulations.

Wilson [Wil74] described the original formulation of a lattice action, with the continuum integrals and derivatives replaced by sums and finite difference equations. Implementation of the fermion field in the lattice formulation is nontrivial because of the fermion doubling problem — there exist 2^d degenerate quarks for each flavour. Wilson introduced a higher dimension operator which lifts the mass of the doubler species with the inverse lattice spacing, a. As

$a \to 0$ the doublers become infinitely massive and the continuum theory is restored. The main drawback to this formulation is that chiral symmetry is violated at $\mathcal{O}(a)$ and hence large scaling violations are observed at finite lattice spacing [EHK98b].

There has been tremendous success in removing $\mathcal{O}(a)$ errors and suppressing $\mathcal{O}(a^2)$ errors in lattice simulations through the development of nonperturbatively improved actions [LSSW96, Z+02, NN95]. These actions display excellent scaling properties [ZLLW05, EHK98b, DLLZ00], providing near continuum results at finite lattice spacing. The overlap formalism [NN95, NN93b, NN94, NN93a] describes an implementation which has an exact lattice chiral symmetry and, to date, is the most physical implementation of chiral fermions on a lattice. Unfortunately, in typical simulations the computational cost of overlap fermions is two orders of magnitude more expensive than Wilson-style actions. For reasons which will become clearer below, most of this additional cost will be recovered as the chiral limit is approached. Efforts have been made towards accelerating the computation time of overlap simulations [KALW02].

Another formulation of lattice fermions is that by Kogut and Susskind [KS75], known as staggered fermions. Staggered fermions remove the doubler problem by distributing the fermion spinor over the corners of a 2^4 hypercube. This implementation maintains a form of chiral symmetry, yet the 16 doubler species have been reduced to 4 *taste* species. Distribution over the hypercube doubles the effective spacing between independent fermion sites — meaning on a typical gauge configuration of dimensions $16^3 \times 32$ at $a \sim 0.125\,\text{fm}$, the fermion field is only sampled at $8^3 \times 16$ and $a \sim 0.250\,\text{fm}$. The advantage of the staggered formalism is that computational costs are significantly reduced. Improvement schemes have been developed to reduce the taste-violation artifacts [Lep99]. Although it is not clear that this theory has a rigorous connection to the continuum [Neu04], impressive results have been obtained at comparably light quark masses [D+04].

Improvement schemes based on Wilson fermions have proven to be an important development towards removing lattice-discretisation artifacts. One successful method is that of nonperturbatively improved clover [SW85, LSSW96, LSS+97]. Nonperturbatively improved clover fermion action removes $\mathcal{O}(a)$ discretisation effects to all orders in the coupling g. Results using this action have been demonstrated to give near-continuum results at finite lattice spacing [EHK98b]. A drawback to all Wilson-style fermion actions is that access to the chiral regime becomes restricted as the exceptional configuration problem is encountered.

The exceptional configuration problem is related to the additive quark mass renormalisation of Wilson quarks [BDE+98]. For a given input quark mass, there is an additive renormalisation which shifts the value of the renormalised

quark mass. The quark-mass renormalisation is dependent both on the gauge configuration and lattice action. An ensemble average critical mass $\tilde{m}_{\rm cr}$ can be defined as the point where the pion mass vanishes. This can be obtained by extracting pion masses, at finite quark masses, from ensemble averages and extrapolating to the point where the pion mass vanishes.

The sensitivity to individual gauge configurations can be understood by studying the behaviour of the low-lying eigenmodes of the Dirac operator. This allows the the critical quark-mass $m_{\rm cr}$ to be determined for each configuration [BDET98, BDE+98]. In particular, the distribution of $m_{\rm cr}$ can be studied for a set of gauge configurations. When working at quark masses far from $m_{\rm cr}$, the role played by the finite width distribution is largely irrelevant. At lighter quark masses, the fluctuation in simulated quark masses on a configuration-by-configuration basis will become more apparent. This will become realised in large statistical errors in ensemble averaged quantities — especially those which exhibit rapid variation near the chiral limit.

Even more dramatic is the potential to perform a simulation below $m_{\rm cr}$ for a given configuration, such that the renormalised quark mass is less than zero. Any such configuration will provide absurd results and are therefore aptly named "exceptional". Any improvement scheme which reduces the width of the $m_{\rm cr}$ distribution will reduce the exceptional configuration problem and allow better access to the light quark regime.

A recently developed improvement scheme involves fat-link irrelevant clover (FLIC) fermions [Z+02]. Fat-link fermion actions couple the quark fields to *smoothed* gauge configurations. The removal of the short-range topological defects has been demonstrated to reduce the exceptional configuration problem [DHK99]. FLIC fermions only use smeared links for the higher dimensional irrelevant operators and retain the untouched links for the physical operators.

Recent studies have shown that FLIC fermions exhibit improvement in the distribution of $m_{\rm cr}$ and hence allow better access to the chiral regime [BKL+04]. The scaling properties of FLIC fermions have also been demonstrated to be equivalent to that of nonperturbatively improved clover [ZLLW05].

Although much progress has been made towards the accurate simulation of QCD in the light quark regime, realistic simulations at the physical quark mass are likely to require $\gtrsim 100\,\text{Tflops}$ of designated computing power. Since this is well beyond the next generation of QCD supercomputers, extrapolation of lattice results, to compare with experiments, will be required for quite some time.

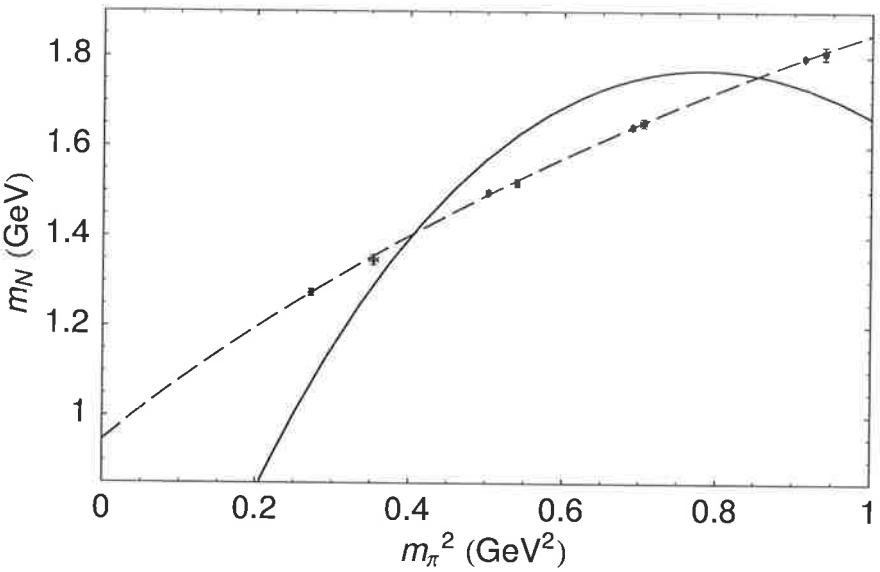

Figure 2.1: Extrapolation based on Eq. (2.26) with c_3 set to the phenomenological value (solid curve) and c_3 as a free parameter (dashed curve).

2.3 The Chiral Extrapolation Problem

The restriction of simulations in lattice QCD to the use of quark masses much heavier than those found in nature necessitates an extrapolation of results to the physical regime. After all, one of the key goals of lattice QCD is to confront experiment in the nonperturbative regime. Understanding how to extrapolate the benchmark calculations, such as the nucleon mass, is therefore paramount in the theoretical development of low-energy QCD.

The nature of spontaneous symmetry breaking in the QCD vacuum dictates that hadron properties should exhibit rapidly-varying nonanalytic behaviour with quark mass. Lattice simulations have so far shown little evidence of this nonanalytic structure[2]. In fact, lattice simulations observe very smooth variation with quark mass — just as would be anticipated in a constituent quark model of hadron structure. For example, masses grow linearly with quark mass and magnetic moments fall like the Dirac moment, $\sim 1/M_q$.

We show some dynamical fermion lattice QCD data from CP-PACS [AK+02] for the nucleon mass as a function of m_π^2 in Fig. 2.1. The data only slightly deviates from a straight line. Approximate chiral symmetry in QCD tells us

[2]There have been some recent breakthroughs, which we will highlight in a later Chapter.

that near the chiral limit the nucleon mass should behave as

$$m_N = c_0 + c_2 m_\pi^2 + c_3 m_\pi^3 + \dots , \tag{2.26}$$

where the phenomenological value for $c_3 = -5.5\,\mathrm{GeV}^{-2}$. First we fit the data with this form and attempt to extract c_3 from the lattice. The resultant fit is shown by the dashed curve in Fig. 2.1. The best-fit value of $c_3 = -0.63\,\mathrm{GeV}^{-2}$, almost an order of magnitude smaller than the physical one. Instead, we could attempt to fit the data constraining the physical c_3. This is a very poor description of the data as seen in the solid curve of Fig. 2.1.

There are two alternatives to explain this failure:

- Lattice QCD does not describe the correct physical theory of the strong interaction, or
- The chiral series truncated in this fashion has poor convergence in the range of quark masses explored on the lattice. This is because either the data lies beyond the radius of convergence, or more terms must be included in the series.

If we are to believe QCD then the poor convergence of the chiral series is clearly the most satisfactory interpretation. We clarify the technical issue of radius-of-convergence versus terms-in-the-series in the proceedings chapters of this Thesis. One point to note at this stage is that if we assume the data *is* within the radius of convergence, then all terms beyond m_π^2 must effectively sum to zero in order to reproduce the lattice data.

The physical explanation for the observation of smooth variation with quark mass is easily understood in terms of chiral quark models, such as the cloudy bag model (CBM) [Tho84]. Chiral quark models of the nucleon incorporate the correct low-energy properties of chiral symmetry, together with a model for the underlying dynamics of the internal quark structure. The cloudy bag model is an extension of the MIT bag model to incorporate the dynamical effects of the pion field. The MIT bag model [CJJ+74, CJJT74] is a relativistic model of free quarks confined to an infinite spherical well. Reflection at the bag surface violates chiral symmetry, which is restored in the CBM by the coupling to the pion field.

The key point of our discussion is that the pion field couples to an internal quark structure of finite size. This finite size necessarily means that there is an associated form factor which suppresses the pion-nucleon interaction for high momentum transfer. In the context of quark mass variation, the result of the form factor is to suppress the effects of the pion cloud for increasing quark mass. This means that there will be a characteristic scale associated with the

transition from dominant chiral physics to a region where chiral-loop effects are negligible [DLM+01]. This transition is set by the size of the source of the pion cloud and the axial form factor of the nucleon, described by a radius of $\langle r^2 \rangle^{1/2}_{\text{axial}} \simeq 0.66\,\text{fm}$ [TW01], suggesting that the scale is of order $1/\langle r^2 \rangle^{1/2}_{\text{axial}} \sim 0.3$–$0.4\,\text{GeV}$. Once the Compton wavelength of the pion becomes smaller than the size of the source, fluctuations of the pion field are rapidly suppressed.

To highlight these effects, we consider the variation of nucleon magnetic moments with quark mass as an example. As a consequence of spontaneous chiral symmetry breaking, the magnetic moment of the nucleons near the chiral limit are known to behave as

$$\begin{aligned} \mu^p &= \mu_0^p - \alpha m_\pi + \mathcal{O}(m_\pi^2)\,, \\ \mu^n &= \mu_0^n + \alpha m_\pi + \mathcal{O}(m_\pi^2)\,. \end{aligned} \tag{2.27}$$

As will be seen later $m_\pi^2 \propto m_q$ and hence the magnetic moments vary with the square-root of the current quark mass. This nontrivial result cannot be described within the simple quark model. The most important feature is that chiral symmetry predicts a model-independent [LP71] value for the coefficient α,

$$\alpha = \frac{g_A^2 m_N}{8\pi f_\pi^2}\,. \tag{2.28}$$

This coefficient is relatively large, taking the physical values for $g_A = 1.26$ and $f_\pi = 0.093\,\text{GeV}$, the leading nonanalytic term contributes $\alpha m_\pi = 0.96\,\mu_\text{N}$ to the physical magnetic moment. This is roughly a third of the physical proton magnetic moment, $\mu^p = 2.793\,\mu_\text{N}$, and a half that of the neutron, $\mu^n = -1.913\,\mu_\text{N}$.

The CBM automatically incorporates this leading chiral behaviour through coupling to the pion cloud. This model has a physical form factor, which provides a natural suppression mechanism for the pion field at larger pion masses. In Fig. 2.2 we show a calculation of the magnetic moment of the proton in the cloudy bag model [TT83, LTW98] for varying quark mass[3]. In this model, we observe that the transition scale between rapid chiral curvature and the smooth Dirac moment is roughly $m_\pi \sim 300$–$500\,\text{MeV}$. This behaviour is typical of all nucleon properties and gives a clear physical explanation of the smooth behaviour observed in lattice simulations which typically lie in the region $m_\pi^2 \gtrsim 0.3\,\text{GeV}^2$. The task for the analysis of lattice results is to incorporate these physical features into a systematic extrapolation procedure. The solution to this problem will be the principal focus of this Thesis.

Based on the quark mass variation found in the CBM, one early proposal for

[3]Details of the calculation are shown in Appendix C.

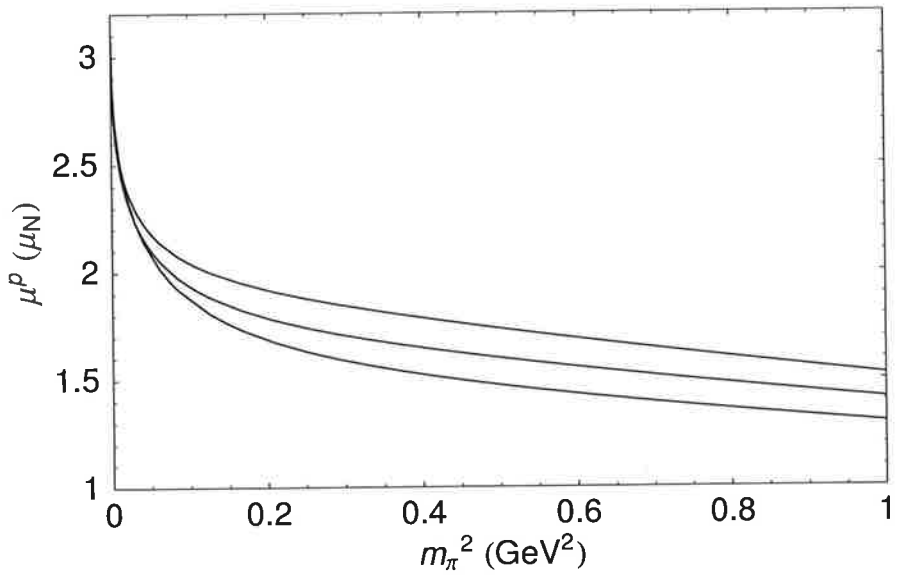

Figure 2.2: Magnetic moment in the cloudy bag model as a function of m_π^2. The three curves, from top–down, correspond to bag radii $R = 1.0, 0.9, 0.8\,\text{fm}$.

the lattice extrapolation problem was to use a Padé approximant [LLT99]

$$\mu^{p(n)} = \frac{\mu_0}{1 \pm \frac{\alpha}{\mu_0} m_\pi + c m_\pi^2}, \tag{2.29}$$

where μ_0 and c are free parameters and α constrained to its model-independent value, Eq. (2.28). By Taylor expansion we see that this form precisely recovers the leading expansion as dictated by chiral symmetry, Eq. (2.27).

We show pioneering lattice data on lattice magnetic moments by Leinweber et al. [LWD91] in Fig. 2.3. An extrapolation based on this Padé approximant is shown by the solid curve. We see that this simple form encapsulates both the rapid nonlinear variation near the chiral limit and the smooth Dirac moment behaviour at large quark mass. This form is also observed to be phenomenologically consistent with the model calculation shown in Fig. 2.2.

The Padé form has been extended to the entire baryon octet with demonstrated success [HJLT00b]. A similar procedure was also extended to perform extrapolations of baryon charge radii [HJLT00a].

Early work also highlighted the importance of incorporating the pion-cloud effects into extrapolations of moments of parton distribution functions (PDFs) [DMN+01, DMT01]. The results found dramatically improved agreement with the experimental moments, compared to naive extrapolations based on linear forms. This work was further developed to obtain accurate estimates of the low-lying moments of spin dependent PDFs from lattice QCD [DMT02].

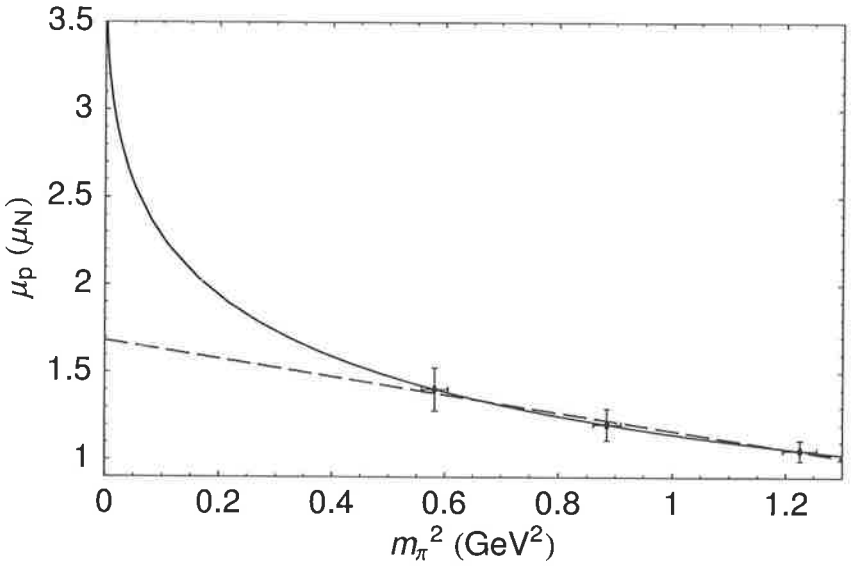

Figure 2.3: Extrapolation of proton magnetic moment lattice QCD data based on the Padé form is shown by the solid curve. The dashed line shows a naive linear extrapolation for comparison.

For the extrapolation of the nucleon mass, it was found that the only way to fit lattice data consistently with chiral symmetry was to explicitly evaluate the loop contribution [LTTW00]. In contrast to simply building in the functional expansion dictated by chiral symmetry, the loop integrals that dictate the chiral behaviour are evaluated with a chosen regularisation scheme. This was subsequently extended to extrapolation of the rho-meson mass [LTTW01].

These studies represented the first steps towards direct application of finite-range regularisation for lattice QCD simulations. One of the major features of this Thesis is the extension of this foundation work, consequently ensuring a systematic approach to the chiral expansion problem. The issue of model-dependence within this formalism has encountered significant criticism [B$^+$03]. these claims are quantitatively addressed and found to be unsubstantiated.

2.4 Constituent Quarks to a Dynamical Theory

In the early historical development of QCD, a nucleon could be described as a system of three constituent quark. As a dynamical theory of interacting quarks and gluons the true structure of the nucleon is much richer than this static quark picture. As highlighted, the consequences of spontaneous symmetry breaking forces model-independent constraints on the low-energy structure of the nucleon.

Here we highlight a couple of key features of the nucleon which take its structure beyond that of the simple quark picture.

One of the key observations of nontrivial structure is seen in the flavour asymmetry of antiquark distributions in the nucleon [Kum98]. The difference in the light quark masses, m_u and m_d, is very small with respect to typical QCD scales and therefore any perturbative calculation of $q\overline{q}$ fluctuations would predict only a small difference between $\overline{u}$ and $\overline{d}$ quarks in the nucleon. Any asymmetry in these distributions can be measured by violations of the Gottfried sum rule [Got67], which under the assumption of charge symmetry states

$$I_G = \int_0^1 \frac{dx}{x}\left(F_2^p(x,Q^2) - F_2^n(x,Q^2)\right) = \frac{1}{3} + \frac{2}{3}\int_0^1 dx\left(\overline{u}(x,Q^2) - \overline{d}(x,Q^2)\right) . \tag{2.30}$$

It is clear that any measured variation of I_G from 1/3 is a direct measurement of the $\overline{u}/\overline{d}$ asymmetry. The first measurement of this asymmetry found [A$^+$91, A$^+$94]

$$I_G = 0.235 \pm 0.026 , \tag{2.31}$$

which is nearly four standard deviations away from the expectation of a symmetric sea. This result describes an excess of $\overline{d}$ to $\overline{u}$ quarks given by

$$\int_0^1 dx\left(\overline{d}(x) - \overline{u}(x)\right) = 0.148 \pm 0.039 . \tag{2.32}$$

This is a remarkable result, demonstrating a rich structure to the physical vacuum. The phenomenology of this asymmetry can be easily explained within a simple pion cloud model and was in fact predicted by Thomas in 1983 [Tho83].

As will be shown in more detail in the following Chapter, the dynamical behaviour of the pion plays an important role in the structure of the nucleon. Here we describe at the simplest phenomenological level how to give interpretation to the discovered asymmetry. A proton wave-function has strong overlap with a bound pion-nucleon system. In particular, at a given time a proton could be found to be a $p\pi^0$ or a $n\pi^+$, where a $\overline{q}$ has been generated to create the pion. Angular momentum selection rules tell us that the proton will have greater overlap with $n\pi^+$ relative to $p\pi^0$. Since the π^+ carries only a $\overline{d}$ antiquark we are led to the conclusion that there is an excess of $\overline{d}$-quarks in the proton relative to $\overline{u}$.

The pion cloud structure of the nucleon also implies other consequences on more elementary observables of the nucleon. The electromagnetic properties of the nucleon are also constrained by the properties of chiral symmetry.

One of the celebrated features of the constituent quark model is the prediction of the ratio of proton to neutron magnetic moments

$$\frac{\mu^p}{\mu^n} = -\frac{3}{2} , \tag{2.33}$$

which is very close to the experimental ratio, -1.46. This agreement is quite remarkable considering the rapid chiral variation with quark mass described by chiral symmetry [LTY01]. Equation (2.27) gives a model independent expansion of the ratio of magnetic moments

$$\frac{\mu^p}{\mu^n} = \frac{\mu_0^p}{\mu_0^n}\left(1 - \left[\frac{1}{\mu_0^n} + \frac{1}{\mu_0^p}\right]\alpha m_\pi\right) + \mathcal{O}(m_\pi^2)\,. \tag{2.34}$$

Constraining the chiral expansions to reproduce the experimental proton moment and the experimental ratio provides

$$\mu_0^p = 3.75\,\mu_{\rm N}\,, \qquad \frac{\mu_0^p}{\mu_0^n} = -1.34\,, \tag{2.35}$$

and hence the numerical value for Eq. (2.34) becomes

$$\frac{\mu^p}{\mu^n} = -1.34 - 0.12\frac{m_\pi}{m_\pi^{\rm phys}} + \mathcal{O}(m_\pi^2)\,. \tag{2.36}$$

The constituent quark model prediction of $-3/2$ is independent of quark mass, yet as a consequence of spontaneous chiral symmetry break we observe that the ratio can change by as much 18% as m_π varies from 0 to just $2m_\pi^{\rm phys}$. Interestingly, if the physical quark mass were slightly larger, $m_\pi \sim 190\,{\rm MeV}$, the experimental ratio would exactly match that of the quark model prediction. In reality, the quark model corresponds to the static quark limit, $m_q \to \infty$, and the observed agreement is rather coincidental [LTY01]. We will return to the behaviour of the ratio at larger quark masses in the context of lattice extrapolations in a later Chapter.

The chiral behaviour of the magnetic moment naturally leads us to consider the behaviour of the charge radii, in particular that of the neutron. The squared charge radius of the neutron is determined by the slope of the electric form factor at zero momentum transfer,

$$\langle r^2\rangle_{\rm ch}^n = -6\frac{d}{dQ^2}G_E^n(Q^2)\Big|_{Q^2=0}\,. \tag{2.37}$$

The Sachs electric and magnetic form factors can be written in terms of the covariant vertex functions F_1 and F_2 as [ESW60, Sac62]

$$\begin{aligned} G_E(Q^2) &= F_1(Q^2) - \frac{Q^2}{4\,m_N^2}F_2(Q^2)\,, \\ G_M(Q^2) &= F_1(Q^2) + F_2(Q^2)\,. \end{aligned} \tag{2.38}$$

The electric charge and magnetic moment correspond to $G_E(Q^2)$ and $G_M(Q^2)$ evaluated at $Q^2 = 0$. The charge is therefore given by $F_1(Q^2 = 0)$ and hence

vanishes for the neutron. The magnetic moment of the neutron is purely anomalous, $F_2^n(Q^2 = 0) = \mu^n$. The charge radius of the neutron can then be expressed as

$$\langle r^2 \rangle_{\rm ch}^n = -6 \frac{d}{dQ^2} F_1^n(Q^2)\Big|_{Q^2=0} + \frac{3}{2} \frac{\mu^n}{m_N^2} \,. \tag{2.39}$$

The second term is known as the Foldy term [Fol52a, Fol52b] and takes the numerical value $-0.126\,\mathrm{fm}^2$. This is extremely close to the experimental result, $\langle r^2 \rangle_{\rm ch}^n = -0.113 \pm 0.003 \pm 0.004\,\mathrm{fm}^2$ [KRHH95].

The phenomenological interpretation of this result has been the subject of considerable debate. It has long been the argument that the Foldy term contributes the dominant part of the charge radius, with the residual portion, involving the Dirac form factor F_1^n, being attributed to some kind of *intrinsic* charge distribution. This is the interpretation given by Foldy [Fol58], where the neutron is assumed point-like with an intrinsic magnetic moment.

The phenomenological interpretation of Foldy's argument is described by the relativistic phenomenon of *Zitterbewegung*. In a semi-classical sense, a free Dirac particle does not travel in a straight line with constant velocity, but undergoes random motion at the speed of light about a central point of uniform trajectory. The physical extent of this random motion is of the order of the Compton wavelength of the particle, $\lambda_C = 2\pi/m$. A structureless, charged particle will therefore exhibit an effective charge distribution of finite extent. In addition, this random motion has a collective flow around the spin axis. This current circulation is then responsible for the Dirac moment of charged fermions, $e\hbar/2m$. The spatial smearing of Zitterbewegung motion will modify the intrinsic electromagnetic structure of fermions. By intrinsic structure, we refer to the properties of the particle at an instantaneous position, independent of the effects of Zitterbewegung.

The Foldy term is a relativistic effect of the Zitterbewegung motion of the neutron having an intrinsic magnetic moment. The random motion of the magnetic moment gives rise to an effective charge distribution and hence contributes to the charge radius. The similarity with the experimental result is remarkable and gives the interpretation of a very small intrinsic charge distribution.

A careful treatment of the relativistic corrections to the charge radius in a quark-diquark model has found that the Foldy term is exactly cancelled by a contribution to F_1 [Isg99]. This supports the interpretation of G_E describing a rest-frame charge distribution. Consideration of the chiral behaviour of electromagnetic properties demonstrates in a model-independent way that the observed agreement is purely coincidental [LTY01].

The leading nonanalytic contribution to the electric charge radius of the

neutron is given by [BZ72, GSS88, LC93]

$$\langle r^2 \rangle^n_{\rm ch} = \frac{1+5g_A^2}{(4\pi f_\pi)^2} \log\left(\frac{m_\pi}{\mu}\right) . \tag{2.40}$$

As a consequence of the approximate chiral symmetry of QCD we observe that the charge radius of the neutron diverges as the quark mass tends to zero, in contrast to the magnetic moment, which behaves as m_π and remains finite as $m_\pi \to 0$. If the physical quark mass were lighter by just a few MeV, the charge radius would be dominated by a contribution from F_1 and the agreement with the Foldy term would be lost. This important result again highlights the role of the pion cloud in nucleon structure.

* * *

Quantum chromodynamics is the fundamental theory describing the strong interaction within the Standard Model. Low-energy properties within this theory cannot be studied by using perturbative methods. The most promising theoretical developments within the field have been proven within the formalism of lattice gauge theory. We have identified the technical issues which cause the computational difficulty of reducing the quark masses in numerical simulations, particularly with dynamical fermions. This restriction to the domain of heavy quarks necessitates an extrapolation to the physical regime.

The chiral extrapolation problem is complicated by the nontrivial nature of the QCD vacuum. This is a direct result of spontaneous chiral symmetry breaking. The observed complexity in the structure of the nucleon is enriched by the nature of the pion cloud. In the following Chapter we describe details of spontaneous symmetry breaking and the immediate consequences. We outline the construction of a low-energy effective field theory of QCD, with application to the chiral extrapolation problem being the principle objective.

3

Chiral Symmetry and Effective Field Theory

Early studies of strong-interaction physics found chiral symmetry to be well respected in the real world, indeed it is recognised as the best hadron symmetry after isospin [Pag75]. The nature of this symmetry and its observed symmetry-breaking patterns have provided a wealth of information for understanding low-energy phenomena in QCD.

In this Chapter we discuss the nature of chiral symmetry and the consequences of spontaneous breaking in the QCD vacuum. We outline the uses of effective field theory and the construction of a low-energy effective theory for QCD — namely chiral perturbation theory.

Calculations in chiral perturbation theory are traditionally carried out using dimensional regularisation — or an equivalent minimal subtraction scheme. We describe the theoretical framework for an alternative scheme which offers many advantages in the context of quark mass variation. Being characterised by the suppression of ultra-violet behaviour in loop diagrams, we refer to this scheme as *finite-range regularisation* (FRR).

3.1 Spontaneous Breaking of Chiral Symmetry

In the absence of a quark mass term, the QCD Lagrangian, Eq. (2.1), is invariant under independent vector and axial-vector chiral transformations, defined by

$$\begin{aligned} \psi(x) &\to e^{-i\boldsymbol{\theta}_V\cdot\boldsymbol{\tau}}\psi(x)\,, \\ \psi(x) &\to e^{-i\boldsymbol{\theta}_A\cdot\boldsymbol{\tau}\gamma_5}\psi(x)\,, \end{aligned} \tag{3.1}$$

respectively. We have collected our quark spinors into a two-component vector,[1]

$$\psi = \begin{pmatrix} u \\ d \end{pmatrix}\,. \tag{3.2}$$

[1] Our discussion in this Chapter will only consider two flavours of light quarks. Inclusion of the strange quark is a trivial extension.

The *rotation* angles in $SU(2)$ space are defined by $\boldsymbol{\theta}_V$ and $\boldsymbol{\theta}_A$, with Pauli spin matrices $\boldsymbol{\tau}$ operating in flavour space. With every continuous symmetry, Noether's Theorem tells us that there exists a classically conserved current. The corresponding vector and axial-vector conserved currents are given by

$$\mathbf{V}^\mu = \overline{\psi}\gamma^\mu \boldsymbol{\tau}\psi \tag{3.3}$$

$$\mathbf{A}^\mu = \overline{\psi}\gamma^\mu\gamma_5 \boldsymbol{\tau}\psi\,. \tag{3.4}$$

Associated with these conserved currents are the classically conserved charges

$$\mathbf{Q}_V = \int d^3x\, \mathbf{V}^0\,, \qquad \mathbf{Q}_A = \int d^3x\, \mathbf{A}^0\,. \tag{3.5}$$

The phenomenon of spontaneous symmetry breaking is characterised by a degeneracy of eigenstates which minimise the action. In a system with an infinite number of degrees of freedom, such as a quantum field theory, one cannot relate these vacuum states via a unitary transformation. A physical system will therefore *choose* a preferred vacuum state. If a symmetry of the action is consequently lost by identification of a unique vacuum then this symmetry is said to be spontaneously broken.

In QCD we have identified chiral transformations as a symmetry of the Lagrangian. The axial charge operators, $\hat{Q}^a_A$, necessarily commute with the Hamiltonian, $[\hat{Q}^a_A, \hat{H}] = 0$. The γ_5 structure in the axial current means that it is negative parity and would therefore imply degenerate parity partners in the low-energy hadron spectrum. This behaviour is not observed in nature. For example, consider the nucleon $|N^+\rangle$ which has positive parity and mass $m_N = 0.940\,\text{GeV}$,

$$\hat{H}|N^+\rangle = m_N|N^+\rangle\,. \tag{3.6}$$

We can define a negative parity partner, $|N^-\rangle = \hat{Q}^a_A|N^+\rangle$, which must be degenerate in mass by the commutation relation. In nature, the lowest excitations of the nucleon carrying the appropriate quantum numbers are the $N(1535)$ and $\Delta(1620)$, both being more than $\sim 600\,\text{MeV}$ larger in mass than the nucleon. Assuming the masses are not significantly altered in going to the chiral limit, spontaneous chiral symmetry breaking is therefore realised by the absence of degenerate chiral multiplets.

Identification of the degenerate eigenstate $|N^-\rangle$, which must exist to maintain the underlying Hamiltonian symmetry, requires further explanation. Preservation of the commutation relation is resolved by the Goldstone Theorem [Gol61], this theorem states that [GSW62]

> *"... if there is a continuous symmetry transformation under which the Lagrangian is invariant, then either the vacuum state is also*

invariant under the transformation, or there must exist spinless particles of zero mass."

In any physical system in which the vacuum state breaks a symmetry there must exist a zero-mass, spinless boson carrying the quantum numbers of this symmetry transformation. This massless boson is referred to as a *Goldstone boson.* The negative parity state $|N^-\rangle$, created by the axial charge operating on the nucleon, then corresponds to a non-interacting system of a nucleon and a massless Goldstone boson. In this way, we have preserved conservation of the axial charge and identified the degenerate eigenstate of opposite parity. The Goldstone bosons therefore provide a connection between the continuum of degenerate vacua.

In QCD, the pions are approximate Goldstone bosons arising from the spontaneous symmetry breaking of the chiral axial-vector current. There are three charge states corresponding to the different isospin projections. The physical pion is only approximately Goldstone because it is not massless the finite mass of the pion is a result of the explicit symmetry breaking given by the finite u and d quark masses.

An explicit quark-mass term in the Lagrangian, $-m_q\overline{\psi}\psi$, is not invariant under axial-vector transformations. The associated Noether currents are no longer conserved and their classical divergences, from the Euler-Lagrange equations, given by

$$\partial_\mu \mathbf{A}^\mu = 2\, i\, m_q\, \overline{\psi}\gamma_5 \boldsymbol{\tau}\psi\,. \tag{3.7}$$

In historical studies of low-energy hadron interactions the hypothesis of partially conserved axial-vector current (PCAC) permitted the development of low-energy theorems based on the approximate chiral symmetries of the strong interaction. This hypothesis can be understood as the assumption that deviations from a chirally symmetric world vary smoothly with the explicit symmetry-breaking parameter. Thus processes, such as π–π scattering, could be calculated assuming an exact chiral symmetry and then violations arising from finite quark mass contributions treated as small perturbations.

As described by Eq. (3.7) we would anticipate that the divergence of the axial-vector current should be small and to leading-order be proportional to m_q. The physical pion is observed to decay to a $\mu\nu$-pair via the weak interaction. The transition matrix-element between the single pion state and the QCD vacuum via the left-handed current must be non-vanishing

$$\langle\Omega|L_\mu|\pi\rangle = \langle\Omega|V_\mu - A_\mu|\pi\rangle \neq 0\,. \tag{3.8}$$

With the vacuum defined to have positive parity and pion field carrying intrinsic negative parity, the matrix element involving V_μ must vanish and hence the decay transition couples exclusively to the axial current. Conversely, it can be stated

that the axial-vector current creates the pion field. For decay of a single-pion state of momentum q_μ, we define the matrix element

$$\langle \Omega | A^a_\mu(x) | \pi^b(q) \rangle = i\,\delta^{ab} f_\pi q_\mu e^{iq.x}\,. \tag{3.9}$$

This equation defines the pion decay constant f_π, which is experimentally determined for the charged pions from the decay $\pi^\pm \to \mu^\pm \nu$.[2] Taking the divergence of Eq. (3.9) gives

$$\langle \Omega | \partial^\mu A^a_\mu(x) | \pi^b(q) \rangle = \delta^{ab} f_\pi m_\pi^2 e^{iq.x}\,, \tag{3.10}$$

and we observe that the divergence of the axial current is proportional to both f_π and m_π^2.

Comparing Eqs. (3.7) and (3.10) we observe that the divergence of the axial current is proportional to both m_q and m_π^2 — implying that the pion mass varies with the square-root of m_q. Treated rigorously, commutation relations between the generators of the chiral transformations with the explicit symmetry breaking terms give the famous Gell-Mann–Oakes–Renner (GOR) relation [GMOR68]

$$f_\pi^2 m_\pi^2 = -\frac{1}{2}(m_u + m_d)\langle \overline{u}u + \overline{d}d \rangle\,. \tag{3.11}$$

Here we have introduced the chiral condensate which takes a value approximately

$$\langle \overline{u}u \rangle = \langle \overline{d}d \rangle \equiv \langle \overline{q}q \rangle \simeq -(225\,\mathrm{MeV})^3\,, \tag{3.12}$$

at a renormalisation scale of $\mu = 1\,\mathrm{GeV}$ [GL82]. With this value we observe the average light-quark mass to be $\hat{m} = (m_u + m_d)/2 \simeq 7\,\mathrm{MeV}$.

As the limit of vanishing quark-mass is approached the pion decay constant and quark condensate remain finite. The pion mass approaches zero in the chiral limit and is realised as a true Goldstone mode of QCD. The finite decay constant at zero quark mass enables the creation of massless states from the vacuum at no energetic cost.

The physical QCD vacuum lies very close to a spontaneously broken phase of an exact chiral symmetry. With the quark masses being so small on hadronic scales, explicit symmetry breaking is small and can systematically be treated as a perturbation. We can utilise these features to enhance our understanding of low-energy QCD. In particular, low-energy phenomena can be described entirely in terms of an effective field theory for the approximate Goldstone bosons. This effective field theory is commonly referred to as chiral perturbation theory.

[2] Decay of the neutral meson is complicated by coupling to the electromagnetic interaction via the triangle diagram, $\pi^0 \to 2\gamma$. This process is intimately related to the nature of the $U(1)$ axial anomaly in QCD.

3.2 Chiral Perturbation Theory

At low-energies the strong interaction is well described by hadronic degrees of freedom. In fact, there is no evidence of explicit quarks and gluons as dynamical fields in this energy regime. QCD at low energies can therefore be described by an effective Lagrangian describing the interactions of the asymptotic fields of the theory. As has been described in detail, the nature of spontaneous chiral symmetry breaking in QCD means that the pion is significantly lighter than all other fields. The dynamical degrees of freedom, or quantum fluctuations, can therefore be described entirely by the pion field. All other particles are treated as *heavy* and are integrated out of the effective theory.

With the quark mass treated as a light energy scale, a simultaneous expansion in small pion momenta and quark mass about the chiral limit can systematically describe QCD up to some energy scale. This effective field theory for QCD, with an appropriate counting scheme for the energy scales, is commonly known as *chiral perturbation theory* (χPT).

The general construction of phenomenological Lagrangians has been outlined by Callan, Coleman, Wess and Zumino [CWZ69, CJCWZ69]. These papers described the tools for creating phenomenological Lagrangians for fields which transform under arbitrary symmetry groups. The use of such Lagrangians as a systematic approach to the study of a more fundamental theory came about with Weinberg's seminal paper [Wei79]. This work is characterised by Weinberg's elementary theorem, if one is to calculate matrix elements based on the most general possible Lagrangian consistent with appropriate symmetries, then the obtained result will be the most general solution — to a given order in the expansion scale. For the most general Lagrangian, one must include *all* interaction terms compatible with the underlying symmetry. This theorem also relies on the definition of an appropriate counting scheme to define the necessary contributions to any order in the expansion.

The most general Lagrangian for the pion, QCD's asymptotic field, based on the fundamental symmetries of QCD will therefore describe a rigorous approach to strong interaction theory in the low-energy regime.

We now describe the construction of the effective pion Lagrangian for low-energy QCD. The QCD generating functional, in the presence of external fields, can be expressed as

$$Z[v,a,s,p] = \int \mathcal{D}A_\mu \mathcal{D}\overline{\psi}\mathcal{D}\psi \exp\left[i\int d^4x\, \mathcal{L}_{\rm QCD}(A_\mu,\overline{\psi},\psi;v,a,s,p)\right], \quad (3.13)$$

where the QCD Lagrangian in the presence of the associated external fields is given by the bare Lagrangian in the chiral limit, Eq. (2.1) with $m_q = 0$, plus

chiral source terms

$$\mathcal{L}_{\rm QCD}(A_\mu, \overline{\psi}, \psi; v, a, s, p) = \mathcal{L}^0_{\rm QCD} + \overline{\psi}(\gamma^\mu v_\mu + \gamma_5\gamma^\mu a_\mu - s + i\gamma_5 p)\psi\,. \qquad (3.14)$$

The external fields v, a, s, p are 2×2 matrices in flavour space and act as sources for the vector, axial-vector, scalar and pseudoscalar fields respectively. The transformation properties of these fields, see Refs. [GL84, BKM95], are defined such that the Lagrangian is left invariant under the local chiral transformations defined in Eq. (3.1).

As we are interested in the low-energy sector of QCD, we can now expand this expression in small momenta of the external fields. Working just in the low-energy sector also means that we are able to integrate out all the quark and gluon fields in the functional integral and replace it by an integration over the pion field with appropriate effective Lagrangian,

$$Z[v, a, s, p] = \int \mathcal{D}U \exp\left[i \int d^4x\, \mathcal{L}_{\chi\rm PT}(U; v, a, s, p)\right]\,. \qquad (3.15)$$

The matrix U contains the pion field, where symmetry under $SU(2) \times SU(2)$ chiral transformations is preserved by the nonlinear relation,

$$U \to U' = V_R U V_L^\dagger\,, \qquad V_{R,L} \in SU(2)\,. \qquad (3.16)$$

In the standard nonlinear representation, U is given by $U = \exp(i\boldsymbol{\tau}.\boldsymbol{\pi}/f)$.

The interactions of the effective field theory are then characterised by the expansion of the effective Lagrangian

$$\mathcal{L}_{\chi\rm PT} = \mathcal{L}_2 + \mathcal{L}_4 + \ldots\,, \qquad (3.17)$$

where the subscript counts the energy dimension of the contributions to the effective theory. In the simplest meson theory a derivative of U or quark mass contribution each count one dimension of energy. The lowest order, $\mathcal{O}(p^2)$ effective Lagrangian describing low-energy QCD is

$$\mathcal{L}_2 = \frac{1}{4} f^2 \left\{ \mathrm{tr}\left[\nabla_\mu U^\dagger \nabla^\mu U + \chi^\dagger U + \chi U^\dagger\right]\right\}\,, \qquad (3.18)$$

where the covariant derivative ∇_μ preserves the symmetry under chiral transformations [GL84, BKM95]

$$\nabla_\mu U = \partial_\mu U - i(v_\mu + a_\mu)U + iU(v_\mu - a_\mu)\,. \qquad (3.19)$$

The couplings to the external scalar and pseudoscalar field are contained in the field χ

$$\chi = 2B(s + ip)\,. \qquad (3.20)$$

Here we see that to leading order we have introduced two low-energy constants, F and B. In principle, these parameters are calculable in terms of the underlying parameters of QCD. Without exact solutions to QCD Green's functions they must be determined phenomenologically, such as by comparison with experiment.

The parameter f describes the normalisation of the field U and from its relation to the axial current is found to correspond to the value of the pion decay constant in the chiral limit.

With the quark mass being contained in the external field, s, the parameter B is therefore a measure of the scale of explicit chiral symmetry breaking in QCD. Expanding the symmetry-breaking component of Eq. (3.18) there is seen to be a vacuum expectation value proportional to the quark masses. Comparing with the underlying Hamiltonian, it is found that B is given by

$$B = \frac{m_\pi^2}{2\hat{m}} = -\frac{\langle \bar{q}q \rangle}{f^2}, \tag{3.21}$$

which we identify as the GOR relation seen above, Eq. (3.11). Using the physical values quoted above, B is found to be approximately $B \simeq 1.3\,\mathrm{GeV}$.

Contributions from next-to-leading order are systematically included by incorporating higher-derivative and quark-mass dependent terms in the $\mathcal{O}(p^4)$ Lagrangian, $\mathcal{L}_4$. In addition to the tree-level contributions from this Lagrangian, working to this order also requires that higher-order loop diagrams from the leading interactions, $\mathcal{L}_2$, must also be calculated. The complete power-counting therefore describes chiral perturbation theory as an expansion in quark-mass and momentum-dependent interactions, together with an expansion of increasing loop complexity [Wei79].

Extension to Baryons

We now wish to also outline a description of baryon fields in the low-energy effective field theory. One significant difference in the inclusion of the nucleon field is that it is non-chiral — the nucleon mass in the chiral limit is finite and similar in magnitude to the scale of chiral symmetry breaking. Care must be taken to ensure that the nucleon field transforms symmetrically under chiral transformations.

We collect the proton and neutron fields into a two component iso-vector

$$\Psi = \begin{pmatrix} \psi_p \\ \psi_n \end{pmatrix}. \tag{3.22}$$

We define a field $u(x)$ as the square-root of the matrix field $U(x) = u^2(x)$, with transformations given by Eq. (3.16),

$$U'(x) = V_R U V_L^\dagger = u'^2(x) \,. \tag{3.23}$$

We introduce the matrices K, which depend nonlinearly on $V_{R,L}$ and U, defined by

$$V_R u = u' K \,. \tag{3.24}$$

These matrices describe how the nucleon field transforms:

$$\Psi' = K\Psi \,. \tag{3.25}$$

For explicit definition of the corresponding covariant derivative of the nucleon field we refer the reader to Refs. [GSS88, BKM95].

We note that the transformation of the nucleon field describes direct couplings to the pion field. Our nucleon is therefore a fermion *dressed* by a sea of pions. The presence of the pions is therefore identified with our earlier discussion of the Goldstone field connecting degenerate vacua.

Because the nucleon field is heavy, we do not consider fluctuations of the nucleon field in the vacuum. Correspondingly, the nucleon field will not effect vacuum-to-vacuum transition elements as described by the pion-only Lagrangian. The nucleon field simply acts as a source field on incoming and outgoing asymptotic states. No processes will create or destroy the nucleon and we can consider an expansion in increasing, even powers of nucleon fields. For the present work, we will only be concerned with the 2-point, nucleon propagator and how it is modified by the interactions with the Goldstone field. The 4-point function would therefore correspond to an analysis of N–N scattering.

Expanding the πN interaction, defined through the covariant derivative, to leading order in the meson fields gives the lowest-order πN Lagrangian [BKM95, TW01],

$$\begin{aligned} \mathcal{L}_{\pi N}^{(1)} &= \overline{\Psi} \mathcal{D}^{(1)} \Psi \\ &= \overline{\Psi} \left\{ \partial\!\!\!/ - M_0 - \frac{g_A}{2f_\pi} \gamma_\mu \gamma_5 \boldsymbol{\tau} (\partial^\mu \boldsymbol{\pi}) \right\} \Psi \,. \end{aligned} \tag{3.26}$$

From this we can read off the pion-nucleon coupling, given by the Goldberger-Treiman relation [GT58]

$$g_{\pi NN} = g_A \frac{M_N}{f_\pi} \,, \tag{3.27}$$

which is exact in the chiral limit. The best empirical value for the pion-nucleon coupling, defined at the pion mass pole, is found to be $g_{\pi NN} = 13.32 \pm$

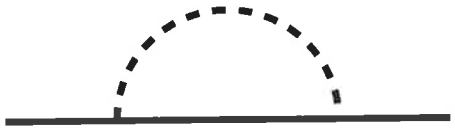

Figure 3.1: The pion-loop induced self-energy correction to the nucleon mass. The solid and dashed lines are the nucleon and pion respectively.

0.03(stat)±0.09(syst) [ELT02]. Inserting the physical values into Eq. (3.27) we produce an estimate of the coupling, 12.87, and observe that the relation is satisfied to $\sim 3\%$.

We have demonstrated how to incorporate the nucleon and the corresponding interactions with the Goldstone field in the framework of chiral effective field theory. We can now study the modifications to the nucleon field induced by coupling to the pion field.

3.3 Regularisation and Renormalisation

In order to define a calculation within a quantum field theory one must regularise and renormalise divergent loop diagrams. Clearly a physical theory is only tractable once quantities are made finite. Regularisation and renormalisation is the two step process of the removal of infinite divergences. Regularisation describes the process of quantifying the asymptotically divergent components of loop integrals. Renormalisation is the subsequent removal of these divergences such that results are finite and any dependence on the intermediate regularisation procedure is removed.

At this point we consider a specific example to discuss the issues of renormalisation. As it will figure prominently in this Thesis, we consider the one-loop pion correction to the nucleon mass as shown in Fig. 3.1. By summing this diagram as a geometric series, this loop is found to give an additive correction to the nucleon mass given by $\chi_\pi I_\pi$. Together with appropriate local-interaction terms, the nucleon mass to leading one-loop order can be expressed as

$$m_N = a_0 + a_2 m_\pi^2 + \chi_\pi I_\pi \,, \tag{3.28}$$

The parameters a_0 and a_2 come from the bare nucleon propagator and its leading quark-mass dependence respectively[3]. The πN vertex describes the leading loop

[3]The term giving rise to a_2 does not appear in the leading-order Lagrangian described by Eq. (3.26)

diagram and the LNA coefficient to the nucleon mass expansion

$$\chi_\pi = -\frac{3}{32\pi f_\pi^2} g_A^2 \,, \tag{3.29}$$

with corresponding loop integral I_π. In the heavy baryon limit, this integral over pion momentum is given by[4]

$$I_\pi = \frac{2}{\pi} \int_0^\infty dk \, \frac{k^4}{k^2 + m_\pi^2} \,. \tag{3.30}$$

This integral diverges as a cubic polynomial for large loop momentum. Its infrared behaviour gives the leading nonanalytic correction to the nucleon mass. This arises from the pole in the pion propagator at complex momentum $k = im_\pi$ and will be determined independent of how the ultraviolet behaviour of the integral is treated. Rearranging Eq. (3.30) we see that the pole contribution can be isolated from the divergent part

$$I_\pi = \frac{2}{\pi} \int_0^\infty dk \, \left(k^2 - m_\pi^2\right) + \frac{2}{\pi} \int_0^\infty dk \, \frac{m_\pi^4}{k^2 + m_\pi^2} \,. \tag{3.31}$$

The second term converges and is given simply by

$$\frac{2}{\pi} \int_0^\infty dk \, \frac{m_\pi^4}{k^2 + m_\pi^2} = m_\pi^3 \,, \tag{3.32}$$

where we now recognise the choice of normalisation of the loop integral, defined such that the coefficient of the LNA term is set to unity. This choice is purely convention and allows for a much more transparent presentation of the differences in the quark-mass expansion with various regularisation schemes.

In the most basic form of renormalisation we could simply imagine absorbing the infinite contributions arising from the first term in Eq. (3.31) into a redefinition of the coefficients a_0 and a_2 in Eq. (3.28). This solution is simply a minimal subtraction scheme and the renormalised expansion can be given without making reference to a renormalisation scale,

$$m_N = c_0 + c_2 m_\pi^2 + \chi_\pi m_\pi^3 \,, \tag{3.33}$$

with the renormalised coefficients defined by

$$c_0 = a_0 + \chi_\pi \frac{2}{\pi} \int_0^\infty dk \, k^2 \,, \tag{3.34}$$

$$c_2 = a_2 - \chi_\pi \frac{2}{\pi} \int_0^\infty dk \,. \tag{3.35}$$

[4]We demonstrate reduction from the relativistic, covariant form of this loop integral in Appendix A.

Equation (3.33) therefore encodes the complete quark mass expansion of the nucleon mass to $\mathcal{O}(m_\pi^3)$. This result will be precisely equivalent to any form of minimal subtraction scheme, where all the ultraviolet behaviour will be absorbed into the two leading coefficients of the expansion. The most commonly implemented form of minimal subtraction is carried out within the framework of dimensional regularisation.

Dimensional regularisation was first developed by 't Hooft and Veltman in 1972 [tHV72]. This procedure has had a profound impact within the field of elementary particle physics — in fact, this work earned the authors the Nobel Prize awarded in 1999. One of the primary features of this scheme is the preservation of local gauge symmetries. Alternative regularisation schemes, which break local gauge invariance, are not suited for elementary field theories constructed on the basis of local gauge symmetries — such as the Standard Model.

The procedure for performing the loop integral within dimensional regularisation is described in Appendix A. The final result to this discussion is that the result is precisely equivalent to the minimal subtraction scheme performed above. The finite part is given simply by m_π^3 and the coefficients, a_0 and a_2, are renormalised by the leading divergences of the loop integral.

We have hinted that dimensional regularisation is best suited for elementary field theories, comprised of point-like constituents. There is no intrinsic scale dependence to interaction vertices. As has been referred to in Chapter 2, the pion and nucleon are extend systems of finite structure and the high momentum components are necessarily suppressed.

A common example in proton structure, which highlights the momentum dependence of coupling to an extended object, is the electromagnetic form factor. We show the electric form factor of the proton in Fig. 3.2. This data at intermediate momentum transfer can be parameterised by a dipole form, $G_E^p = (1 + Q^2/\lambda^2)^{-2}$, with mass scale $\lambda^2 = 0.71\,\mathrm{GeV}^2$.

An external current coupled at zero momentum transfer ($Q^2 = 0$) determines the net charge of the object. Coupling at high momentum transfer is suppressed by the finite size of the proton's charge distribution. Physically, this can be reconciled by observing that the photon probe, of finite wavelength, only resolves a fraction of the net charge. The interaction of the pion and nucleon is quite similar in nature, with the πN form factor also being characterised by a dipole of mass $\sim 1\,\mathrm{GeV}$ [TW01].

An alternative regularisation scheme to that described by minimal subtraction, would be to suppress high-momentum contributions to loop diagrams by introducing a functional regulator which vanishes sufficiently fast for $k \to \infty$. Motivated by the physical form factor and the finite size of the nucleon, we refer to this prescription as *finite-range regularisation* (FRR).

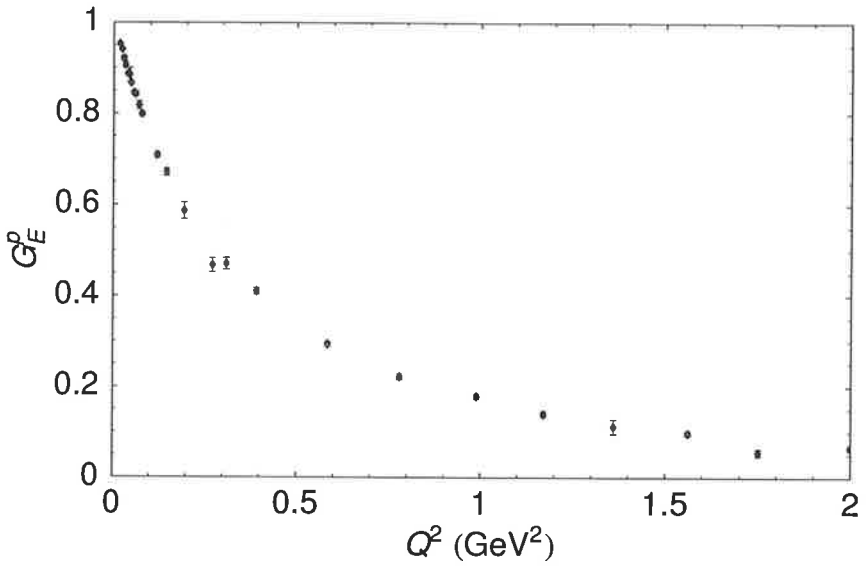

Figure 3.2: Experimental measurement of the proton's electric form factor — Hohler*et al.* [H+76].

In general, we implement FRR by introducing a regulator $u^2(k)$ which ensures the convergence of the integral for $k \to \infty$,

$$I_\pi^{\rm FRR} = \frac{2}{\pi}\int_0^\infty dk\, \frac{k^4}{k^2+m_\pi^2} u^2(k)\,. \tag{3.36}$$

For pedagogical purposes we select the simplest FRR to describe the renormalisation procedure. We integrate loop integrals to a sharp cut-off scale Λ, $u^2(k) = \theta(\Lambda - k)$. Various alternative regulators will be considered in the proceeding Chapter. For the sharp cut-off, Eq. (3.36) becomes

$$I_\pi^{\rm SC} = \frac{2}{\pi}\int_0^\Lambda dk\, \frac{k^4}{k^2+m_\pi^2}\,, \tag{3.37}$$

which upon explicit evaluation we find

$$I_\pi^{\rm SC} = \frac{2\Lambda^3}{3\pi} - \frac{2\Lambda}{\pi}m_\pi^2 + \frac{2}{\pi}m_\pi^3 \arctan\frac{\Lambda}{m_\pi}\,. \tag{3.38}$$

We can now consider the renormalisation of the quark-mass expansion by Taylor expanding this expression about the chiral limit

$$I_\pi^{\rm SC} = \frac{2\Lambda^3}{3\pi} - \frac{2\Lambda}{\pi}m_\pi^2 + m_\pi^3 - \frac{2}{\pi\Lambda}m_\pi^4 + \ldots\,. \tag{3.39}$$

Combining this expansion with the leading analytic terms in the expansion enables the appropriate renormalisation for the low-energy constants. Evaluating

Eq. (3.28) with a sharp cut-off FRR and expanding the result gives the renormalised expansion

$$m_N = a_0 + a_2 m_\pi^2 + \chi_\pi \left(\frac{2\Lambda^3}{3\pi} - \frac{2\Lambda}{\pi} m_\pi^2 + m_\pi^3 - \frac{2}{\pi\Lambda} m_\pi^4 + \dots \right) , \tag{3.40}$$

where for comparison with Eq. (3.33) we make the identification

$$c_0 = a_0 + \chi_\pi \frac{2\Lambda^3}{3\pi} , \tag{3.41}$$

$$c_2 = a_2 - \chi_\pi \frac{2\Lambda}{\pi} . \tag{3.42}$$

Substituting these expressions into Eq. (3.40), we find a renormalised expansion,

$$m_N = c_0 + c_2 m_\pi^2 + \chi_\pi m_\pi^3 - \chi_\pi \frac{2}{\pi\Lambda} m_\pi^4 + \dots , \tag{3.43}$$

which is precisely Eq. (3.33) up to $\mathcal{O}(m_\pi^3)$.

We have now demonstrated the mathematical equivalence of minimal subtraction and finite-range regularisation schemes. This renormalisation can be extended to any finite order in the quark-mass expansion to maintain equivalence.

A key feature of FRR is that the regularisation scale, Λ, remains finite. In a traditional approach to a vertex regularisation scheme as outlined, the scale parameter is removed by taking it to infinity. It is clear that as $\Lambda \to \infty$ we will simply recover exactly the same expression as given by a minimal subtraction scheme. With Λ as an adjustable parameter, the regularisation given here therefore includes a greater class of regularisation schemes, which incorporates minimal subtraction as a subset. A finite Λ allows efficiency in separating the long- and short-distance interaction scales [DHB99].

For the general case of Eq. (3.36) we describe the Taylor expansion as

$$I_\pi^{\mathrm{FRR}} = b_0 + b_2 m_\pi^2 + m_\pi^3 + \dots , \tag{3.44}$$

and the corresponding renormalisation is given by

$$c_0 = a_0 + \chi_\pi b_0 , \tag{3.45}$$

$$c_2 = a_2 - \chi_\pi b_2 . \tag{3.46}$$

With the infinities removed from our effective field theory, for two distinct regularisation prescriptions, we are now prepared to apply the developed theory to physical observables.

* * *

We have described the elementary features of the nature of chiral symmetry in low-energy QCD. In particular, the spontaneous breakdown of chiral symmetry and consequent appearance of approximate Goldstone bosons. With development of an effective field theory for QCD in the low-energy domain, we have described the construction of the quark-mass expansion of the nucleon mass about the chiral limit.

This quark-mass expansion relies on a regularisation and renormalisation prescription for dealing with ultraviolet divergent loop integrals. We have described a minimal subtraction and finite-range regularisation schemes.

The regularisation tools developed in this Chapter are the first step towards the construction of an appropriate extrapolation form for modern lattice QCD simulations. Before attempting the extrapolation problem we first wish to investigate the convergence properties of different regularisation schemes.

4

Convergence of the Quark Mass Expansion

We have shown in the previous Chapter that chiral perturbation theory provides us with a tool for constructing a quark-mass expansion of hadronic properties about the chiral limit. As described, there are issues to be considered in how to most efficiently regularise divergent loop integrals. With modern lattice QCD simulations restricted to the domain of heavy quarks, it is essential to minimise the errors associated with truncation of the chiral series. A quantitative analysis of the truncation process is of fundamental importance for the determination of the applicability of the effective field theory in the context of lattice QCD.

In this Chapter, we set out to systematically study the expansion of the nucleon mass about the chiral limit. We consider a number of different regularisation schemes in order to provide an unbiased assessment of the qualities of each scheme. We find that finite-range regularisation offers superior convergence properties over minimal subtraction, or dimensional regularisation. The main features of this research were originally published in Ref. [YLT03].

4.1 Issues of Convergence

An early study of the quark mass expansion in χPT was carried out by Hatsuda [Hat90] within the model framework of Nambu and Jona-Lasinio (NJL) [NJL61a, NJL61b]. The NJL model has had a wide ranging success in the application to QCD phenomena. Modern applications have included studies of the QCD phase diagram at large temperature and density [HK94, SKP99] and the structure of nuclear matter in medium [VW91, BT01]. Hatsuda considered various properties within the model, such as the quark condensate and meson decay constant. The quark mass dependence of these quantities could therefore be studied by changing the input parameters of the model. It was found that the quark-mass expansion about the chiral limit is quite slowly converging. In fact, truncating the series to just the first few terms was unable to reproduce the full result at the physical strange quark mass — with convergence to roughly $m_q \sim 30$–$50\,\mathrm{MeV}$. Remarkably, the discrepancies cancel in the calculation of the meson mass and

by coincidence the GOR relation ($m_\pi^2 \propto m_q$) is consequently found to hold over a wide range of quark mass.

The convergence properties of the quark mass expansion of the nucleon self-energy loops (I_π) was studied early on by Stuckey and Birse [SB97]. The pion-loop induced self-energy correction to the nucleon mass was evaluated with a finite-range regulator. Taylor expanding their expressions, they found that one would require terms beyond $\mathcal{O}(m_\pi^7)$ to reach convergence at the physical kaon mass.

These studies highlighted that there may be potential problems in truncating the chiral expansion as a naive Taylor series. With the smooth behaviour of lattice QCD results at moderate to large pion masses, as described in the previous Chapter, it was demonstrated early that successful application of the EFT requires a more sophisticated analysis [LTTW00]. The solution was realised in the physical description of the source of the pion field being of finite physical extent. This provided a natural mechanism for the suppression of chiral physics at larger quark masses consistent with the empirical observation in lattice QCD.

Studying the problem in further detail, we have found that these problems of convergence arise from the more fundamental issue of regularisation of effective field theory. The importance of regularising effective field theory at a finite mass scale, *below where the theory breaks down*, was addressed in a lecture series by Lepage [Lep97]. Applications of EFT within nuclear systems have also had a long-standing appreciation for the principle of a finite regularisation scale [vK99]. The formulation of chiral EFT with a finite-range (or long distance) regularisation was first developed by Donoghue *et al.* [DHB99], where they demonstrated dramatically improved convergence properties of the 3-flavour expansion incorporating the physical strange quark mass.

As an example case, Lepage [Lep97] considered the problem of solving the Schrödinger equation for an unknown potential by development of an EFT. The key physical idea of the effective field theory is to introduce an energy scale, λ, above which one does not attempt to understand the physics. For example, the energy region above that cut-off may involve new physics — e.g., in the very high energy limit, physics beyond the Standard Model. Because one does not pretend to control physics above the scale λ, one should not include momenta above λ in computing radiative corrections. Instead, one introduces renormalisation constants which depend on the choice of cut-off so that, to the order one works, physical results are independent of λ.

As Lepage points out, "it makes little sense to reduce a (ie. increase $\lambda \sim 1/a$) below the range" in which we understand the physics, because the "structure they see there is almost certainly wrong." When it comes to specific problems with the development of an effective theory of NN scattering, this line of argu-

ment leads him to conclude that "the problem is with dimensional regularisation — and not with effective field theory." In particular, dimensional regularisation involves integrating loop momenta in the EFT over momenta all the way to infinity — way beyond the scale where the effective theory has any physical significance.

In the present discussion of maximising the convergence of the chiral expansion, we learn from Lepage's investigation that one should *not* take the regulator parameter to ∞. Efficiency of the expansion will therefore be compromised by implementing dimensional regularisation, or any other equivalent minimal subtraction scheme. The most physically relevant theory will therefore be obtained by choosing a finite regulator scale, below where the theory omits essential physics, and constrain the renormalisation constants by matching to data. The process of determining the renormalised constants will therefore eliminate the dependence on the regulator.

Finite-range regularisation schemes are very well motivated by quite general physical arguments. The arbitrary nature of the choice of functional form of cut-off regularisation has raised questions of model-dependence [BL99,B+03]. These claims of model-dependence have not been quantified in any systematic fashion. We set out to make a detailed investigation of the level of model-dependence in finite-range regularisation. This study will also provide information on the convergence properties of the quark-mass expansion under various regularisation schemes.

4.2 Constraining the Chiral Expansion

To leading nonanalytic order the chiral expansion of the nucleon mass is given by

$$M_N^{(3)} = a_0 + a_2 m_\pi^2 + \chi_{N\pi} I_{N\pi}(m_\pi, \Lambda) + a_4' m_\pi^4 \,. \tag{4.1}$$

The superscript (3) is used to denote our power counting scheme, where we count in powers of the quark mass. The single pion-loop self-energy contribution to the nucleon mass has been written in a regularisation generic form. As outlined in the previous Chapter, divergences in the loop-integral must be regularised in order to obtain the renormalised expansion. The leading analytic terms in the expansion, ie. $m_\pi^{0,2}$, are generated by local terms in the chiral Lagrangian. The renormalised coefficients therefore are completely described by low-energy constants of the chiral Lagrangian to this order.

We have used a prime notation for a_4' to indicate that this parameter need not be explicitly calculated to this order. This parameter is chosen to minimise any residual model-dependence in the choice of regularisation scheme

[DHB99, YLT03, BHM04]. The necessity for inclusion of this term is amplified if working with the truncated Taylor series of dimensional regularisation. This was highlighted in Section 2.3 where the series truncated at m_π^3 failed to fit the data. Physically, the term a_4' acts as a counterterm to remove, as far as possible, any incorrect, ultraviolet behaviour from the loop contribution.

As an alternative procedure to the fitting of the next analytic parameter (a_4' in this case), the formulation of FRR allows freedom in the choice of regulator scale, Λ. The vastly improved convergence properties of FRR EFT are founded on the principle that the regulator parameter, Λ, remains finite. This leaves the task of choosing an appropriate value for the regulator parameter. At the same time, results from an acceptable EFT should be largely independent of the regulator parameter.

This raises an apparent contradiction to the formulation of a quantum field theory — we are attempting to choose an optimum value of Λ and still retain independence from this specific choice. The solution to this problem is to recall that the sensitivity of the results on the regulator parameter diminishes as the expansion is carried out to higher orders. Upon renormalisation, all discrepancies between differing Λ values are contained in the remaining higher-order terms. Hence the focus must be on improving the convergence properties of low orders of the chiral expansion. Optimizing Λ with higher-order terms of the residual series set to zero ensures that convergence will be enhanced. Calculating to beyond leading order in the expansion will then be guaranteed to be a small perturbation on the leading result.

Lattice simulation results combined with the experimental value gives a description of the nucleon mass over a wide range of quark mass. This offers the potential to obtain an *ab initio* estimate of the appropriate mass scale Λ which will minimise sensitivity to higher-order terms in the expansion. Being motivated by the physical πN form-factor, one would expect to regularise the dipole form at $\Lambda \sim 1.0\,\mathrm{GeV}$ or below. As shown by Eq. (3.43), choosing Λ large will produce results in exact agreement with minimal subtraction. Recent work of Bernard et al. [BHM04] classified the regime of sharp cut-off Λ required to produce results equivalent to dimensional regularisation.

Our leading-order fits therefore have three free fit parameters to be determined. We fit a_0 and a_2 of Eq. (4.1) for all regularisation schemes, in additional to a_4' for DR and Λ for FRR.

In Section 3.3 we described in detail the procedure for regularisation and renormalisation of the loop integral for dimensional regularisation, or equivalent minimal subtraction, and finite-range regularisation. In addition to the DR expansion, we study the expansion with numerous functional forms in the FRR

formalism. We select four different finite-range regulators, $u(k)$:

$$\text{Sharp cut-off (SC)} \qquad \theta(\Lambda - k) \tag{4.2}$$

$$\text{Monopole (MON)} \qquad \frac{\Lambda^2}{\Lambda^2 + k^2} \tag{4.3}$$

$$\text{Dipole (DIP)} \qquad \left(\frac{\Lambda^2}{\Lambda^2 + k^2}\right)^2 \tag{4.4}$$

$$\text{Gaussian (GAU)} \qquad \exp\left(-\frac{k^2}{\Lambda^2}\right) . \tag{4.5}$$

Functional forms, where available, for the integrals and corresponding renormalisation coefficients are given in Appendix A.

All regularisation schemes then give the following renormalised expansion about the chiral limit

$$M_N^{(3)} = c_0 + c_2 m_\pi^2 + \chi_{N\pi} m_\pi^3 + c_4' m_\pi^4 + \mathcal{O}(m_\pi^4) , \tag{4.6}$$

where now all expansions are identical up to $\mathcal{O}(m_\pi^3)$ and any regulator dependence is contained in c_4' and higher order terms. With the coefficient $\chi_{N\pi}$ set to its phenomenological value, there are three free parameters in order to constrain the expansion.

The ability to constrain these parameters precisely would require exact knowledge of how the nucleon mass varies over a range of quark masses. Experiment only offers a single quark mass and cannot constrain the expansion. The expansion can only be constrained by taking information from an alternative source.

Lattice QCD provides a non-perturbative method for studying the variation of M_N with m_q. In principle, this allows one to fix the parameters of the chiral expansion using data obtained in simulations performed at varying quark mass. With the lightest dynamical simulation data point at $m_\pi \sim 500\,\text{MeV}$ it is unclear, a priori, if the effective field theory maintains applicability to this scale of quark mass. Fortunately, the self-consistency found within our results indicate that the EFT can be reliably applied in this range of quark mass.

Making use of dynamical simulation results of lattice QCD enables us to constrain an expression for M_N as a function of the quark mass. In this study, we use results of a 2-flavour simulation of the CP-PACS Collaboration [AK+02]. The lattice results have been obtained using improved gluon and quark actions on fine, large volume lattices with high statistics. Specifically, simulations are performed using an Iwasaki gluon action [Iwa85] and the mean-field improved clover fermion action.

In this work we concentrate on only those results with $m_{\text{sea}} = m_{\text{val}}$ and the two largest values of β (i.e. the finest lattice spacings, $a \sim 0.09$–$0.13\,\text{fm}$). This

Reference	a (fm)	N	$m_\pi L$	m_π^2 (GeV^2)	M_N (GeV)
CP-PACS	0.130	24	15.1	0.9130(18)	1.798(4)
	0.123		12.4	0.6893(18)	1.643(5)
	0.118		10.2	0.5023(11)	1.497(6)
	0.111		7.1	0.2718(16)	1.275(7)
	0.102		12.0	0.9395(31)	1.809(15)
	0.099		10.1	0.7035(44)	1.652(9)
	0.095		8.5	0.5394(30)	1.519(9)
	0.092		6.7	0.3535(56)	1.348(12)

Table 4.1: Lattice data used to constrain the chiral expansion. We also display the physical lattice spacing and spatial dimension (N) of the lattice. Results from CP-PACS Collaboration [AK$^+$02].

Regulator	a_0	a_2	a_4	Λ	χ^2/dof
DR	0.885	3.51	3.10	$\cdots$	3.8
SC	1.274	0.691	$\cdots$	0.690	0.61
MON	2.763	0.446	$\cdots$	0.880	0.44
DIP	1.795	0.527	$\cdots$	1.380	0.46
GAU	1.324	1.423	$\cdots$	1.072	0.48

Table 4.2: Fit parameters, in units of appropriate powers of GeV, of the residual chiral series for various regularisation schemes to leading order, $\mathcal{O}(m_\pi^3)$. Determined by fitting to the physical nucleon mass and lattice data $< 0.8\,\mathrm{GeV}^2$.

ensures that the results obtained represent accurate estimates of the continuum, infinite-volume theory at the simulated quark masses. As described in Chapter 2, we use the QCD Sommer scale [EHK98a] to set the scale for each independent set of gauge field configurations. We list the data in Table 4.1.

Together with the physical nucleon mass, we use the lattice data lying below $m_\pi^2 < 0.8\,\mathrm{GeV}^2$ to constrain our leading-order expansion formula, Eq. (4.1). The resultant fits for various regularisation schemes are displayed in Fig. 4.1. The corresponding fit parameters are seen in Table 4.2. The parameters listed in this table are bare quantities and hence *renormalisation scheme dependent.* Comparison of the chiral expansion should only be performed upon renormalisation of the loop contributions. The resulting expansion coefficients of these leading-order fits are seen in Table 4.3. The level of agreement between the terms is excellent. Most notably, we highlight the power of renormalisation to remove

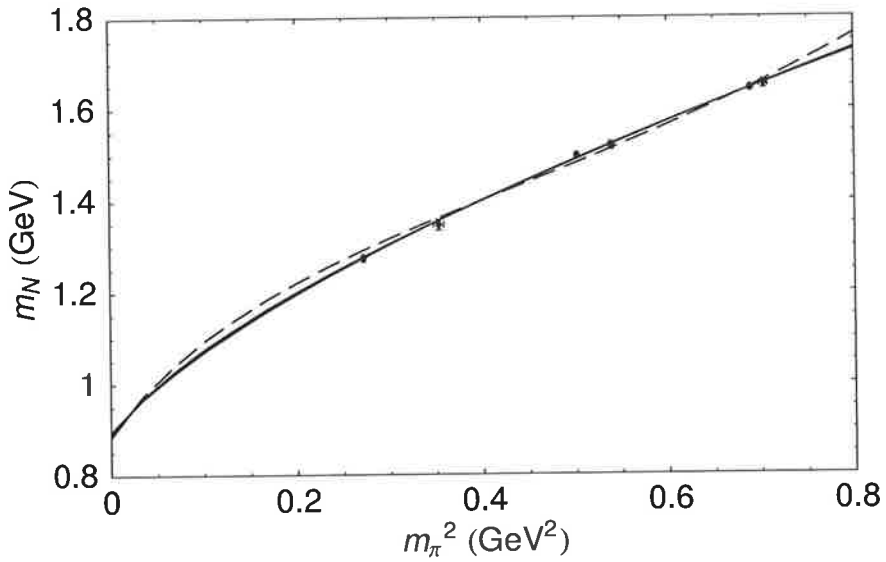

Figure 4.1: Leading order ($\mathcal{O}(m_\pi^3)$) fits for various regularisation expansions constrained to physical nucleon mass and lattice data. The solid lines depict the four FRR fits and the dashed curve shows the dimensionally regularised form.

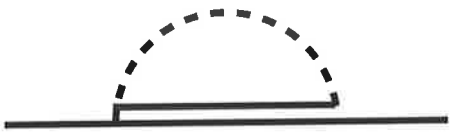

Figure 4.2: The $\pi\Delta$-loop self-energy correction to the nucleon mass. The solid, double and dashed lines are the nucleon, Δ and pion respectively.

the large discrepancies observed among the bare parameters.

It is evident from the χ^2/dof of the leading-order fit, that the expansion based on dimensional regularisation is incompatible with the lattice results up to pion masses $m_\pi^2 \sim 0.7\,\mathrm{GeV}^2$. The FRR expansions to this order produce qualitatively consistent results, although fitting the data does not quantify a convergent expansion. We therefore extend the analysis beyond leading order to include the next-to-leading nonanalytic contributions (NLNA) to the nucleon mass. Most importantly, we incorporate contributions arising from the one-loop π–Δ diagram.

The contribution to the nucleon mass from coupling to a $\pi\Delta$ intermediate state is shown in Fig. 4.2. This provides another term to the expansion given by

$$\chi_{\Delta\pi} I_{\pi\Delta}\,, \tag{4.7}$$

Regulator	c_0	c_2
DR	0.885	3.51
SC	0.892	3.10
MON	0.896	2.86
DIP	0.896	2.89
GAU	0.895	2.92

Table 4.3: Renormalised expansion parameters, in units of appropriate powers of GeV, for various regularisation schemes of leading-order fits, Eq. (4.6). Bare parameters shown in Table 4.2.

with $I_{\pi\Delta}$ describing the loop integral analogous to I_π. In the simplest form, where we use a minimal subtraction scheme (like dimensional regularisation) and with the N–Δ mass-splitting taken to be large, we obtain

$$I_{\pi\Delta}^{\mathrm{DR}} = -\frac{3}{4\pi\Delta} m_\pi^4 \log\frac{m_\pi}{\mu}\,, \tag{4.8}$$

with $\Delta = m_\Delta - m_N$ and μ a scale to define the logarithm. The coefficient describing this interaction is given by

$$\chi_{\Delta\pi} = -\frac{3}{32\pi f_\pi^2}\frac{8}{9}\mathcal{C}^2\,, \tag{4.9}$$

where we use the $SU(6)$ value for the coupling given by $\mathcal{C} = -2D$.

In the context of the expansion to large pion masses, it is important to realise that Eq. (4.8) used the approximation $m_\pi/\Delta \ll 1$. At just twice the physical pion mass this ratio approaches unity. Mathematically the region $m_\pi \approx \Delta$ is dominated by a square root branch cut which starts at $m_\pi = \Delta$. Using dimensional regularisation, the loop integral is given by [BM96]:

$$\begin{aligned} I_{\pi\Delta}^{\mathrm{DR(BP)}} = {} & \frac{1}{2\pi}\left(2\Delta^3 - 3m_\pi^2\Delta\right)\log\frac{m_\pi^2}{\mu^2} \\ & - \frac{1}{\pi}\left(\Delta^2 - m_\pi^2\right)^{3/2}\log\left(\frac{\Delta - \sqrt{\Delta^2 - m_\pi^2}}{\Delta + \sqrt{\Delta^2 - m_\pi^2}}\right)\,. \end{aligned} \tag{4.10}$$

for $m_\pi < \Delta$, while for $m_\pi > \Delta$ the second logarithm becomes an arctangent. To access the higher quark masses in the chiral expansion, currently of most relevance to lattice QCD, one requires a more sophisticated expression than that given by Eq. (4.8).

The loop integral with a finite-range regulator is given by

$$I_{\pi\Delta} = \frac{2}{\pi}\int_0^\infty dk\, \frac{k^4 u^2(k)}{\omega(k)[\Delta + \omega(k)]}\,, \tag{4.11}$$

with $\omega(k) = \sqrt{k^2 + m_\pi^2}$, in the limit $\Delta \to 0$ we identify this with Eq. (3.30). This form will automatically preserve the branch structure at $m_\pi = \Delta$. Similarly to the leading-order result, the finite contributions to the leading analytic terms in m_π^2 must be absorbed into the renormalised expansion. This time we must ensure that we carry out our renormalisation procedure including terms at m_π^4 to ensure that all[1] possible contributions are accounted for — the formal heavy-baryon expansion parameters at this order have been calculated by Steininger et al. [SMF98]. Similar to a_4' in Eq. (4.1), it will be necessary to allow freedom at the next analytic order, this time m_π^6, to absorb any residual regulator dependence.

In summary, we now have our nucleon mass expansion to NLNA given by

$$\begin{aligned} m_N &= a_0 + a_2 m_\pi^2 + a_4 m_\pi^4 + a_6 m_\pi^6 \\ &\quad + \chi_{N\pi} I_\pi + \chi_{\pi\Delta} I_{\pi\Delta} \,. \end{aligned} \tag{4.12}$$

Once again, with appropriate renormalisation, the expansion is equivalent for all regularisation schemes

$$\begin{aligned} m_N &= c_0 + c_2 m_\pi^2 + + \chi_{N\pi} m_\pi^4 + c_4 m_\pi^4 \\ &\quad - \chi_{\pi\Delta} \frac{3}{4\pi\Delta} m_\pi^4 \log \frac{m_\pi}{\mu} + \ldots \end{aligned} \tag{4.13}$$

We note that the scale of the logarithm implies a μ-dependence on the coefficient c_4,

$$c_4(\mu') = c_4(\mu) - \chi_{\pi\Delta} \frac{3}{4\pi\Delta} \log \frac{\mu}{\mu'} \,. \tag{4.14}$$

Determining c_4 from the data will ensure that there is no residual dependence on the scale. We choose to set $\mu = 1\,\mathrm{GeV}$.

We show the NLNA curves constrained to the physical nucleon mass and the lattice data in Fig. 4.3. We observe excellent qualitative agreement between all regularisation schemes to this order. The resulting expansion parameters are displayed in Table 4.4.

Similarly to the leading-order case, the dependence on the regularisation scheme is removed upon renormalisation, with the renormalised expansion coefficients given in Table 4.5. The level of agreement for the leading two terms, c_0 and c_2, is once again remarkable, particularly between the FRR schemes. We note that the values of c_4 among the latter three FRR schemes are consistent.

[1] The present analysis only considers the one-loop diagrams arising from the leading order Lagrangian. A tadpole loop arising from expansion of the explicit chiral symmetry breaking term is neglected.

Regulator	a_0	a_2	a_4	a_6	Λ	χ^2/dof
DR	0.882	3.82	6.65	−4.24	···	0.47
DR(BP)	0.825	4.37	9.71	−2.77	···	0.46
SC	1.03	1.12	−0.292	···	0.418	0.49
MON	1.56	0.884	−0.203	···	0.496	0.50
DIP	1.20	0.972	−0.229	···	0.785	0.49
GAU	1.12	1.02	−0.246	···	0.616	0.49

Table 4.4: Fit parameters, in units of appropriate powers of GeV, of the residual chiral series for various regularisation schemes to next-leading order, Eq. (4.12). Determined by fitting physical nucleon mass and lattice data $< 0.8\,\mathrm{GeV}^2$.

Regulator	c_0	c_2	c_4
DR	0.882	3.82	6.65
DR(BP)	0.884	3.64	8.50
SC	0.894	3.04	13.5
MON	0.898	2.80	23.4
DIP	0.897	2.84	22.0
GAU	0.897	2.87	20.6

Table 4.5: Renormalised expansion parameters, in units of appropriate powers of GeV, for various regularisation schemes of leading-order fits, Eq. (4.13). Bare parameters shown in Table 4.2.

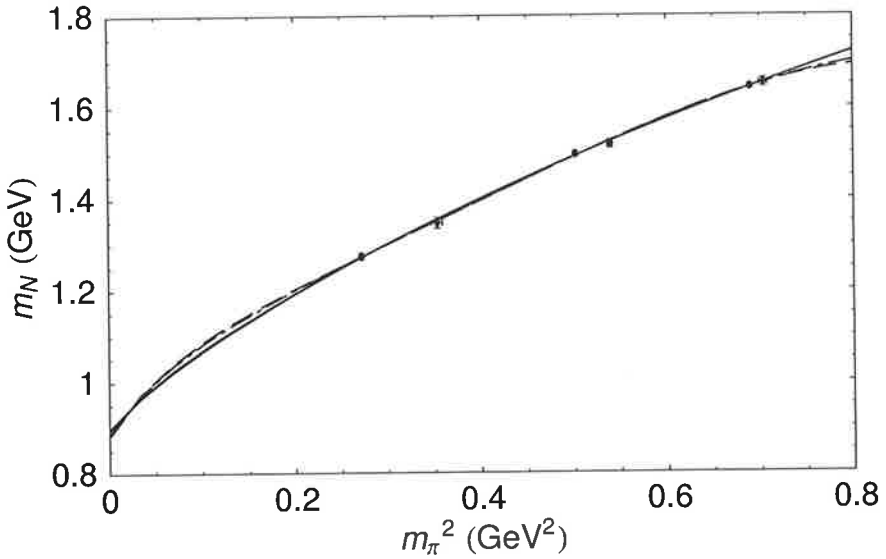

Figure 4.3: Next-leading order ($\mathcal{O}(m_\pi^4)$) fits for various regularisation expansions constrained to physical nucleon mass and lattice data. The solid lines depict the four FRR fits and the dashed and dash-dot curves show the dimensionally regularised forms, with and without the branch-point respectively.

The efficiency of the FRR schemes is highlighted by comparison between the bare and renormalised coefficients of m_π^4, a_4 and c_4. Whereas the renormalised coefficients are quite large for the three smooth FRR schemes, the bare coefficients of the residual expansion are a factor of 100 smaller. We remember that regularising the loop integrals with a finite-range regulator ensures that the contributions are suppressed for increasing pion masses. Divergences will arise from large coefficients in the residual series alone. By adjustment of Λ we observe FRR effectively distributing weight to the loop contributions and hence improving the convergence properties at large quark mass.

If we trust the renormalised expansion of the smooth FRR schemes then we can easily understand the behaviour of the DR fits. The dimensionally regularised curves have large values for the bare parameter a_4, yet the small (or zero) renormalisation does not yield a c_4 that is consistent with the magnitude of the FRR results. The DR schemes therefore fail to obtain a fit which is compatible with the large value of c_4 and smooth behaviour of the lattice data.

These six curves now represent our best estimates for the variation of the nucleon mass over a wide range of quark (pion) masses. We now wish to analyse each of these regularisations in an unbiased fashion. For each curve, we attempt to reproduce the given curve with each of the alternative regularisation

prescriptions. It is a fundamental tenet of quantum field theory, that *physical observables are independent of regularisation scheme.*

4.3 Investigating Regularisation Equivalence

In the limit of vanishing quark mass, the expansions given by all regularisation schemes are identical. One can therefore switch from one scheme to another without loss of generality — provided one is close enough to the chiral limit. Of more practical importance in the present context, is the issue of the range of quark masses where regularisation schemes maintain their equivalence.

We make use of the six constraint curves, $M(m_\pi)$, as determined at NLNA in the previous section. We then attempt to reproduce the same curve by any other regularisation scheme. By doing a one-to-one comparison over different ranges of pion mass we are able to determine the effective convergence range of each scheme.

For each constraint curve, $M(m_\pi)$, we have six *test* regularisation schemes, $F(m_\pi)$. We refit the free parameters of the test curves to the constraint over increasing windows of pion mass.

This is achieved by defining our matching criteria between two curves by the measure χ^2, which defines a normalised, mean-square area between the curves,

$$\chi^2(m_W, \bar{\delta}) \equiv \frac{\int_0^{m_W^2} dm_\pi^2 \, [F(m_\pi) - M(m_\pi)]^2}{\int_0^{m_W^2} dm_\pi^2 \, \bar{\delta}^2} \tag{4.15}$$

$$= \frac{1}{m_W^2 \, \bar{\delta}^2} \int_0^{m_W^2} dm_\pi^2 \, [F(m_\pi) - M(m_\pi)]^2 \, , \tag{4.16}$$

where we normalise to an average deviation of $\bar{\delta}$, which we choose to set at $\bar{\delta} = 1\,\mathrm{MeV}$. For computational purpose, we approximate the integral over m_π^2 by the Riemann sum, dividing the region into N segments of size $h = m_W^2/N$,

$$\int_0^{m_W^2} dm_\pi^2 \, f(m_\pi^2) \to h \sum_{i=1}^{N} f(ih) \, , \tag{4.17}$$

with h fixed to $0.001\,\mathrm{GeV}^2$. For each upper limit, m_W^2, the measure χ^2 is minimised in the parameter space of the test function form, $F(m_\pi)$.

All regularisation prescriptions have precisely the same structure in the limit $m_\pi \to 0$. As our test window moves out to larger pion mass the variation of χ^2 will describe the utility of each expansion. Accurate reproduction of the expansion coefficients also serves to test the convergence over a given range.

The variation of χ^2 as a function of the upper limit of the curve matching window, m_W, is plotted in Fig. 4.4. By our choice of normalisation, $\bar{\delta} = 1$, a measure $\chi^2 = 1$ corresponds to an average deviation between the curves of 1 MeV. The first feature that one notices is that, if the BP scheme is used as the constraint curve, *all* schemes are able to describe it very well for m_π^2 up to $\sim 0.5\,\mathrm{GeV}^2$ and beyond. On the other hand, we see from the lower four graphs of Fig. 4.4 that DR the form is only equivalent to the FRR forms up to $\sim 0.3\,\mathrm{GeV}^2$, with the BP curve performing marginally better, $\sim 0.35\,\mathrm{GeV}^2$. This already provides an indication that the FRR forms are more adaptable to describe the expansion over a wider range of pion masses.

In contrast between these significant discrepancies between the FRR and DR schemes, the agreement between the different FRR formulations is exceptional. Marginal differences are observed between the sharp cut-off and the smooth FRR forms. The error between the monopole, dipole and Gaussian forms are below the resolution of this plot. This is an exceptional result, especially considering the wide range of quark masses considered, and puts to rest any questions of model-dependence in the choice of regulator, such as raised by Refs. [BL99, B$^+$03, BHM04]. The improved convergence properties of the FRR schemes are observed to be independent of the functional form of regulator. This highlights the importance of the rapid convergence of the residual series of the FRR expansions, in contrast to the large divergences encountered with the DR forms.

Perhaps a more important measure of the applicability of a given scheme is the ability to accurately produce the low-energy constants of the renormalised chiral expansion. We test how well the these parameters are reproduced as the curve-matching window is increased. Taking the same best-fit parameters as obtained from our curve-matching measure over a given range of pion masses, we extract the renormalised expansion parameters. With the branch-point DR curve taken as our constraint, we show the leading term, c_0, as a function of the curve-fitting window in Fig. 4.5. A similar curve, with the dipole form taken as the constraint, is shown in Fig. 4.6.

It is clear from Fig. 4.5 that, whatever scheme is used to extract c_0 from the BP constraint curve, it is determined with an accuracy better than 1% — as long as the fitting window is smaller than $0.7\,\mathrm{GeV}^2$. Our 1% cut is defined such that the contribution from the given term to the physical nucleon mass is accurate to within 1%. This means for c_0 we have $\delta c_0/M_N < 1\%$ or in the case of c_2, we require $\delta c_2 m_\pi^2/M_N < 1\%$.

With the dipole as the constraint, Fig. 4.6 shows that the dimensional regularisation schemes do not give an accurate description of c_0 once the matching window extends beyond $0.5\,\mathrm{GeV}^2$. Conversely, all the FRR schemes are in ex-

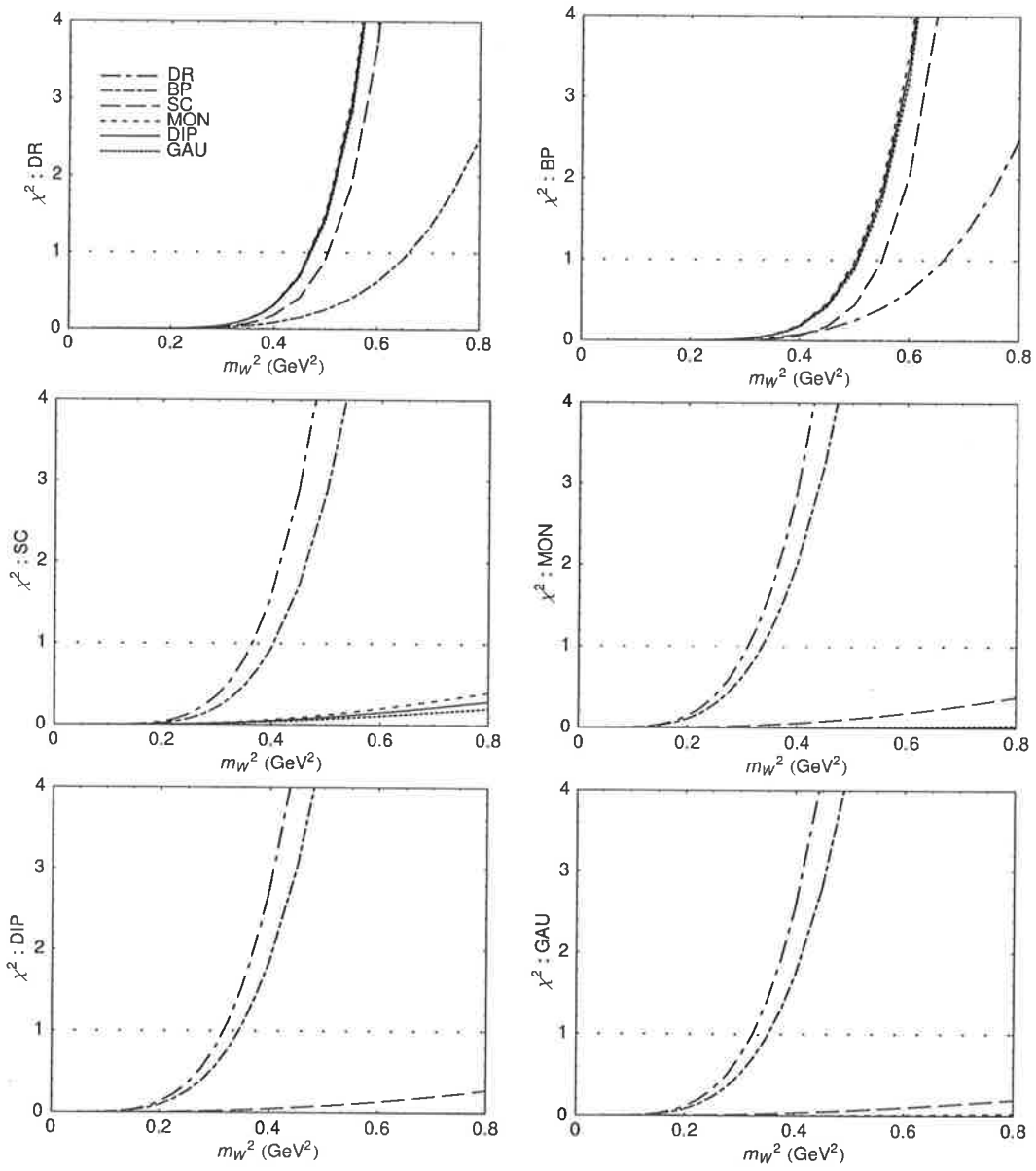

Figure 4.4: Mean-square area between the constraint curve (indicated on the ordinate) and each of the test curves, plotted as a function of the curve fitting window $(0, m_W^2)$. Normalisation chosen such that $\chi^2 = 1$ describes a fixed deviation of 1 MeV.

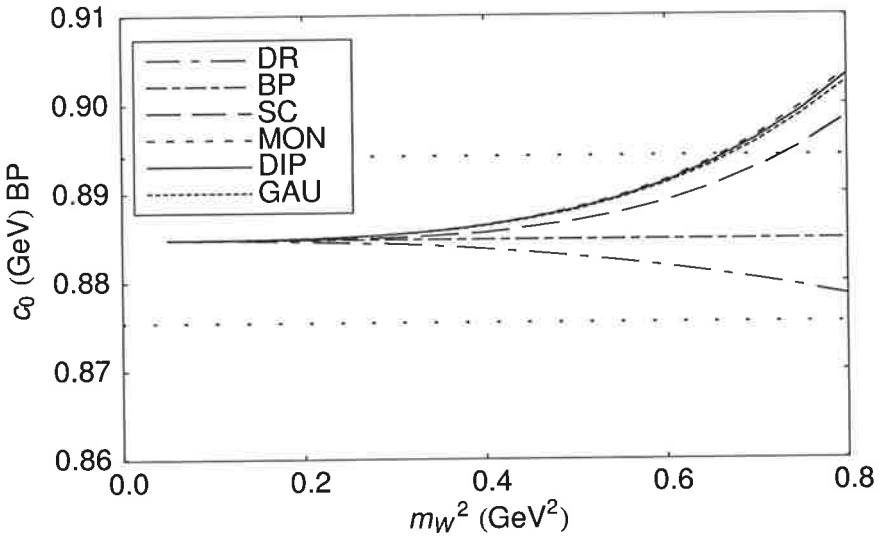

Figure 4.5: Recovered c_0 from various regularisation schemes constrained to the dimensionally regularised (BP) curve. c_0 is plotted as a function of the curve-fitting window $(0, m_W^2)$. The dashed horizontal line indicates the maximum deviation of c_0 to within 1% of the physical nucleon mass.

cellent agreement over the entire range.

For the coefficient c_2, Figs. 4.7 and 4.8 display similar results to those found for the leading term. All methods yield the correct value of c_2 based on the BP constraint curve within 1% out to a fit window of $0.7\,\mathrm{GeV}^2$. We highlight that the breakdown beyond $0.7\,\mathrm{GeV}^2$ does not come as a surprise, since the original BP curve already encounters a power divergence beyond the last constraint from the lattice data, as seen in Fig. 4.3.

With the FRR forms taken as the constraints, the dimensionally regularised forms fail to accurately reproduce c_2 beyond $0.4\,\mathrm{GeV}^2$. We show the case of the dipole constraint in Fig. 4.8. The agreement between all FRR schemes is once again found to be remarkable over the entire range.

The results found in this section demonstrate that one cannot use a chiral expansion based upon dimensional regularisation, to the order described, to analyse data with m_π^2 over an upper limit around $0.4\,\mathrm{GeV}^2$. This is assuming that one has perfect data all the way down to the chiral limit. In a practical case of a lattice QCD simulation, there will be limited data points of finite accuracy and, most importantly, restricted to values above some lower-bound in m_π^2. These considerations mean that using DR-based forms, for analysis of lattice data, will be restricted to the case where all of the data included must lie

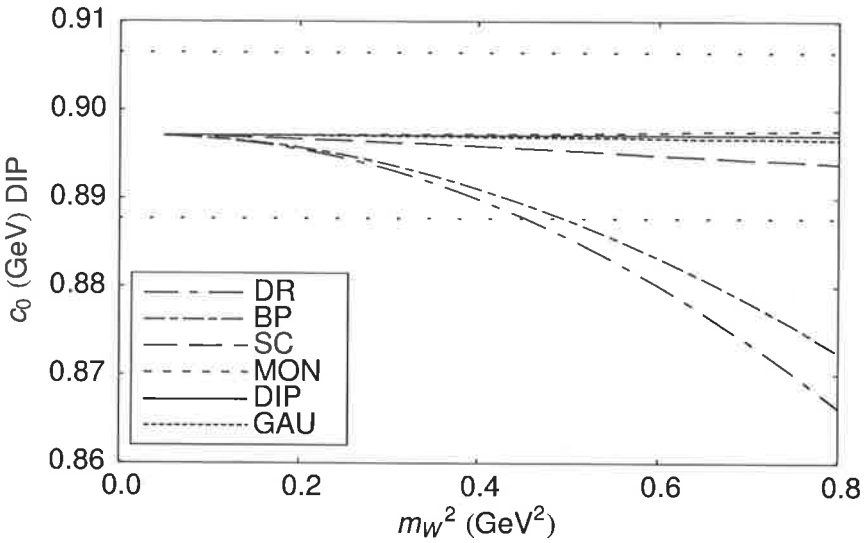

Figure 4.6: Recovered c_0 from various regularisation schemes constrained to the dipole regularised curve. c_0 is plotted as a function of the curve-fitting window $(0, m_W^2)$. The dashed horizontal line indicates the maximum deviation of c_0 to within 1% of the physical nucleon mass.

well below $m_\pi^2 < 0.4\,\mathrm{GeV}^2$. With the described alternative given by FRR, it is apparent that the improved convergence properties will enable reliable analysis of lattice data in the region up to $0.8\,\mathrm{GeV}^2$ or greater. This is a regime where we already have impressive data from CP-PACS [AK+02, N+04], MILC [B+01], JLQCD [A+03] and QCDSF-UKQCD [AK+04]. In particular, the FRR approach offers the ability to extract reliable fits where the low-mass region is excluded from the available data, ie., application to the *chiral extrapolation problem* — this will be addressed in detail in the proceeding Chapter.

4.4 Enhanced Convergence with FRR

As to be expected from the formulation of the effective field theory, we have demonstrated the equivalence of all regularisation schemes for the expansion about the chiral limit. In particular, we have found that the low-energy expansion coefficients are consistent between all regularisations, both DR and FRR, provided one limits the range of pion masses to $m_\pi^2 \leq 0.4\,\mathrm{GeV}^2$. The formalism of FRR offers the ability to extend the applicable range beyond that permitted within a DR expansion. We find that all the FRR curves are able to describe any of the expansions, including those constrained within DR, over a significantly

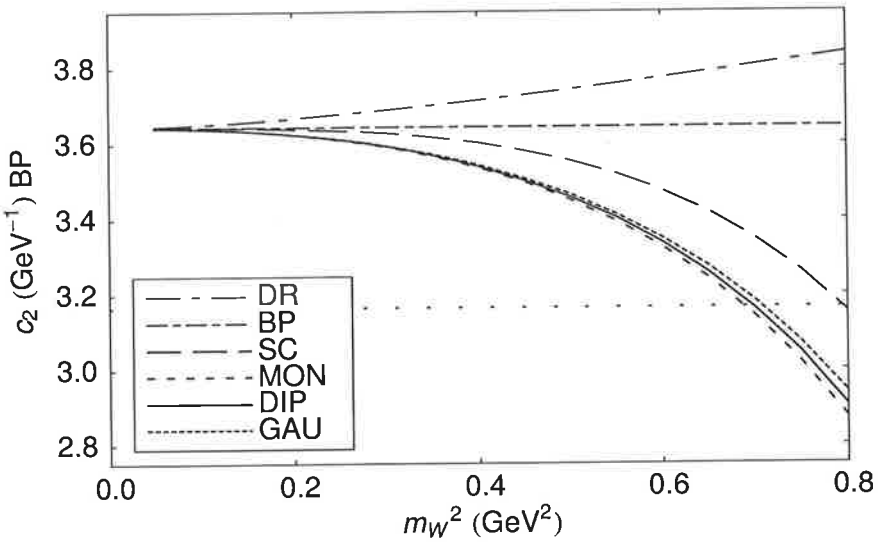

Figure 4.7: Recovered c_2 from various regularisation schemes constrained to the dimensionally regularised (BP) curve. c_2 is plotted as a function of the curve-fitting window $(0, m_W^2)$. The dashed horizontal line indicates the maximum deviation c_2 can take such that the error in the quantity $c_2 m_\pi^2$ is less than 1% of the physical nucleon mass at the physical pion mass.

enhanced range of pion masses $0 \leq m_\pi^2 \leq 0.7\,\mathrm{GeV}^2$.

This range can be extended further by acknowledging that the DR curves are not applicable beyond $m_\pi^2 \sim 0.4\,\mathrm{GeV}^2$. Therefore the original constraint curves, which fit lattice data up to $m_\pi^2 \sim 0.7\,\mathrm{GeV}^2$, are beyond the reliable range of the expansion. Considering just the FRR schemes, we observe equivalence over the entire range of pion masses considered $0 \leq m_\pi^2 \leq 0.8\,\mathrm{GeV}^2$. The agreement between the three smooth FRR scheme is incredibly precise. We therefore conclude that the use of dimensional regularisation is not efficient for the present application of effective field theory.

The failure of dimensionally-regularised χPT can be understood by recognising that the only mass scale appearing is that of the pseudoscalar meson. As the pseudoscalar mass increases, physical processes become dominated by short-distance physics. Because the loop contributions are not suppressed for large momentum scales, the chiral loops are therefore modeling the high-energy behaviour of the theory; beyond the regime which is well described by the low-energy effective field theory. At these higher momentum scales the hadronic degrees of freedom are no longer elementary, but composed of a finite structure of QCD constituents, quarks and gluons. The point-like interactions described

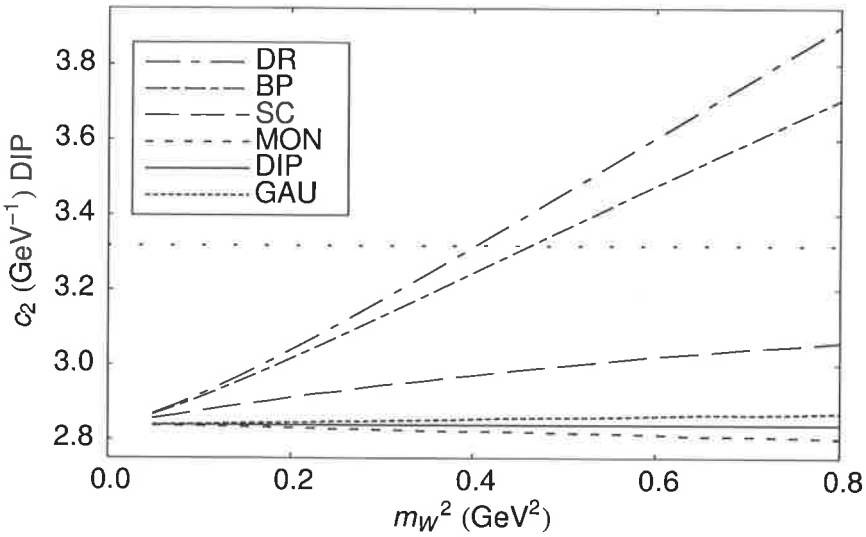

Figure 4.8: Recovered c_2 from various regularisation schemes constrained to the dipole regularised curve. c_2 is plotted as a function of the curve-fitting window $(0, m_W^2)$. The dashed horizontal line is as described in Fig. 4.7.

by DR therefore leads to a badly divergent series expansion at higher order.

Fortunately the separation of scales, between low- and high-energy, can be achieved by incorporating a finite energy scale, above which loop contributions are suppressed. This scale is easily identified as the finite size of the nucleon — in particular, the size of the pion-field source. As described in Section 2.3, this is a physical scale, $\Lambda_{SOURCE} \sim 1/\langle r^2 \rangle_{\text{axial}}^{1/2} \sim 0.3$–$0.4\,\text{GeV}$, and surprisingly small. The finite size of the nucleon will only be generated in the dimensionally-regularised expansion at higher order.

Similar to the shift from the logarithm to the arctangent in the explicit treatment of the Δ in the branch-point DR expansion, one should not expect a series expansion to be compatible beyond $\sim \Lambda_{SOURCE}$, without incorporation of this scale. The FRR formalism can then be seen as treating this scale nonperturbatively and therefore permits a reliable expansion up to and beyond Λ_{SOURCE}.

Although the FRR procedure relies on choosing a functional form of regulator, we conclude that the physical expansion is insensitive to this choice. This result is a consequence of the procedure which guarantees the stability under truncation of higher-order terms. Higher-order terms, which are implicit in the structure of FRR, are essentially summing to zero in the regime of large quark masses such that the chiral series is stable to truncation.

The regularisations described have been derived rigorously up to the order

one is working, such as $\mathcal{O}(m_\pi^4)$ in the NLNA curve presented in this Chapter. Any regularisation scheme cannot therefore be taken to give any information on the higher order terms in the expansion. We find, nevertheless, that the three smooth FRR schemes give rise to a significantly large m_π^5 contribution.

The two-loop calculation of the m_π^5 term in heavy-baryon χPThas been calculated by McGovern and Birse [MB99]. These contributions are intimately related to the Goldberger-Treiman relation [GT58] and the deviation of the πNN coupling from the chiral limit. Importantly, the m_π^5 coefficient[2] arises from quark-mass variation of the axial coupling g_A/f_π and the Q^2-dependence of the πNN form factor [YLMT]. In addition to a small correction to the m_π^5 coefficient, the variation of the coupling gives rise to a new nonanalytic contribution at $m_\pi^5 \log m_\pi$. The Q^2-dependence of the interaction dominates the m_π^5 correction. The monopole, dipole and Gaussian forms of FRR already imitate this Q^2 variation and hence, for the respective Λ values, give a coefficient consistent with the two-loop calculation of McGovern and Birse. Thereby, we observe that the one-loop calculation in FRR is already giving rise to a reasonable approximation to higher-order contributions in dimensionally regularised χPT.

The one-loop estimates of the m_π^5 contribution are certainly model-dependent — they depend on Λ^{-2}. Going to higher order in the chiral expansion will remove this Λ-dependence through renormalisation [YLT]. Importantly, these higher-order corrections will only appear as small perturbations from the one-loop estimates. The convergence of the FRR expansions is therefore manifest.

The precise agreement between the smooth finite-range regulated results over the entire pion-mass range considered, $0 \leq m_\pi^2 \leq 0.8$ GeV^2, confirms that the shape of the regulator is irrelevant provided that the regulator parameter is optimised by the fit to the data. The approach is systematically improved by simply going to higher order in the chiral expansion, introducing additional analytic terms as appropriate to maintain model independence.

* * *

With a selection of regularisation schemes we obtain our best estimate of the nucleon mass variation over a wide range of quark masses. Using the physical nucleon mass and modern lattice QCD simulation data enables us to constrain the parameters of the NLNA chiral expansion of the nucleon mass. General principles of quantum field theory tell us that we should be able to change

[2] At higher orders it is important to account for discrepancies of the GOR relation, such that $m_\pi^5 \not\propto m_q^{5/2}$. Since we are working with lattice masses, we always use the renormalised pion mass m_π.

regularisation scheme without changing our physical conclusions. This feature is observed is the low-energy, low-quark-mass regime, where the theory is well-defined.

We find that the use of dimensional regularisation, in the context of the quark mass expansion, for the effective field theory restricts the convergence of the chiral series. At best, we find that the NLNA extrapolation based on DR(BP) is only applicable at pion masses below $m_\pi^2 < 0.4\,\mathrm{GeV}^2$. As an alternative to DR, we find that finite-range regularisation offers superior convergence properties over a much wider range of pion mass — in fact, convergence is observed over the entire range considered $m_\pi^2 \lesssim 0.8\,\mathrm{GeV}^2$.

The characteristic feature of FRR is the finite regulator scale which acts to give a physical description of the finite size of the pion-nucleon interaction. Mathematically, this scale offers the advantage to enhance the convergence of the expansion by minimising the divergences of the residual chiral series. Importantly, the results are insensitive to the choice of ultra-violet regulator and display no dependence on the functional form.

The techniques described using FRR, therefore mean that we have a reliable chiral expansion for performing a *model-independent* chiral extrapolation of modern lattice QCD data.

5

Nucleon Mass Extrapolation for Lattice QCD

As outlined in the Introduction, the chiral extrapolation problem is of fundamental importance for modern lattice QCD simulations to make contact with physical observations of Nature. The character of chiral symmetry breaking in low-energy QCD complicates the problem, because hadron properties exhibit nonanalytic variation with quark mass.

Fortunately, these nonanalytic structures involve coupling constants defined in the chiral limit, which are essentially model-independent [LP71]. The only further obstruction they add is that the ultra-violet behaviour of the loop integrals must be regularised. With the results of Chapter 4 at hand, we find that FRR techniques in chiral EFT are best suited for the chiral extrapolation problem.

We constrain the free parameters of the chiral expansion to the lattice data alone. In contrast to the previous Chapter, we no longer constrain the theory to the physical nucleon mass and therefore provide a true *extrapolation* to the physical regime. This enables us to determine the best theoretical calculation of the nucleon mass from nonperturbative QCD. The principal results discussed in this Chapter have appeared in Ref. [LTY04].

5.1 Extrapolation Formula

We review the formulae for the chiral expansion of the nucleon mass as described in detail in Chapter 4. To leading nonanalytic order, $\mathcal{O}(m_\pi^3)$ we use the following expression to fit lattice QCD data, Eq. (4.1)

$$M_N^{(3)} = a_0 + a_2 m_\pi^2 + a_4 m_\pi^4 + \chi_{N\pi} I_\pi(m_\pi, \Lambda)\,. \tag{5.1}$$

The regulator dependence remains implicit, with details of the regularisation and renormalisation prescriptions have been shown in Section 3.3 and Appendix A. For example, in dimensional regularisation we have the form

$$M_N^{(3)\mathrm{DR}} = c_0 + c_2 m_\pi^2 + a_4 m_\pi^4 + \chi_{N\pi} m_\pi^3\,, \tag{5.2}$$

Figure 5.1: The tadpole-loop correction to the nucleon mass. The solid and dashed lines are the nucleon and pion, respectively.

with the parameters c_0, c_2 and a_4 to be determined from lattice data. For comparison, we also show the dipole FRR form

$$M_N^{(3)\mathrm{DIP}} = a_0 + a_2 m_\pi^2 + a_4 m_\pi^4 + \chi_{N\pi} \frac{\Lambda^5 (m_\pi^2 + 4 m_\pi \Lambda + \Lambda^2)}{16 (m_\pi + \Lambda)^4}, \tag{5.3}$$

with free parameters a_0, a_2 and a_4. We note that the differing fit parameters, a_i and c_i, are defined for simplicity with no loss of generality. Whereas with the dipole, it is convenient to fit the bare parameters, this is not possible in DR because these values are set to infinity through the renormalisation procedure.

We also summarise our functional extrapolation forms for going beyond leading order. In particular, we include contributions arising from coupling to the decuplet Δ-baryon as described in the previous Chapter. We again study both forms of the Δ–π diagram — with and without the correct branch structure at $m_\pi = M_\Delta - M_N$. For the extrapolation analysis we also include a *tadpole* loop contribution arising from expansion of the $\mathcal{O}(m_q)$ chiral Lagrangian, as shown in Figure 5.1. A chiral invariant expansion in higher powers of the pion field generates this $\pi\pi NN$ vertex proportional to the quark mass. The tadpole loop produces a nonanalytic contribution at $m_\pi^4 \log m_\pi$, being the same order as the $\Delta\pi$ interaction. By including this additional contribution we ensure that we have all nonanalytic contributions to $\mathcal{O}(m_\pi^4)$ in the heavy-baryon expansion.

The tadpole diagram appears with a coupling proportional to the renormalised m_q expansion coefficient, c_2. The corresponding loop integral can be expressed as

$$I_{\mathrm{tad}} = m_\pi^2 \int dk \frac{2k^2}{\sqrt{k^2 + m_\pi^2}}, \tag{5.4}$$

with coefficient given by

$$\chi_{\mathrm{tad}} = -c_2 \frac{3}{16\pi^2 f_\pi^2}. \tag{5.5}$$

We note that in evaluating I_{tad} with a FRR we must subtract the leading con-

stant from the integral such that the renormalisation of c_2 remains linear,

$$\tilde{I}_{\rm tad} = m_\pi^2 \int dk \left\{ \frac{2k^2}{\sqrt{k^2+m_\pi^2}} - 2k \right\} u^2(k) \,. \tag{5.6}$$

With these two additional contributions we now have our complete expression for the extrapolation formula at next-to-leading order, $\mathcal{O}(m_\pi^4)$,

$$\begin{aligned} m_N^{(4)} &= a_0 + a_2 m_\pi^2 + a_4 m_\pi^4 + a_6 m_\pi^6 \\ &\quad + \chi_\pi I_\pi + \chi_{\pi\Delta} I_{\pi\Delta} + \chi_{\rm tad} \tilde{I}_{\rm tad} \,. \end{aligned} \tag{5.7}$$

Expressions for the loop integrals for the various regularisation schemes are shown in Appendix A, with the corresponding renormalised expansions given in Appendix B. In the simplest dimensionally regularised form the renormalised expression is given by

$$\begin{aligned} M_N &= c_0 + c_2 m_\pi^2 + \chi_{N\pi} m_\pi^3 + c_4 m_\pi^4 \\ &\quad + \left(-\chi_{\pi\Delta} \frac{3}{4\pi\Delta} + \chi_{\rm tad} \right) m_\pi^4 \log \frac{m_\pi}{\mu} + c_6' m_\pi^6 . \end{aligned} \tag{5.8}$$

The scale-dependence of c_4 has been left implicit and all calculations are performed with $\mu = 1\,\text{GeV}$.

We remind the reader that all regularisation schemes are equivalent to this order of the chiral expansion.

The key feature of finite-range regularization (FRR) is the presence of an additional adjustable regulator parameter which provides an opportunity to suppress short distance physics from the loop integrals of the effective field theory. This short-distance physics is otherwise treated incorrectly, as the effective fields are not realized in QCD at short distances.

The advantage of FRR is offered in the ability to shift weight between the loop integrals and the residual expansion, characterised by the *bare* parameters, a_i. Whereas the residual expansion will encounter a power divergence as m_π becomes large, the FRR loop integrals will tend to zero as a power of Λ/m_π. Since lattice calculated masses are observed to be smoothly varying [TLY03], there should exist a range of Λ values for which the residual series is reliably convergent.

Tuning a precise value of Λ is unnecessary, as the higher order terms are effectively summing to zero where the lattice data is being fit. In addition, the extrapolation of lattice data has no information in the light-quark regime and therefore prevents an accurate determination of an adjustable Λ. We therefore choose the best-fit Λ (rounded to the nearest 100 MeV) found in the NLNA fits of Section 4.2.

Regulator	a_0	a_2	a_4	Λ	χ^2/dof
Dim. Reg.	0.715	4.24	2.38	–	0.96
Sharp Cutoff	1.00	1.14	−0.286	*0.4*	0.40
Monopole	1.27	1.01	−0.241	*0.5*	0.40
Dipole	1.10	1.05	−0.251	*0.8*	0.40
Gaussian	1.01	1.57	−0.266	*0.6*	0.40

Table 5.1: Bare, unrenormalised, parameters extracted from the leading-order fits to lattice data. All quantities are in units of appropriate powers of GeV.

5.2 Results

We fit our extrapolation curves to recent nucleon mass data obtained in lattice QCD by CP-PACS [AK+02]. This is the same data considered in the previous Chapter — with an additional two points in the range $0.8 < m_\pi^2 < 1.0\,\mathrm{GeV}^2$. These results have been obtained using a high statistics ensemble, which has enabled very precise measurements for a number of quark masses. It is only the extreme precision of the data which allows the determination of as many as four fit parameters to be reliably determined. Because this group used the mean-field improved clover fermion action with an Iwasaki gauge action on fine lattices and large volumes, we assume that the results represent accurate estimates of the infinite-volume, continuum theory. The simulation results are shown in Table 4.1, where it is observed the physical lattice spacings are in the range $a \sim 0.09$–$0.13\,\mathrm{fm}$ and all lattice volumes respect the condition $m_\pi L > 2\pi$.

We first fit the data with the leading-order expansion given by Eq. (5.1). The resultant fit parameters are shown in Table 5.1. The corresponding fit curves are shown in Fig. 5.2. To this order, we observe that all FRR prescriptions are in excellent agreement with each other and give a good description of the physical nucleon mass. The dimensionally regularised curve does not offer the same level of agreement as the FRR curves. We compare the renormalised expansion coefficients from the various fits in Table 5.2.

We now attempt to fit our next-to-leading order form, $\mathcal{O}(m_\pi^4)$, given by Eq. (5.7). The resultant fit parameters are shown in Table 5.3. The large coefficients of the residual series for the DR forms suggests that there could potentially be significant errors associated with the truncation of the series at this order. In particular, the large value of a_4 means that the fit curves are diverging rapidly with pion mass. The coefficient a_6 appears small but is significantly larger than the FRR counterparts. In contrast, the small values for a_4 and a_6 for the FRR curves, combined with the convergent large-m_π behaviour of the loop contribu-

Regulator	c_0	c_2
Dim. Reg.	0.715	4.24
Sharp Cutoff	0.931	2.53
Monopole	0.928	2.38
Dipole	0.927	2.42
Gaussian	0.930	2.40

Table 5.2: Renormalised expansion coefficients extracted from the leading-order fits to lattice data. All quantities are in units of appropriate powers of GeV.

Regulator	a_0	a_2	a_4	a_6	Λ	χ^2/dof
Dim. Reg.	0.827	3.58	3.63	−0.711	–	0.43
Dim. Reg. (BP)	0.792	4.15	8.92	0.384	–	0.41
Sharp Cutoff	1.06	0.56	−0.55	0.116	*0.4*	0.40
Monopole	1.74	0.30	−0.48	0.082	*0.5*	0.40
Dipole	1.30	0.37	−0.49	0.089	*0.8*	0.40
Gaussian	1.08	1.22	−0.50	0.095	*0.6*	0.40

Table 5.3: Bare, unrenormalised, parameters extracted from the fits to lattice data displayed in Figure 5.3. All quantities are in units of appropriate powers of GeV.

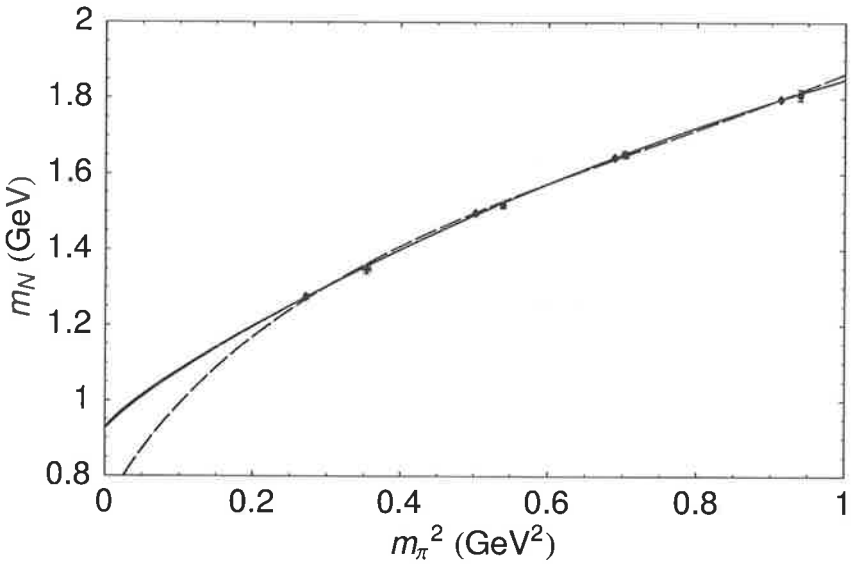

Figure 5.2: Leading-order fits to lattice data based on leading-order chiral expansion with various ultra-violet regulators. The sharp cut-off, monopole, dipole and Gaussian cases are depicted by solid lines — indistinguishable on this plot. The dimensionally regularised form is represented by the dashed curve.

tions, indicates that the truncation of higher-order contributions is reliable.

The corresponding extrapolation curves are displayed in Fig. 5.3. The agreement at this order between all regularisation schemes is remarkable. This is highlighted by the renormalised coefficient, c_0, shown in Table 5.4. The observed agreement in c_0 correspondingly means that the extrapolation to extract the physical nucleon mass is consistent with for all regularisation schemes. The discrepancy between the curves becomes more apparent as we analyse the low-order terms in the expansion, particularly c_2 and c_4. These parameters will enter more significantly in other low-energy properties of the nucleon — such as the pion-nucleon sigma commutator, which we discuss below.

The large renormalised value for c_4, found consistently for all FRR schemes, supports the argument that the DR forms will be sensitive to higher-order contributions. The large values of a_4 for the DR fits seen in Table 5.3 suggest that the χ^2-minimisation is attempting to balance between the correct, large values of c_4 and a non-divergent curve which reproduces the smooth lattice-data.

Determination of the coefficient c_2 is especially important for the extraction of the pion-nucleon sigma commutator, being defined as

$$\sigma_{\pi N} = \frac{1}{3}\langle N|[\hat{Q}_A^a,[\hat{Q}_A^a,\hat{H}]]|N\rangle\,, \tag{5.9}$$

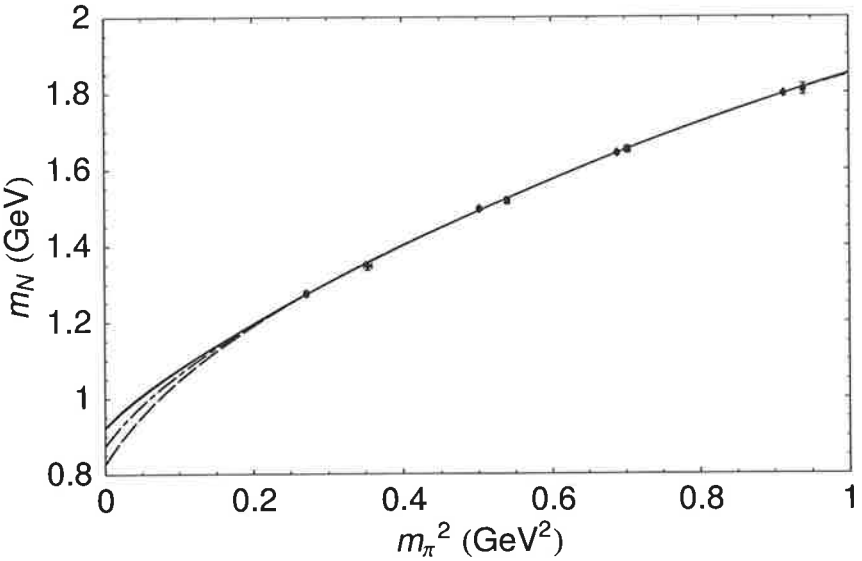

Figure 5.3: Next-to-leading order fits to lattice data for various ultra-violet regulators. The sharp cut-off, monopole, dipole and Gaussian cases are depicted by solid lines — indistinguishable on this plot. The dimensional regularised forms are illustrated by the dashed curves, with the correct branch point corresponding to the higher curve.

where $\hat{Q}_A^a$ is the axial charge operator defined by Eq. (3.5) and $\hat{H}$ the Hamiltonian. From the discussion in Chapter 3 we note that the commutator vanishes in the chiral limit. This quantity therefore acts as a measure of explicit chiral symmetry breaking, where the double commutator exposes the quark-mass dependence of $\hat{H}$,

$$\sigma_{\pi N} = \langle N|(m_u \bar{u}u + m_d \bar{d}d)|N\rangle \,. \tag{5.10}$$

In the isospin-symmetric limit we can formulate the sigma term as

$$\sigma_{\pi N} = \hat{m}\frac{\partial M_N}{\partial \hat{m}} = m_\pi^2 \frac{\partial M_N}{\partial m_\pi^2} \,, \tag{5.11}$$

where we have made use of the GOR relation, Eq. (3.11). Since the physical quark masses are small, the physical $\sigma_{\pi N}$ is dominated by the leading quark-mass dependence of M_N, which is described by c_2. With a large uncertainty on the empirical value of the sigma term [GLS91]

$$\sigma_{\pi N} = 45 \pm 8\,\text{MeV} \,, \tag{5.12}$$

the accurate extraction of this quantity from lattice QCD will further enhance our understanding of nucleon structure.

Regulator	c_0	c_2	c_4
Dim. Reg.	0.827(56)	3.58(25)	3.6(8)
Dim. Reg. (BP)	0.875(56)	3.14(25)	7.2(8)
Sharp cutoff	0.923(65)	2.61(33)	11.8(8)
Monopole	0.923(65)	2.45(33)	20.6(15)
Dipole	0.922(65)	2.49(33)	18.9(15)
Gaussian	0.923(65)	2.48(33)	18.3(15)

Table 5.4: Renormalised expansion coefficients in the chiral limit obtained from various regulator fits to lattice data. (All quantities are in units of appropriate powers of GeV.) Errors are statistical in origin arising from the errors in the lattice data. Deviations in the central values indicate systematic errors associated with the chiral extrapolation.

We quote our final values for the extrapolated nucleon mass and sigma commutator in Table 5.5. In this table, we also show the results from the leading-order fits. The comparison between the $\mathcal{O}(m_\pi^3)$ and $\mathcal{O}(m_\pi^4)$ results further establish the enhanced convergence achieved by using FRR techniques. Where the results of the FRR extrapolations vary by a few MeV between the $\mathcal{O}(m_\pi^3)$ and $\mathcal{O}(m_\pi^4)$ results, the DR forms vary by order 100 MeV or more.

To the date of publication in Physical Review Letters [LTY04], the results displayed in Table 5.5 represent the most comprehensive and systematic extraction of the physical nucleon mass and $\sigma_{\pi N}$ from lattice QCD. This therefore corresponds to the most advanced nonperturbative calculation of the nucleon mass — one of the most fundamental observables of low-energy QCD.

5.3 Remaining Issues

The impressive results obtained in this Chapter could lead to the conclusion that low-energy QCD has now been solved by the successful combination of lattice gauge theory and effective field theory. In this section we wish to address some remaining issues which highlight that there is still a wealth of research before there is a complete description of low-energy QCD.

From Table 5.5 we see that the statistical errors quoted are quite significant — being of order 6% for the nucleon mass and even greater for the sigma term. Since our curves are only constrained by the lattice data, the dominant source of this error bound is the large void between the physical pion mass and the lightest lattice pion mass.

	LNA	NLNA	
Regulator	m_N	m_N	$\sigma_{\pi N}$
Dim. Reg.	0.784	0.884 ± 0.051	50.3 ± 5.0
Dim. Reg. (BP)	...	0.923 ± 0.051	42.7 ± 5.0
Sharp cutoff	0.968	0.961 ± 0.058	33.9 ± 6.5
Monopole	0.964	0.960 ± 0.058	33.0 ± 6.5
Dipole	0.963	0.959 ± 0.058	33.4 ± 6.5
Gaussian	0.966	0.961 ± 0.058	33.2 ± 6.5

Table 5.5: The nucleon mass, m_N (GeV), and the sigma commutator, $\sigma_{\pi N}$ (MeV), extrapolated to the physical pion mass obtained from the $\mathcal{O}(m_\pi^4)$ chiral expansion. We list the nucleon mass extrapolated at $\mathcal{O}(m_\pi^3)$ to display the remarkable convergence of the FRR schemes.

As all data points are statistically independent, we define the region of one-sigma deviation from the best-fit curve by $(\chi^2 - \chi^2_{\rm min}) < 1$. We use a standard χ^2 measure, weighted by the squared error of the simulated data point and $\chi^2_{\rm min}$ corresponds to the optimum fit to the data.[1]

To give a pictorial view of how the error bound grows with extrapolation distance we choose the dipole curve to represent a characteristic curve. We show the one-sigma variation from the best-fit curve by the shaded region in Fig. 5.4. It is clear that a simulated point at a pion mass, $m_\pi^2 \sim 0.1\,{\rm GeV}^2$, would greatly reduce the statistical error in the extrapolation. A simulation in this regime should be accessible to the next generation of dynamical simulations in QCD.

Although the data selected for this analysis was chosen to minimise the effects of lattice discretisation, they have been assumed to describe continuum results. The lattice data will have small corrections as one takes the limits $a \to 0$ and $V \to \infty$. These corrections will slightly alter the extrapolation to the chiral limit.

With continued development in action improvement it is foreseeable that results obtained at finite lattice spacing, ~ 0.1 fm, will give an excellent description of the continuum theory. Any residual corrections should be able to be handled quite trivially.

As simulations go further into the chiral regime, the corrections associated with the finite volume will become increasingly significant. These effects are infrared dominated and hence all the tools of the low-energy effective theory

[1]This χ^2 measure is not the same, although similar, as that used in the curve-matching analysis of Chapter 4.

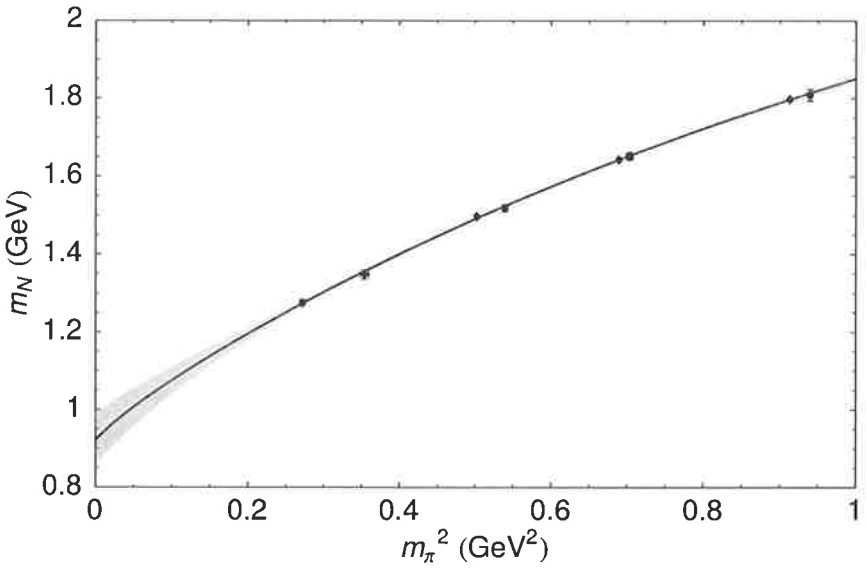

Figure 5.4: Error analysis for the extraction of the nucleon mass, at next-to-leading order, using a dipole regulator. The shaded region corresponds to the region allowed within the present statistical errors.

developed in this Thesis can be extended to incorporate finite-volume corrections. Initial studies of the volume corrections in χPT have been performed in Refs. [LTTW00, YLTW02]. Recent studies have analysed the volume dependence of the nucleon mass in chiral effective field theory [Bea04] and also the corresponding application to the extrapolation problem [AK$^+$04]. Finite-volume corrections are addressed in the following Chapters.

Another issue with the lattice simulation is the procedure for determining the physical scale. As described in Chapter 2, we choose the QCD Sommer scale, r_0, to define the lattice spacing. This method is insensitive to chiral physics and hence allows us to study quark-mass variation of nucleon properties, independent of lattice artifacts. This scale is based on phenomenological models of heavy-quark systems and a complete assessment of sources of error would incorporate some uncertainty, eg. $\sim r_0 = 0.50 \pm 0.01$ fm. In addition, the scale is determined on a finite lattice and will also be subject to $\mathcal{O}(a^2)$ discretisation errors.

Ultimately, one would like to be able to determine the scale, independent of any model calculations. Direct determination from the light hadron spectrum would seem ideal, only this will always be contaminated by large chiral corrections. It will therefore be necessary to have a complete and thorough treatment of the chiral extrapolation to accurately set the scale this way. Alternatively, it seems that the mass-splittings in some heavy-quark systems show

little dependence on quark mass and these could be fit directly to set the lattice spacing [D+97, D+04].

Related to this problem comes the determination of the nonanalytic coefficients from the lattice simulation. In this work, we have set the coefficients to their best phenomenological values for accurate extrapolations using this knowledge of low-energy QCD. For a true *ab initio* calculation, one would wish to determine these coefficients directly from nonperturbative simulations of lattice QCD. Only with a large number of points at light-quark mass, on large volumes will this become possible.

The results shown in this Chapter have demonstrated the solution to the chiral extrapolation problem, neglecting lattice artifacts. The final remark to be made is that this study has only focussed on the nucleon mass. There are many more QCD observables which will also require extrapolation from the large quark masses simulated in lattice calculations. Utilising the techniques of finite-range regularisation will be essential for the reliable extrapolation to the chiral regime. To name a couple, FRR will be extremely useful for the analysis of excited-state spectroscopy [MCLT03] and electromagnetic structure functions [ALTY04].

* * *

We have shown that the extremely precise dynamical simulation data from CP-PACS permits one to determine four parameters in the $\mathcal{O}(m_\pi^4)$ chiral extrapolation formula, Eq. (5.7). Both the dimensionally regularised and FRR forms give an accurate description of the data which is consistent with the physical nucleon mass. With a large shift of the DR result from the $\mathcal{O}(m_\pi^3)$ result to $\mathcal{O}(m_\pi^4)$, one cannot be guaranteed of sufficient convergence. In contrast, the FRR results show very little variation when extended to higher order. Combined with the results of Chapter 4, the stability of the FRR extrapolation is established.

The results shown in Table 5.5 display a systematically accurate extrapolation of the nucleon mass — with model-independence at the level of to 2 parts in 1000. The insensitivity to the choice of finite-range regulator also provides a sigma commutator accurate to within 3%. Although there is still a large statistical error associated with the large extrapolation distance, the suitable combination of lattice gauge theory and effective field theory has enabled a state-of-the-art nonperturbative calculation of the nucleon mass.

Future work will see the extension of FRR techniques to a wide range of QCD observables for the reliable extrapolation to the physical regime. Increased computing power will improve access to the light-quark domain and reduce the statistical uncertainty of the present calculation.

6

Quenched Chiral Perturbation Theory

Quenched QCD has been studied extensively in lattice gauge theory. Finite-range regularised chiral perturbation has been demonstrated to provide an efficient tool for the analysis of modern lattice QCD simulations. We now wish to address the corresponding issue of chiral extrapolation for the quenched modification of QCD. Simulations of quenched QCD (QQCD) modify the path-integral measure, Eq. (2.9), by setting the fermion determinant to a constant,

$$\det M = 1 \,. \tag{6.1}$$

In the context of a lattice simulation, the effect of quenching alters the distribution of gauge fields sampled by the Monte Carlo integration. The summation over an ensemble of gauge fields describes a distorted integration over gauge field configurations, which no longer accurately samples the true QCD vacuum.

The physical consequence of this procedure is the removal of $q\overline{q}$ pair-creation in the QCD vacuum. The only quarks which are contained in any simulation are those created explicitly by the interpolating fields. This simplification is commonly referred to as the *valence* or *quenched approximation.*[1]

This absence of $q\overline{q}$ pairs in the QQCD vacuum alters the low-energy structure from the physical theory. As a result, we have a new low-energy effective field theory for the quenched theory, namely quenched chiral perturbation theory (QχPT).

In this Chapter, we outline the formalism of constructing a low-energy effective theory for quenched QCD. In particular, we describe applications of the theory in the baryon sector. The quark mass expansion of the nucleon mass are presented in two distinct formalisms. The first we will work with the graded symmetry approach to the QχPT devised by Bernard and Goltermann [BG92] and subsequently extended to baryons by Labrenz and Sharpe [LS96]. As an alternative, we also work with the physically intuitive approach of Leinweber [Lei04] which is characterised by a pictorial view of the quark-flow involved in meson-

[1] Use of the terminology *"approximation"* is certainly an embellishment, since any systematic connection to the physical theory has been abandoned.

baryon interactions. This is similar to the original work of Sharpe in the meson sector [Sha92].

6.1 Graded-symmetry Approach

As described in Chapter 3, χPT describes a systematic approach to the study of QCD at low energies. Quenched χPT (QχPT) provides the analogous low energy effective theory for QQCD [Sha92, BG92, LS96].

This is achieved by defining a Lagrangian, which is equivalent to the quenched theory simulated on the lattice. With the Lagrangian of 3-flavour QCD, Eq. (2.1), in shorthand notation,

$$\mathcal{L}_{\mathrm{QCD}} = \mathcal{L}^{\mathrm{gauge}} + \bar{\psi}(i\not{D} - M)\psi\,, \tag{6.2}$$

where the quark fields are collected into $\psi^{\top} = (q_u, q_d, q_s)$, and corresponding mass matrix $M = \mathrm{diag}(m_u, m_d, m_s)$. For a field theoretic definition of quenched QCD, this Lagrangian is extended to include a set of bosonic quark fields, $\tilde{q}$ [Mor87]. The new quark fields are therefore given by $Q^{\top} = (q_u, q_d, q_s, \tilde{q}_u, \tilde{q}_d, \tilde{q}_s)$, and importantly, these additional *ghost* quark fields are degenerate in mass with the original quark fields, such that the new matrix is given by $\hat{M} = \mathrm{diag}(m_u, m_d, m_s, m_u, m_d, m_s)$. The physical removal of sea-quark loops is therefore realised by considering the generating functional of this modified theory,

$$\mathcal{Z}_{\mathrm{QQCD}} = \int \mathcal{D}A\mathcal{D}\bar{Q}\mathcal{D}Q \exp(iS^{\mathrm{gauge}} + i\int d^4x \bar{Q}(x)(i\not{D} - M)Q(x))\,. \tag{6.3}$$

Whereas integration over the standard quark fields produces the fermion determinant, the anticommuting nature of the ghost quarks gives rise to the inverse of the same determinant,

$$\mathcal{Z}_{\mathrm{QQCD}} = \int \mathcal{D}A \exp(iS^{\mathrm{gauge}}) \frac{\det(i\not{D} - M)}{\det(i\not{D} - M)}\,. \tag{6.4}$$

The fermion determinant is therefore effectively removed from the path-integral measure. The inclusion of this set of bosonic quarks has therefore simulated the lattice technique of setting the fermion determinant to a constant.

The symmetries of this quenched QCD Lagrangian are exploited to develop the appropriate low-energy effective field theory. The standard chiral symmetry group of $SU(3)_L \times SU(3)_R$ is replaced by the graded symmetry group, $SU(3|3)_L \times SU(3|3)_R$, incorporating the appropriate mixing of the ghost-quark sector.

We now summarise the calculation of baryon masses in quenched chiral perturbation theory, as described by Labrenz and Sharpe [LS96].

Beginning with the chiral Lagrangian for full QCD, given by

$$\mathcal{L} = \mathcal{L}_{\pi} + \mathcal{L}_{B\pi} + \mathcal{L}_{T\pi}\,, \tag{6.5}$$

where the octet (decuplet) baryon fields are described by B (T). Explicitly, the octet-baryon Lagrangian can be expressed as

$$\begin{aligned}
\mathcal{L}_{B\pi} &= i\mathrm{tr}\,(\bar{B}v\cdot\mathcal{D}B) \\
&\quad +2D\mathrm{tr}\,(\bar{B}S^{\mu}\{A^{oct}_{\mu},B\}) + 2F\mathrm{tr}\,(\bar{B}S^{\mu}[A^{oct}_{\mu},B]) \\
&\quad +2\mu b_D\mathrm{tr}\,(\bar{B}\{\mathcal{M}^{+},B\}) + 2\mu b_F\mathrm{tr}\,(\bar{B}[\mathcal{M}^{+},B]) \\
&\quad +2\mu b_0\mathrm{tr}\,(\bar{B}B)\mathrm{tr}\,(\mathcal{M}^{+}) + 2g_s\mathrm{tr}\,(\bar{B}S^{\mu}B)\mathrm{tr}\,(A^{sin}_{\mu})\,,
\end{aligned} \tag{6.6}$$

and correspondingly for the decuplet,

$$\begin{aligned}
\mathcal{L}_{T\pi} &= -i\bar{T}^{\nu}(v\cdot\mathcal{D})T_{\nu} + \Delta M\bar{T}^{\nu}T_{\nu} \\
&\quad +2\mathcal{H}\bar{T}^{\nu}S^{\mu}A^{oct}_{\mu}T_{\nu} + \mathcal{C}(\bar{T}^{\nu}A^{oct}_{\nu}B + \bar{B}A^{oct}_{\nu}T^{\nu}) \\
&\quad +c\bar{T}^{\nu}\mathcal{M}^{+}T_{\nu} - \bar{\sigma}\bar{T}^{\nu}T_{\nu}\mathrm{tr}\,(\mathcal{M}^{+}) \\
&\quad +2g'_s\bar{T}^{\nu}S^{\mu}T_{\nu}\mathrm{tr}\,(A^{sin}_{\mu})\,.
\end{aligned} \tag{6.7}$$

A complete decription of all symbols can be found in Ref. [LS96]. These Lagrangians are extended beyond the standard form, to incorporate explicit coupling to the flavour-singlet η' field, defined through the couplings, g_s and g'_s [YLTW02]. The octet and singlet components of the meson matrix, A, are labeled for clarity.

The flavour singlet η' remains light in the quenched approximation, and is therefore an effective degree of freedom in the low energy sector. Such excitations must be incorporated into the low-energy analysis. Within full QCD, resummation of internal loop diagrams renders the η' massive and hence it plays no role in the low-energy dynamics. For this reason couplings to such flavour-singlet states are neglected in full QCD. In our analysis, we wish to compare the low-energy structure of the quenched and physical theories. A flavour-singlet coupling, like $NN\eta'$, must be included in the chiral Lagrangian of QCD, in order that it is treated on equal footing with the quenched theory. This coupling will not alter any results of the physical theory, as any diagram would involve the propagation of a heavy η'.

The effective chiral Lagrangian of quenched QCD is given by [LS96]

$$\mathcal{L}^{(Q)} = \mathcal{L}^{(Q)}_{\Phi} + \mathcal{L}^{(Q)}_{B\Phi} + \mathcal{L}^{(Q)}_{T\Phi}\,, \tag{6.8}$$

where meson and baryon states are now understood to be constructed of ordinary quarks and the ghost, bosonic quarks. The general Lagrangian for the

heavy fields can be written in terms of the rank-three tensor fields as defined in Ref. [LS96]. The octet baryons are described by the tensor-field, $\mathcal{B}$, with interactions characterised by

$$\begin{aligned}\mathcal{L}^{(Q)}_{\mathcal{B}\Phi} &= i(\bar{\mathcal{B}}v\cdot\mathcal{D}\mathcal{B}) \\ &\quad +2\alpha(\bar{\mathcal{B}}S^\mu\mathcal{B}A_\mu)+2\beta(\bar{\mathcal{B}}S^\mu A_\mu\mathcal{B}) \\ &\quad +2\gamma_s(\bar{\mathcal{B}}S^\mu\mathcal{B})\,\mathrm{str}(A_\mu)+\alpha_M(\bar{\mathcal{B}}\mathcal{B}\mathcal{M}^+) \\ &\quad +\beta_M(\bar{\mathcal{B}}\mathcal{M}^+\mathcal{B})+\sigma(\bar{\mathcal{B}}\mathcal{B})\,\mathrm{str}(\mathcal{M}^+)\,, \end{aligned} \tag{6.9}$$

where str denotes a supertrace, as given in Ref. [LS96]. The corresponding Lagrangian for the decuplet field, $\mathcal{T}$, is described by

$$\begin{aligned}\mathcal{L}^{(Q)}_{\mathcal{T}\Phi} &= -i(\bar{\mathcal{T}}^\nu(v\cdot\mathcal{D})\mathcal{T}_\nu)+\Delta M(\bar{\mathcal{T}}^\nu\mathcal{T}_\nu) \\ &\quad +2\mathcal{H}(\bar{\mathcal{T}}^\nu S^\mu A_\mu\mathcal{T}_\nu)-\sqrt{\frac{3}{2}}\mathcal{C}[\bar{\mathcal{T}}^\nu A_\nu B+\bar{B}A_\nu\mathcal{T}^\nu] \\ &\quad +2\gamma_s'(\bar{\mathcal{T}}^\nu S^\mu\mathcal{T}_\nu)\,\mathrm{str}(A_\mu) \\ &\quad +c\bar{\mathcal{T}}^\nu\mathcal{M}^+\mathcal{T}_\nu-\bar{\sigma}(\bar{\mathcal{T}}^\nu\mathcal{T}_\nu)\mathrm{tr}\,(\mathcal{M}^+)\,. \end{aligned} \tag{6.10}$$

In any lattice simulation of quenched QCD, the external sources of baryon propagators will only create valence-type quarks. The ghost fields, which describe the cancellation of internal quark loops, will not appear in any external baryon fields. Comparison with the QCD chiral Lagrangian can be achieved by restriction of the indices on the tensor fields, $\mathcal{B}$ and $\mathcal{T}$, to those corresponding to the physical quarks. The details of this procedure are described in Ref. [LS96]. Performing these restrictions on the octet-baryon, quenched chiral Lagrangian (Eq. (6.9)) one finds:

$$\begin{aligned}\mathcal{L}^{(Q)}_{\mathcal{B}\Phi}|_R &= i(\bar{\mathcal{B}}v\cdot\mathcal{D}\mathcal{B})|_R \\ &\quad +\frac{2}{3}(2\alpha-\beta)\mathrm{tr}\,(\bar{B}S^\mu A_\mu B)+\frac{1}{3}(-\alpha-4\beta)\mathrm{tr}\,(\bar{B}S^\mu BA_\mu) \\ &\quad +\frac{1}{3}(\alpha+4\beta+6\gamma_s)\mathrm{tr}\,(\bar{B}S^\mu B)\mathrm{tr}\,(A_\mu) \\ &\quad +\frac{1}{3}(2\alpha_M-\beta_M)\mathrm{tr}\,(\bar{B}\mathcal{M}^+B)+\frac{1}{6}(-\alpha_M-4\beta_M)\mathrm{tr}\,(\bar{B}B\mathcal{M}^+) \\ &\quad +\frac{1}{6}(\alpha_M+4\beta_M+6\sigma)\mathrm{tr}\,(\bar{B}B)\mathrm{tr}\,(\mathcal{M}^+)\,. \end{aligned} \tag{6.11}$$

Equating this with the QCD chiral Lagrangian, Eq. (6.6), provides the following relations between the parameters of the quenched chiral Lagrangian and the

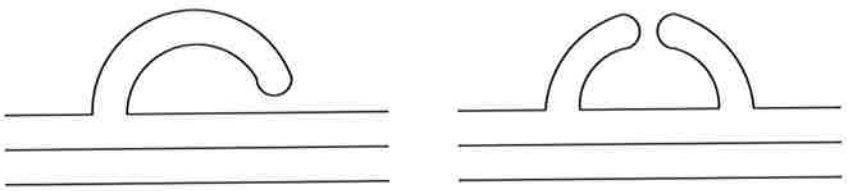

(a) (b)

Figure 6.1: Quark flow diagrams for the chiral η' loop contributions appearing in QQCD: (a) single hairpin, (b) double hairpin.

physical theory provides [LS96, YLTW02]

$$\frac{2}{3}(2\alpha - \beta) = 2D + 2F\,, \tag{6.12}$$

$$\frac{1}{3}(-\alpha - 4\beta) = 2D - 2F\,, \tag{6.13}$$

$$\frac{1}{3}(\alpha + 4\beta + 6\gamma_s) = 2g_s\,, \tag{6.14}$$

$$\frac{1}{3}(2\alpha_M - \beta_M) = 2\mu b_D + 2\mu b_F\,, \tag{6.15}$$

$$\frac{1}{6}(-\alpha_M - 4\beta_M) = 2\mu b_D - 2\mu b_F\,, \tag{6.16}$$

$$\frac{1}{6}(\alpha_M + 4\beta_M + 6\sigma) = 2\mu b_0\,. \tag{6.17}$$

Although the couplings of the quenched theory have no rigorous connection with the physical theory, we work with the assumption that the relations above hold to a good approximation.

Loop corrections in the quenched theory are evaluated by calculating all diagrams described by the couplings in Eqs. (6.9) and (6.10). For a loop correction, the summation over all intermediate meson-baryon states will include standard meson and baryons, plus those loops which contain hadrons comprised of a mixture of quark and ghost-quark states. For the complete calculation of the chiral corrections to the baryon masses in quenched QCD we refer the reader to Refs. [LS96, YLTW02]. Expressions for the nonanalytic contributions are summarised in the following Chapter.

The flavour-singlet η' requires special attention, particularly for estimating the appropriate quenched coupling strengths. The parameter, g_s (g_s'), describes the coupling of the flavour-singlet η' to the baryon octet (decuplet). Within QCD, the single vertex has two topologically different quark-flow diagrams, as illustrated by the left and right-hand vertices of Fig. 6.1(a). The left is that of a $q\bar{q}$ insertion on one of the valence quark lines and the right is a pure gluonic,

mediated via a hairpin-style $q\bar{q}$ annihilation. The total coupling is a sum of these two contributions. Denoting the hairpin vertex coupling by $\gamma_{\rm QCD}$ and $\gamma'_{\rm QCD}$ for octet and decuplet baryons respectively we have

$$g_s = \frac{1}{\sqrt{6}} g_{\eta' NN} + \gamma_{\rm QCD} \,, \tag{6.18}$$

$$g'_s = \frac{1}{\sqrt{6}} g_{\eta' \Delta\Delta} + \gamma'_{\rm QCD} \,. \tag{6.19}$$

The first of these interactions, $g_{\eta' NN}$ ($g_{\eta' \Delta\Delta}$) is related to the axial couplings by SU(6) phenomenology. We take the standard approach and assign

$$g_{\eta' NN} = \sqrt{2} g_{\eta NN} = \sqrt{\frac{2}{3}} (3F - D) \,, \tag{6.20}$$

$$g_{\eta' \Delta\Delta} = \sqrt{2} g_{\eta \Delta\Delta} = \sqrt{\frac{2}{3}} \mathcal{H} \,. \tag{6.21}$$

As in the case of the physical theory, the terms γ_s and γ'_s describe both types of flavour-singlet coupling, not just that arising through the hairpin alone. Analogous to Eq. (6.19), the quenched couplings can be described by

$$\gamma_s = \frac{1}{\sqrt{6}} g_{\eta' NN} + \gamma \,, \tag{6.22}$$

$$\gamma'_s = \frac{1}{\sqrt{6}} g_{\eta' \Delta\Delta} + \gamma' \,, \tag{6.23}$$

where the terms γ and γ' now correspond to the pure hairpin couplings, as used in Ref. [LS96]. Here we note the terms $g_{\eta' NN}$ and $g_{\eta' \Delta\Delta}$ are chosen to retain their physical values in the quenched theory. This is consistent with the working assumption that the chiral parameters F and D are unchanged between the two theories.

To relate the flavour-singlet contributions to the physical theory, Eq. (6.14) provides

$$\frac{1}{3}\alpha + \frac{4}{3}\beta + \sqrt{\frac{2}{3}} g_{\eta' NN} + 2\gamma = \sqrt{\frac{2}{3}} g_{\eta' NN} + 2\gamma_{\rm QCD} \,, \tag{6.24}$$

and combining with Eqs. (6.12,6.13), one arrives at [YLTW02]

$$\gamma = \gamma_{\rm QCD} + D - F \,. \tag{6.25}$$

The computation for the decuplet is much simpler, where one finds

$$\gamma' = \gamma'_{\rm QCD} \,. \tag{6.26}$$

In estimating the hairpin-type couplings in full QCD one assumes that they are relatively small, $\gamma_{\rm QCD} \ll g_{\eta' NN}$, due to OZI-type suppression [Clo79]. With

analogous arguments for the decuplet, we take $\gamma_{\rm QCD} = \gamma'_{\rm QCD} = 0$. In summary, γ and γ' are described by [YLTW02]

$$\gamma = D - F\,, \quad \gamma' = 0\,. \tag{6.27}$$

6.2 Diagrammatic Method

A simpler, somewhat more intuitive approach, to the calculation of nonanalytic corrections to hadron properties in quenched chiral perturbation theory has been developed by Leinweber [Lei02, Lei04]. This method uses results of the physical EFT, combined with a pictorial view of the underlying quark dynamics, to distinguish the sea and valence components of chiral-loop diagrams.

To demonstrate the implementation of this approach, an example calculation is presented. In particular, the modification of the leading nonanalytic contribution to the nucleon mass, as induced by the quenched approximation. The relevant couplings for this calculation are given by [Lei04, RSY99]

$$\begin{aligned} f_{NN\pi} &= F + D, & f_{\Lambda NK} &= -\tfrac{1}{\sqrt{3}}\,(3F + D), \\ f_{NN\eta} &= \tfrac{1}{\sqrt{3}}\,(3F - D), & f_{\Sigma NK} &= D - F, \\ f_{NN\eta'} &= \sqrt{\tfrac{2}{3}}\,(3F - D). \end{aligned} \tag{6.28}$$

All the leading, one-loop diagrams contributing to the nucleon mass are displayed in Fig. 6.2. The proton is chosen to give an explicit representation of the relevant quark flavours. For each of the meson-loop diagrams, a quark-flow diagram depicts the minimal dynamics of the underlying quark field. These skeleton diagrams should be interpreted to contain an arbitrary number of additional quark and gluon lines.

The familiar result of the pion contribution in full QCD, Eq. (3.29), is observed in the sum of the π^0 and π^+ loop contributions to the nucleon, given by the respective terms,

$$-\left(f_{NN\pi}^2 + 2f_{NN\pi}^2\right)\frac{m_\pi^3}{32\pi f_\pi^2} = -3(D+F)^2\frac{m_\pi^3}{32\pi f_\pi^2}\,. \tag{6.29}$$

The factor of 2 for the π^+ loop is an isospin factor. To describe all the light-quark loop diagrams, the η and η' contributions must also be summed, providing a net contribution

$$-\left(3f_{NN\pi}^2 + f_{NN\eta}^2 + f_{NN\eta'}^2\right)\frac{m_\pi^3}{32\pi f_\pi^2} = -(4D^2 + 12F^2)\frac{m_\pi^3}{32\pi f_\pi^2}\,. \tag{6.30}$$

Recognition of the flavour symmetry of QCD enables linear combinations of diagrams to isolate the contributions involving a quark loop and those of the

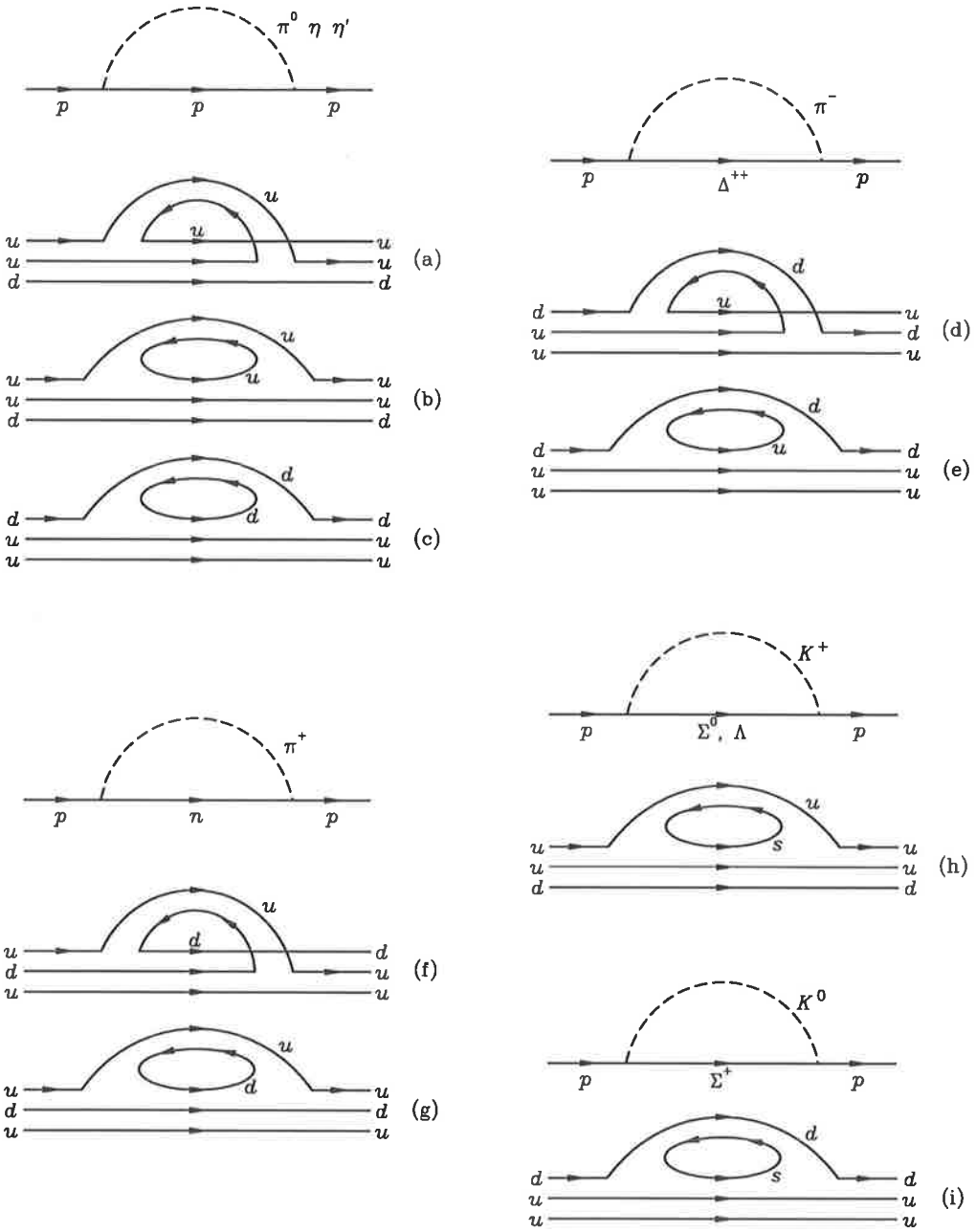

Figure 6.2: Quark flow diagrams contributing to the chiral corrections to the nucleon mass.

purely valence sector. Flavour-symmetry dictates that if the flavour of sea-quark in a loop diagram is changed, without changing its mass, then the contribution is equal. For example, the contribution from Fig. 6.2(g) is precisely equal to Fig. 6.2(h). Subtracting diagram (h) (with $m_K = m_\pi$ and $M_\Lambda = M_\Sigma = M_N$) from the total $p \to n\pi^+$ diagram will therefore determine the purely quenched

result.

In summary, the relations between the diagrams are given by

$$(b) = (g) = (h)\,, \quad (c) = (e) = (i)\,, \tag{6.31}$$

where the inclusion of a diagram including a doubly-charged proton, $p \to p^{++}\pi$, should now be apparent. In QCD, a *uuu*-quark proton is forbidden by the Pauli exclusion principle. Therefore, for intermediate $N\pi$ states[2], the net sum of diagrams (d) and (e) which amounts to zero. In the absence of the cancellation of diagram (e), a *uuu* proton can propagate and hence diagram (d) provides a finite contribution in the quenched theory.

Using the relationship between the diagrams, Eq. (6.31), and the known kaon-loop contributions, Eq. (6.28), the sea contributions can be subtracted from the total result, Eq. (6.30). The final contribution to the m_π^3 dependence of the nucleon mass in quenched QCD is given by

$$-\frac{8}{3}(3DF - D^2)^2 \frac{m_\pi^3}{32\pi f_\pi^2}\,. \tag{6.32}$$

This result is in agreement with the result of Labrenz and Sharpe [LS96].

This method is particularly useful for the analysis of the electromagnetic form factors, where the individual flavour sectors become increasingly important [L+05].

[2]Clearly, a contribution from the excited Δ^{++}-baryon is possible.

7

Baryon Masses in Quenched QCD

Studies of the quenched approximation in lattice QCD have provided enhanced accessibility to the development of improved algorithms and numerical techniques, with limited computing resources. With the quenched approximation offering greater access to the chiral regime, we study the extrapolation problem in the modified theory to further develop an understanding of the chiral behaviour of hadron properties.

Using the appropriate low-energy EFT, we study the chiral behaviour of the nucleon and Delta masses in quenched QCD. In particular, the techniques of finite-range regularisation are applied to exploit the improved convergence properties of the chiral series.

In studying a matched ensemble of quenched and dynamical simulations from the MILC Collaboration [B+01], we find that FRR offers a connection between the masses observed in the two theories [YLTW02]. This remarkable discovery allows the opportunity to take quenched simulation results and estimate the corrections in going to the dynamical theory.

This behaviour leads to an improved understanding of the magnitude of chiral loop corrections in the physical nucleon. We find that less than one-third of the physical nucleon–Delta mass-splitting arises from interaction with the pion field. The remainder therefore being the result of short-range gluon interactions within the baryons.

7.1 Quenched Expansion Formulae

Extrapolation formulae, analogous to those of QCD in Chapter 5, are constructed for the quenched modification of QCD. In addition to the nucleon mass, the chiral behaviour of the decuplet Δ-baryon is also investigated. The nature of the Delta in quenched QCD is particularly interesting because of a repulsive interaction in the $N\pi$ channel.

We first summarise our expression for the expansion of both the nucleon and Delta masses in quenched and physical QCD,

$$M_B = a_0^B + a_2^B m_\pi^2 + a_4^B m_\pi^4 + \Sigma_B(m_\pi, \Lambda)\,, \tag{7.1}$$

	QCD	QQCD
G_{NN}	$(F+D)^2$	$\frac{8}{9}(3DF-D^2)$
$G_{N\Delta}$	$\frac{8}{9}\mathcal{C}^2$	$\frac{4}{9}\mathcal{C}^2$
$G_{\Delta\Delta}$	$\frac{25}{81}\mathcal{H}^2$	$\frac{20}{81}\mathcal{H}^2$
$G_{\Delta N}$	$\frac{2}{9}\mathcal{C}^2$	$-\frac{2}{9}\mathcal{C}^2$

Table 7.1: Chiral couplings appearing in the pion-loop contributions in dynamical and quenched QCD. In numerical calculations we have used the couplings arising from $SU(6)$ relations [BSS93], $\mathcal{C}=-2D$ and $\mathcal{H}=-3D$.

where we denote the baryon by $B=N,\Delta$ and all loop contributions are collected into Σ_B.

The simple one-loop integrals are summarised as

$$I_\pi(m_\pi,\Delta,\Lambda)=\frac{2}{\pi}\int_0^\infty dk\,\frac{k^4u^2(k,\Lambda)}{\sqrt{k^2+m_\pi^2}[\Delta+\sqrt{k^2+m_\pi^2}]}\,, \tag{7.2}$$

which we recognise as Eqs. (3.30) and (4.11). For baryon B, the pion-loop component of the chiral corrections can be described by the sum of two terms

$$\chi^B_{\pi N}I_\pi(m_\pi,M_N-M_B,\Lambda)+\chi^B_{\pi\Delta}I_\pi(m_\pi,M_\Delta-M_B,\Lambda)\,, \tag{7.3}$$

where the physical mass-splitting is used in the definition of the integrals. For the $\Delta\to N\pi$ diagram, the mass-splitting in Eq. (7.2) becomes negative and a pole exists in the integrand corresponding to the opening of the decay channel. In this case, I_π is defined by the principal value of the integral.

The coefficients $\chi^B_{\pi N}$ and $\chi^B_{\pi\Delta}$ differ between QCD and the quenched theory. These coefficients are given by

$$\chi^B_{\pi B'}=-\frac{3}{32\pi f_\pi^2}G_{BB'}\,, \tag{7.4}$$

with the values of $G_{BB'}$ listed in Table 7.1 [LS96].

In addition to the pion-loop diagrams, the flavour-singlet η' is also a low-energy degree of freedom, as described in the previous Chapter. Within full QCD, η'-loops do not play a role in the chiral expansion because the η' remains massive in the chiral limit. In the quenched approximation the η' behaves as a Goldstone boson and the η' propagator has the same kinematic structure as that of the pion [Sha92].

As a consequence, there are two new chiral loop contributions unique to the quenched theory. The first of these corresponds to an axial-hairpin diagram, such

	N	Δ
$\Gamma_B^{(1)}$	$\frac{4}{3}(3F-D)\gamma$	$\frac{20}{27}\mathcal{H}\gamma'$
$\Gamma_B^{(2)}$	$(3F-D)^2$	$\frac{5}{9}\mathcal{H}^2$

Table 7.2: Couplings used in flavour singlet η' self-energies.

as that depicted in Fig. 6.1(a). This diagram gives an additional contribution to the chiral expansion of baryon masses which is nonanalytic at order m_π^3.

The single-hairpin diagram has the exact same kinematic structure as the simple pion-loop graphs, with the contribution to the nucleon and Delta masses given by

$$\chi^B_{\eta'(1)} I_\pi(m_\pi, 0, \Lambda)\,. \tag{7.5}$$

The coefficient is given by

$$\chi^B_{\eta'(1)} = -\frac{3}{32\pi f_\pi^2}\Gamma_B^{(1)}\,, \tag{7.6}$$

with the expressions for $\Gamma^{(1)}$ displayed in Table 7.2 [LS96]. The coupling γ (γ') describes the hairpin-baryon vertex shown in Fig. 6.1(a). This is topologically different from any coupling which appears in the physical low-energy theory.

The second of these new η' loop diagrams arises from the double hairpin vertex, as pictured in Fig. 6.1(b). This contribution is particularly interesting because it involves two Goldstone boson propagators and is therefore the source of more singular nonanalytic behaviour — linear in m_π. This contribution is described by

$$\chi^B_{\eta'(2)} I^{(2)}_{\eta'}(m_\pi, \Lambda)\,, \tag{7.7}$$

with the loop integral defined by

$$I^{(2)}_{\eta'}(m_\pi, \Lambda) = -\frac{4}{3\pi}\int_0^\infty dk \frac{k^4 u^2(k)}{(k^2+m_\pi^2)^2}. \tag{7.8}$$

The coefficient involves another new parameter, unique to the quenched approximation, which measures the strength of the double-hairpin interaction, m_0. This dimensionful parameter is related to the physical η' mass, as the summation of quark-loop diagrams through this double-hairpin coupling can be seen to generate a finite mass for the η', even in the chiral limit. We estimate a value, $m_0^2 = 0.42\,\mathrm{GeV}^2$, based upon phenomenology and lattice results [KFM+94, BDET00, DH02]. The coefficient of this diagram is given by

$$\chi^B_{\eta'(2)} = -\frac{m_0^2}{32\pi f_\pi^2}\Gamma_B^{(2)}\,, \tag{7.9}$$

and $\Gamma_B^{(2)}$ shown in Table 7.2. The contribution from the double-hairpin η' is positive and therefore describes a repulsive interaction. This acts to raise the mass of the baryon as the chiral limit is approached. The momentum dependence of the double hairpin vertex, which is believed to be small, is neglected.

The explicit appearance of unphysical parameters, like γ and m_0, causes the low-energy EFT of quenched QCD to be disconnected from that of QCD. This is not true for the partially-quenched sector, where all unphysical η' couplings can be integrated out, and hence there is a smooth connection to the physical theory [SS00, SS01]. Partially-quenched QCD describes the situation where sea-quark contributions to the fermion determinant are explicitly evaluated, but the masses simulated in the sea do not match those of the valence sector.

The net contribution of all the chiral-loop corrections to the nucleon and Delta baryons can be summarised as

$$\begin{aligned}\Sigma_B &= \chi^B_{\pi N} I_\pi(m_\pi, M_N - M_B, \Lambda) + \chi^B_{\pi\Delta} I_\pi(m_\pi, M_\Delta - M_B, \Lambda) \\ &\quad + \chi^B_{\eta'(1)} I_\pi(m_\pi, 0, \Lambda) + \chi^B_{\eta'(2)} I^{(2)}_{\eta'}(m_\pi, \Lambda)\,. \end{aligned} \tag{7.10}$$

The contributions of QCD are recovered by setting the η' diagrams to zero, and adjusting the pion-loop coefficients to their physical values.

7.2 Extrapolation to the Chiral Regime

The chiral expansions of the quenched and dynamical baryon masses, Eq. (7.1), are now constrained to their respective lattice results. The lattice data considered in this analysis comes from the paper of Bernard *et al.* [B+01]. These simulations were performed using an improved Kogut-Susskind (staggered) quark action, which is known to have good scaling properties [B+00]. These results have been obtained on matched lattice sizes, such that all lattice spacings ($a \simeq 0.13\,\mathrm{fm}$) and volumes ($16^3$) remain constant. Comparison of the quenched and dynamical spectra should therefore be insensitive to discretisation artifacts.

We continue to determine the lattice scale using the Sommer scale [Som94, EHK98a]. The definition of r_0 is described by Eq. (2.25) at a distance scale $\simeq 0.5\,\mathrm{fm}$. The present analysis uses a slightly modified version, defining the force at $r_1 = 0.35\,\mathrm{fm}$ via $r_1^2 F(r_1) = 1.00$ [B+01].

The physical simulations have been performed on lattices with $2+1$ flavours of dynamical quarks. The simulation results, in physical units, are listed in Table 7.3. Only the few heaviest quark masses simulated on these lattices respect the condition on finite-volume effects, $m_\pi L \gtrsim 2\pi$. For this reason, the chiral expansion formulae are modified to account for finite-volume corrections.

$m_\pi L$	m_π^2 (GeV^2)	M_N (GeV)	M_Δ (GeV)
7.7	0.5321(4)	1.592(8)	1.740(12)
7.0	0.4246(4)	1.502(4)	1.650(13)
6.0	0.3184(2)	1.389(4)	1.581(9)
5.0	0.2161(2)	1.275(4)	1.477(10)
3.6	0.1080(2)	1.140(9)	1.348(18)
7.4	0.4760(4)	1.569(10)	1.774(18)
5.7	0.2882(3)	1.409(7)	1.636(18)
4.7	0.1946(2)	1.322(10)	1.585(22)
3.4	0.1000(2)	1.214(13)	1.510(25)

Table 7.3: Lattice data used for the analysis of quenched versus physical baryon masses. The upper five points are results of the dynamical simulations, and the lower four from corresponding quenched analysis. All simulations on a $16^3 \times 32$ lattice at spacing, $a \simeq 0.13\,\mathrm{fm}$. Results from MILC Collaboration [B$^+$01].

Chiral effective field theory is constructed on the low-energy degrees of freedom of QCD. The effects of the finite-volume lattice will therefore be dominated by the modified behaviour of these low-energy degrees of freedom. In the present context, this means that the chiral loop diagrams considered will be altered by an infrared suppression of the integrand. The requirement that Green functions are periodic [GL88] restricts momentum components to the values

$$k_i = \frac{2\pi n_i}{L}, \quad n_i = 0,\ \pm 1,\ \pm 2,\ \ldots\ . \tag{7.11}$$

For the p-wave loop contributions considered in this Chapter, the integrand vanishes for $k = 0$. Strength in the integrand is not sampled until one component of k reaches $2\pi/L$. Since chiral physics is dominated by the infrared behaviour of loop integrals, the nonanalytic terms of the chiral expansion exhibit substantial threshold effects.

Within the FRR formalism, the extension to incorporate finite-volume effects is straightforward. The continuous momentum integrals, I_π and $I^{(2)}_{\eta'}$, are replaced by sums over the discrete momentum states. This is implemented by making the substitution [LTTW01, YLTW02]

$$4\pi \int_0^\infty k^2 dk = \int d^3k \to \frac{1}{V}\left(\frac{2\pi}{a}\right)^3 \sum_{k_x,k_y,k_z}\ . \tag{7.12}$$

The lattice data is then directly fit to Eq. (7.1), with Σ_B modified to incorporate the finite-volume corrections of the effective field theory. The fit parameters,

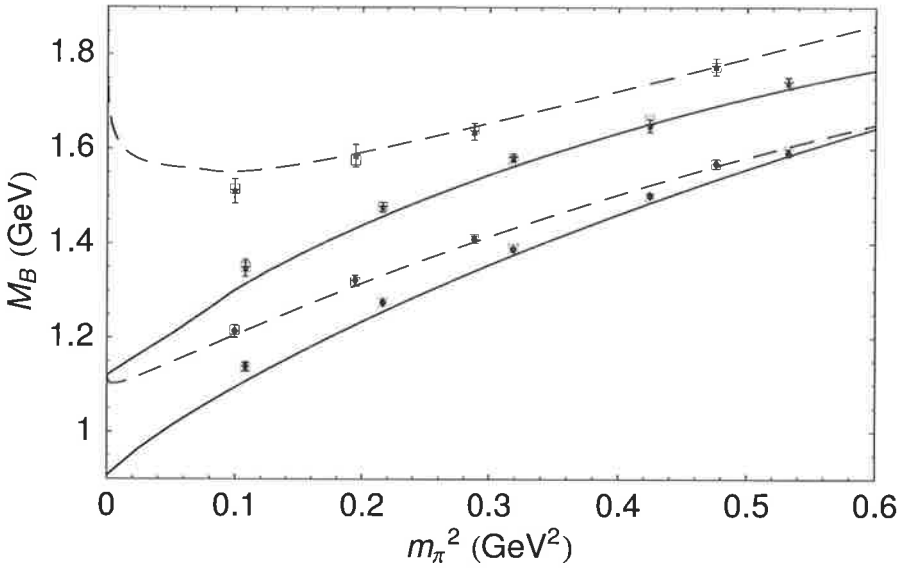

Figure 7.1: Fit (open squares) to lattice data [B$^+$01] with appropriate, finite-volume, chiral corrections. The infinite-volume limits of the dynamical (quenched) fits are shown by the solid (dashed) curves. The lower two curves and data points are for the nucleon, while the upper two are for the Δ.

a_i, characterise local, short-distance interactions and should be largely insensitive to finite-volume effects. The infinite-volume result of the chiral fit is estimated by replacing the momentum sums by their continuum integral analogues, with the a_i's held fixed.

The scale of the quenched and physical simulations has been matched at a short to intermediate distance scale. The inter-quark forces of the nucleon constituents will be effectively matched across both simulations. The internal structure of the nucleon will therefore be of similar scale in both quenched and dynamical simulations. The regulator scale, Λ, which governs the transition between short- and long-distance physics, will be chosen the same for both quenched and dynamical extrapolations.

The dependence on the choice of regulator is not the focus of the present analysis — this has been discussed in great detail in Chapters 4 and 5. Integrals are regularised with a dipole, of preferred mass scale, $\Lambda = 0.8\,\mathrm{GeV}$.

The fits to the lattice simulation results of the nucleon and Delta are shown in Fig. 7.1. On this plot, we see that both the nucleon and Delta baryons lie systematically higher in the quenched approximation, relative to their physical counterparts. A highlight of the extrapolation curves is the prediction of an enhanced N–Δ splitting in the quenched approximation, as the light quark regime

	a_0	a_2	a_4
N (Dynamical)	1.23(1)	1.13(8)	−0.35(12)
N (Quenched)	1.20(1)	1.10(8)	−0.42(13)
Δ (Dynamical)	1.40(3)	1.11(18)	−0.56(25)
Δ (Quenched)	1.43(3)	0.76(21)	−0.04(33)

Table 7.4: Fit parameters of Eq. (7.1), with finite-volume corrections, constrained to staggered fermion simulations of quenched and dynamical QCD. The chiral corrections are regularised with a dipole, $\Lambda = 0.8\,\mathrm{GeV}$. (Units are in appropriate powers of GeV.)

	a_0	a_2	a_4
N (Dynamical)	0.99(1)	1.44(7)	−0.56(10)
N (Quenched)	1.10(1)	1.22(9)	−0.50(14)
Δ (Dynamical)	1.21(3)	1.40(19)	−0.77(27)
Δ (Quenched)	1.45(3)	0.63(19)	0.10(31)

Table 7.5: Parameters of fit to lattice data based on a polynomial in m_π^2, with chiral corrections neglected.

is approached. This prediction has recently been observed with FLIC fermion simulations [BKL+04], as discussed below.

We display the bare, fit parameters in Table 7.4. The renormalisation of the leading expansion parameters can be obtained in a similar fashion to that of Chapters 4 and 5. The importance of renormalisation for obtaining the physical expansion about the chiral limit has been emphasised throughout this Thesis. In the present analysis, there is more to be learned on the nature of the underlying chiral dynamics, and the low-energy expansion parameters of the quenched theory are not of particular interest.

A key feature of Table 7.4 is that the bare parameters of the expansion display a remarkable level of agreement between the quenched and physical theories. This is highlighted by contrasting with a corresponding fit which neglects the chiral-loop effects. In Table 7.5, we show a fit to the data based on a simple quadratic in m_π^2 — Eq. (7.1), with $\Sigma_B = 0$.

The extent of the agreement between the quenched and physical simulations, once the chiral loops have been accounted for, is remarkable. This discovery is embraced to investigate the possibility of simultaneously fitting both data sets with common fit parameters. The entire difference between the fit curves are

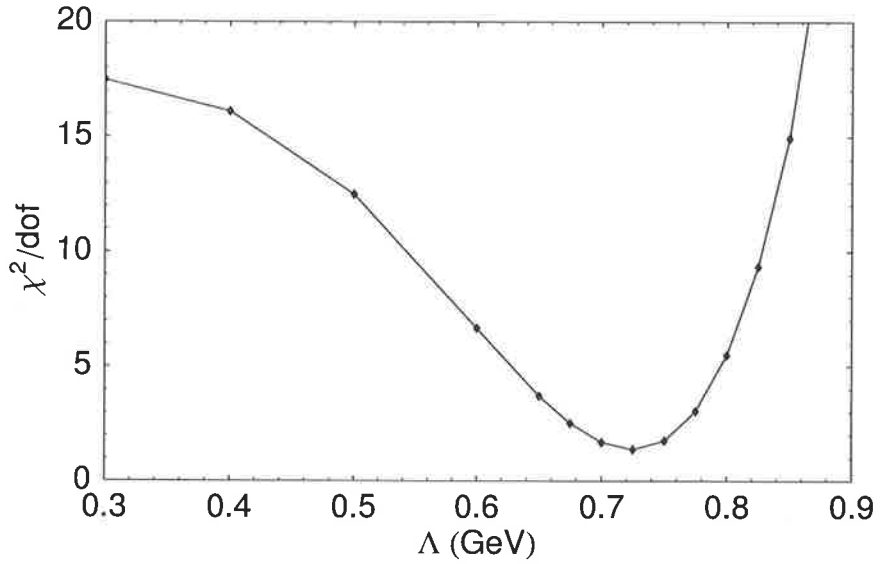

Figure 7.2: Net χ^2/dof for various regulator masses, Λ. The minimum of this curve describes a Λ which provides optimal agreement between the residual series of the quenched and physical masses.

to be encoded in the chiral corrections. The preliminary fit, Fig. 7.1, used the preferred dipole mass of $\Lambda = 0.8\,\text{GeV}$, which is now tuned to optimise the agreement between the simulations. In Fig. 7.2 we show the net χ^2/dof for the simultaneous fits to the quenched and dynamical data. This measure combines the χ^2 of the nucleon and Delta fits. We show the resultant fits for the optimum value of the dipole regulator, $\Lambda = 0.725$, in Fig. 7.3. These fits are extraordinary, considering each baryon has been fit with a common set of a_i parameters, describing both quenched and dynamical data.

The differences in the quenched and dynamical baryon spectra can be predominantly described by the differences in the appropriate chiral corrections, evaluated with a suitable regulator. This is a profound result, which offers a phenomenological link between quenched QCD and reality. This observation offers the potential to analyse quenched simulation data and obtain physical estimates by restoration of the appropriate chiral-loop effects.

Recent FLIC fermion simulations of quenched QCD, approaching the chiral regime [BKL+04], are investigated to test this hypothesis. The simulation results for the baryon masses are shown in Table 7.6. Figure 7.4 show the fits to the quenched FLIC fermion results based on Eq. (7.1). The adjustment for the finite-volume corrections is displayed by the fit-boxes, relative to the dashed curve. These fits use the optimal regulator mass, $\Lambda = 0.725\,\text{GeV}$, the value that

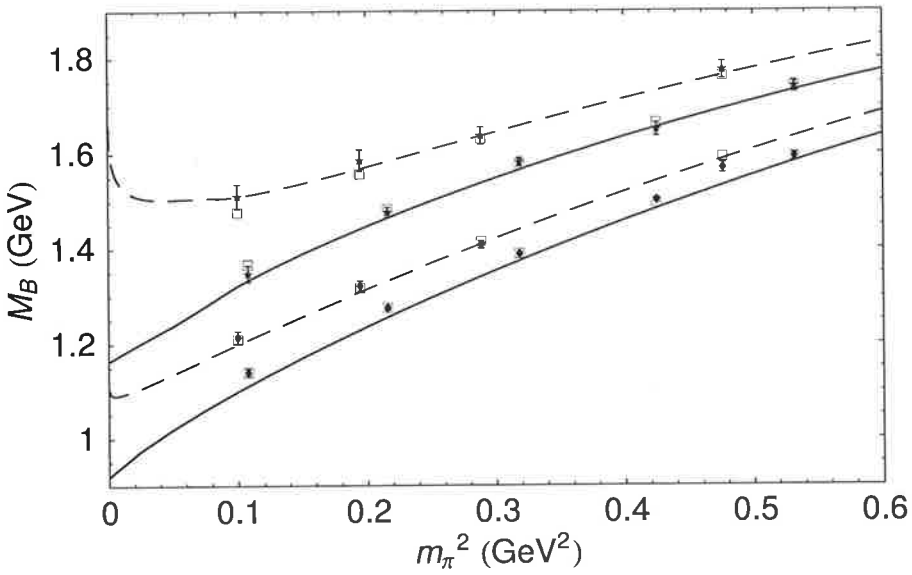

Figure 7.3: Simultaneous fit to both quenched and dynamical data, with a common set of bare parameters. Graph description the same as for Fig. 7.1.

gave the best simultaneous description of the quenched and dynamical results with staggered fermions.

One feature to note is the enhanced N-Δ mass splitting as the chiral limit is approached in quenched QCD — as predicted by the present analysis (originally appearing in Ref. [YLTW02]). As the chiral limit is approached, the deviations of the boxes from the dashed curves in Fig. 7.4 become enhanced. This is a direct consequence of the infrared suppression of the chiral corrections on a finite-volume. Large lattice volumes will be required to observe the dramatic curvature of the continuum theory[1].

Based upon the analysis of the staggered fermion results, we can estimate QCD corrections to the FLIC fermion data. The bare fit parameters, a_i, are obtained by fitting the quenched lattice results with finite-volume, quenched chiral EFT. The physical chiral-loop corrections are then added to this bare expansion polynomial. These estimates of the physical theory are shown by the solid curves in Fig. 7.4. The agreement with the experimental masses is astonishing. The majority of the discrepancy between the observations of quenched lattice QCD and the physical theory can be described by the chiral-loop corrections.

This result is certainly model-dependent and is rather sensitive to the choice

[1]Simulations of the Δ-baryon on a large enough volume, and small enough quark masses, will encounter the p-wave decay threshold. Advanced techniques will be required to access the resonant state.

$m_\pi L$	m_π^2 (GeV^2)	M_N (GeV)	M_Δ (GeV)
10.8	0.691(3)	1.629(8)	1.845(10)
10.0	0.593(3)	1.554(9)	1.791(11)
9.0	0.486(3)	1.468(11)	1.732(12)
8.0	0.379(4)	1.383(11)	1.673(14)
6.9	0.284(3)	1.301(11)	1.622(16)
6.0	0.215(4)	1.243(12)	1.592(17)
4.8	0.138(4)	1.190(15)	1.565(18)
4.0	0.094(4)	1.159(21)	1.550(19)

Table 7.6: Quenched lattice data used of FLIC fermions. All simulations on a $20^3 \times 32$ lattice, at spacing, $a \simeq 0.128\,\text{fm}$. Results from Boinepalli et al. [BKL$^+$04].

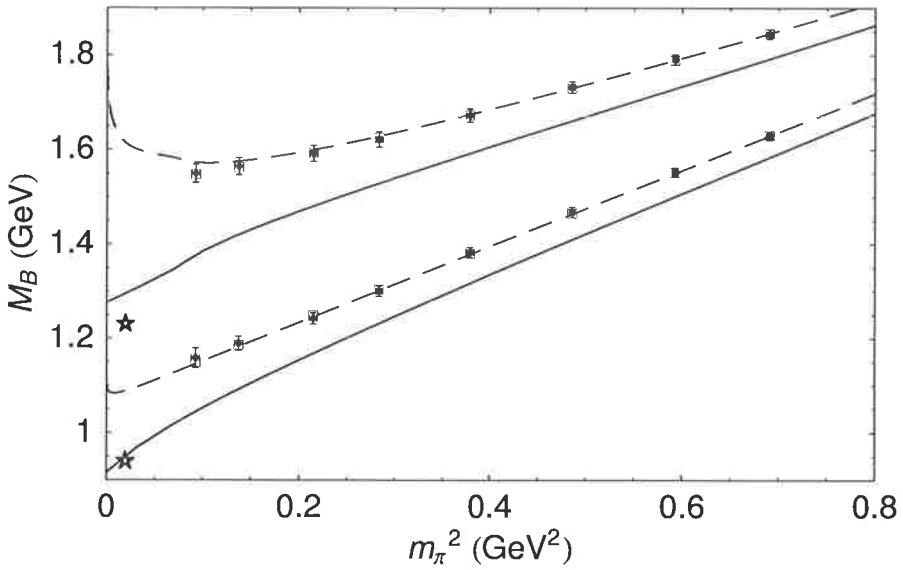

Figure 7.4: Finite-volume fits to FLIC fermion results (⧫) are described by the box symbols. The resulting infinite-volume fits are shown by the dashed curves. The solid lines give a phenomenological estimate of the corrections in going to dynamical QCD. The stars denote the physically observed masses.

of Λ. Nevertheless, this discovery provides valuable insight into the dynamics of the hadronic spectrum in QCD.

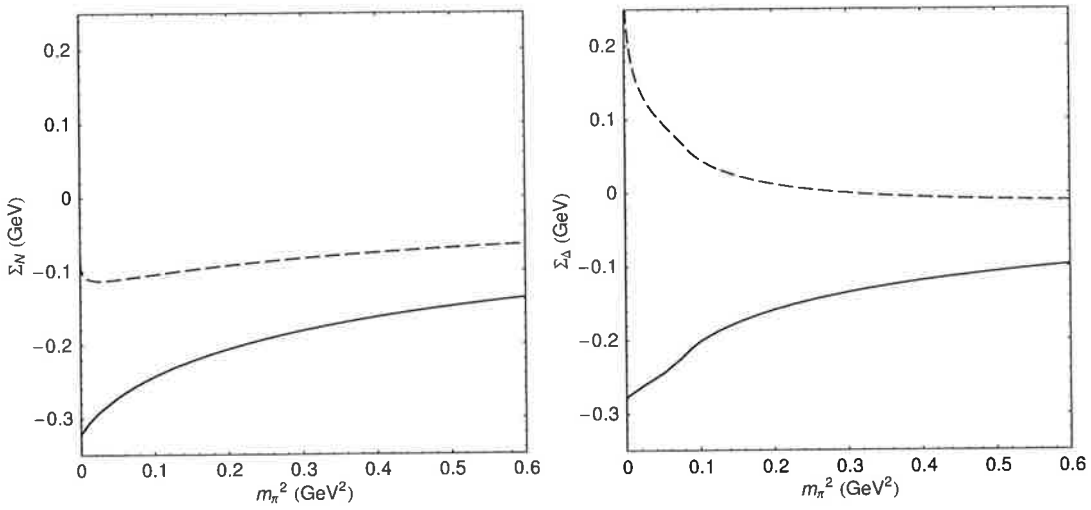

Figure 7.5: The net chiral corrections, Σ_B, for the physical and quenched theory are shown by the solid and dashed curves, respectively. Contributions to the nucleon (Delta) mass are displayed in the left (right) figure. All curves evaluated with a dipole regulator, $\Lambda = 0.8\,\text{GeV}$.

7.3 Physical Insights

To gain further insight into the dynamics of how the meson-loop corrections affect the baryon masses, the loop corrections, Σ_B, are plotted in Fig. 7.5. Shown are the corrections to the nucleon and Delta masses arising from chiral loops, over a range of pion masses. Whereas the chiral corrections in QCD are quite similar for the nucleon and Delta, there are significant differences in the quenched theory. Individual contributions are illustrated in Ref. [YLTW02].

For the nucleon, the effects of quenching are primarily to reduce the magnitude of the chiral corrections. This is dramatically different for the Delta, where interaction with the $N\pi$ becomes repulsive, raising the mass of the resonant state in the quenched theory.

This repulsive interaction can easily be understood by considering a pictorial, quark-flow description of the processes contributing to the N–π loop in full QCD. Figure 7.6 shows all different topological contributions to the $\Delta^{++} \to N\pi$ loop diagram. Diagrams (b) and (c) both indicate the propagation of an unphysical uuu octet baryon. Because there is no physical doubly-charged nucleon, these two processes must sum to zero in the physical theory, *i.e.* (c)=−(b). QCD is also flavour-blind and knows nothing of the quark flavour propagating in the loop, meaning that processes (a) and (b) are identical, for degenerate u and d

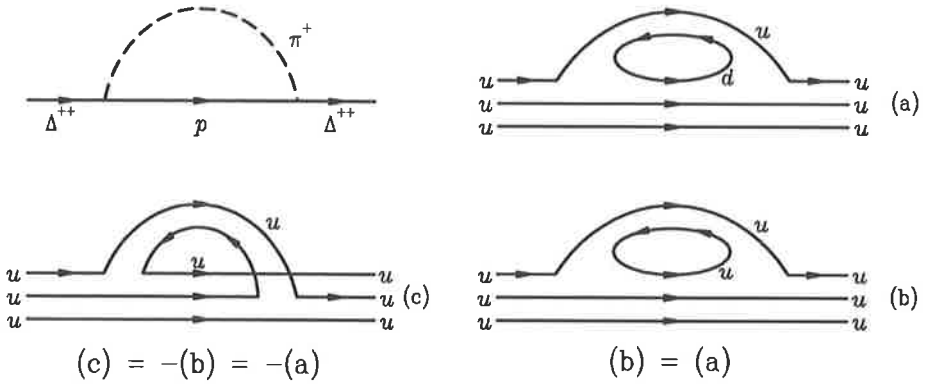

Figure 7.6: Pictorial quark-flow view of the N–π chiral loop contributions to the Δ baryon in full QCD.

quark masses. In the quenched theory, diagrams (a) and (b) are absent and the only remaining diagram is (c), which is a uuu quark state, degenerate with the nucleon. By deduction, this contribution is precisely the same in magnitude as Fig. 7.6(a) with the opposite sign, this is seen by the coefficients in Table 7.1. The significance of this unphysical nucleon was highlighted in the original work of Labrenz and Sharpe [LS96].

It has been recognised that other excited states lie systematically high in the quenched approximation. Using chirally improved quark actions, the BGR Collaboration have noted that there seems to be a correlation between the quenched discrepancies and the physically observed widths [G+04]. As chiral extrapolation techniques for excited states are developed [MCLT03], it will be interesting to see if more quenched spectroscopy can be similarly understood in terms of chiral interactions.

Very near the chiral limit in the quenched curves of Fig. 7.5, there is an upward turning lip, which arises from the linear m_π behaviour of the double-hairpin η' contribution. The magnitude of the correction is quite small for the nucleon, and appears to be more significant for the Delta. In both cases though, it seems observation will require lattice simulation results below the physical pion mass.

The analysis of lattice data has demonstrated the ability to describe the primary difference between quenched and dynamical simulations in terms of the meson-loop self-energies. This helps to develop an increased understanding of the origins of the mass-splittings in the physical baryon spectrum.

Figure 7.7 shows the difference in the chiral corrections for the N and Δ in quenched and full QCD, for a range of dipole regulator parameters, $\Lambda = 0.8 \pm 0.1\,\text{GeV}$. It is quite clear that there is a difference of between 150 and

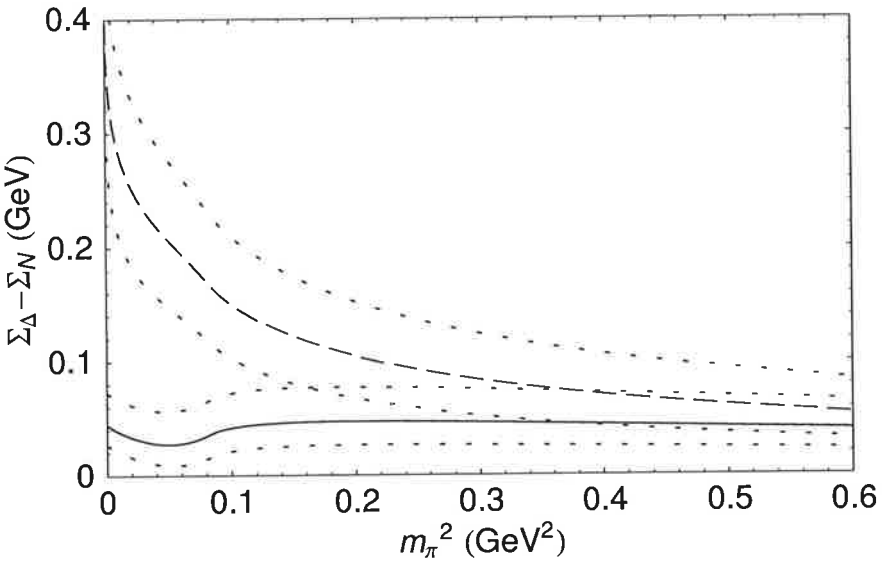

Figure 7.7: Meson-loop contribution to the Δ–N mass splitting in both quenched (dashed curve) and full (solid curve) QCD. The central curves are evaluated with a dipole, $\Lambda = 0.8\,\text{GeV}$. The upper and lower dotted curves display variation of the regulator scale by $\pm 0.1\,\text{GeV}$, respectively.

250 MeV between the quenched and full QCD cases. This difference was essential in accounting for the clear discrepancy in the behaviour of the baryon masses in QQCD and QCD, as highlighted in Fig. 7.4. This therefore provides confidence in interpreting these results to say how much of the physical N-Δ mass splitting is associated with pion loops, in today's leading phenomenological models. The residual mass-splitting is accordingly attributed to some short-range, non-hadronic processes, such as gluon exchange.

An examination of the solid curve of Fig. 7.7, indicating the chiral corrections in QCD, suggests that only about 50 MeV of the observed, 300 MeV, N–Δ splitting arises from pion interactions. This is in agreement with the argument of Isgur in Ref. [Isg00], that the spin-dependent, hyperfine forces in hadrons, cannot be dominated by mesonic interactions.

* * *

An investigation of the quark mass dependence of the N and Δ masses within the quenched approximation has been presented. The leading chiral behaviour of hadron masses is known to differ in quenched QCD from the physical theory. Techniques of finite-range regularisation have been introduced to QχPT and the subsequent chiral expansion, fit to modern simulation results.

Remarkably, a comparison of the two fits suggests that the properties of the N and Δ, stripped of their chiral corrections, are essentially the same in quenched and physical QCD — provided the lattice scale is set using the Sommer scale. This observation appears dependent on an optimal regulator shape and size[2], and the assumption that the axial coefficients are similar in quenched and dynamical QCD. This result identifies a phenomenological link between the results of quenched lattice simulations and the real world. This link has been demonstrated to provide excellent estimates of the nucleon and Delta masses in QCD — from a purely quenched simulation.

The N–Δ mass-splitting is observed to be significantly enhanced in the quenched approximation — a consequence of the modified chiral behaviour of the quenched theory. The study of these chiral corrections has provided an enhanced understanding of the role of meson interactions in the baryon spectrum.

[2]The phenomenological insight gained is true for any finite-range regulator. The degree to which the discovered success could be repeated with a different regulator has not yet been quantified.

8

Nucleon Magnetic Moments

The electromagnetic form factors describe the fundamental charge and current distributions of the nucleon. Beyond the nucleon mass, which has been discussed in great detail, description of the electromagnetic properties of the nucleon presents a further test of nonperturbative QCD.

All lattice QCD simulation results, to date, of the electromagnetic structure of baryons are restricted to the quenched approximation. Combined with the relatively large quark masses, the analysis of modern simulation results requires all the machinery developed throughout this Thesis.

Previous studies of the chiral extrapolation of magnetic moments have assumed that simulation results give a good description of the physical theory. These investigations have ranged from χPT, with heavy-quark phenomenology [LLT99, HJLT00b][1], to the more ambitious direct application of dimensionally regularised χPT [HW02, G$^+$05]. Recent work has applied FRR to the extrapolation of Δ-baryon magnetic moments in physical QCD [CLT03]. The electromagnetic form factors, at finite momentum transfer, have also seen renewed interest [G$^+$05, ALTY04].

In this work, the chiral expansion of the physical magnetic moments is studied, within the framework of finite-range regularisation. With lattice simulations limited to the quenched approximation, the necessary adjustments to the chiral expansion are examined. Constraining the expansion formulae to lattice results enables the analysis of the behaviour of the proton magnetic moment in the chiral regime. Finite-volume effects are also investigated and found to be quite small, for the lattice simulation parameters considered.

The discovery of a phenomenological link between quenched and physical QCD, as described in Chapter 7, is extended to the magnetic moments. This allows estimates of QCD magnetic moments to be obtained from results of a pure quenched simulation. It is observed that there is little deviation between the two theories over a wide range of quark mass — despite marked differences in the nonanalytic structure.

Extending the analysis beyond leading order is found to improve the estimate

[1] While these studies are exact χPT to leading order, a systematic extension to higher-order does not appear perceivable.

of the physical proton magnetic moment. While the difference between leading and next-to-leading order is evident, they remain equivalent within statistical uncertainties.

The principal research of this Chapter has been presented in Ref. [YLT05], with preliminary analyses appearing in Refs. [L+03, YLT04b, YLT04a].

8.1 Chiral Expansion

Similarly to the construction of the expansion of the nucleon mass, Eq. (4.1), the most general expansion of the magnetic moment can be written as

$$\begin{aligned} \mu_B &= a_0^B + a_2^B m_\pi^2 + a_4^B m_\pi^4 + \dots \\ &\quad \chi_{B\mu} I_\mu + \dots , \end{aligned} \tag{8.1}$$

where the isospin of the nucleon is denoted by $B = p$ or n. The formal expansion of the magnetic moments has been described by Jenkins *et al.* [JLMS93], where the leading (renormalised) coefficients are expressed in terms of the underlying chiral Lagrangian. In Eq. (8.1), the term $\chi_{B\mu} I_\mu$ denotes the leading nonanalytic (LNA) chiral correction to the baryon magnetic moment of Fig. 8.1. The coefficients of the leading loop-diagrams arise from the tree-level meson–baryon interaction vertices and are known to high precision. For example, the coefficient of the leading nonanalytic contribution to the proton magnetic moment is given by

$$\chi_{p\mu} = -\frac{g_A^2 M_N}{8\pi f_\pi^2} . \tag{8.2}$$

With a demonstrated difficulty in the direct determination of these nonanalytic coefficients from lattice simulations, these terms of the expansion are fixed to their phenomenological values.

The short-distance contributions, encoded by the analytic terms, are not constrained by the low-energy effective field theory. Following the same procedure as outlined for the mass extrapolation, these parameters can be determined nonperturbatively by fitting to lattice QCD data.

The loop-integral, I_μ, evaluated within the usual minimal subtraction renormalisation scheme, gives m_π. The linear divergence of the integral is absorbed into the renormalisation of a_0. The poor expansion properties of the chiral series, evaluated in dimensional regularisation, has been demonstrated in Chapters 4 and 5.

To exploit the improved convergence of the chiral expansion, finite-range regularisation is applied to the magnetic moment expansion. The loop integral,

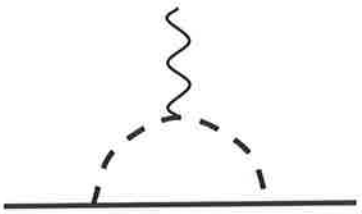

Figure 8.1: Leading one-loop diagram contributing to the nucleon magnetic moment. The solid, dashed and wiggly lines describe nucleon, pion and electromagnetic currents, respectively.

I_μ, in the heavy baryon limit can be expressed as

$$I_\mu = -\frac{1}{2\,\pi^2}\int d^3\vec{k}\frac{(\hat{q}\times\vec{k})^2}{(\vec{k}^2+m_\pi^2)^2}\,u^2(k)\,, \tag{8.3}$$

for ultra-violet regulator, $u(k)$, $k=|\vec{k}|$ and $\hat{q}=\vec{q}/|\vec{q}|$. Performing the angular integral gives

$$I_\mu = -\frac{4}{3\,\pi}\int dk\frac{k^4u^2(k)}{(k^2+m_\pi^2)^2}\,. \tag{8.4}$$

For a dipole regulator, explicit evaluation of the loop integral gives

$$I_\mu^{\rm DIP} = -\frac{\Lambda^5(m_\pi+5\Lambda)}{24(m_\pi+\Lambda)^5}\,. \tag{8.5}$$

The appropriate renormalisation of the chiral expansion is obtained through a power series expansion of the loop contributions. The Taylor expansion in m_π, of the dipole form, provides

$$I_\mu^{\rm DIP} = -\frac{5}{24}\Lambda + m_\pi - \frac{35}{12\,\Lambda}m_\pi^2 + \ldots\,. \tag{8.6}$$

The leading nonanalytic contribution is observed, independent of regularisation,

$$\chi_{B\mu}I_\mu^{\rm DIP\ (LNA)} = \chi_{B\mu}m_\pi\,, \tag{8.7}$$

with a finite renormalisation of all other terms in the series. Explicitly, for a renormalised expansion defined by by

$$\mu_B = c_0^B + \chi_{B\mu}m_\pi + c_2^Bm_\pi^2 + \ldots\,, \tag{8.8}$$

the corresponding renormalisation of the analytic terms is defined by

$$\begin{aligned} c_0^B &= a_0^B - \chi_{B\mu}\frac{5}{24}\Lambda\,, \\ c_2^B &= a_2^B - \chi_{B\mu}\frac{35}{12\,\Lambda}\,. \end{aligned} \tag{8.9}$$

This renormalisation ensures the mathematical equivalence of all regularisation prescriptions to any given order.

In summary, in working to leading order in the chiral expansion with a dipole FRR, the quark-mass dependence of nucleon magnetic moments in QCD is given by

$$\mu_B = a_0^B + a_2^B m_\pi^2 - \chi_{B\mu} \frac{\Lambda^5 (m_\pi + 5\Lambda)}{24(m_\pi + \Lambda)^5} \,. \tag{8.10}$$

To this order, inclusion of a term at m_π^4 is not necessary. This term will need to be reinstated at next-to-leading order — upon inclusion of nonanalytic contributions at $m_\pi^2 \log m_\pi$.

8.2 Quenched Considerations

Modern simulations of the electromagnetic form factors in lattice QCD are restricted to the quenched approximation [G$^+$05, ZLWZ04, ZBL$^+$04]. As highlighted by Chapters 6 and 7, the chiral effective field theory is modified by the absence of $q\bar{q}$-pairs in the vacuum. Meson loop diagrams are restricted to those where the loop is comprised of valence quarks — those quark fields that are continuously connected to the interpolating fields of the baryon correlation function. This has the effect of modifying the effective π–N coupling constants [Sav02, Lei04] and the corresponding factors χ_B are changed accordingly.

The contributions to nucleon magnetic moments in both quenched and dynamical QCD are summarised by the introduction of the coupling-strength parameter, β_B^π, defined through

$$\chi_{B\mu} = \frac{M_N}{8\pi f_\pi^2} \beta_B^\pi \,. \tag{8.11}$$

Values of the parameters, β_B^π, are provided in Table 8.1 [Sav02, Lei04]. The standard phenomenological values are used, $f_\pi = 93\,\text{MeV}$ and $g_A = D + F = 1.26$. The relative strengths in D- and F-style couplings are given by the SU(6) estimate, $D/F = 3/2$.

In addition to the modification of the pion-loop contributions, the flavour-singlet η'-meson also becomes important. In a similar way to that observed in our study of the nucleon mass, the η' gives rise to more singular behaviour near the chiral limit. With zero charge, the η' does not make a direct contribution to the magnetic moment of the nucleon. The leading enhancement of the moment comes from η'-dressing of the current insertion as in Fig. 8.2. The singular behaviour arises from the double-hairpin diagram of the η' propagator. This

Baryon	β_B^{π}	$\beta_B^{\pi\,(\mathrm{Q})}$
p	$-(F+D)^2$	$-\frac{4}{3}D^2$
n	$(F+D)^2$	$\frac{4}{3}D^2$

Table 8.1: Coefficients of the leading pion-loop contributions to nucleon magnetic moments in QCD and QQCD. The superscript (Q) denotes a quenched quantity.

double-hairpin diagram has a logarithmic divergence near the chiral limit. This is a pathological feature of the quenched approximation, where the magnetic moment tends to infinity near the chiral limit. This is not possible in the physical theory, as angular momentum quantization ensures that the induced magnetic field of the meson-loop remains finite, even in the chiral limit [LTY01].

The vertex-correction, induced double-hairpin diagram, provides a contribution to the nucleon magnetic moment in the quenched approximation [Sav02],

$$\chi_{\eta'}^{(\mathrm{Q})}\,\mu_B^{(\mathrm{Q})\mathrm{tree}}\,I_{\eta'}\,, \tag{8.12}$$

with coefficient

$$\chi_{\eta'}^{(\mathrm{Q})} = \frac{m_0^2\,(3F-D)^2}{12\,\pi^2\,f_\pi^2}\,. \tag{8.13}$$

The hairpin strength is set to the same value used in the spectrum analysis, $m_0^2 = 0.42\,\mathrm{GeV}^2$.

The loop integral describing the vertex correction, in the heavy-baryon limit, is given by

$$I_{\eta'} = -\int dk \frac{k^4 u^2(k)}{\omega_k^5}\,, \tag{8.14}$$

with $\omega_k = \sqrt{k^2+m_\pi^2}$. The normalisation of the integral is defined such that the leading-nonanalytic term is $\log m_\pi$.

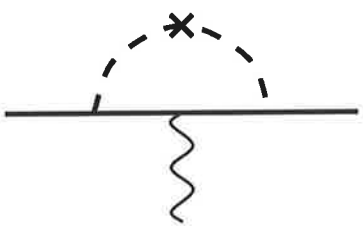

Figure 8.2: Double-hairpin η' vertex correction to nucleon magnetic moment.

Because the moment is logarithmically divergent in the chiral limit, the expansion cannot be defined relative to this point. Equation 8.12 describes the coefficient of the vertex correction proportional to the tree-level moment, $\mu_B^{(\mathrm{Q})\mathrm{tree}}$ [Sav02]. To define this quantity, independent of ultraviolet-regularisation, requires a finite tree-level moment. This must therefore be chosen as the renormalised moment, evaluated at finite quark mass. The scale dependence of choosing a particular quark mass is removed by replacing the tree level coefficient by the renormalised magnetic moment at *each* quark mass $\mu_B^{(\mathrm{Q})\mathrm{tree}} = \mu_B^{(\mathrm{Q})}$[2].

For quenched simulations, the appropriate expansion is given by

$$\begin{aligned} \mu_B^{(\mathrm{Q})} &= a_0^{B\,(\mathrm{Q})} + a_2^{B\,(\mathrm{Q})} m_\pi^2 + \\ &\quad + \chi_{B\mu}^{(\mathrm{Q})}\, I_\mu + \chi_{B\eta'}^{(\mathrm{Q})}\, \mu_B^{(\mathrm{Q})}\, I_{\eta'}\,, \end{aligned} \tag{8.15}$$

which is analogous to the QCD expression, Eq. (8.1). Lattice results are used to constrain the parameters $a_i^{B\,(\mathrm{Q})}$. The magnetic moment at arbitrary m_π is then identified as

$$\begin{aligned} \mu_B^{(\mathrm{Q})} &= \Big\{ a_0^{B\,(\mathrm{Q})} + a_2^{B\,(\mathrm{Q})} m_\pi^2 + a_4^{B\,(\mathrm{Q})} m_\pi^4 \\ &\quad + \chi_{B\mu}^{(\mathrm{Q})} I_\mu \Big\} \left(1 - \chi_{B\eta'}^{(\mathrm{Q})} I_{\eta'}\right)^{-1}. \end{aligned} \tag{8.16}$$

8.3 Extrapolation of Lattice Magnetic Moments

The simulation results of lattice QCD can describe the variation of the magnetic moments over a range of quark masses. This allows the nonperturbative determination of the free parameters of the chiral expansion.

Recent calculations in lattice QCD have studied the electromagnetic form factors of the nucleon [G+05, ZLWZ04, ZBL+04]. These calculations extend the pioneering calculations by Leinweber *et al.* in Refs. [LWD91]. Results by Göckeler *et al.* [G+05] have been obtained using the nonperturbatively improved clover (NPIC) fermion action [LSS+97]. Simulations of the three-point functions using FLIC fermions have been performed by Zanotti *et al.* [ZLWZ04, ZBL+04]. For the present investigation, only the six most accurate data points from the FLIC data set are selected. The results of both the NPIC and FLIC simulations are displayed in Fig. 8.3. The precision of the FLIC fermion results reflects the use of improved unbiased estimation techniques [LWD91], improved actions and high statistics. All results above $m_\pi^2 = 0.8\,\mathrm{GeV}^2$ have been excluded from the current study.

[2]This approximation will be accurate provided $\chi_{\eta'}^{(\mathrm{Q})} \mu_B^{(\mathrm{Q})\mathrm{tree}} I_{\eta'}$ makes only small contributions for $m_\pi > m_\pi^{\mathrm{phys}}$. This is satisfied for all finite-range regulator scales considered.

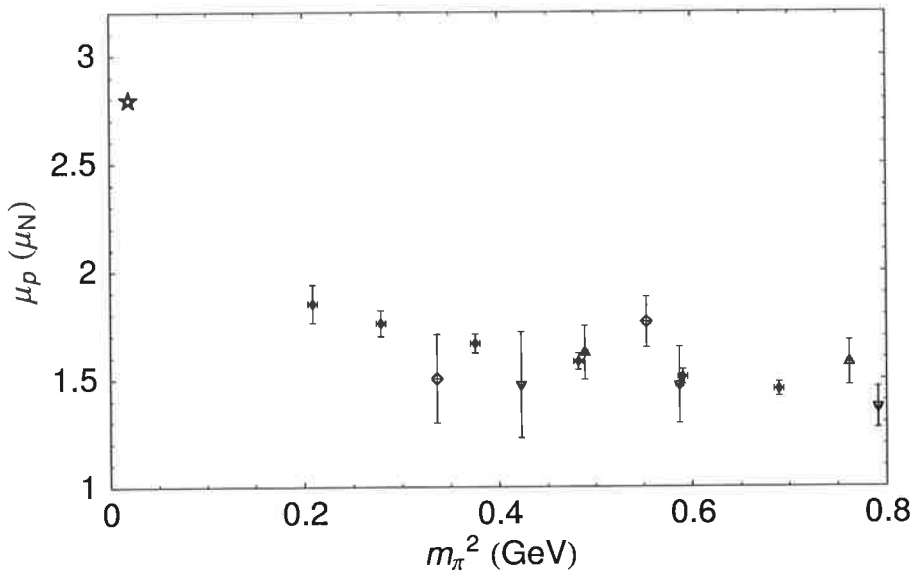

Figure 8.3: The solid diamonds (♦) illustrate the FLIC fermion results [ZLWZ04, ZBL+04] and the open symbols describe nonperturbatively improved clover results [G+05], at $\beta = 6.0$ ($\triangledown$), $\beta = 6.2$ ($\triangle$) and $\beta = 6.4$ ($\Diamond$). The experimental moment is shown by the star.

The expansion, Eq. (8.15), is constrained to the entire lattice data set, with the resultant fit curve shown in Fig. 8.4. The solid curve describes the fit with the preferred dipole regulator scale, $\Lambda = 0.8\,\text{GeV}$. The upper and lower dashed curves display the dependence on this scale, showing $\Lambda = 1.0$ and $0.6\,\text{GeV}$, respectively.

The results are quite insensitive to the regulator scale. The variation in the proton moment, evaluated at the physical pion mass, is similar to the statistical uncertainty of the FLIC simulation result at the lightest quark mass considered. The sensitivity to Λ will be reduced by increasing the chiral expansion to higher order.

Finite Volume Effects

Simulations in lattice QCD are always performed on a finite volume at finite lattice spacing. There will necessarily exist corrections in extending the theory to the infinite-volume continuum. Ultimately, both these discretisation artifacts will be built into the effective field theory to characterise a complete description of the variation of hadron properties with m_q, a and L.

There have been studies in EFT which incorporate new local operators

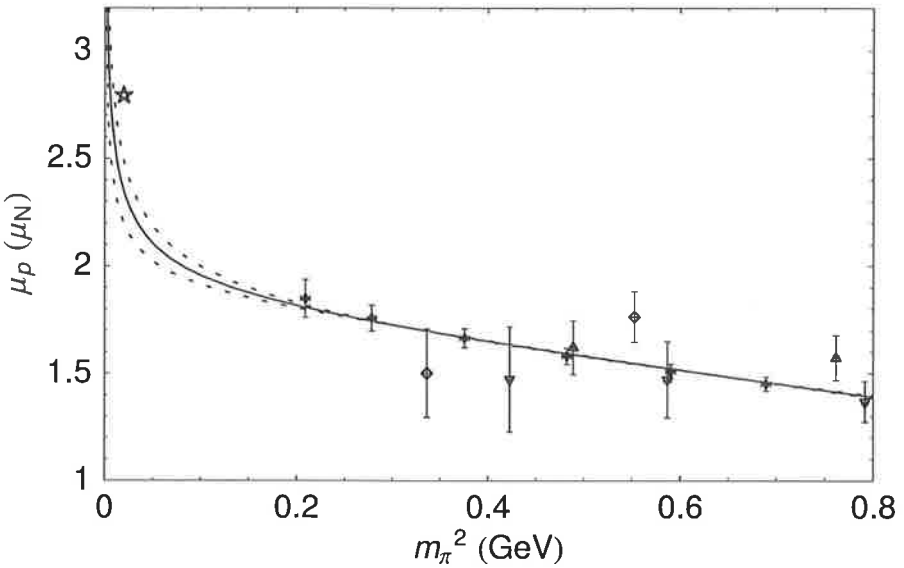

Figure 8.4: Leading-order fit of Eq. (8.15) to quenched lattice data. The solid curve displays the preferred regulator scale, $\Lambda = 0.8\,\text{GeV}$. The insensitivity of the scale is shown by the upper and lower dotted curves, corresponding to $\Lambda = 1.0$ and $0.6\,\text{GeV}$, respectively. Data is the same as described in Fig. 8.3.

into the chiral Lagrangian reflecting the $\mathcal{O}(a)$ dependence of hadronic observables [RS02, BRS03, Aok03]. There have been significant advances in the formulation of lattice QCD to remove $\mathcal{O}(a)$ errors and suppress those at $\mathcal{O}(a^2)$. The finite lattice-spacing effects are therefore minimised through nonperturbative improvement schemes, such as NPIC [LSSW96], overlap [NN95] and FLIC [Z$^+$02]. These actions have been demonstrated to exhibit excellent scaling properties at finite lattice spacing [EHK98b, DLLZ00, ZLLW05]. Therefore, the lattice data currently under study already represent an excellent approximation to the continuum limit.

The effects of finite lattice volume will be more apparent, with the lightest simulated FLIC fermion result at the dimensionless measure $m_\pi L = 4.8$. Correspondingly, there will be significant corrections associated with the suppression of infrared physics. Similarly to the analysis of Chapter 7, we extend the effective field theory to incorporate finite-volume effects. The dominant corrections from the finite-volume will lie in the corrections to the chiral-loop integrals. The continuous loop integrals over the pion momenta are replaced by a summation over the discrete momenta of the finite box, as described by Eq. (7.12).

Evaluation of the loop integrals on a finite volume in FRR is a rather simple extension. This allows the features of finite-range regularisation to carry over to

the finite volume case. For example, Eq. (8.3) becomes

$$I_{\mu L} = -\frac{1}{2\,\pi^2}\left(\frac{2\pi}{L}\right)^3 \sum_{\vec{k}} \frac{(\hat{q}\times\vec{k})^2}{(\vec{k}^2+m_\pi^2)^2}\,u^2(k)\,. \tag{8.17}$$

The discretized momenta on a cube are given by $\vec{k} = k_{\rm min}\vec{\mathbf{n}}$ for $\vec{\mathbf{n}} \in \mathbb{Z}^3$, with the minimum nontrivial momentum given by $k_{\rm min} = 2\pi/L$. A similar modification is made to the η' loop integral, Eq. (8.14).

The high precision of the FLIC fermion data, obtained by Ref. [ZBL+04], means that the fits are dominated by these points and the results of Ref. [G+05] have consequently been neglected. The FLIC fermion simulations have been carried out on a physical lattice volume, $V = (2.56\,\text{fm})^3$.

In Fig. 8.5, the results based on the finite-volume, quenched EFT, shown by the open boxes, are fit to lattice results. The quality of fit should be judged by the comparing the boxes to the lattice data. The solid curve represents the infinite-volume limit, with the discrete sum loop-integrals being replaced by their continuous counterparts. The dashed curves, which show the insensitivity to the regulator parameter, display the infinite-volume corrected results for $\Lambda = 0.6$ and 1.0 GeV.

This systematic uncertainty is smaller than the statistical uncertainty of the lightest quark mass considered here, and could be suppressed further through the introduction of higher-order terms in the chiral expansion or through the introduction of precise lattice QCD results at light quark masses.

8.4 Chiral Unquenching

Although the lattice simulations have been restricted to quenched QCD, the magnetic moments of the physical theory can be estimated by correcting the long-distance chiral contributions. The results of Section 7.2 demonstrated that the differences in the quenched and dynamical baryon spectrum can be described by the chiral loop corrections, evaluated with a FRR. This provides a phenomenological link, relating quenched QCD to the physical theory.

This allows quenched simulation results to be *unquenched*, with application to FLIC fermion simulations, of baryon masses, with demonstrated success. Upon replacing the chiral loops of QQCD by their QCD counterparts the nucleon and Delta are found to be in good agreement with experiment.

By applying the same principle to the calculation of magnetic moments in quenched QCD one can obtain improved estimates of the physical magnetic moment. The fit parameters, $a_i^{B\,(\rm Q)}$, are determined by fitting finite-volume

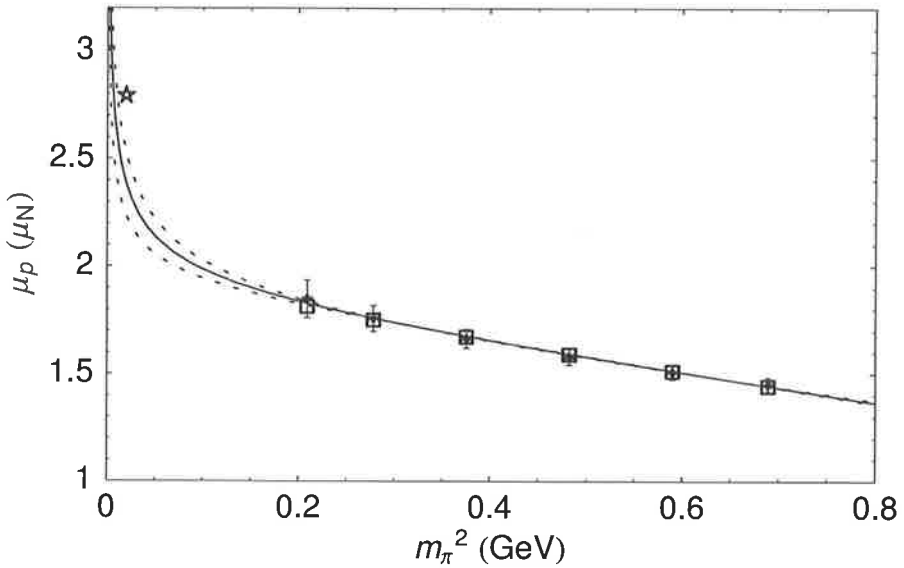

Figure 8.5: Finite-volume FRR-EFT fit to FLIC fermion results for fixed volume. The boxes display the finite-volume fit to the lattice data points, for dipole regulator parameter fixed to $\Lambda = 0.8\,\mathrm{GeV}$. The solid curve indicates the correction to the infinite volume. The upper and lower dashed curves describe the corresponding infinite-volume corrected curve for $\Lambda = 1.0$ and $0.6\,\mathrm{GeV}$, respectively — the discrete fit points for these Λ values are not shown.

quenched lattice QCD using Eq. (8.15) with discretized momenta and a dipole regulator of 0.8 GeV. The estimate of the quenching effects are obtained under the assumption that the bare residual expansion parameters are unchanged in infinite-volume QCD when $\Lambda = 0.8\,\mathrm{GeV}$. That is, the full QCD result can be described by Eq. (8.10) with the identification $a_i^{B\,(\mathrm{Q})} = a_i^B$. By fitting with finite-volume FRR-EFT both quenching and finite-volume corrections are incorporated in the final estimate. We show the infinite-volume QCD estimate of the proton magnetic moment by the dashed curve in Fig. 8.6.

In a similar manner, the infinite-volume limit of QQCD is estimated by fitting the parameters $a_i^{B\,(\mathrm{Q})}$ of Eq. (8.15) using finite-volume discretized momenta and a dipole regulator of 0.8 GeV in the loop integrals. The correction is estimated by Eq. (8.16) calculated with infinite-volume continuous momenta in the loop integrals. Figure 8.6 illustrates that the finite volume corrections are minor in the regime of the lattice QCD simulation results.

We emphasize that this result is a phenomenological estimate, as the size of the correction is Λ dependent. The primary feature of Fig. 8.6 is that the observable differences are quite small, despite the fact that the quenched and

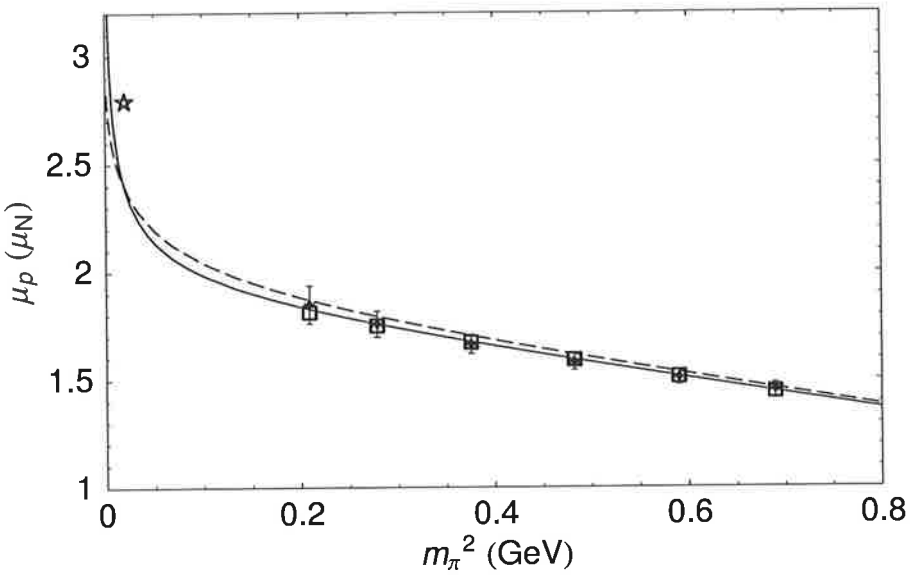

Figure 8.6: Correcting the finite-volume quenched approximation to the infinite-volume limit of full QCD. The boxes and solid curve are the same as those shown in Fig. 8.4. The dashed curve shows estimates of the proton magnetic moment in full QCD, as described in the text.

physical theory have significantly different chiral structure. The logarithmic divergence appears to only become apparent well below the physical pion mass. Within the current formalism of lattice QCD, it seems such observation would be a formidable task, particularly given the large finite volume required to reveal the η' contribution.

The results here, based on the leading chiral corrections, indicate that proton magnetic moments evaluated in quenched simulations give a good approximation to the true theory. The enhancement from the η'-loop compensates for the reduction in the standard pion-loop from QCD to QQCD. The similarity in the effective curvature was also highlighted by Savage [Sav02].

8.5 Beyond Leading Order

The analysis is extended beyond leading-order, with an investigation of higher-order terms in the FRR expansion. In particular, effects of the Δ-baryon are explicitly treated in the expansion. The coupling to the Δ-resonance is understood to play a significant role in spin-dependent properties of the nucleon. The leading contribution from the Δ-baryon, shown in Fig. 8.7, can be summarised

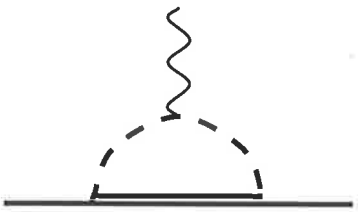

Figure 8.7: Leading pion-loop contribution to nucleon magnetic moment from the Δ resonance.

Table 8.2: Coefficients of the leading decuplet, pion-loop contributions to nucleon magnetic moments in QCD and QQCD [Sav02], $\mathcal{C} = -2D$.

Baryon	$\beta^{\pi}_{B\Delta}$	$\beta^{\pi\,(\mathrm{Q})}_{B\Delta}$
p	$-\frac{2}{9}\mathcal{C}^2$	$-\frac{1}{6}\mathcal{C}^2$
n	$\frac{2}{9}\mathcal{C}^2$	$\frac{1}{6}\mathcal{C}^2$

as

$$\chi^{\Delta\,(\mathrm{Q})}_{B\mu}\, I_\mu(m_\pi, \Delta, \Lambda)\,, \tag{8.18}$$

where, analogous to Eq. (8.11), the corresponding couplings are given by

$$\chi^{\Delta}_{B\mu} = \frac{M_N}{8\pi f_\pi^2}\,\beta^{\pi}_{B\Delta}\,, \tag{8.19}$$

and Table 8.2. The loop integral is also modified by the fact that the intermediate baryon propagator is non-degenerate with the external state. With the mass-splitting given by Δ, Eq. (8.3) becomes

$$I_\mu(m_\pi, \Delta, \Lambda) = -\frac{4}{3\,\pi}\int dk \frac{(\Delta + 2\omega_k)k^4 u^2(k)}{2\omega_k^3(\Delta + \omega_k)^2}\,. \tag{8.20}$$

The full expression for the expansion, at this order, is given by

$$\begin{aligned}\mu_B^{(\mathrm{Q})} \;=\; & a_0^{B\,(\mathrm{Q})} + a_2^{B\,(\mathrm{Q})} m_\pi^2 + a_4^{B\,(\mathrm{Q})} m_\pi^4 \\ & + \chi^{(\mathrm{Q})}_{B\eta'}\,\mu_B^{(\mathrm{Q})}\, I_{\eta'} + \chi^{(\mathrm{Q})}_{B\mu}\, I_\mu(m_\pi, 0, \Lambda) + \chi^{\Delta\,(\mathrm{Q})}_{B\mu}\, I_\mu(m_\pi, \Delta, \Lambda)\,,\end{aligned} \tag{8.21}$$

We compare the extrapolation, including the Δ, with the leading order result in Fig. 8.8. The leading-order result, with volume corrections, as shown in Fig. 8.5, is displayed by the solid curve. The boxes describe the finite-volume fit at next-to-leading order, with the corresponding infinite-volume corrections described by the dash-dot curve. Increased curvature is realised in these beyond

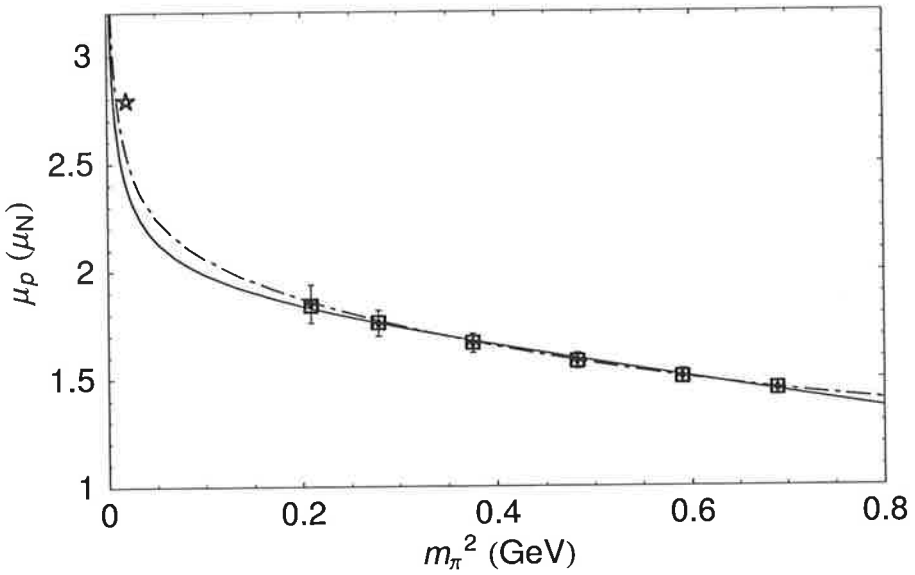

Figure 8.8: The role of Δ contributions in the extrapolation of the proton magnetic moment. The solid curve displays the leading-order extrapolation of Eq. (8.16), without explicit decuplet contributions, as seen in Fig. 8.4. Equation (8.16) is extended to include the pion contributions with decuplet baryons in Eq. (8.21). The dotted curve displays the quenched fit of Eq. (8.21) to lattice simulation results.

leading-order fits. This arises both from the explicit Δ loop contribution and the additional degree of freedom given by $a_4 m_\pi^4$. Although the curvature appears to be somewhat enhanced, the difference between the leading-order extrapolation and the one including the Δ, is at the scale of the error bar of the lightest simulation result. Without a statistically significant difference in the curves, the extrapolation shows little sensitivity to the inclusion of the Δ. Nevertheless, accurate extraction of the the low-energy constants, to this order, will require explicit inclusion of the correct nonanalytic structure, as given by the Δ diagram.

With regard to the estimation of full QCD corrections, the inclusion of the decuplet is again a small effect. With the Δ, the QCD estimate of the proton magnetic moment at the physical quark mass is increased by 0.15 μ_N, from the leading-order result. Comparison of the QCD estimates described at leading and next-to-leading order are shown in Fig. 8.9.

Finally, the prediction of the physical proton magnetic moment obtained by including the Δ contributions and compensating for the finite lattice volume is 2.54(30) μ_N, where the uncertainty is statistical in origin. This result agrees well with the experimental value of 2.79 μ_N.

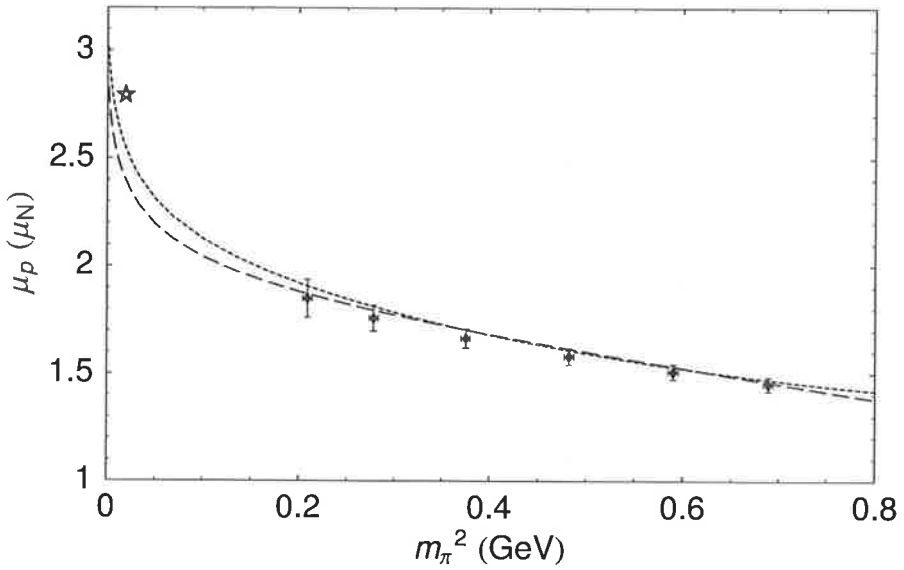

Figure 8.9: Estimates of the QCD magnetic moment of the proton. Curves are based on finite-volume and quenched chiral corrections. The dashed curve displays the leading-order result, seen in Fig. 8.6. The dotted curve describes the result at next-to-leading order.

Further improvement on this result is given by explicitly including the physics of the K-meson contributions. These results have been applied to the entire baryon-octet magnetic moments and the observed agreement with experiment is excellent [L$^+$04a, L$^+$05]. This has also enabled the accurate determination of the strangeness magnetic moment of the proton, found to be $G_M^s = -0.046 \pm 0.019\ \mu_N$ [L$^+$05, L$^+$04b].

This novel understanding of the quark mass dependence of the magnetic moments has implications for cosmological observations of the temporal variation of the fine structure constant (α) [FLTY04]. Experimental measurements of variation of the fine structure constant are also sensitive to small variations in the quark masses. For a range of experimental observations, the work in Ref. [FLTY04] provides limits on the correlated variation of α and m_q.

* * *

Nucleon magnetic moments in QQCD become logarithmically divergent as the chiral limit is approached. Fortunately for modern lattice simulations, the results indicate that this pathological behaviour only becomes apparent for pion masses well below the physical value.

The effects of the finite volume in modern simulations at moderate quark masses appear to be quite small. With the onset of increased curvature, by

the dominant infrared behaviour of loop integrals in the chiral limit, the finite-volume effects will become significant.

Estimates for the proton magnetic moment in QCD have been obtained, through the application of the discovered link between QCD and the quenched approximation. Although differences are evident, the moments are remarkably similar over a wide range of quark mass — resulting from a coincidental correspondence between the chiral corrections of the two theories.

The dynamical nature of QCD becomes increasingly more significant as the chiral regime is approached. A linear extrapolation from the heaviest simulated masses would produce a magnetic moment of less than 2.0 μ_N. The physical value can only be explained by the dynamics of the meson dressings. At light quark mass, the long-ranging extent of the charge circulation of the pion field induces a large contribution to the magnetic moment, the order of nearly one third of the total observed value relative to the naive linear extrapolation. This gives a significantly enhanced picture of the dynamic structure of the nucleon, far beyond that offered by the constituent quark model.

9

Summary and Conclusion

QCD presents a fascinating challenge for the study of strongly-interacting quantum field theory. With continued development, the strongly-interacting component of the Standard Model will be tested against observation. An enhanced understanding of the theory will provide much improved guidance to the next generation of experimental programs, where the nonperturbative QCD "noise" must be separated from the electro-weak effects.

In this Thesis we have focused on the low-energy properties of the nucleon. In particular, the mass and electromagnetic structure has been studied in the application of effective field theory to lattice gauge theory.

The only available rigorous formulation of the QCD path integral is given by lattice gauge theory. This has provided a powerful tool in the study of nonperturbative QCD. For computational reasons, approximations are required and these must be understood if one is to draw comparisons with experiment. The restriction which has been of most interest in the present work is the simulation with relatively large quark masses.

The rich dynamic structure of the nucleon causes the quark-mass extrapolation to be a nontrivial procedure. The physical nucleon displays a strong coupling to the lightest pseudoscalar meson, the pion. An enhanced picture of the dynamics of the nucleon is described by its interactions with the pion field.

Preserving this physical role of the pion field is fundamental to any chiral extrapolation procedure. A systematic approach to this problem is provided by chiral perturbation theory. Construction of this theory is based upon the symmetries of QCD. Provided all contributions, to a well-defined counting scheme, are accounted for, this theory defines a rigorous approach to the study of QCD at low energies and small quark-masses.

How to quantify the domain of "small quark-mass" is of significant interest, especially for the chiral extrapolation problem. A strong extrapolation procedure is reliant on being within the effective convergence range of the effective field theory. Varying rates of convergence are offered by different regularisation schemes, which induce alternative resummations of the chiral series.

The traditional implementations of chiral perturbation theory have been based upon dimensional regularisation. Although this scheme has had an enormous success in the description of elementary fields, early investigations demon-

strated dimensional regularisation to be incompatible with lattice simulation results. The origins of this failure are revealed in the way dimensional regularisation treats particles of extended structure. Dimensional regularisation, or any other minimal subtraction renormalisation scheme, treats the quantum fields as point-like objects. Necessarily, the ultraviolet behaviour in loop integrals becomes modeled by the low-energy coefficients of the effective field theory — an immediate contradiction is realised. Large counterterms are therefore required to remove the incorrect treatment of the high-energy physics and, consequently, the series becomes slowly converging and highly divergent.

An alternative regularisation scheme was presented, which has the feature of suppressing loop integrals for momenta above some characteristic energy scale. Finite-range regularisation encompasses the extended structure of the nucleon, at one-loop order, in a very natural fashion. This extended structure is only generated within the dimensionally regularised formalism at increasing orders of the expansion.

Although various choices in FRR have significantly different ultraviolet behaviour, this investigation has found that results are insensitive to the choice of regulator. The most consequential result of this analysis is the markedly improved convergence of the chiral expansion formulated with FRR — sufficient for reliable extrapolation of modern lattice simulation results to the physical quark mass.

The quenched modification of QCD, as commonly implemented in lattice simulations, has proven a valuable framework to provide an enhanced understanding of the role of chiral physics in the nucleon. The absence of vacuum quark fluctuations in quenched QCD causes the low-energy effective field theory to be altered from the physical theory. The calculation of these essential alterations has been outlined for two different methods.

The modifications of the effective field theory has a significant impact on the subsequent chiral extrapolation. It is observed that the chiral behaviour of the Delta baryon is especially pronounced in the quenched theory. In particular, the N–Δ mass difference is significantly enhanced as the chiral limit is approached — a prediction which has recently been identified in FLIC fermion simulations.

From the use of finite-range regularisation, a remarkable connection between the quenched and physical theories has been deduced. This link has provided the opportunity to gain improved physical estimates from simulations of quenched QCD. A successful application of this hypothesis has been demonstrated.

The discovery of this phenomenological link has provided an improved understanding of the origins of the mass-splittings in the baryon spectrum. It has been found that most of the mass discrepancy between the nucleon and Delta is to be attributed to short-range gluonic interactions.

Quenched QCD has also been used to investigate the electromagnetic structure of the nucleon. In particular, the quark-mass dependence of the proton magnetic moment was studied in finite-range regularised quenched chiral perturbation theory. The results of the baryon-mass analysis were applied to generate physical estimates of the moment, based on quenched lattice simulation results. Although the chiral behaviour of the quenched and physical theories are considerably different, only small discrepancies from the physical theory were observed over a wide range of quark mass.

With the chiral corrections to the nucleon magnetic moment being rapidly suppressed for increasing quark mass, the improvement offered by using finite-range regularisation techniques, compared to dimensional regularisation, was further established.

The applications of finite-range regularisation have provided a wealth of insight into the structure of the nucleon, with the most enlightening discovery being a solution to the problem which motivated this investigation. High-precision lattice QCD data, combined with the effective resummation of the chiral series provided by FRR, has enabled the accurate extrapolation of the nucleon mass. With residual lattice artifacts yet to be accounted for, and a significant statistical error associated with the large extrapolation distance, this work has contributed the most advanced first-principles calculation of the nucleon mass in QCD.

With a rigorous extrapolation procedure at hand, further development of FRR to a wider ranging class of observables will be a natural progression. This promises a prosperous future for the advancement of hadronic physics in non-perturbative QCD.

A

Loop Regularisation

The 4-dimensional covariant loop-integral contributing to the nucleon mass shift, in the heavy baryon limit is given by [DHB99]

$$\tilde{I} = \int \frac{d^4k}{(2\pi)^4} \frac{k_i k_j}{(k_0 - i\epsilon)(k^2 - m^2 + i\epsilon)} . \tag{A.1}$$

For reduction to the nonrelativistic form, we consider a monopole regularisation,

$$\begin{aligned}
\tilde{I} &= \int \frac{d^4k}{(2\pi)^4} \frac{k_i k_j}{(k_0 - i\epsilon)(k^2 - m^2 + i\epsilon)} \left(\frac{\Lambda^2}{k^2 - \Lambda^2} \right)^2 && \text{(A.2)} \\
&= \int \frac{d^3\mathbf{k}}{(2\pi)^4} \int dk_0 \frac{k_i k_j}{(k_0 - i\epsilon)(k_0^2 - \mathbf{k}^2 - m^2 + i\epsilon)} \left(\frac{\Lambda^2}{k_0^2 - \mathbf{k}^2 - \Lambda^2 + i\epsilon} \right)^2 && \text{(A.3)} \\
&= \int \frac{d^3\mathbf{k}}{(2\pi)^4} \int dk_0 \frac{k_i k_j}{(k_0 - i\epsilon)(k_0 - \omega + i\epsilon)(k_0 + \omega - i\epsilon)} \\
&\quad \times \left(\frac{\Lambda^2}{(k_0 - \Omega + i\epsilon)(k_0 + \Omega - i\epsilon)} \right)^2 , && \text{(A.4)}
\end{aligned}$$

with $\omega = \sqrt{\mathbf{k}^2 + m^2}$ and $\Omega = \sqrt{\mathbf{k}^2 + \Lambda^2}$. Cauchy integration gives

$$\begin{aligned}
\tilde{I} &= -(2\pi i) \int \frac{d^3\mathbf{k}}{(2\pi)^4} \left\{ \left(\frac{k_i k_j \Lambda^4}{k_0 (k_0 + \omega)(k_0^2 - \Omega^2)^2} \right) \Bigg|_{k_0 = \omega} \right. \\
&\quad \left. + \frac{d}{dk_0} \left(\frac{k_i k_j \Lambda^4}{k_0 (k_0^2 - \omega^2)(k_0 + \Omega)^2} \right) \Bigg|_{k_0 = \Omega} \right\} && \text{(A.5)} \\
&= -(2\pi i) \int \frac{d^3\mathbf{k}}{(2\pi)^4} \left\{ \frac{k_i k_j \Lambda^4}{2\omega^2(\omega^2 - \Omega^2)} + \frac{k_i k_j \Lambda^4 (\omega^2 - 2\Omega^2)}{2\Omega^4(\Omega^2 - \omega^2)^2} \right\} && \text{(A.6)} \\
&= -i \int \frac{d^3\mathbf{k}}{(2\pi)^3} \left\{ \frac{k_i k_j \Lambda^4}{2(\mathbf{k}^2 + m^2)(\mathbf{k}^2 + \Lambda^2)^2} \right\} && \text{(A.7)} \\
&= -i \frac{\delta_{ij}}{6} \int \frac{d^3\mathbf{k}}{(2\pi)^3} \left\{ \frac{\mathbf{k}^2}{(\mathbf{k}^2 + m^2)} \frac{\Lambda^4}{(\mathbf{k}^2 + \Lambda^2)^2} \right\} . && \text{(A.8)}
\end{aligned}$$

Performing the angular integral gives

$$\tilde{I} = -i \frac{2\pi \delta_{ij}}{3} \int \frac{dk}{(2\pi)^3} \left\{ \frac{k^4}{(k^2 + m^2)} \frac{\Lambda^4}{(k^2 + \Lambda^2)^2} \right\} , \tag{A.9}$$

where we use $k = |\mathbf{k}|$. As $\Lambda \to \infty$, this is precisely the form given by Eq. (3.30), up to the normalisation scale,

$$\tilde{I} = -i\frac{\delta_{ij}}{24\pi} I_\pi \,. \tag{A.10}$$

We now give analytic expression for the various FRR integrals, where possible. The complete expressions for the finite-range regularised integrals are given. For a degenerate intermediate baryon state, I_π, we obtain

$$I_\pi^{\mathrm{SC}} = \frac{2\Lambda^3}{3\pi} - \frac{2\Lambda}{\pi}m^2 + \frac{2}{\pi}m^3 \arctan\left(\frac{\Lambda}{m}\right), \tag{A.11}$$

$$I_\pi^{\mathrm{MON}} = \frac{\Lambda^4(2m+\Lambda)}{2(m+\Lambda)^2}, \tag{A.12}$$

$$I_\pi^{\mathrm{DIP}} = \frac{\Lambda^5(m^2+4m\Lambda+\Lambda^2)}{16(m+\Lambda)^4}. \tag{A.13}$$

For the more complicated integral, $I_{\pi\Delta}$, as defined by Eq. (4.11), we obtain for the sharp cut-off

$$\begin{aligned} I_{\pi\Delta}^{\mathrm{SC}} = \frac{1}{3\pi}\Bigg\{ & 6\Delta^2\Lambda + 2\Lambda^3 - 6\Lambda m^2 - 3\Delta\Lambda\sqrt{\Lambda^2+m^2} \\ & +3\Delta\left(-2\Delta^2+3m^2\right)\log\left(\frac{\Lambda+\sqrt{\Lambda^2+m^2}}{m}\right) \\ & -6(\Delta^2-m^2)^{\frac{3}{2}}\Bigg[\log\left(\frac{-\Delta-m+\sqrt{\Delta^2-m^2}}{\Delta+m+\sqrt{\Delta^2-m^2}}\right) \\ & +\log\left(\frac{\Delta+\Lambda+\sqrt{\Delta^2-m^2}+\sqrt{\Lambda^2+m^2}}{-\Delta-\Lambda+\sqrt{\Delta^2-m^2}-\sqrt{\Lambda^2+m^2}}\right)\Bigg]\Bigg\}. \end{aligned} \tag{A.14}$$

For the monopole regularised integral we obtain

$$\begin{aligned} I_{\pi\Delta}^{\mathrm{MON}} = & \frac{\Lambda^4}{2\pi(\Lambda^2+\Delta^2-m^2)^2}\frac{1}{\Lambda^2-m^2} \\ & \Bigg[\Lambda(3\pi m^4 + m^2(-3\pi\Delta^2+2\Delta\Lambda-4\pi\Lambda^2)) \\ & +\Lambda(-2\Delta^3+3\pi\Delta^2\Lambda-2\Delta\Lambda^2+\pi\Lambda^3)) \\ & -2(\Lambda^2-m^2)(\Delta^2-m^2)^{3/2}\log\left(\frac{\Delta-\sqrt{\Delta^2-m^2}}{\Delta+\sqrt{\Delta^2-m^2}}\right) \\ & +\frac{\Delta\Lambda(3m^4+2\Delta^2\Lambda^2-3m^2(\Lambda^2+\Delta^2))}{(\Lambda^2-m^2)^{1/2}}\log\left(\frac{\Lambda-\sqrt{\Lambda^2-m^2}}{\Lambda+\sqrt{\Lambda^2-m^2}}\right)\Bigg]. \end{aligned} \tag{A.15}$$

For the dipole regularised integral we obtain

$$
\begin{aligned}
I_{\pi\Delta}^{\mathrm{DIP}} \;=\; & \frac{\Lambda^5}{48\left(\Lambda^2-m^2\right)^{\frac{7}{2}}\left(\Delta^2+\Lambda^2-m^2\right)^4\pi}\Bigg\{\sqrt{\Lambda^2-m^2} \\
& \Bigg[-16\,\Delta\,\Lambda^{11}+4\,\Delta\,\Lambda^9\left(6\,\Delta^2-11\,m^2\right)+6\,\Delta\,\Lambda\,m^4\left(-\Delta^2+m^2\right)^3 \\
& +2\,\Delta\,\Lambda^3 m^2\left(-\Delta^2+m^2\right)^2\left(-16\,\Delta^2+37\,m^2\right) \\
& +6\,\Delta\,\Lambda^7\left(8\,\Delta^4-44\,\Delta^2 m^2+37\,m^4\right) \\
& -2\,\Delta\,\Lambda^5\left(-\Delta+m\right)\left(\Delta+m\right)\left(4\,\Delta^4-98\,\Delta^2 m^2+121\,m^4\right) \\
& +3\,\Lambda^{12}\pi-3\,m^6\left(-\Delta^2+m^2\right)^3\pi-9\,\Lambda^{10}\left(-3\,\Delta^2+4\,m^2\right)\pi \\
& +9\,\Lambda^2 m^4\left(-\Delta^2+m^2\right)^2\left(-\Delta^2+4\,m^2\right)\pi \\
& -9\,\Lambda^4 m^2\left(-\Delta+m\right)\left(\Delta+m\right)\left(\Delta^4-11\,\Delta^2 m^2+7\,m^4\right)\pi \\
& +9\,\Lambda^8\left(-3\,\Delta^4-3\,\Delta^2 m^2+7\,m^4\right)\pi \\
& -3\,\Delta^2\,\Lambda^6\left(\Delta^4-30\,\Delta^2 m^2+30\,m^4\right)\pi\Bigg] \\
& -48\,\Lambda^3\left(\Delta^2-m^2\right)^{\frac{3}{2}}\left(\Lambda^2-m^2\right)^{\frac{7}{2}}\log\left(\frac{\Delta-\sqrt{\Delta^2-m^2}}{\Delta+\sqrt{\Delta^2-m^2}}\right) \\
& -3\,\Delta\Bigg[m^6\left(-\Delta^2+m^2\right)^3+8\,\Lambda^{10}\left(-2\,\Delta^2+3\,m^2\right) \\
& -3\,\Lambda^2 m^4\left(-\Delta^2+m^2\right)^2\left(-2\,\Delta^2+5\,m^2\right) \\
& -4\,\Lambda^8 m^2\left(-14\,\Delta^2+15\,m^2\right)+\Lambda^6 m^4\left(-34\,\Delta^2+35\,m^2\right) \\
& +3\,\Lambda^4 m^4\left(8\,\Delta^4-13\,\Delta^2 m^2+5\,m^4\right)\Bigg]\log\left(\frac{\Lambda-\sqrt{\Lambda^2-m^2}}{\Lambda+\sqrt{\Lambda^2-m^2}}\right)\Bigg\}. \qquad \text{(A.16)}
\end{aligned}
$$

B

Renormalised Expansions

The Taylor expansions, necessary for the renormalisation of the chiral expansion are now defined. For a generic regulator, the Taylor expansion of the integral, I_π, is given by

$$I_\pi = b_0 + b_2 m^2 + m^3 + b_4 m^4 + \dots . \tag{B.1}$$

For the case where the intermediate state being non-degenerate, $I_{\pi\Delta}$, the m^3 contribution becomes a logarithm and the expansion is given by

$$I_{\pi\Delta} = b_{0\Delta} + b_{2\Delta} m^2 + b_{4\Delta} m^4 - \frac{3}{4\,\pi\,\Delta} m^4 \log m + \dots \tag{B.2}$$

In Table B.1 we summarise the b_i expansion coefficients. We were unable to obtain neat analytic expressions for the Gaussian regulator and hence all relevant calculations have been performed numerically. For both DR and BP schemes the b_i of the I_π diagram can trivially be treated as zero. The expansion terms, $b_{i\,\Delta}$ for the $I_{\pi\Delta}$ diagram are more complicated and are summarised in the following.

In the DR case, the $b_{i\,\Delta}$ can again be treated as zero. From the expansion of Eq. (4.10), for the BP case one finds that the appropriate coefficients are given by (with renormalisation scale 1.0 GeV)

$$\begin{aligned} b_{0\Delta}^{\mathrm{BP}} &= \frac{\Delta^3}{\pi} \log(4\Delta^2)\,, \\ b_{2\Delta}^{\mathrm{BP}} &= -\frac{\Delta}{2\,\pi} \left[1 + 3\log(4\Delta^2)\right]\,, \\ b_{4\Delta}^{\mathrm{BP}} &= \frac{3}{16\,\pi\,\Delta} \left[3 + 4\log 2 + 2\log(\Delta^2)\right]\,. \end{aligned} \tag{B.3}$$

Regulator	b_0	b_2	b_4
Sharp	$\frac{2\Lambda^3}{3\pi}$	$-\frac{2\Lambda}{\pi}$	$-\frac{2}{\pi\Lambda}$
Monopole	$\frac{\Lambda^3}{2}$	$-\frac{\Lambda}{2}$	$-\frac{3}{2\Lambda}$
Dipole	$\frac{\Lambda^3}{16}$	$-\frac{5\Lambda}{16}$	$-\frac{35}{16\Lambda}$

Table B.1: Expansion coefficients for the finite regulators.

The Taylor expansion of the FRR forms, Eqs. (A.14) to (A.16), provides the renormalisation for these forms. For the sharp cut-off, expressions are given by

$$
\begin{aligned}
b_{0\Delta}^{\mathrm{SC}} &= \frac{1}{3\pi}\left[6\Delta^2\Lambda - 3\Delta\Lambda^2 + 2\Lambda^3 + 6\Delta^3 \log\frac{\Delta}{\Delta+\Lambda}\right], \\
b_{2\Delta}^{\mathrm{SC}} &= \frac{1}{\pi(\Delta+\Lambda)}\left[-\Lambda(3\Delta+2\Lambda) - 3\Delta(\Delta+\Lambda)\log\frac{\Delta}{\Delta+\Lambda}\right], \\
b_{4\Delta}^{\mathrm{SC}} &= \frac{-1}{16\pi\Delta(\Delta+\Lambda)^2}\left[7\,\Delta^2 + 2\,\Delta\,\Lambda - 9\,\Lambda^2 + 12\,(\Delta+\Lambda)^2\,\log\frac{\Delta+\Lambda}{2\,\Delta\,\Lambda}\right].
\end{aligned}
\tag{B.4}
$$

For the monopole we obtain

$$
\begin{aligned}
b_{0\Delta}^{\mathrm{MON}} &= \frac{\Lambda^4}{2\,\pi(\Delta^2+\Lambda^2)^2}\left[-2\,\Delta^3 - 2\,\Delta\,\Lambda^2 + 3\,\Delta^2\,\Lambda\,\pi + \Lambda^3\,\pi + 2\,\Delta^3\,\log\left(\frac{\Delta^2}{\Lambda^2}\right)\right], \\
b_{2\Delta}^{\mathrm{MON}} &= -\frac{\Lambda^2}{2\,\pi(\Delta^2+\Lambda^2)^3}\Big[\Delta^5 + 6\,\Delta^3\,\Lambda^2 + 5\,\Delta\,\Lambda^4 - 3\,\Delta^2\,\Lambda^3\,\pi + \Lambda^5\,\pi \\
&\qquad -2\,\Delta\,\Lambda^2\,(\Delta^2 - 3\,\Lambda^2)\,\log\left(\frac{\Delta}{\Lambda}\right)\Big], \\
b_{4\Delta}^{\mathrm{MON}} &= -\frac{1}{16\,\pi\,\Delta(\Delta^2+\Lambda^2)^4}\Big[13\,\Delta^8 + 54\,\Delta^6\,\Lambda^2 + 108\,\Delta^4\,\Lambda^4 + 58\,\Delta^2\,\Lambda^6 - 9\,\Lambda^8 \\
&\qquad -24\,\Delta^3\,\Lambda^5\,\pi + 24\,\Delta\,\Lambda^7\,\pi - 6\,\Lambda^4\,\left(\Delta^4 - 6\,\Delta^2\,\Lambda^2 + \Lambda^4\right)\log\left(4\Delta^2\right) \\
&\qquad -6\,\left(\Delta^8 + 4\,\Delta^6\,\Lambda^2 + 5\,\Delta^4\,\Lambda^4 + 10\,\Delta^2\,\Lambda^6\right)\log\left(4\Lambda^2\right)\Big].
\end{aligned}
\tag{B.5}
$$

For the dipole we obtain

$$
\begin{aligned}
b_{0\Delta}^{\mathrm{DIP}} &= \frac{\Lambda^4}{48\pi(\Delta^2+\Lambda^2)^4}\Big[8\,\Delta^7 + 48\,\Delta^5\,\Lambda^2 + 24\,\Delta^3\,\Lambda^4 - 16\,\Delta\,\Lambda^6 - 3\,\Delta^6\,\Lambda\,\pi \\
&\qquad -27\,\Delta^4\,\Lambda^3\,\pi + 27\,\Delta^2\,\Lambda^5\,\pi + 3\,\Lambda^7\,\pi + 96\,\Delta^3\,\Lambda^4\,\log\frac{\Delta}{\Lambda}\Big],
\end{aligned}
$$

$$
\begin{aligned}
b_{2\Delta}^{\mathrm{DIP}} &= -\frac{\Lambda^2}{48\pi(\Delta^2+\Lambda^2)^5}\Big[8\,\Delta^9 + 36\,\Delta^7\,\Lambda^2 + 36\,\Delta^5\,\Lambda^4 + 188\,\Delta^3\,\Lambda^6 + 180\,\Delta\,\Lambda^8 \\
&\qquad +3\,\Delta^6\,\Lambda^3\,\pi + 45\,\Delta^4\,\Lambda^5\,\pi - 135\,\Delta^2\,\Lambda^7\,\pi + 15\,\Lambda^9\,\pi \\
&\qquad -48\,\left(5\,\Delta^3\,\Lambda^6 - 3\,\Delta\,\Lambda^8\right)\log\frac{\Delta}{\Lambda}\Big],
\end{aligned}
$$

$$
\begin{aligned}
b_{4\Delta}^{\mathrm{DIP}} \;=\; & \frac{-1}{48\,\Delta\left(\Delta^2+\Lambda^2\right)^6\pi}\Big[54\,\Delta^{12}+326\,\Delta^{10}\Lambda^2+819\,\Delta^8\Lambda^4+1062\,\Delta^6\Lambda^6 \\
& +1154\,\Delta^4\Lambda^8+612\,\Delta^2\Lambda^{10}-27\,\Lambda^{12}+3\,\Delta^7\Lambda^5\pi \\
& +63\,\Delta^5\Lambda^7\pi-315\,\Delta^3\Lambda^9\pi+105\,\Delta\,\Lambda^{11}\pi \\
& -6\,\Lambda^8\left(35\,\Delta^4-42\,\Delta^2\Lambda^2+3\,\Lambda^4\right)\log\left(4\Delta^2\right) \\
& -6\,\Delta^2\Big(3\,\Delta^{10}+18\,\Delta^8\Lambda^2 \\
& +45\,\Delta^6\Lambda^4+60\,\Delta^4\Lambda^6+10\,\Delta^2\Lambda^8+60\,\Lambda^{10}\Big)\log\left(4\Lambda^2\right)\Big]. \qquad \text{(B.6)}
\end{aligned}
$$

C

Model Magnetic Moments

Here we summarise the calculation of the proton magnetic moments in the cloudy bag model as displayed in Fig. 2.2. Here we summarise the results of previous work [TT83, Tho84, LTW98].

The quark wave function in the infinite spherical well of radius R is simply the MIT bag solution [CJJ+74, CJJT74]

$$\psi(r) = \begin{bmatrix} g(r) \\ i\boldsymbol{\sigma}.\hat{r}f(r) \end{bmatrix} \chi\,\theta(R-r)\,, \tag{C.1}$$

where the spin-isospin information is carried by χ. The ground state solutions for finite mass quarks are given by

$$\begin{aligned} g(r) &= N\sqrt{\frac{E+m_q}{E}}j_0\left(\frac{\omega r}{R}\right) \\ f(r) &= N\sqrt{\frac{E-m_q}{E}}j_1\left(\frac{\omega r}{R}\right) \end{aligned} \tag{C.2}$$

with j_0, j_1 spherical Bessel functions and

$$E(m_q, R) = \frac{1}{R}\sqrt{\omega^2 + (m_q R)^2} \tag{C.3}$$

and normalisation constant given by

$$N^{-2} = 4\pi R^2 j_0^2(\omega)\frac{2E(ER-1)+m_q}{E(E-m_q)}\,. \tag{C.4}$$

The linear boundary condition, describing a vanishing flux through the bag surface, determines the eigenfrequency

$$\tan\omega = \frac{\omega}{1 - m_q R - \sqrt{\omega^2 + (m_q R)^2}}\,. \tag{C.5}$$

The contributions to the nucleon magnetic form factor from quark contributions in the bag is given by

$$G_M^{(\mathrm{bag})}(q) = 2m_N \int_V d^3r \frac{j_1(qr)}{q}[2g(r)f(r)]\,. \tag{C.6}$$

	C_{NN}	$C_{\Delta\Delta}$	$C_{N\Delta}$
p	$\frac{1}{18}g_A^2$	$\frac{80}{81}\mathcal{C}^2$	$-\frac{32}{27}g_A\mathcal{C}$
n	$\frac{1}{3}g_A^2$	$\frac{10}{27}\mathcal{C}^2$	$-\frac{16}{9}g_A\mathcal{C}$

Table C.1: Coefficients of vertex renormalisation diagrams for the proton (p) and neutron (n) magnetic moments.

Direct coupling of the electromagnetic current to the pion field gives the following contributions to the proton magnetic moment

$$G_M^{(\pi N)}(q^2=0) = \frac{g_A^2 m_N}{6\pi^2 f_\pi^2}\int dk\,\frac{k^4u^2(k)}{\omega_k^4}\,, \tag{C.7}$$

$$G_M^{(\pi\Delta)}(q^2=0) = \frac{\mathcal{C}^2 m_N}{27\pi^2 f_\pi^2}\int dk\,\frac{(2\omega_k+\Delta)k^4u^2(k)}{2\omega_k^3(\omega_k+\Delta)^2}\,, \tag{C.8}$$

with the pion energy given by $\omega_k=\sqrt{k^2+\pi^2}$ and $u(k)$ the CBM form factor

$$u(k) = 3\frac{j_1(kR)}{kR}\,. \tag{C.9}$$

This solution for the form factor is determined in the chiral limit and we do not include any variation of the form factor with quark mass in this model.

There are also corrections to the magnetic moment from vertex and wave-function renormalisation graphs. The net contribution to coupling to quarks in the bag, including the one-loop pion dressings, is summarised as

$$\begin{aligned} G_M^{(q)}(q^2=0) &= Z_2\,\mu_N^{(\text{tree})}G_M^{(\text{bag})}(q^2=0)+G_M^{NN}(q^2=0) \\ &\quad +G_M^{\Delta\Delta}(q^2=0)+G_M^{N\Delta}(q^2=0)\,, \end{aligned} \tag{C.10}$$

where the tree contributions are defined by $\mu_p^{(\text{tree})}=1$ and $\mu_n^{(\text{tree})}=-2/3$. Z_2 defines the bare baryon probability, with expression provided in Ref. [LTW98]. The vertex corrections are given by

$$G_M^{BB'}(q^2=0) = \frac{C_{BB'}}{8\pi^2 f_\pi^2}\int dk\,\frac{k^4u^2(k)}{(\Delta_{BN}+\omega_k)(\Delta_{B'N}+\omega_k)\omega_k}G_M^{(q)}(q^2=0)\,, \tag{C.11}$$

with mass-splitting given by $\Delta_{BN}=M_B-M_N$ and the coefficients $C_{BB'}$ defined in Table C.1.

D

List of Publications

Primary refereed journal articles are appended.

- "Systematic uncertainties in the precise determination of the strangeness magnetic moment of the nucleon"
  D. B. Leinweber, S. Boinepalli, A. W. Thomas, A. G. Williams, R. D. Young, J. M. Zanotti and J. B. Zhang
  contributed to Proceedings of Workshop on QCD Down Under, Barossa Valley and Adelaide, Australia, 10-19 Mar 2004.

- "Finite-range regularisation and chiral extrapolation"
  R. D. Young, D. B. Leinweber and A. W. Thomas
  contributed to Proceedings of Workshop on QCD Down Under, Barossa Valley and Adelaide, Australia, 10-19 Mar 2004.

- "Towards a connection between nuclear structure and QCD",
  A. W. Thomas, P. A. M. Guichon, D. B. Leinweber and R. D. Young,
  contributed to 18th Nishinomiya-Yukawa Memorial Symposium on Strangeness in Nuclear Matter, Nishinomiya, Japan, 4-5 Dec 2003.

- "Precise determination of the strangeness magnetic moment of the nucleon"
  D. B. Leinweber, S. Boinepalli, I. C. Cloet, A. W. Thomas, A. G. Williams, R. D. Young, J. M. Zanotti and J. B. Zhang
  submitted to Phys. Rev. Lett.
  arXiv:hep-lat/0406002

- "Leading quenching effects in the proton magnetic moment"
  R. D. Young, D. B. Leinweber and A. W. Thomas
  submitted to Phys. Rev. D
  arXiv:hep-lat/0406001

- "Hadron structure and QCD: Effective field theory for lattice simulations"
  D. B. Leinweber, A. W. Thomas and R. D. Young
  Lattice Hadron Physics, ed. A.C. Kalloniatis, D.B. Leinweber and A.G. Williams. Lecture Notes in Physics, Springer-Verlag (Heidelberg), *in press.*

- "The nucleon mass in chiral effective field theory"
  R. D. Young, D. B. Leinweber and A. W. Thomas
  contributed to Proceedings of 3rd International Workshop on Numerical Analysis and Lattice QCD, Edinburgh, Scotland, 30 Jun - 4 Jul 2003.

- "Limits on variations of the quark masses, QCD scale, and fine structure constant"
  V. V. Flambaum, D. B. Leinweber, A. W. Thomas and R. D. Young
  Phys. Rev. D **69**, 115006 (2004) [arXiv:hep-ph/0402098]

- "The strangeness magnetic moment of the nucleon from FLIC fermions"
  D. B. Leinweber, S. Boinepalli, A. W. Thomas, A. G. Williams, R. D. Young, J. M. Zanotti and J. B. Zhang
  Nucl. Phys. Proc. Suppl. **128**, 132 (2004) [arXiv:hep-lat/0406003]

- "Chiral extrapolation and physical insights"
  R. D. Young, D. B. Leinweber and A. W. Thomas
  Nucl. Phys. Proc. Suppl. **128**, 227 (2004) [arXiv:hep-lat/0311038]

- "Chiral structure in baryon magnetic moments"
  R. D. Young, D. B. Leinweber and A. W. Thomas
  Nucl. Phys. Proc. Suppl. **129**, 290 (2004) [arXiv:hep-lat/0309187]

- "Observing chiral nonanalytic behavior with FLIC fermions"
  D. B. Leinweber, A. W. Thomas, A. G. Williams, R. D. Young, J. M. Zanotti and J. B. Zhang
  Nucl. Phys. A **737**, 177 (2004) [arXiv:nucl-th/0308083]

- "Nucleon electromagnetic form factors from lattice QCD"
  J. D. Ashley, D. B. Leinweber, A. W. Thomas and R. D. Young
  Eur. Phys. J. **A19**, 9-14 (2004) [arXiv:hep-lat/0308024]

- "Progress in the calculation of nucleon form factors and parton distribution functions"
  A. W. Thomas, J. D. Ashley, W. Detmold, D. B. Leinweber, W. Melnitchouk and R. D. Young
  Nucl. Phys. A **721**, 915 (2003)

- "QCD and hadron structure"
  A. W. Thomas, D. B. Leinweber, R. D. Young and S. V. Wright
  Mod. Phys. Lett. A **18**, 347 (2003)

- "Physical nucleon properties from lattice QCD"
  D. B. Leinweber, A. W. Thomas and R. D. Young
  Phys. Rev. Lett. **92**, 242002 (2004) [arXiv:hep-lat/0302020]

- "Convergence of chiral effective field theory"
  R. D. Young, D. B. Leinweber and A. W. Thomas
  Prog. Part. Nucl. Phys. **50**, 399 (2003) [arXiv:hep-lat/0212031]

- "Recent developments in quark nuclear physics"
  A. W. Thomas, D. B. Leinweber and R. D. Young
  Eur. Phys. J. A **18**, 241 (2003) [arXiv:hep-lat/0406004]

- "FLIC fermions and hadron phenomenology"
  D. B. Leinweber, J. N. Hedditch, W. Melnitchouk, A. W. Thomas,
  A. G. Williams, R. D. Young, J. M. Zanotti and J. B. Zhang
  Eur. Phys. J. A **18**, 247 (2003) [arXiv:nucl-th/0211014]

- "Quenched chiral physics in baryon masses."
  R. D. Young, D. B. Leinweber, A. W. Thomas and S. V. Wright
  Proceedings of Workshop on Physics at the Japan Hadron Facility,
  Adelaide, Australia, 14-21 Mar 2002. [arXiv:nucl-th/0211026]

- "Chiral analysis of quenched baryon masses"
  R. D. Young, D. B. Leinweber, A. W. Thomas and S. V. Wright
  Phys. Rev. D **66**, 094507 (2002) [arXiv:hep-lat/0205017]

- "Chiral behaviour of baryon masses in quenched lattice QCD"
  R. D. Young, D. B. Leinweber, A. W. Thomas and S. V. Wright
  Nucl. Phys. Proc. Suppl. **109A**, 55 (2002)

- "Chiral symmetry and the intrinsic structure of the nucleon"
  D. B. Leinweber, A. W. Thomas and R. D. Young
  Phys. Rev. Lett. **86**, 5011 (2001) [arXiv:hep-ph/0101211]

Bibliography

[A+91] P. Amaudruz et al. The Gottfried sum from the ratio F2(n) / F2(p). *Phys. Rev. Lett.*, 66:2712–2715, 1991.

[A+94] M. Arneodo et al. A reevaluation of the Gottfried sum. *Phys. Rev.*, D50:1–3, 1994.

[A+03] S. Aoki et al. Light hadron spectroscopy with two flavors of O(a)-improved dynamical quarks. *Phys. Rev.*, D68:054502, 2003.

[AK+02] A. Ali Khan et al. Light hadron spectroscopy with two flavors of dynamical quarks on the lattice. *Phys. Rev.*, D65:054505, 2002.

[AK+04] A. Ali Khan et al. The nucleon mass in N(f) = 2 lattice QCD: Finite size effects from chiral perturbation theory. *Nucl. Phys.*, B689:175–194, 2004.

[ALTY04] J. D. Ashley, D. B. Leinweber, Anthony W. Thomas, and R. D. Young. Nucleon electromagnetic form factors from lattice QCD. *Eur. Phys. J.*, A19:9–14, 2004.

[Aok03] Sinya Aoki. Chiral perturbation theory with Wilson-type fermions including a**2 effects: N(f) = 2 degenerate case. *Phys. Rev.*, D68:054508, 2003.

[B+00] Claude W. Bernard et al. Scaling tests of the improved Kogut-Susskind quark action. *Phys. Rev.*, D61:111502, 2000.

[B+01] Claude Bernard et al. The QCD spectrum with three quark flavors. *Phys. Rev.*, D64:054506, 2001.

[B+03] Claude Bernard et al. Panel discussion on chiral extrapolation of physical observables. *Nucl. Phys. Proc. Suppl.*, 119:170–184, 2003.

[BDE+98] William A. Bardeen, A. Duncan, E. Eichten, G. Hockney, and H. Thacker. Light quarks, zero modes, and exceptional configurations. *Phys. Rev.*, D57:1633–1641, 1998.

[BDET98] William A. Bardeen, A. Duncan, E. Eichten, and H. Thacker. Quenched approximation artifacts: A study in two-dimensional QED. *Phys. Rev.*, D57:3890–3901, 1998.

[BDET00] W. Bardeen, A. Duncan, E. Eichten, and H. Thacker. Anomalous chiral behavior in quenched lattice QCD. *Phys. Rev.*, D62:114505, 2000.

[Bea04] Silas R. Beane. Nucleon masses and magnetic moments in a finite volume. *Phys. Rev.*, D70:034507, 2004.

[BG92] Claude W. Bernard and Maarten F. L. Golterman. Chiral perturbation theory for the quenched approximation of QCD. *Phys. Rev.*, D46:853–857, 1992.

[BHM04] Veronique Bernard, Thomas R. Hemmert, and Ulf-G. Meissner. Cutoff schemes in chiral perturbation theory and the quark mass expansion of the nucleon mass. *Nucl. Phys.*, A732:149–170, 2004.

[BKL+04] Sharada Boinepalli, Waseem Kamleh, Derek B. Leinweber, Anthony G. Williams, and James M. Zanotti. Improved chiral properties of FLIC fermions. 2004.

[BKM95] V. Bernard, N. Kaiser, and Ulf-G. Meissner. Chiral dynamics in nucleons and nuclei. *Int. J. Mod. Phys.*, E4:193–346, 1995.

[BL99] T. Becher and H. Leutwyler. Baryon chiral perturbation theory in manifestly Lorentz invariant form. *Eur. Phys. J.*, C9:643–671, 1999.

[BM96] M. K. Banerjee and J. Milana. The decuplet revisited in chi(PT). *Phys. Rev.*, D54:5804–5811, 1996.

[BRS03] Oliver Bar, Gautam Rupak, and Noam Shoresh. Simulations with different lattice Dirac operators for valence and sea quarks. *Phys. Rev.*, D67:114505, 2003.

[BSS93] Malcolm N. Butler, Martin J. Savage, and Roxanne P. Springer. Strong and electromagnetic decays of the baryon decuplet. *Nucl. Phys.*, B399:69–88, 1993.

[BT01] W. Bentz and Anthony W. Thomas. The stability of nuclear matter in the Nambu–Jona-Lasinio model. *Nucl. Phys.*, A696:138–172, 2001.

[BZ72] M. A. B. Beg and A. Zepeda. Pion radius and isovector nucleon radii in the limit of small pion mass. *Phys. Rev.*, D6:2912–2918, 1972.

[CJCWZ69] Curtis G. Callan Jr., Sidney R. Coleman, J. Wess, and Bruno Zumino. Structure of phenomenological Lagrangians. 2. *Phys. Rev.*, 177:2247–2250, 1969.

[CJJ+74] A. Chodos, R. L. Jaffe, K. Johnson, Charles B. Thorn, and V. F. Weisskopf. A new extended model of hadrons. *Phys. Rev.*, D9:3471–3495, 1974.

[CJJT74] A. Chodos, R. L. Jaffe, K. Johnson, and Charles B. Thorn. Baryon structure in the bag theory. *Phys. Rev.*, D10:2599, 1974.

[Clo79] F. E. Close. *An Introduction to Quarks and Partons.* 1979. Academic Press/London, 481p.

[CLT03] I. C. Cloet, D. B. Leinweber, and Anthony W. Thomas. Delta baryon magnetic moments from lattice QCD. *Phys. Lett.*, B563:157–164, 2003.

[CWZ69] Sidney R. Coleman, J. Wess, and Bruno Zumino. Structure of phenomenological Lagrangians. 1. *Phys. Rev.*, 177:2239–2247, 1969.

[D+97] C. T. H. Davies et al. Further precise determinations of alpha(s) from lattice QCD. *Phys. Rev.*, D56:2755–2765, 1997.

[D+04] C. T. H. Davies et al. High-precision lattice QCD confronts experiment. *Phys. Rev. Lett.*, 92:022001, 2004.

[DH02] Thomas DeGrand and Urs M. Heller. Witten-Veneziano relation, quenched QCD, and overlap fermions. *Phys. Rev.*, D65:114501, 2002.

[DHB99] John F. Donoghue, Barry R. Holstein, and Bugra Borasoy. SU(3) baryon chiral perturbation theory and long distance regularization. *Phys. Rev.*, D59:036002, 1999.

[DHK99] Thomas DeGrand, Anna Hasenfratz, and Tamas G. Kovacs. Investigating and optimizing the chiral properties of lattice fermion actions. *Nucl. Phys.*, B547:259–280, 1999.

[DLLZ00] S. J. Dong, F. X. Lee, K. F. Liu, and J. B. Zhang. Chiral symmetry, quark mass, and scaling of the overlap fermions. *Phys. Rev. Lett.*, 85:5051–5054, 2000.

[DLM+01] W. Detmold, D. B. Leinweber, W. Melnitchouk, A. W. Thomas, and S. V. Wright. A new slant on hadron structure. *Pramana*, 57:251–262, 2001.

[DMN+01] W. Detmold, W. Melnitchouk, J. W. Negele, D. B. Renner, and A. W. Thomas. Chiral extrapolation of lattice moments of proton quark distributions. *Phys. Rev. Lett.*, 87:172001, 2001.

[DMT01] W. Detmold, W. Melnitchouk, and A. W. Thomas. Parton distributions from lattice QCD. *Eur. Phys. J. direct*, C13:1–15, 2001.

[DMT02] W. Detmold, W. Melnitchouk, and A. W. Thomas. Moments of isovector quark distributions from lattice QCD. *Phys. Rev.*, D66:054501, 2002.

[DP00] Massimo Di Pierro. From Monte Carlo integration to lattice quantum chromodynamics: An introduction. 2000. Lectures given at the GSA Summer School on Physics on the Frontier and in the Future, Batavia, Illinois, 31 Jul - 7 Aug 2000.

[EHK98a] R. G. Edwards, U. M. Heller, and T. R. Klassen. Accurate scale determinations for the Wilson gauge action. *Nucl. Phys.*, B517:377–392, 1998.

[EHK98b] R. G. Edwards, U. M. Heller, and T. R. Klassen. The effectiveness of non-perturbative O(a) improvement in lattice QCD. *Phys. Rev. Lett.*, 80:3448–3451, 1998.

[ELT02] Torleif E. O. Ericson, B. Loiseau, and Anthony W. Thomas. Determination of the pion nucleon coupling constant and scattering lengths. *Phys. Rev.*, C66:014005, 2002.

[ESW60] F. J. Ernst, R. J. Sachs, and K. C. Wali. Electromagnetic form factors of the nucleon. *Phys. Rev.*, 119:1105–1114, 1960.

[FLTY04] V. V. Flambaum, D. B. Leinweber, A. W. Thomas, and R. D. Young. Limits on variations of the quark masses, QCD scale, and fine structure constant. *Phys. Rev.*, D69:115006, 2004.

[Fol52a] L. L. Foldy. The electromagetic properties of Dirac paricles. *Phys. Rev.*, 87:688–693, 1952.

[Fol52b] L. L. Foldy. The electron-neutron interaction. *Phys. Rev.*, 87:693–696, 1952.

[Fol58] L. L. Foldy. Neutron-electron interaction. *Rev. Mod. Phys.*, 30:471–481, 1958.

[G+04] Christof Gattringer et al. Quenched spectroscopy with fixed-point and chirally improved fermions. *Nucl. Phys.*, B677:3–51, 2004.

[G+05] M. Gockeler et al. Nucleon electromagnetic form factors on the lattice and in chiral effective field theory. *Phys. Rev.*, D71:034508, 2005.

[GL82] J. Gasser and H. Leutwyler. Quark masses. *Phys. Rept.*, 87:77–169, 1982.

[GL84] J. Gasser and H. Leutwyler. Chiral perturbation theory to one loop. *Ann. Phys.*, 158:142, 1984.

[GL88] J. Gasser and H. Leutwyler. Spontaneously broken symmetries: Effective Lagrangians at finite volume. *Nucl. Phys.*, B307:763, 1988.

[GLS91] J. Gasser, H. Leutwyler, and M. E. Sainio. Sigma term update. *Phys. Lett.*, B253:252–259, 1991.

[GMOR68] Murray Gell-Mann, R. J. Oakes, and B. Renner. Behavior of current divergences under SU(3) x SU(3). *Phys. Rev.*, 175:2195–2199, 1968.

[Gol61] J. Goldstone. Field theories with 'superconductor' solutions. *Nuovo Cim.*, 19:154–164, 1961.

[Got67] Kurt Gottfried. Sum rule for high-energy electron - proton scattering. *Phys. Rev. Lett.*, 18:1174, 1967.

[GSS88] J. Gasser, M. E. Sainio, and A. Svarc. Nucleons with chiral loops. *Nucl. Phys.*, B307:779, 1988.

[GSW62] Jeffrey Goldstone, Abdus Salam, and Steven Weinberg. Broken symmetries. *Phys. Rev.*, 127:965–970, 1962.

[GT58] M. L. Goldberger and S. B. Treiman. Decay of the pi meson. *Phys. Rev.*, 110:1178–1184, 1958.

[H+76] G. Hohler et al. Analysis of electromagnetic nucleon form-factors. *Nucl. Phys.*, B114:505, 1976.

[Hat90] T. Hatsuda. Convergence radius of the chiral perturbation in the large N(c) limit. *Phys. Rev. Lett.*, 65:543–546, 1990.

[HJLT00a] E. J. Hackett-Jones, D. B. Leinweber, and A. W. Thomas. Incorporating chiral symmetry and heavy quark theory in extrapolations of octet baryon charge radii. *Phys. Lett.*, B494:89–99, 2000.

[HJLT00b] E. J. Hackett-Jones, D. B. Leinweber, and A. W. Thomas. Incorporating chiral symmetry in extrapolations of octet baryon magnetic moments. *Phys. Lett.*, B489:143–147, 2000.

[HK94] Tetsuo Hatsuda and Teiji Kunihiro. QCD phenomenology based on a chiral effective Lagrangian. *Phys. Rept.*, 247:221–367, 1994.

[HW02] Thomas R. Hemmert and Wolfram Weise. Chiral magnetism of the nucleon. *Eur. Phys. J.*, A15:487–504, 2002.

[Isg99] Nathan Isgur. Interpreting the neutron's electric form-factor: Rest frame charge distribution or Foldy term? *Phys. Rev. Lett.*, 83:272–275, 1999.

[Isg00] Nathan Isgur. Critique of a pion exchange model for interquark forces. *Phys. Rev.*, D62:054026, 2000.

[Iwa85] Y. Iwasaki. Renormalization group analysis of lattice theories and improved lattice action: Two-dimensional nonlinear O(N) sigma model. *Nucl. Phys.*, B258:141–156, 1985.

[JLMS93] Elizabeth Jenkins, Michael E. Luke, Aneesh V. Manohar, and Martin J. Savage. Chiral perturbation theory analysis of the baryon magnetic moments. *Phys. Lett.*, B302:482–490, 1993.

[KALW02] Waseem Kamleh, David H. Adams, Derek B. Leinweber, and Anthony G. Williams. Accelerated overlap fermions. *Phys. Rev.*, D66:014501, 2002.

[KFM+94] Y. Kuramashi, M. Fukugita, H. Mino, M. Okawa, and A. Ukawa. eta-prime meson mass in lattice QCD. *Phys. Rev. Lett.*, 72:3448–3451, 1994.

[KRHH95] S. Kopecky, P. Riehs, J. A. Harvey, and N. W. Hill. New measurement of the charge radius of the neutron. *Phys. Rev. Lett.*, 74:2427–2430, 1995.

[KS75] John B. Kogut and Leonard Susskind. Hamiltonian formulation of Wilson's lattice gauge theories. *Phys. Rev.*, D11:395, 1975.

[Kum98] S. Kumano. Flavor asymmetry of antiquark distributions in the nucleon. *Phys. Rept.*, 303:183–257, 1998.

[L+03] D. B. Leinweber et al. Observing chiral nonanalytic behavior with FLIC fermions. 2003.

[L+04a] D. B. Leinweber et al. The strangeness magnetic moment of the nucleon from FLIC fermions. *Nucl. Phys. Proc. Suppl.*, 128:132–140, 2004.

[L+04b] D. B. Leinweber et al. Systematic uncertainties in the precise determination of the strangeness magnetic moment of the nucleon. 2004. Contribution to Proceedings of Workshop on QCD Down Under, Barossa Valley and Adelaide, Australia.

[L+05] D. B. Leinweber et al. Precise determination of the strangeness magnetic moment of the nucleon. 2005. to appear Phys. Rev. Lett.

[LC93] Derek B. Leinweber and Thomas D. Cohen. Chiral corrections to lattice calculations of charge radii. *Phys. Rev.*, D47:2147–2150, 1993.

[Lei02] Derek B. Leinweber. Quenched chiral perturbation theory for baryon form factors. *Nucl. Phys. Proc. Suppl.*, 109:45–49, 2002.

[Lei04] Derek B. Leinweber. Quark contributions to baryon magnetic moments in full, quenched and partially quenched QCD. *Phys. Rev.*, D69:014005, 2004.

[Lep97] G. P. Lepage. How to renormalize the Schroedinger equation. 1997.

[Lep99] G. Peter Lepage. Flavor-symmetry restoration and Symanzik improvement for staggered quarks. *Phys. Rev.*, D59:074502, 1999.

[LLT99] Derek B. Leinweber, Ding H. Lu, and Anthony W. Thomas. Nucleon magnetic moments beyond the perturbative chiral regime. *Phys. Rev.*, D60:034014, 1999.

[LP71] Ling-Fong Li and Heinz Pagels. Perturbation theory about a Goldstone symmetry. *Phys. Rev. Lett.*, 26:1204–1206, 1971.

[LS96] James N. Labrenz and Stephen R. Sharpe. Quenched chiral perturbation theory for baryons. *Phys. Rev.*, D54:4595–4608, 1996.

[LSS+97] Martin Luscher, Stefan Sint, Rainer Sommer, Peter Weisz, and Ulli Wolff. Non-perturbative O(a) improvement of lattice QCD. *Nucl. Phys.*, B491:323–343, 1997.

[LSSW96] Martin Luscher, Stefan Sint, Rainer Sommer, and Peter Weisz. Chiral symmetry and O(a) improvement in lattice QCD. *Nucl. Phys.*, B478:365–400, 1996.

[LTTW00] Derek B. Leinweber, Anthony W. Thomas, Kazuo Tsushima, and Stewart V. Wright. Baryon masses from lattice QCD: Beyond the perturbative chiral regime. *Phys. Rev.*, D61:074502, 2000.

[LTTW01] D. B. Leinweber, A. W. Thomas, K. Tsushima, and S. V. Wright. Chiral behaviour of the rho meson in lattice QCD. *Phys. Rev.*, D64:094502, 2001.

[LTW98] D. H. Lu, Anthony W. Thomas, and Anthony G. Williams. Electromagnetic form factors of the nucleon in an improved quark model. *Phys. Rev.*, C57:2628–2637, 1998.

[LTY01] D. B. Leinweber, A. W. Thomas, and R. D. Young. Chiral symmetry and the intrinsic structure of the nucleon. *Phys. Rev. Lett.*, 86:5011–5014, 2001.

[LTY04] D. B. Leinweber, Anthony W. Thomas, and R. D. Young. Physical nucleon properties from lattice QCD. *Phys. Rev. Lett.*, 92:242002, 2004.

[LWD91] Derek B. Leinweber, R. M. Woloshyn, and Terrence Draper. Electromagnetic structure of octet baryons. *Phys. Rev.*, D43:1659–1678, 1991.

[MB99] Judith A. McGovern and Michael C. Birse. On the absence of fifth-order contributions to the nucleon mass in heavy-baryon chiral perturbation theory. *Phys. Lett.*, B446:300–305, 1999.

[MCLT03] D. Morel, B. Crouch, D. B. Leinweber, and Anthony W. Thomas. Physical baryon resonance spectroscopy from lattice QCD. 2003.

[McN03] Craig McNeile. Meson and baryon spectroscopy on a lattice. 2003. Prepared for Int. Rev. Nucl. Phys, Vol.9, Hadronic Physics from Lattice QCD, ed. by A.M. Green.

[Mor87] A. Morel. Chiral logarithms in quenched QCD. *J. Phys. (France)*, 48:1111–1119, 1987.

[N+03] T. Nakano et al. Observation of S = +1 baryon resonance in photo-production from neutron. *Phys. Rev. Lett.*, 91:012002, 2003.

[N+04] Y. Namekawa et al. Light hadron spectroscopy in two-flavor QCD with small sea quark masses. *Phys. Rev.*, D70:074503, 2004.

[Neu04] H. Neuberger. Lattice field theory: Past, present and future. 2004.

[NJL61a] Yoichiro Nambu and G. Jona-Lasinio. Dynamical model of elementary particles based on an analogy with superconductivity. I. *Phys. Rev.*, 122:345–358, 1961.

[NJL61b] Yoichiro Nambu and G. Jona-Lasinio. Dynamical model of elementary particles based on an analogy with superconductivity. II. *Phys. Rev.*, 124:246–254, 1961.

[NN93a] Rajamani Narayanan and Herbert Neuberger. Chiral fermions on the lattice. *Phys. Rev. Lett.*, 71:3251–3254, 1993.

[NN93b] Rajamani Narayanan and Herbert Neuberger. Infinitely many regulator fields for chiral fermions. *Phys. Lett.*, B302:62–69, 1993.

[NN94] Rajamani Narayanan and Herbert Neuberger. Chiral determinant as an overlap of two vacua. *Nucl. Phys.*, B412:574–606, 1994.

[NN95] Rajamani Narayanan and Herbert Neuberger. A construction of lattice chiral gauge theories. *Nucl. Phys.*, B443:305–385, 1995.

[Pag75] Heinz Pagels. Departures from chiral symmetry; a review. *Phys. Rept.*, 16:219, 1975.

[Ric99] D. G. Richards. Lattice gauge theory: QCD from quarks to hadrons. 1999. Lectures given at 14th Annual HUGS at CEBAF (HUGS 99), Newport News, Virginia, 1-18 Jun 1999.

[RS02] Gautam Rupak and Noam Shoresh. Chiral perturbation theory for the Wilson lattice action. *Phys. Rev.*, D66:054503, 2002.

[RSY99] T. A. Rijken, V. G. J. Stoks, and Y. Yamamoto. Soft-core hyperon nucleon potentials. *Phys. Rev.*, C59:21–40, 1999.

[S+03] S. Stepanyan et al. Observation of an exotic S = +1 baryon in exclusive photoproduction from the deuteron. *Phys. Rev. Lett.*, 91:252001, 2003.

[Sac62] R. J. Sachs. High-energy behavior of nucleon electromagnetic form factors. *Phys. Rev.*, 126:2256–2260, 1962.

[Sav02] Martin J. Savage. The magnetic moments of the octet baryons in quenched chiral perturbation theory. *Nucl. Phys.*, A700:359–376, 2002.

[SB97] Richard E. Stuckey and Michael C. Birse. Baryon masses in a chiral expansion with meson-baryon form factors. *J. Phys.*, G23:29–40, 1997.

[Sha92] Stephen R. Sharpe. Quenched chiral logarithms. *Phys. Rev.*, D46:3146–3168, 1992.

[SKP99] T. M. Schwarz, S. P. Klevansky, and G. Papp. The phase diagram and bulk thermodynamical quantities in the NJL model at finite temperature and density. *Phys. Rev.*, C60:055205, 1999.

[SMF98] Sven Steininger, Ulf-G. Meissner, and Nadia Fettes. On wave function renormalization and related aspects in heavy fermion effective field theories. *JHEP*, 09:008, 1998.

[Som94] R. Sommer. A new way to set the energy scale in lattice gauge theories and its applications to the static force and alpha-s in SU(2) Yang-Mills theory. *Nucl. Phys.*, B411:839–854, 1994.

[SS00] Stephen R. Sharpe and Noam Shoresh. Physical results from unphysical simulations. *Phys. Rev.*, D62:094503, 2000.

[SS01] Stephen R. Sharpe and Noam Shoresh. Partially quenched chiral perturbation theory without phi0. *Phys. Rev.*, D64:114510, 2001.

[SW85] B. Sheikholeslami and R. Wohlert. Improved continuum limit lattice action for QCD with Wilson fermions. *Nucl. Phys.*, B259:572, 1985.

[Tho83] Anthony W. Thomas. A limit on the pionic component of the nucleon through SU(3) flavor breaking in the sea. *Phys. Lett.*, B126:97, 1983.

[Tho84] A. W. Thomas. Chiral symmetry and the bag model: A new starting point for nuclear physics. *Adv. Nucl. Phys.*, 13:1–137, 1984.

[tHV72] Gerard 't Hooft and M. J. G. Veltman. Regularization and renormalization of gauge fields. *Nucl. Phys.*, B44:189–213, 1972.

[TLY03] Anthony W. Thomas, Derek B. Leinweber, and Ross D. Young. Recent developments in quark nuclear physics. *Eur. Phys. J.*, A18:241–245, 2003.

[TT83] S. Theberge and Anthony W. Thomas. Magnetic moments of the nucleon octet calculated in the cloudy bag model. *Nucl. Phys.*, A393:252, 1983.

[TW01] Anthony W. Thomas and Wolfram Weise. *The Structure of the Nucleon.* Wiley-VCH, Berlin, 2001.

[vK99] U. van Kolck. Effective field theory of nuclear forces. *Prog. Part. Nucl. Phys.*, 43:337–418, 1999.

[VW91] U. Vogl and W. Weise. The Nambu and Jona Lasinio model: Its implications for hadrons and nuclei. *Prog. Part. Nucl. Phys.*, 27:195–272, 1991.

[Wei79] Steven Weinberg. Phenomenological Lagrangians. *Physica*, A96:327, 1979.

[Wil74] Kenneth G. Wilson. Confinement of quarks. *Phys. Rev.*, D10:2445–2459, 1974.

[YLMT] R. D. Young, D. B. Leinweber, J. A. McGovern, and A. W. Thomas. The Goldberger-Treiman discrepancy and higher-order contributions to the nucleon mass expansion. In preparation.

[YLT] R. D. Young, D. B. Leinweber, and A. W. Thomas. Regularisation schemes for the chiral expansion of the nucleon mass. In preparation.

[YLT03] R. D. Young, D. B. Leinweber, and Anthony W. Thomas. Convergence of chiral effective field theory. *Prog. Part. Nucl. Phys.*, 50:399–417, 2003.

[YLT04a] R. D. Young, D. B. Leinweber, and Anthony W. Thomas. Chiral extrapolation and physical insights. *Nucl. Phys. Proc. Suppl.*, 128:227–232, 2004.

[YLT04b] R. D. Young, D. B. Leinweber, and Anthony W. Thomas. Chiral structure in baryon magnetic moments. *Nucl. Phys. Proc. Suppl.*, 129-130:290–292, 2004.

[YLT05] R. D. Young, D. B. Leinweber, and A. W. Thomas. Leading quenching effects in the proton magnetic moment. *Phys. Rev.*, D71:014001, 2005.

[YLTW02] R. D. Young, D. B. Leinweber, A. W. Thomas, and S. V. Wright. Chiral analysis of quenched baryon masses. *Phys. Rev.*, D66:094507, 2002.

[Z+02] James M. Zanotti et al. Hadron masses from novel fat-link fermion actions. *Phys. Rev.*, D65:074507, 2002.

[ZBL+04] J. M. Zanotti, S. Boinepalli, D. B. Leinweber, A. G. Williams, and J. B. Zhang. Electromagnetic form factors with FLIC fermions. *Nucl. Phys. Proc. Suppl.*, 128:233–239, 2004.

[ZLLW05] J. M. Zanotti, B. Lasscock, D. B. Leinweber, and A. G. Williams. Scaling of flic fermions. *Phys. Rev.*, D71:034510, 2005.

[ZLWZ04] J. M. Zanotti, D. B. Leinweber, A. G. Williams, and J. B. Zhang. Electromagnetic form factors with FLIC fermions. *Nucl. Phys. Proc. Suppl.*, 129:287–289, 2004.

Chiral Symmetry and the Intrinsic Structure of the Nucleon

D. B. Leinweber, A. W. Thomas, and R. D. Young
Special Research Centre for the Subatomic Structure of Matter, and Department of Physics and Mathematical Physics, Adelaide University, Adelaide SA 5005, Australia
(Received 22 January 2001)

Understanding hadron structure within the framework of QCD is an extremely challenging problem. In order to solve it, it is vital that our thinking should be guided by the best available insight. Our purpose here is to explain the model-independent consequences of the approximate chiral symmetry of QCD for two famous results concerning the structure of the nucleon. We show that both the apparent success of the constituent quark model in reproducing the ratio of the proton to neutron magnetic moments and the apparent success of the Foldy term in reproducing the observed charge radius of the neutron are coincidental. That is, a relatively small change of the current quark mass would spoil both results.

DOI: 10.1103/PhysRevLett.86.5011 PACS numbers: 13.40.Gp, 12.38.Gc, 12.39.Fe, 12.39.Jh

The chiral properties of QCD have been the subject of considerable attention, from chiral quark models [1,2,3] to the less ambitious, but more systematic, approach of chiral perturbation theory [4]. Most recently one has begun to realize the importance of chiral symmetry in describing the dependence of hadron properties such as masses [5] and magnetic moments [6] on quark mass. This is vital if one is to compare lattice QCD calculations, which are presently confined to current quark masses, $\bar{m}$, of order 40–80 MeV or higher, with experimental data.

For our purposes the essential point is that chiral symmetry is dynamically broken. The resulting Goldstone bosons enter the calculation of hadron properties through loops which lead to a characteristic dependence on $\bar{m}$ which is not analytic. Indeed for the magnetic moment of the nucleons one finds a leading nonanalytic behavior proportional to $m_q^{1/2}$. In the chiral limit $m_\pi^2 \propto m_q$ and

$$\begin{aligned} \mu^p &= \mu_0^p - \alpha m_\pi + \mathcal{O}(m_\pi^2), \\ \mu^n &= \mu_0^n + \alpha m_\pi + \mathcal{O}(m_\pi^2). \end{aligned} \tag{1}$$

It is a crucial property of the leading nonanalytic (LNA) coefficient, α, that it is entirely determined by the axial charge of the nucleon and the pion decay constant (both in the chiral limit):

$$\alpha = \frac{g_A^2 M_N}{8\pi f_\pi^2}. \tag{2}$$

Taking the one-loop value of $g_A (= F_1 + D_1 = 0.40 + 0.61)$ from chiral perturbation theory [7] we find $\alpha = 4.41$. [Note that all magnetic moments will be in nuclear magnetons (μ_N) and all masses in GeV.]

Clearly the LNA term is large, of order 0.6 μ_N, at the physical pion mass. This is one-third of the magnetic moment of the neutron. Provided the $\mathcal{O}(m_\pi^2)$ terms are small at the physical pion mass we can use Eq. (1) to extract the proton and neutron magnetic moments in the chiral limit:

$$\begin{aligned} \mu_0^p &\cong \mu^p + \alpha m_\pi^{\text{phys}}, \\ \mu_0^n &\cong \mu^n - \alpha m_\pi^{\text{phys}}. \end{aligned} \tag{3}$$

One then finds a model-independent expression for the dependence of the proton to neutron magnetic moment ratio on the pion mass:

$$\frac{\mu^p}{|\mu^n|} = \frac{\mu_0^p}{|\mu_0^n|}\left(1 + \left[\frac{1}{|\mu_0^n|} - \frac{1}{|\mu_0^p|}\right]\alpha m_\pi\right) + \mathcal{O}(m_\pi^2). \tag{4}$$

Constraining the chiral expansions to reproduce the experimental proton moment μ^p and the experimental ratio $\mu^p/|\mu^n|$ provides

$$\mu_0^p = 3.41\ \mu_N, \qquad \frac{\mu_0^p}{|\mu_0^n|} = 1.37, \tag{5}$$

and

$$\frac{\mu^p}{|\mu^n|} = 1.37 + 0.09\,\frac{m_\pi}{m_\pi^{\text{phys}}} + \mathcal{O}(m_\pi^2). \tag{6}$$

As a consequence of Eq. (6), we see that the ratio of the p to the n magnetic moments varies from 1.37 to 1.55 (a variation of order 13%) as m_π varies from 0 to $2m_\pi^{\text{phys}}$. In terms of the underlying quark mass, such a variation corresponds to a current quark mass variation from 0 to just 20 MeV. Within the constituent quark model this ratio would remain constant at 3/2, independent of the change of quark mass.

A study by Leinweber *et al.* [6] suggests a new method for describing the mass dependence of baryon magnetic moments which satisfies the chiral constraints imposed by QCD. We briefly summarize the main results of that analysis. A series expansion of $\mu_{p(n)}$ in powers of m_π is not a valid approximation for m_π larger than the physical mass. On the other hand, the simple Padé approximant

$$\mu^{p(n)} = \frac{\mu_0^{p(n)}}{1 \pm \frac{\alpha}{\mu_0^{p(n)}} m_\pi + \beta^{p(n)} m_\pi^2}, \tag{7}$$

has the correct leading nonanalytic (LNA) behavior of chiral perturbation theory

$$\mu^{p(n)} = \mu_0^{p(n)} \mp \alpha m_\pi,$$

and also builds in the expected behavior at large m_π. At heavy quark masses we expect that the magnetic moment should fall off as the Dirac moment

$$\mu = \frac{e_q}{2m_q} \propto \frac{1}{m_\pi^2}$$

as m_π becomes moderately large. (Note that this form is valid provided $m_\pi^2 \propto \bar{m}$, which seems to be true for m_π up to at least 1 GeV within lattice simulations.) A fit of the Padé approximant to lattice QCD data [8,9] leads to predictions of the magnetic moments of 2.90(20) and $-1.79(21)$ μ_N to be compared with 2.793 and -1.193 μ_N for p and n, respectively. The smooth transition between the chiral and heavy quark regimes provided by the Padé approximant models the lattice QCD results well.

Figure 1 shows a similar fit to the lattice data, this time constrained to pass through the experimental moments, and providing the solid curve in Fig. 2 for the p/n ratio of magnetic moments.

The Padé approximate fit parameters are $(\mu_0, \beta) = (3.33, 0.527)$ and $(-2.41, 0.427)$, for p and n, respectively.

Figure 2 also shows the result of the constituent quark model (dashed line) and the variation of the ratio predicted by the leading nonanalytic behavior of chiral perturbation theory in Eq. (6) (dotted line). The importance of the terms of order m_π^2 and higher are revealed by the ratio calculated using the Padé approximant of Eq. (7) (solid curve). The values of $\mu_0^{p(n)}$ vary slightly in the chiral expansion and the Padé due to these small higher order corrections at the physical pion mass. However, it is important to note that the slopes of the curves agree exactly in the chiral limit, as demanded by chiral perturbation theory.

The key point is that the ratio displays a significant quark mass dependence. It is roughly linear in m_π until m_π is of order $2m_\pi^{\text{phys}}$. It is amusing to imagine the excitement had the pion mass been 100 MeV heavier at 240 MeV where the Padé crosses the constituent quark model prediction of 3/2. However the constituent quark model prediction really corresponds to the $m_\pi \to \infty$ limit, and Fig. 2 suggests this limit is approached rather slowly.

The surprising consequences of chiral symmetry for this famous ratio naturally lead us to reconsider the neutron charge radius. The squared charge radius of the neutron ($\langle r^2 \rangle_{\text{ch}}^n$) is obtained from the slope of the neutron electric form factor, $G_{En}(Q^2)$ as $Q^2 \to 0$:

$$\langle r^2 \rangle_{\text{ch}}^n = -6 \frac{d}{dQ^2} G_E(Q^2)|_{Q^2=0} . \tag{8}$$

The Sachs electric and magnetic form factors can be written in terms of the covariant vertex functions F_1 and F_2 as

$$\begin{aligned} G_E(Q^2) &= F_1(Q^2) - \frac{Q^2}{4M_N^2} F_2(Q^2), \\ G_M(Q^2) &= F_1(Q^2) + F_2(Q^2). \end{aligned} \tag{9}$$

Note that for a neutral charge particle $F_1(Q^2 = 0)$ vanishes and hence $F_2(Q^2 = 0)$ is simply the magnetic moment of the particle. Now the charge radius squared of the neutron can be written as

$$\langle r^2 \rangle_{\text{ch}}^n = -6 \frac{d}{dQ^2} F_{1n}(Q^2)|_{Q^2=0} + \frac{3}{2} \frac{\mu^n}{M_N^2} . \tag{10}$$

Experimentally $\langle r^2 \rangle_{\text{ch}}^n = -0.113 \pm 0.003 \pm 0.004$ fm^2 [10], while the last term in Eq. (10), the Foldy term [11], is numerically -0.126 fm^2.

The close agreement between the Foldy term and the observed mean square charge radius of the neutron has

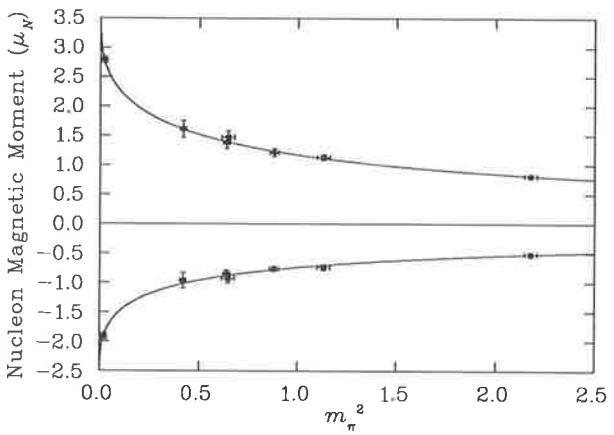

FIG. 1. Extrapolation of lattice QCD magnetic moments (•, LDW [8]; ■, WDL [9]) for the proton (upper curve) and neutron (lower curve) to the chiral limit. The curves are constrained to pass through the experimentally measured moments which are indicated by asterisks.

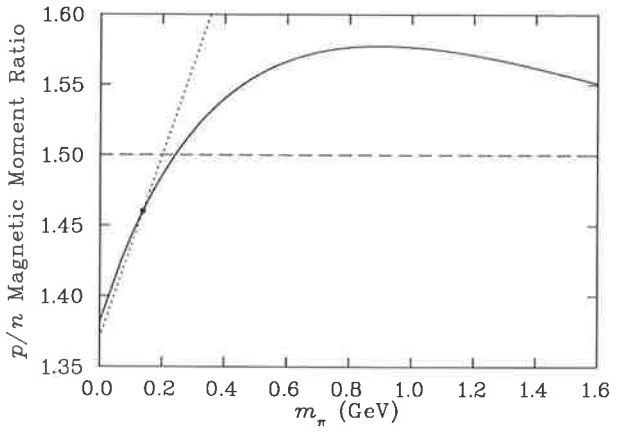

FIG. 2. Ratio of the magnitudes of the proton to neutron magnetic moments. The solid curve describes the predictions of the Padé approximant while the dashed line denotes the constituent quark model prediction of 3/2. The dotted line is the leading nonanalytic behavior of chiral perturbation theory. The experimental measurement is indicated by the solid point.

led to considerable controversy. It has been argued that the difference, namely, the term involving the Dirac form factor (F_{1n}), should be interpreted as the true indication of the intrinsic charge distribution of the neutron. Clearly this would be quite insignificant. On the other hand, decades of modeling the structure of the nucleon have suggested that the neutron must have a nontrivial intrinsic charge distribution. Pre-QCD it was clear that the long-range tail must be negative, corresponding to the emission of a negative pion ($n \to p\pi^-$), but old-fashioned meson theory was incapable of describing the interior of the neutron. Post-QCD this was resolved in the cloudy bag model [3,12], where the convergence of an expansion in numbers of pions was assured—provided the quark confinement region was fairly large and the decuplet states [in this case the $\Delta(1232)$] was included on the same footing as the nucleon [13]. The neutron charge distribution then originated mainly from the Fock component of its wave function consisting of a π^- cloud and a positive core of confined quarks. Alternatively, within the constituent quark model, it was proposed that the repulsive gluon exchange interaction between the two d quarks would tend to force them to the exterior of the neutron—again yielding a positive core and a negative tail [14].

In view of these expectations of an internal charge distribution, the interpretation of $\langle r^2\rangle^n_{\rm ch}$ in terms of the Foldy term has been controversial. Isgur [15] has recently shown that a careful treatment of relativistic corrections for the calculation of $\langle r^2\rangle^n_{\rm ch}$, in a quark-di-quark model, leads to a recoil contribution that cancels the Foldy term exactly, hence restoring the interpretation in terms of an intrinsic charge distribution—see also [16]. We now show that the study of the chiral behavior of $\langle r^2\rangle^n_{\rm ch}$ and μ^n supports this idea, establishing in a model-independent way that the observed similarity between the experimental value and the Foldy term is purely accidental.

It is a little appreciated consequence of the approximate chiral symmetry of QCD that the mean square charge radius of the nucleon has a leading nonanalytic term proportional to $\ln m_\pi$ [17]:

$$\langle r^2\rangle^{p(n)}_{\rm ch}|_{\rm LNA} = \mp\frac{1 + 5g_A^2}{(4\pi f_\pi)^2}\ln\left(\frac{m_\pi}{\Lambda}\right), \qquad (11)$$

where the upper and the lower sign correspond to p and n, respectively. As a result, the charge radii of both p and n diverge logarithmically as the quark mass tends to zero. Physically this is easy to understand; as $m_\pi \to 0$ the Heisenberg uncertainty principle allows the pion cloud, and therefore the charge density, to extend to infinite distance. For the magnetic moment, on the other hand, there is no divergence—indeed the neutron magnetic moment increases in magnitude by about 30% as the pion mass moves from its physical value to zero. (Loosely speaking, even though the pion may be at a large distance it moves slowly; its angular momentum is constrained to one by angular momentum conservation.)

To summarize, whereas a change of order 5 MeV in the light quark mass leads to a 30% change in the Foldy term, the neutron charge radius $\langle r^2\rangle^n_{\rm ch}$ becomes infinite. Hence, the similarity of $\langle r^2\rangle^n_{\rm ch}$ and the Foldy term is purely an accident. A small change in the quark mass leads to completely different values. This physics is not captured in the constituent quark model where a 5 MeV change in the light quark mass corresponds to a change in the constituent quark mass from roughly 340 to 335 MeV. In this case the neutron charge radius originates in the one-gluon-exchange interaction which is proportional to the inverse square of the constituent quark mass and therefore $\langle r^2\rangle^n_{\rm ch}$ would change by only 3%.

In summary, chiral perturbation theory provides model-independent constraints on the quark mass dependence of nucleon magnetic moments and charge radii which compel one to conclude that the apparent success of the constituent quark model to predict the p/n magnetic moment is accidental. Had the pion mass been lighter than the observed value, the p/n ratio would drop further from the constituent quark model prediction of 3/2, the latter corresponding to the $m_\pi \to \infty$ limit. The coincidence of the Foldy term and the observed neutron charge radius is also accidental. Here a small change in the quark mass to the chiral limit increases the neutron moment by about 30% while the charge radius becomes infinite. These results, which are a rigorous consequence of the chiral symmetry of QCD, cannot be simulated in conventional constituent quark models.

This work was supported by the Australian Research Council.

[1] A. Manohar and H. Georgi, Nucl. Phys. **B234**, 189 (1984).
[2] G. E. Brown and M. Rho, Phys. Lett. **82B**, 177 (1979).
[3] S. Théberge, A. W. Thomas, and G. A. Miller, Phys. Rev. D **22**, 2838 (1980); A. W. Thomas, Adv. Nucl. Phys. **13**, 1 (1984).
[4] S. Weinberg, Physica (Amsterdam) **96A**, 327 (1979); J. Gasser and H. Leutwyler, Ann. Phys. (N.Y.) **158**, 142 (1984); E. Jenkins, M. Luke, A. V. Manohar, and M. J. Savage, Phys. Lett. B **302**, 482 (1993); V. Bernard, N. Kaiser, and U.-G. Meißner, Int. J. Mod. Phys. E **4**, 193 (1995).
[5] D. B. Leinweber, A. W. Thomas, K. Tsushima, and S. V. Wright, Phys. Rev. D **61**, 074502 (2000).
[6] D. B. Leinweber, D. H. Lu, and A. W. Thomas, Phys. Rev. D **60**, 034014 (1999); E. J. Hackett-Jones, D. B. Leinweber, and A. W. Thomas, Phys. Lett. B **489**, 143–147 (2000).
[7] E. Jenkins, M. Luke, A. V. Manohar, and M. J. Savage, Phys. Lett. B **302**, 482 (1993).
[8] D. B. Leinweber, T. Draper, and R. M. Woloshyn, Phys. Rev. D **46**, 3067 (1992).
[9] W. Wilcox, T. Draper, and K. Liu, Phys. Rev. D **46**, 1109 (1992).
[10] S. Kopecky *et al.*, Phys. Rev. Lett. **74**, 2427 (1995).

[11] L. L. Foldy, Phys. Rev. **87**, 688 (1947).
[12] S. Theberge, G. A. Miller, and A. W. Thomas, Can. J. Phys. **60**, 59 (1982).
[13] L. R. Dodd, A. W. Thomas, and R. F. Alvarez-Estrada, Phys. Rev. D **24**, 1961 (1981).
[14] R. Carlitz, S. D. Ellis, and R. Savit, Phys. Lett. **64B**, 85 (1976); N. Isgur, G. Karl, and R. Koniuk, Phys. Rev. Lett. **41**, 1269 (1978).
[15] N. Isgur, Phys. Rev. Lett. **83**, 272 (1999).
[16] M. Bawin and S. A. Coon, nucl-th/0101005 [Nucl. Phys. A (to be published)].
[17] M. A. B. Bég and A. Zepeda, Phys. Rev. D **6**, 2912 (1972); J. Gasser, M. E. Sainio, and A. Svarc, Nucl. Phys. **B307**, 779 (1988); D. B. Leinweber and T. D. Cohen, Phys. Rev. D **47**, 2147 (1993).

PHYSICAL REVIEW D 66, 094507 (2002)

Chiral analysis of quenched baryon masses

R. D. Young,[1] D. B. Leinweber,[1] A. W. Thomas,[1] and S. V. Wright[1,2]
[1]*Special Research Centre for the Subatomic Structure of Matter and Department of Physics and Mathematical Physics, University of Adelaide, Adelaide SA 5005, Australia*
[2]*Division of Theoretical Physics, Department of Mathematical Sciences, University of Liverpool, Liverpool L69 3BX, United Kingdom*
(Received 17 May 2002; published 27 November 2002)

We extend to quenched QCD an earlier investigation of the chiral structure of the masses of the nucleon and the delta in lattice simulations of full QCD. Even after including the meson-loop self-energies which give rise to the leading and next-to-leading nonanalytic behavior (and hence the most rapid variation in the region of light quark mass), we find surprisingly little curvature in the quenched case. Replacing these meson-loop self-energies by the corresponding terms in full QCD yields a remarkable level of agreement with the results of the full QCD simulations. This comparison leads to a very good understanding of the origins of the mass splitting between these baryons.

DOI: 10.1103/PhysRevD.66.094507 PACS number(s): 12.38.Gc, 12.38.Aw, 12.39.Fe, 12.40.Yx

I. INTRODUCTION

The quenched approximation is a widely used tool for studying nonperturbative QCD within numerical simulations of lattice gauge theory. With an appropriate choice of the lattice scale and at moderate to heavy quark masses, this approximation has been shown to give only small, systematic deviations from the results of full QCD with dynamical fermions. Although no formal connection has been established between full and quenched QCD, the similarity of the results has led to the belief that the effects of quenching are small and hence that quenched QCD provides a reasonable approximation to the full theory [1].

Improved lattice actions, together with advances in high performance computing, have been responsible for significant improvements in the calculation of baryon masses at moderate to light quark masses within the quenched approximation [2–5]. Simulations with dynamical fermions have proven to be more difficult, but results have been reported with pion masses as low as 320 MeV [4,6].

The fact that one is restricted to quark masses much larger than the physical values means that, in addition to all the usual extrapolations (e.g., to the infinite volume and continuum limits), if one wants to compare with empirical hadron observables, one must also have a reliable method of extrapolation to the chiral limit. Any such extrapolation must incorporate the appropriate chiral corrections, arising from Goldstone boson loops, which give rise to rapid, nonlinear variations as the chiral limit is approached.

Studies of the exactly soluble Euler-Heisenberg problem [7], suggest that one can develop surprisingly accurate extrapolation functions, provided one builds in the correct behavior in *both* the small and large mass limits. For QCD, Leinweber *et al.* [8] have suggested an extrapolation method which ensures both the exact low mass limit of chiral perturbation theory [technically its leading (LNA) and next-to-leading nonanalytic (NLNA) behavior] and the heavy quark limit of heavy quark effective theory (HQET). The transition between the chiral and heavy quark regimes is characterized by a mass scale Λ, related to the inverse of the size of the pion cloud source.

This approach is equivalent to the formulation of chiral perturbation theory (χPT) using a finite-range regulator with extent governed by Λ [9]. The resummation of the chiral expansion arising from the finite-range regulator suppresses the rapid nonanalytic variation of hadron properties once the pion Compton wavelength is smaller than this scale (i.e. $m_\pi > \Lambda$). The importance of incorporating such behavior has been successfully demonstrated for a number of hadronic observables, including masses [8,10], the sigma commutator [11], magnetic moments [12–15], charge radii [16] and parton distribution functions [17–19].

The impressive results found using these methods have led us to the present investigation of the problem of the chiral extrapolation of baryon masses in quenched QCD. The chiral properties within the quenched approximation are known to differ from those of full QCD in a number of very interesting ways [20–25]. For example, not only are the effective couplings at the pion-baryon vertices significantly altered in quenched QCD (QQCD) but, because the η' behaves as a Goldstone boson in QQCD, one must also consider η' loops.

Here we first review previous work [8] which reported a successful method for extrapolating baryon masses as calculated in full QCD lattice simulations. The modified chiral structure of quenched baryon masses [23] is presented next. We show how to construct the various meson loop induced self-energies [26] in order to preserve the leading-nonanalytic and next-to-leading nonanalytic structure appropriate to QQCD, while incorporating the established behavior at heavier quark masses. This is followed by a detailed application to the extrapolation of the quenched N and Δ masses to the chiral limit. Finally, we use the observed similarity of the structure of baryons stripped of their Goldstone boson clouds, in full and quenched QCD, to explore whether one can make a connection between the masses calculated in QQCD and those obtained in a dynamical simulation. The remarkable agreement obtained suggests a number of further tests and also leads us, with considerable confidence, to an interpretation of the origin of the N-Δ mass splitting.

II. QCD EXTRAPOLATION

In general, the coefficients of the LNA and NLNA terms in a chiral expansion of baryon masses are very large. For instance, the LNA term for the nucleon mass is $\delta m_N^{(\mathrm{LNA})} = -5.6 m_\pi^3$ (with m_π and $\delta m_N^{(\mathrm{LNA})}$ in GeV). With $m_\pi = 0.5$ GeV, quite a low mass for current simulations, this yields $\delta m_N^{(\mathrm{LNA})} = 0.7$ GeV—a huge contribution. Furthermore, in this region hadron masses in both full and quenched lattice QCD are found to be essentially linear in m_π^2 or equivalently quark mass, whereas $\delta m_N^{(\mathrm{LNA})}$ is highly nonlinear. The challenge is therefore to ensure the appropriate LNA and NLNA behavior, *with the correct coefficients*, as $m_\pi \to 0$, while making the transition to linear behavior as m_π increases, sufficiently rapidly to describe the actual lattice data.

A reliable method for achieving all this was proposed by Leinweber *et al.* [8]. They fit the full (unquenched) lattice data with the form

$$M_B = \alpha_B + \beta_B m_\pi^2 + \Sigma_B(m_\pi, \Lambda), \tag{1}$$

where Σ_B is the total contribution from those pion loops which give rise to the LNA and NLNA terms in the self-energy of the baryon. For the N these correspond to the processes $N \to N\pi \to N$ and $N \to \Delta\pi \to N$, while for the Δ we need $\Delta \to \Delta\pi \to \Delta$ and $\Delta \to N\pi \to \Delta$. Explicitly,

$$\Sigma_N = \sigma_{NN}^\pi + \sigma_{N\Delta}^\pi,$$

$$\Sigma_\Delta = \sigma_{\Delta\Delta}^\pi + \sigma_{\Delta N}^\pi. \tag{2}$$

In the heavy baryon limit, these four contributions ($B \to B'\pi \to B$) can be summarized as

$$\sigma_{BB'}^\pi = -\frac{3}{16\pi^2 f_\pi^2} G_{BB'} \int_0^\infty dk \frac{k^4 u^2(k)}{\omega(k)[\omega_{BB'} + \omega(k)]}, \tag{3}$$

where $\omega(k) = \sqrt{k^2 + m_\pi^2}$ is the intermediate pion energy and $\omega_{BB'} = (M_{B'} - M_B)$ is the physical baryon mass splitting and $f_\pi = 93$ MeV. The coefficients $G_{BB'}$ are standard SU(6) couplings and are summarized in Sec. IV. The ultraviolet regulator, $u(k)$, has a very natural physical interpretation as the Fourier transform of the source of the pion field. The LNA and NLNA structure of these diagrams is associated with the infrared behavior of the corresponding integrals and hence is independent of the choice of regularization scheme. The use of such a regulator effectively suppresses the self-energies like Λ^2/m_π^2 for $m_\pi \gg \Lambda$, the characteristic mass scale of the cutoff. A common choice of regulator, which we use throughout this work, is the dipole form, $u(k) = \Lambda^4/(\Lambda^2 + k^2)^2$.

In terms of the underlying effective field theory, the shape of the regulator is irrelevant to the formulation of χPT [9]. However, current lattice simulation results encourage us to look for an efficient formulation which maximizes the applicable pion-mass range accessed via one- or two-loop order. An optimal regulator (motivated by phenomenology) will effectively re-sum the chiral expansion encapsulating the physics in the first few terms of the expansion. The approach is systematically improved by simply going to higher order in the chiral expansion. Our experience with dipole and monopole vertex regulators indicates that the shape of the regulator has little effect on the extrapolated results, provided lattice QCD simulation results are used to constrain the optimal regulator parameter on an observable-by-observable basis [8,10].

In a phenomenological sense, the linear term of Eq. (1), which dominates for $m_\pi \gg \Lambda$, encompasses the quark mass dependence of the pion-cloud source—the baryon without its pion dressing. This term also serves to account for loop diagrams involving heavier mesons (integrated out of the effective field theory), which have much slower variation with quark mass. Given the current state of the art in lattice simulations, data in the low to intermediate mass range are unable to reliably constrain the optimal parameter Λ. There is considerable phenomenological support for choosing a dipole regulator parameter somewhat smaller than found for the axial form factor of the nucleon, which is 1.03 ± 0.04 GeV [27–29]. However, it is important to understand that the anticipated development of supercomputing resources and techniques are such that Λ may be optimally constrained by full QCD simulation data in the near future.

Fitting lattice results to Eq. (1) is straightforward. Upon calculating the described self-energies for a given choice of Λ, the fitting procedure amounts to a simple linear fit in α_B and β_B.

III. QUENCHED CHIRAL PERTURBATION THEORY

Standard chiral perturbation theory is a low energy effective field theory built upon the symmetries of QCD [30,31]. It amounts to an expansion of Green's functions in powers of momenta and quark mass about the chiral limit ($m_q = 0$). In the case of baryon masses, χPT tells us the leading behavior of the quark mass expansion. Because χPT is an effective field theory, the renormalization procedure must be performed order by order in perturbation theory. At higher and higher order, more and more unknown parameters are introduced. These unknowns only play a role in analytic terms of the expansion. The coefficients of the leading nonanalytic terms are constrained by chiral symmetry [32]—they are independent of regularization and the order of the chiral expansion. In connecting the results of lattice QCD to the physical world it is essential that one incorporate the correct nonanalytic structure of the low energy theory.

Quenched χPT (QχPT) provides the analogous low energy effective theory for QQCD [21–23]. Sea quark loops are removed from QCD by including a set of degenerate, commuting (bosonic) quark fields. These bosonic fields have the effect of exactly cancelling the fermion determinant in the functional integration over the quark fields. This gives a Lagrangian for a field theory which is equivalent to the quenched approximation simulated on the lattice. The low energy effective theory is then constructed on the basis of the symmetries of this Lagrangian.

The leading chiral expansion of baryon masses in the quenched approximation has been calculated by Labrenz and

TABLE I. Coefficients of the lowest order nonanalytic terms in the chiral expansions of the N and Δ masses, with values from both full and quenched QCD listed for comparison ($\nu^{-1}=16\pi f_\pi^2$, $\Delta M = M_\Delta - M_N$).

B	c_i	QCD	QQCD
N	c_1	0	$-\frac{1}{2}(3F-D)^2 m_0^2 \nu$
	c_3	$-\frac{3}{2}(F+D)^2 \nu$	$\{\frac{4}{3}(D^2-3DF)-2(3F-D)\gamma\}\nu$
	c_{4L}	$\frac{3}{\pi}(F+D)^2 \frac{32}{25}\frac{3}{8\Delta M}\nu$	$\frac{\mathcal{C}^2}{2\pi\Delta M}\nu$
Δ	c_1	0	$-\frac{5}{18}\mathcal{H}^2 m_0^2 \nu$
	c_3	$-\frac{3}{2}(F+D)^2 \nu$	$\{-\frac{10}{27}\mathcal{H}^2-\frac{10}{9}\mathcal{H}\gamma'\}\nu$
	c_{4L}	$-\frac{3}{\pi}(F+D)^2 \frac{8}{25}\frac{3}{8\Delta M}\nu$	$\frac{\mathcal{C}^2}{2\pi\Delta M}\frac{4}{25}\nu$

Sharpe [23]. For the reasons already mentioned in the Introduction, it differs from the corresponding expansion in full QCD. In particular, the chiral expansion coefficients take different values and new, nonanalytic behavior is also introduced. The explicit form can be expressed as

$$M_B = M_B^{(0)} + c_1^B m_\pi + c_2^B m_\pi^2 + c_3^B m_\pi^3 + c_4^B m_\pi^4 + c_{4L}^B m_\pi^4 \log m_\pi + \ldots \quad (4)$$

with the coefficients of the terms which are nonanalytic in the quark mass listed in Table I. We note that in Ref. [23] the N and Δ were treated as degenerate states in the chiral limit. Experience in other situations suggests that it is more accurate to retain a finite mass difference, in which case off–diagonal terms such as $N\to\Delta\pi\to N$ lead to the nonanalytic behavior of the form $m_\pi^4 \log m_\pi$.

The contribution linear in m_π is unique to the quenched approximation. The quenched theory therefore exhibits a more singular behavior in the chiral limit. The origin of this behavior is the Goldstone nature of the η' in QQCD and specifically the process shown in Fig. 1(b). We note also that the coefficients of the chiral expansion involve new couplings, γ and γ', which are related to the flavor-singlet, hairpin-baryon couplings for N and Δ respectively, illustrated in Fig. 1(a). In the formalism of Ref. [23] these are related to the couplings of full QCD via the relations

$$\gamma = D - F, \qquad \gamma' = 0, \quad (5)$$

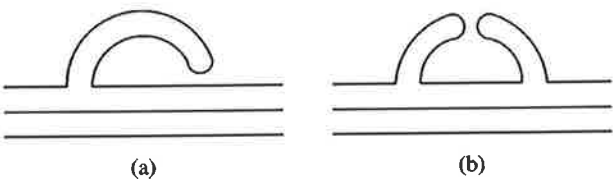

FIG. 1. Quark flow diagrams for the chiral η' loop contributions appearing in QQCD: (a) single hairpin, (b) double hairpin.

TABLE II. Chiral couplings appearing in the self-energy integrals, Eq. (3) for full QCD and Eq. (6) for QQCD. In numerical calculations we have used the couplings arising from $SU(6)$ relations [34], $\mathcal{C}=-2D$ and $\mathcal{H}=-3D$.

	G_{NN}	$G_{N\Delta}$	$G_{\Delta\Delta}$	$G_{\Delta N}$
QCD	$(F+D)^2$	$\frac{32}{25}(F+D)^2$	$(F+D)^2$	$\frac{8}{25}(F+D)^2$
QQCD	$\frac{8}{9}(3DF-D^2)$	$\frac{16}{9}D^2$	$\frac{20}{9}D^2$	$-\frac{8}{9}D^2$

as described in Appendix B. There is some uncertainty over the flavor singlet couplings, especially in connection with Okubo-Zweig-Iizuka (OZI) violation associated with the U(1) axial anomaly [33]. While this may modify our calculated curves at extremely light quark mass, it would have no significant effect on the fit to lattice data at large quark mass nor on the comparison of current quenched and full QCD data.

IV. QUENCHED SELF-ENERGIES

Our aim is to apply a similar procedure for the chiral extrapolation of quenched QCD data to that which has proven successful for the physical theory. That is, we wish to generalize Eq. (1) to replace the LNA and NLNA self-energy terms arising in full QCD by their quenched analogues. The pion loop contributions have the same kinematic structure as those in full QCD. A simple redefinition of the couplings, $G_{BB'}$, in the expressions for the self-energies ensures that the correct LNA and NLNA of QχPT is maintained. Thus, the analytic expressions for the pion cloud corrections to the masses of the N and Δ are of the same form as the full QCD integrals [c.f. Eq. (3)]:

$$\tilde{\sigma}_{BB'}^{\pi} = -\frac{3}{16\pi^2 f_\pi^2}\tilde{G}_{BB'}\int_0^\infty dk \frac{k^4 u^2(k)}{\omega(k)[\omega_{BB'}+\omega(k)]}, \quad (6)$$

where the quenched couplings, $\tilde{G}_{BB'}$, are listed in Table II, together with their physical counterparts. Assuming a weak N_f dependence of the chiral parameters, we describe the quenched self-energies using the same tree level values of $D=0.76$ and $F=0.50$ as in full QCD.

Within the quenched approximation η' loops also contribute to the low energy effective theory, whereas they are usually neglected in the physical case. This is because a resummation of internal loop diagrams (coming from the fermion determinant) means that the η' remains massive in the chiral limit of full QCD. On the other hand, the absence of these virtual loops in the quenched approximation causes the flavor singlet η' to behave as a Goldstone boson [21,22]. As a consequence of this feature of the quenched theory, there are two new types of loop contributions to be considered. A schematic view of these processes is shown in Fig. 1.

The first of these two contributions, shown in Fig. 1(a), arises from a single "hairpin" interaction. As discussed above, it is responsible for the term proportional to γ (γ') in the chiral expansion of the N (Δ) mass. These couplings are discussed in considerable detail in Appendix B. The structure

TABLE III. Couplings used in flavor singlet η' self-energies. We take $m_0^2=0.42$ GeV^2, lying between phenomenological and lattice estimates [35–37]. The momentum dependence of the double hairpin vertex, which is believed to be small, is neglected.

	$N_B^{(1)}$	$N_B^{(2)}$ (GeV^2)
N	$\frac{4}{3}(3F-D)\gamma$	$\frac{2}{9}(3F-D)^2 m_0^2$
Δ	$\frac{20}{27}\mathcal{H}\gamma'$	$\frac{10}{81}\mathcal{H}^2 m_0^2$

of this diagram is exactly the same as the pion loop contribution where the internal baryon is degenerate with the external state. The integral representing this diagram is then the same as that for $\tilde{\sigma}^{\pi}_{BB}$,

$$\tilde{\sigma}_B^{\eta'(1)} = -\frac{3}{16\pi^2 f_\pi^2} N_B^{(1)} \int_0^\infty dk \frac{k^4 u^2(k)}{\omega^2(k)}. \tag{7}$$

The factors $N_B^{(1)}$, providing the correct nonanalytic behavior in the chiral expansion [Eq. (4)], are displayed in Table III.

The second of these new η' loop diagrams arises from the double hairpin vertex, pictured in Fig. 1(b). This contribution is particularly interesting because there are two meson propagators and it is therefore responsible for the nonanalytic term linear in m_π—this term being unique to the quenched case. The integral corresponding to this self energy can be written in a similar way:

$$\tilde{\sigma}_B^{\eta'(2)} = \frac{3}{16\pi^2 f_\pi^2} N_B^{(2)} \int_0^\infty dk \frac{k^4 u^2(k)}{\omega^4(k)}. \tag{8}$$

Note the sign change and the higher power of ω in the denominator. The coefficients, $N_B^{(2)}$, providing the correct nonanalytic behavior in Eq. (4)—in this case the coefficient of m_π—are given in Table III. The sum of these four contributions then gives the net meson-loop induced self-energies within the quenched approximation,

$$\tilde{\Sigma}_B = \tilde{\sigma}^{\pi}_{BB} + \tilde{\sigma}^{\pi}_{BB'} + \tilde{\sigma}_B^{\eta'(1)} + \tilde{\sigma}_B^{\eta'(2)}. \tag{9}$$

The individual contributions to the N and Δ masses over a range of pion mass are plotted in Figs. 2 and 3. These are all evaluated with the dipole regulator mass parameter $\Lambda = 0.8$ GeV. The corresponding self-energies from full QCD are also shown for comparison. We note that in QQCD the contributions are typically quite a bit smaller and the double-hairpin graph, $\tilde{\sigma}_B^{\eta'(2)}$, is repulsive. The differences are enhanced for the Δ where $\tilde{\sigma}^{\pi}_{\Delta N}$ is also repulsive. We observe that the rapid, nonlinear behavior (which is effectively much larger in full QCD) is restricted to the region $m_\pi^2 \lesssim 0.2$ GeV^2, above which the self-energies are quite smoothly varying functions of the quark mass.

V. FITTING PROCEDURE

The lattice data considered in this analysis come from the recent paper of Bernard *et al.* [4]. These simulations were performed using an improved Kogut-Susskind quark action, which is known to have good scaling properties [38]. Unlike the standard Wilson fermion action, masses determined at finite lattice spacing are excellent estimates of the continuum limit results.

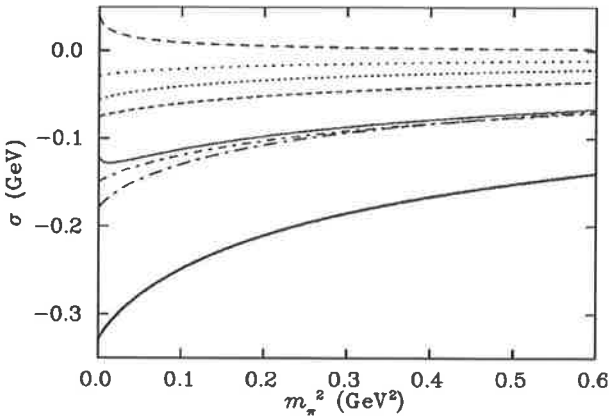

FIG. 2. Various self-energy contributions to M_N for dipole mass, $\Lambda = 0.8$ GeV. From top down at $m_\pi^2 = 0.1$ GeV^2, the curves correspond to (where a $\sim$ over the symbol denotes a quenched QCD contribution) $\tilde{\sigma}_N^{\eta'(2)}, \tilde{\sigma}_N^{\eta'(1)}, \tilde{\sigma}^{\pi}_{NN}, \tilde{\sigma}^{\pi}_{N\Delta}$, total quenched $\tilde{\Sigma}_N$, $\sigma^{\pi}_{N\Delta}$, σ^{π}_{NN} and total physical Σ_N.

We are particularly concerned with the chiral extrapolation of baryon masses and how their behavior is affected by the quenched approximation. In such a study, it is essential that the method of scale determination be free from chiral contamination. One such method involves the static-quark potential. As low-lying pseudoscalar mesons made of light quarks exhibit negligible coupling to hadrons containing only heavy valence quarks, the low energy effective field theory plays no role in the determination of the scale for these systems. In fixing the scale through such a procedure one constrains all simulations, quenched, 2-flavor, 3-flavor

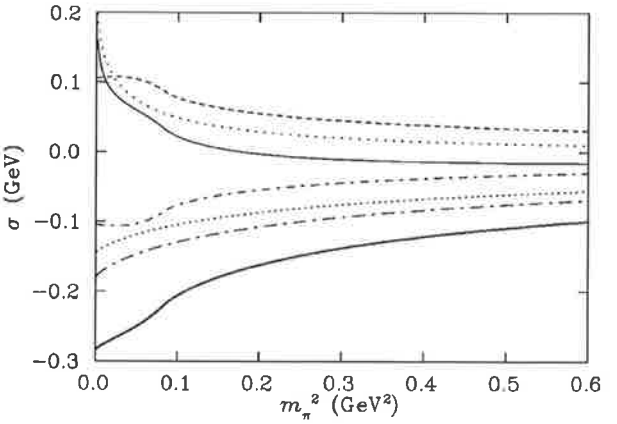

FIG. 3. Various self-energy contributions to M_Δ for dipole mass, $\Lambda = 0.8$ GeV. From top down at $m_\pi^2 = 0.1$ GeV^2, the curves correspond to (where a $\sim$ over the symbol denotes a quenched QCD contribution) $\tilde{\sigma}^{\pi}_{\Delta N}, \tilde{\sigma}_\Delta^{\eta'(2)}$, total quenched $\tilde{\Sigma}_\Delta$, $\sigma^{\pi}_{\Delta N}$, $\tilde{\sigma}^{\pi}_{\Delta\Delta}$, $\sigma^{\pi}_{\Delta\Delta}$ and total physical Σ_Δ.

etc., to match phenomenological static-quark forces. Effectively, the short range (0.35–0.5 fm) interactions are matched across all simulations.

A commonly adopted method involving the static-quark potential is the Sommer scale [39,40]. This procedure defines the force, $F(r)$, between heavy quarks at a particular length scale, namely $r_0 \simeq 0.5$ fm. Choosing a narrow window to study the potential avoids complications arising in dynamical simulations where screening and ultimately string breaking is encountered at large separations. The lattice data analyzed in this report use a variant of this definition, choosing to define the force at $r_1 = 0.35$ fm via $r_1^2 F(r_1) = 1.00$ [4].

As we remarked earlier, the nonanalytic chiral behavior is governed by the infrared regions of the self-energy integrals. The fact that the lattice calculations are performed on a finite volume grid means that the self-energy integrals implicit in current lattice simulations do not include the exact chiral behavior. It is important to take this into account in the fitting procedure and we therefore follow Ref. [10] in replacing the continuum self-energy integrals used in the fitting process by a discrete sum over the meson momenta available on the lattice:

$$4\pi \int_0^\infty k^2 dk = \int d^3k \approx \frac{1}{V}\left(\frac{2\pi}{a}\right)^3 \sum_{k_x,k_y,k_z} . \qquad (10)$$

The self-energy integrals calculated in this way are what should be directly compared with the lattice data, and we illustrate these by open squares in subsequent figures. Upon obtaining the optimal fit parameters, one can evaluate the integrals exactly and therefore obtain the infinite-volume, continuum limit. The latter is the result which should be compared with experiment at the physical pion mass.

We now proceed to fit quenched lattice data with the form

$$\tilde{M}_B = \tilde{\alpha}_B + \tilde{\beta}_B m_\pi^2 + \tilde{\Sigma}_B(m_\pi, \Lambda) \qquad (11)$$

[by analogy with the form used in full QCD, Eq. (1)], with the self-energies evaluated, as we have just outlined, using the momentum grid corresponding to the specific lattice simulation. Phenomenologically speaking, the linear terms in Eq. (11) may be thought of as accounting for the quark mass dependence of the pion-cloud source. This form then automatically includes the expected heavy quark behavior where the π and η' loop contributions are suppressed.

The effective field theory regulator, motivated by the physical structure of the meson-baryon vertex, characterizes the finite size of the pion source. Quenched simulations of hadronic charge radii performed at moderate to heavy quark masses [41] have been demonstrated to be consistent with experiment once the meson-cloud properties of full QCD are taken into account [16,42]. This indicates that the size of the meson-cloud source is expected to be of similar size in both quenched and physical QCD. For this reason we proceed to fit both quenched and physical data with a common value of Λ. For a fixed choice of Λ, fitting to lattice data amounts to a linear fit in α and β. It turns out that, for a range of values of Λ, the values of α and β found for the QQCD data are surprisingly close to the values found for the fit to dynamical QCD data. This strongly suggests that the self-energies included here, which contain the LNA and NLNA behavior appropriate to each type of simulation, contain the primary effect of quenching. To illustrate the point, Fig. 4 shows a measure, δ, of the difference between the quenched and dynamical data sets over the range of m_π considered. This measure is proportional to the net area contained between the straight lines obtained from the fits and has been normalized to the case where the self-energy diagrams are totally neglected. The improved agreement between data sets over the range of dipole masses highlights the effectiveness of this self-energy correction. It is also worth noting that the χ^2/d.o.f. is also improved by incorporating the self-energies into the fit. For the preferred dipole mass, $\Lambda = 0.8$ GeV, this is better by a factor 2. Results of both the physical and quenched fits are shown together in Fig. 5. The parameters of the best fits are displayed in Table IV. Here we see the remarkable agreement of the linear term of our fitting formulas, Eqs. (1) and (11). This strongly suggests that the behavior of the meson-cloud source is very similar in quenched and full QCD. The primary difference between the quenched and physical results can then be described by the meson-loop induced self-energies.

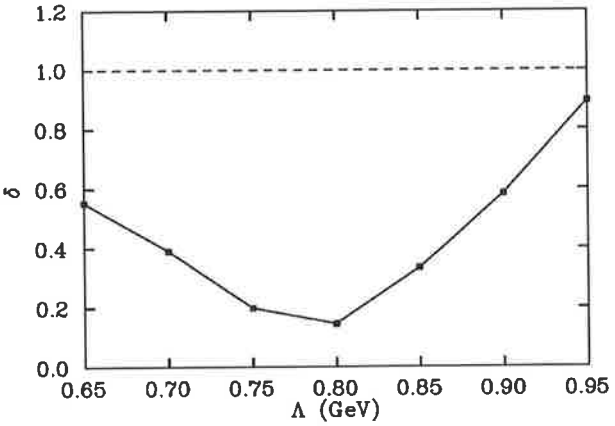

FIG. 4. The value δ is a measure of the difference between the quenched and dynamical data sets after accounting for the relevant self-energy diagrams. This measure is proportional to the net area contained between the straight lines obtained from the fits and has been normalized to the case where the self-energy diagrams are totally neglected.

This observation suggests that it may well be possible to make a connection between quenched simulations and hadron properties in the real world. One would fit quenched data with appropriate self-energies to obtain the linear behavior of the meson-cloud source. Then the quenched self-energies would be replaced by their full-QCD counterparts, hence obtaining more physical results. It is clearly very important to test this result further on other hadrons (e.g. for other members of the octet) and against dynamical simulations at lower quark masses.

VI. Δ-N HYPERFINE SPLITTING

The analysis of lattice data has demonstrated the ability to describe the primary difference between quenched and dy-

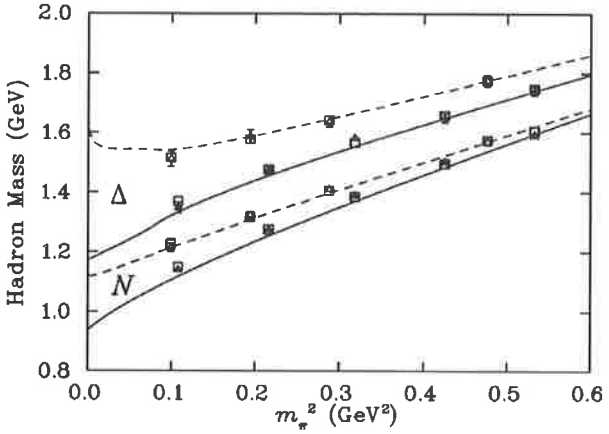

FIG. 5. Fit (open squares) to lattice data [4] (quenched △, dynamical ▲) with adjusted self-energy expressions accounting for finite volume and lattice spacing artifacts. The infinite-volume, continuum limit of quenched (dashed lines) and dynamical (solid lines) are shown. The lower curves and data points are for the nucleon and the upper ones for the Δ.

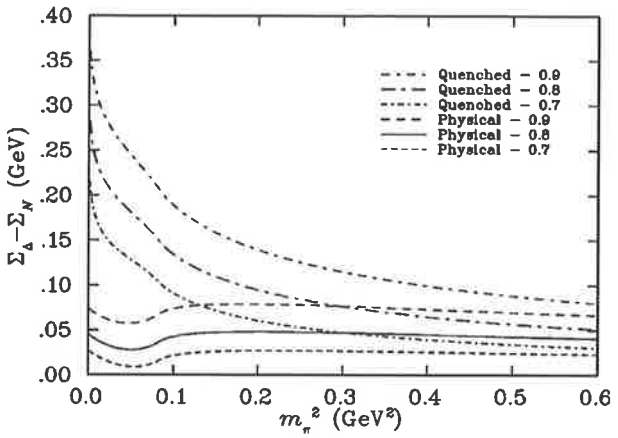

FIG. 6. Meson-loop contribution to the Δ-*N* mass splitting in both quenched and full QCD—for several values of the dipole mass.

namical simulations in terms of the meson-loop self-energies. Figure 6 shows the difference in the self-energy terms for the *N* and Δ in quenched and full QCD, for several values of the common dipole-regulator mass. It is quite clear that there is a difference of between 150 and 250 MeV between the quenched and full QCD cases. Since this difference was essential in accounting for the clear differences in the behavior of the baryon masses in QQCD and full QCD shown in Fig. 5, we have some confidence in using these results to say how much of the physical *N*-Δ mass splitting is associated with pion loops and how much comes from short range processes, such as gluon exchange. In fact, an examination of Fig. 6 for the case of full QCD suggests fairly clearly that only about 50 MeV of the observed 300 MeV *N*-Δ splitting arises from pion loops. Of course, this result is more dependent on the assumption of the *same* dipole mass parameter at every vertex than the fits to the *N* and Δ masses individually. Nevertheless, it seems unlikely that more than a third of the total splitting could come from this source.

VII. CONCLUSIONS

We have investigated the quark mass dependence of the *N* and Δ masses within the quenched approximation. The leading chiral behavior of hadron masses is known to differ in quenched QCD from the physical theory. This knowledge has been used to guide us in the construction of an effective field theory which encompasses the correct chiral structure, and is consistent with current lattice simulations. This procedure of fitting lattice data with a linear term together with the meson-loop corrections which give rise to the LNA and NLNA behavior has been demonstrated previously to fit dynamical QCD simulation results remarkably well. Here we have shown that the application of the same procedure to quenched results is able to consistently fit the data in that case as well. We note that this approach encapsulated in Eqs. (1) and (11) is a finite-range regulated effective field theory consistent with the traditional dimensional regularization approach to χPT. By calculating next-order loop contributions it is systematically improvable and model independent [9].

Remarkably, a comparison of the two fits suggests that the properties of the *N* and Δ, stripped of their pion clouds, are essentially the same in quenched and full QCD, once the scale is set using the Sommer scale appropriate to heavy quark systems. This observation is dependent on an optimal regulator shape and size, and the assumption that the axial coefficients are similar in quenched and full QCD. Therefore this result should be regarded as a phenomenological link. The extent to which this observation is model independent requires the investigation of alternative regulators and new accurate lattice results approaching the light quark-mass regime. At present, the success of this result further motivates use of the phenomenologically preferred dipole, which gives a most accurate description of the shape of the pion-cloud source. It is clearly essential to test this finding against further full QCD simulations at lighter quark masses as well as for other hadrons.

We have demonstrated that although the quenched approximation gives rise to more singular behavior in the chiral limit, this is not likely to be observed in lattice simulations as these contributions are quickly suppressed with increasing quark mass. Indeed our results suggest that it will be very

TABLE IV. Best fit parameters for both full and quenched data sets with dipole regulator, $\Lambda = 0.8$ GeV. The second set correspond to a simple linear fit, where the self-energy contributions have been neglected. All masses are in GeV.

Self-energy	Simulation	α_N	β_N	α_Δ	β_Δ
Dipole	Physical	1.27(2)	0.90(5)	1.45(3)	0.74(8)
	Quenched	1.24(2)	0.85(6)	1.45(4)	0.72(11)
Nil	Physical	1.04(2)	1.07(5)	1.28(3)	0.88(8)
	Quenched	1.14(2)	0.92(6)	1.44(4)	0.69(11)

hard to detect any significant chiral curvature in the case of the nucleon, while for the Δ there may be some small, upward curvature. The Δ-N mass splitting increases to around 400 MeV at the physical point in QQCD. As a consequence of this behavior, the Δ mass in the quenched approximation is expected to differ from the physical mass by approximately 25%. Finally, we have shown that while a fraction of the physical N-Δ mass difference can be attributed to a difference in pion self-energy loops, this is unlikely to amount to more than a third of the observed splitting.

ACKNOWLEDGMENTS

We would like to thank S. Sharpe for numerous enlightening discussions concerning QχPT as well as W. Detmold, M. Oettel, A. Williams and J. Zanotti for helpful conversations. This work was supported by the Australian Research Council and the University of Adelaide.

APPENDIX A: ANALYTIC INTEGRATION

Here we summarize analytic expressions for the self-energy integrals. It should be noted that these expressions are not used in fitting lattice data. For the purpose of fitting, the continuum integral is replaced by a discrete sum over the available momenta on the corresponding lattice, as described in Eq. (10).

Firstly we consider the case of the simple meson-loop digram where the internal baryon line has degenerate mass with the external state:

$$\sigma = -\frac{3}{16\pi^2 f_\pi^2} G \int_0^\infty dk \frac{k^4 u^2(k)}{\omega^2(k)}. \tag{A1}$$

Using a sharp cutoff, $u(k)=\theta(\Lambda-k)$, the integral can be expressed as

$$\sigma = -\frac{3G}{16\pi^2 f_\pi^2}\left[m_\pi^3 \arctan\left(\frac{\Lambda}{m_\pi}\right) + \frac{\Lambda^3}{3} - \Lambda m_\pi^2 \right]. \tag{A2}$$

The LNA behavior of this can then be immediately read from this,

$$\sigma|^{\mathrm{LNA}} = -\frac{3G}{32\pi f_\pi^2} m_\pi^3. \tag{A3}$$

Alternatively, our preferred dipole $u(k)=\Lambda^4/(\Lambda^2+k^2)^2$, also provides an analytic expression for this self-energy,

$$\sigma = -\frac{3G}{512\pi f_\pi^2} \frac{\Lambda^5}{(\Lambda+m_\pi)^4}(m_\pi^2 + 4\Lambda m_\pi + \Lambda^2). \tag{A4}$$

This gives precisely the same LNA behavior as the sharp cutoff, as expected because the nonanalytic behavior is due to the infrared behavior of the integral. It is associated with the residue of the pion propagator pole, and hence independent of an ultraviolet cutoff.

The case of the double meson propagator can also be performed analytically,

$$\sigma = \frac{3}{16\pi^2 f_\pi^2} N \int_0^\infty dk \frac{k^4 u^2(k)}{\omega^4(k)}. \tag{A5}$$

For $u(k)=\theta(\Lambda-k)$,

$$\sigma = \frac{3}{16\pi^2 f_\pi^2} \times N \frac{3m_\pi^2\Lambda + 2\Lambda^3 - 3m_\pi(m_\pi^2+\Lambda^2)\arctan\left(\frac{\Lambda}{m_\pi}\right)}{2(m_\pi^2+\Lambda^2)}. \tag{A6}$$

For $u(k)=\Lambda^4/(\Lambda^2+k^2)^2$,

$$\sigma = \frac{3N}{512\pi f_\pi^2} \frac{\Lambda^5(m_\pi+5\Lambda)}{(\Lambda+m_\pi)^5}. \tag{A7}$$

Once again both integrals give the same LNA behavior,

$$\sigma|^{\mathrm{LNA}} = -\frac{9N}{64\pi f_\pi^2} m_\pi. \tag{A8}$$

For the off-diagonal contributions, where the internal baryon is not degenerate with the external state,

$$\sigma = -\frac{3}{16\pi^2 f_\pi^2} G \int_0^\infty dk \frac{k^4 u^2(k)}{\omega(k)[\omega_{BB'}+\omega(k)]}, \tag{A9}$$

with $\omega_{BB'}$ finite. The results do not have a simple form. The full expression for the case of a sharp cutoff form factor can be found in Ref. [8]. We show the LNA contribution to this diagram for reference,

$$\sigma|^{\mathrm{LNA}} = -\frac{9G}{128\,\pi^2 f_\pi^2} \frac{m_\pi^4}{\omega_{BB'}} \log m_\pi. \tag{A10}$$

APPENDIX B: FLAVOR SINGLET IN FULL AND QUENCHED QCD

This appendix serves to clarify the derivation of the hairpin meson-baryon couplings in quenched χPT.

The flavor singlet η' remains light in the quenched approximation, and is therefore an effective degree of freedom in the low energy sector. Such excitations must therefore be incorporated into the low-energy analysis. Within full QCD, resummation of internal loop diagrams renders the η' massive and hence it plays no role in the low-energy dynamics. For this reason couplings to such flavor singlet states are neglected. In our analysis, we wish to compare the low-energy structure of the quenched and physical theories. In this case, a flavor singlet coupling, like $NN\eta'$, must be included in the chiral Lagrangian of full QCD in order that it is

treated on equal footing with the quenched theory. This coupling will not alter any results of the physical theory as any diagram would involve the propagation of a heavy η'.

Here we derive best estimates for the flavor singlet couplings in quenched QCD. This is achieved by comparison of the quenched and full chiral Lagrangians, under the standard assumption that the couplings exhibit negligible change between the two theories [23]. We follow the notation of Labrenz and Sharpe [23] in the analysis of such contributions. All symbols retain the same meaning, unless otherwise specified.

The chiral Lagrangian for full QCD can be expressed as

$$\mathcal{L}=\mathcal{L}_{\pi}+\mathcal{L}_{B\pi}+\mathcal{L}_{T\pi}. \tag{B1}$$

The standard octet and decuplet Lagrangians are given with an additional coupling to an SU(3) flavor singlet state. For clarity we label the octet and singlet parts of the meson matrix, A:

$$\mathcal{L}_{B\pi}=i\mathrm{tr}(\bar{B}v\cdot\mathcal{D}B)+2D\mathrm{tr}(\bar{B}S^{\mu}\{A_{\mu}^{oct},B\})+2F\mathrm{tr}(\bar{B}S^{\mu}[A_{\mu}^{oct},B])+2\mu b_{D}\mathrm{tr}(\bar{B}\{\mathcal{M}^{+},B\})+2\mu b_{F}\mathrm{tr}(\bar{B}[\mathcal{M}^{+},B])$$
$$+2\mu b_{0}\mathrm{tr}(\bar{B}B)\mathrm{tr}(\mathcal{M}^{+})+2g_{s}\mathrm{tr}(\bar{B}S^{\mu}B)\mathrm{tr}(A_{\mu}^{sin}), \tag{B2}$$

$$\mathcal{L}_{T\pi}=-i\bar{T}^{\nu}(v\cdot\mathcal{D})T_{\nu}+\Delta M\bar{T}^{\nu}T_{\nu}+2\mathcal{H}\bar{T}^{\nu}S^{\mu}A_{\mu}^{oct}T_{\nu}+\mathcal{C}(\bar{T}^{\nu}A_{\nu}^{oct}B+\bar{B}A_{\nu}^{oct}T^{\nu})+c\bar{T}^{\nu}\mathcal{M}^{+}T_{\nu}-\bar{\sigma}\bar{T}^{\nu}T_{\nu}\mathrm{tr}(\mathcal{M}^{+})$$
$$+2g_{s}'\bar{T}^{\nu}S^{\mu}T_{\nu}\mathrm{tr}(A_{\mu}^{sin}). \tag{B3}$$

The new parameters, g_s and g_s', describe couplings of the flavor singlet η' to baryon octet and decuplet states respectively. Within full QCD the single vertex has two topologically different quark flow diagrams as illustrated by the left and right-hand vertices of Fig. 1(a). The left is that of a $q\bar{q}$ insertion on one of the valence quark lines and the right is a pure gluonic coupling through a hairpin-style $q\bar{q}$ annihilation. The total coupling is a sum of these two contributions. Denoting the hairpin vertex coupling by γ_{QCD} and γ'_{QCD} for octet and decuplet baryons respectively we have

$$g_s=\frac{1}{\sqrt{6}}g_{\eta' NN}+\gamma_{\mathrm{QCD}}, \tag{B4}$$

$$g_s'=\frac{1}{\sqrt{6}}g_{\eta'\Delta\Delta}+\gamma'_{\mathrm{QCD}}. \tag{B5}$$

The first of these interactions, $g_{\eta' NN}$ ($g_{\eta'\Delta\Delta}$) is related to the axial couplings by SU(6) phenomenology. We take the standard approach and assign

$$g_{\eta' NN}=\sqrt{2}g_{\eta NN}=\sqrt{\frac{2}{3}}(3F-D), \tag{B6}$$

$$g_{\eta'\Delta\Delta}=\sqrt{2}g_{\eta\Delta\Delta}=\sqrt{\frac{2}{3}}\mathcal{H}. \tag{B7}$$

The effective chiral Lagrangian of quenched QCD is [23]

$$\mathcal{L}^{(Q)}=\mathcal{L}_{\Phi}^{(Q)}+\mathcal{L}_{\mathcal{B}\Phi}^{(Q)}+\mathcal{L}_{\mathcal{T}\Phi}^{(Q)}, \tag{B8}$$

where meson and baryon states are now understood to be constructed of ordinary quarks and bosonic quarks. The general Lagrangian for the heavy fields can be written in terms of the rank-3 tensor fields as defined in Ref. [23], $\mathcal{B}$ and $\mathcal{T}$,

$$\mathcal{L}_{\mathcal{B}\Phi}^{(Q)}=i(\bar{\mathcal{B}}v\cdot\mathcal{D}\mathcal{B})+2\alpha(\bar{\mathcal{B}}S^{\mu}\mathcal{B}A_{\mu})+2\beta(\bar{\mathcal{B}}S^{\mu}A_{\mu}\mathcal{B})$$
$$+2\gamma_{s}(\bar{\mathcal{B}}S^{\mu}\mathcal{B})\mathrm{str}(A_{\mu})+\alpha_{M}(\bar{\mathcal{B}}\mathcal{B}\mathcal{M}^{+})+\beta_{M}(\bar{\mathcal{B}}\mathcal{M}^{+}\mathcal{B})$$
$$+\sigma(\bar{\mathcal{B}}\mathcal{B})\mathrm{str}(\mathcal{M}^{+}), \tag{B9}$$

$$\mathcal{L}_{\mathcal{T}\Phi}^{(Q)}=-i(\bar{\mathcal{T}}^{\nu}(v\cdot\mathcal{D})\mathcal{T}_{\nu})+\Delta M(\bar{\mathcal{T}}^{\nu}\mathcal{T}_{\nu})+2\mathcal{H}(\bar{\mathcal{T}}^{\nu}S^{\mu}A_{\mu}\mathcal{T}_{\nu})$$
$$-\sqrt{\frac{3}{2}}\mathcal{C}[\bar{\mathcal{T}}^{\nu}A_{\nu}\mathcal{B}+\bar{\mathcal{B}}A_{\nu}\mathcal{T}^{\nu}]+2\gamma_{s}'(\bar{\mathcal{T}}^{\nu}S^{\mu}\mathcal{T}_{\nu})\mathrm{str}(A_{\mu})$$
$$+c\bar{\mathcal{T}}^{\nu}\mathcal{M}^{+}\mathcal{T}_{\nu}-\bar{\sigma}(\bar{\mathcal{T}}^{\nu}\mathcal{T}_{\nu})\mathrm{tr}(\mathcal{M}^{+}). \tag{B10}$$

It should be noted that the terms γ_s and γ_s' describe both types of flavor-singlet coupling, not just that arising through the hairpin alone. Similarly to Eq. (B5), in the quenched theory these can be described by

$$\gamma_{s}=\frac{1}{\sqrt{6}}g_{\eta' NN}+\gamma, \tag{B11}$$

$$\gamma_{s}'=\frac{1}{\sqrt{6}}g_{\eta'\Delta\Delta}+\gamma', \tag{B12}$$

where the terms γ and γ' now correspond to the pure hairpin couplings as used in Ref. [23]. Here we also note the terms $g_{\eta' NN}$ and $g_{\eta'\Delta\Delta}$ are unchanged in going to the quenched theory; this is consistent with the assumption that the chiral parameters F and D are unchanged between the two theories.

One can then relate the quenched chiral Lagrangian back to that of full QCD by restricting the indices on the tensor fields, $\mathcal{B}$ and $\mathcal{T}$, to those corresponding to the physical quarks. The details of this procedure are described in Ref. [23]. Performing these restrictions on the octet-baryon, quenched chiral Lagrangian [Eq. (B9)] one finds

$$\mathcal{L}^{(Q)}_{\mathcal{B}\Phi}|_R = i(\bar{\mathcal{B}}v\cdot\mathcal{D}\mathcal{B})|_R + \frac{2}{3}(2\alpha-\beta)\mathrm{tr}(\bar{B}S^\mu A_\mu B) + \frac{1}{3}(-\alpha-4\beta)\mathrm{tr}(\bar{B}S^\mu B A_\mu) + \frac{1}{3}(\alpha+4\beta+6\gamma_s)\mathrm{tr}(\bar{B}S^\mu B)\mathrm{tr}(A_\mu)$$
$$+\frac{1}{3}(2\alpha_M-\beta_M)\mathrm{tr}(\bar{B}\mathcal{M}^+B) + \frac{1}{6}(-\alpha_M-4\beta_M)\mathrm{tr}(\bar{B}B\mathcal{M}^+) + \frac{1}{6}(\alpha_M+4\beta_M+6\sigma)\mathrm{tr}(\bar{B}B)\mathrm{tr}(\mathcal{M}^+). \quad \text{(B13)}$$

Equating this with Eq. (B2) gives

$$\frac{2}{3}(2\alpha-\beta)=2D+2F, \quad \text{(B14)}$$

$$\frac{1}{3}(-\alpha-4\beta)=2D-2F, \quad \text{(B15)}$$

$$\frac{1}{3}(\alpha+4\beta+6\gamma_s)=2g_s, \quad \text{(B16)}$$

$$\frac{1}{3}(2\alpha_M-\beta_M)=2\mu b_D+2\mu b_F, \quad \text{(B17)}$$

$$\frac{1}{6}(-\alpha_M-4\beta_M)=2\mu b_D-2\mu b_F, \quad \text{(B18)}$$

$$\frac{1}{6}(\alpha_M+4\beta_M+6\sigma)=2\mu b_0. \quad \text{(B19)}$$

In extracting the flavor-singlet part, Eq. (B16) provides us with

$$\frac{1}{3}\alpha+\frac{4}{3}\beta+\sqrt{\frac{2}{3}}g_{\eta' NN}+2\gamma=\sqrt{\frac{2}{3}}g_{\eta' NN}+2\gamma_{\mathrm{QCD}}, \quad \text{(B20)}$$

and combining with Eqs. (B14), (B15) one arrives at

$$\gamma=\gamma_{\mathrm{QCD}}+D-F. \quad \text{(B21)}$$

The restrictions are much simpler for the decuplet case and one finds

$$\gamma'=\gamma'_{\mathrm{QCD}}. \quad \text{(B22)}$$

In estimating the hairpin-type couplings in full QCD one assumes that they are relatively small, $\gamma_{\mathrm{QCD}} \ll g_{\eta' NN}$, due to OZI-type suppression [43]. With analogous arguments for the decuplet, we take $\gamma_{\mathrm{QCD}}=\gamma'_{\mathrm{QCD}}=0$. We do note that the U(1) axial anomaly may be effective in overcoming the OZI rule in the case of η' couplings [33], but as we mentioned in the text the main conclusions of our present analysis are not very sensitive to the precise value of the η'-nucleon coupling.

[1] CP-PACS Collaboration, S. Aoki *et al.*, Phys. Rev. Lett. **84**, 238 (2000).
[2] UKQCD Collaboration, K.C. Bowler *et al.*, Phys. Rev. D **62**, 054506 (2000).
[3] CP-PACS Collaboration, K. Kanaya *et al.*, Nucl. Phys. B (Proc. Suppl.) **73**, 189 (1999).
[4] C. Bernard *et al.*, Phys. Rev. D **64**, 054506 (2001).
[5] CSSM Lattice Collaboration, J.M. Zanotti *et al.*, Phys. Rev. D **65**, 074507 (2002).
[6] CP-PACS Collaboration, S. Aoki *et al.*, Phys. Rev. D **60**, 114508 (1999).
[7] G.V. Dunne, A.W. Thomas, and S.V. Wright, Phys. Lett. B **531**, 77 (2002).
[8] D.B. Leinweber, A.W. Thomas, K. Tsushima, and S.V. Wright, Phys. Rev. D **61**, 074502 (2000).
[9] J.F. Donoghue, B.R. Holstein, and B. Borasoy, Phys. Rev. D **59**, 036002 (1999).
[10] D.B. Leinweber, A.W. Thomas, K. Tsushima, and S.V. Wright, Phys. Rev. D **64**, 094502 (2001).
[11] D.B. Leinweber, A.W. Thomas, and S.V. Wright, Phys. Lett. B **482**, 109 (2000).
[12] D.B. Leinweber, D.H. Lu, and A.W. Thomas, Phys. Rev. D **60**, 034014 (1999).
[13] E.J. Hackett-Jones, D.B. Leinweber, and A.W. Thomas, Phys. Lett. B **489**, 143 (2000).
[14] D.B. Leinweber and A.W. Thomas, Phys. Rev. D **62**, 074505 (2000).
[15] T.R. Hemmert and W. Weise, hep-lat/0204005.
[16] E.J. Hackett-Jones, D.B. Leinweber, and A.W. Thomas, Phys. Lett. B **494**, 89 (2000).
[17] W. Detmold, W. Melnitchouk, J.W. Negele, D.B. Renner, and A.W. Thomas, Phys. Rev. Lett. **87**, 172001 (2001).
[18] W. Detmold, W. Melnitchouk, and A.W. Thomas, EPJdirect **13**, 1 (2001).
[19] W. Detmold, W. Melnitchouk, and A.W. Thomas, Phys. Rev. D **66**, 054501 (2002).
[20] S.R. Sharpe, Phys. Rev. D **41**, 3233 (1990).
[21] S.R. Sharpe, Phys. Rev. D **46**, 3146 (1992).
[22] C.W. Bernard and M.F.L. Golterman, Phys. Rev. D **46**, 853 (1992).
[23] J.N. Labrenz and S.R. Sharpe, Phys. Rev. D **54**, 4595 (1996).
[24] D.B. Leinweber, Nucl. Phys. B (Proc. Suppl.) **109**, 45 (2002).
[25] M.J. Savage, Nucl. Phys. **A700**, 359 (2002).
[26] R.D. Young, D.B. Leinweber, A.W. Thomas, and S.V. Wright, Nucl. Phys. B (Proc. Suppl.) **109A**, 55 (2002).
[27] A.W. Thomas and W. Weise, *The Structure of the Nucleon* (Wiley-VCH, Berlin, 2001).
[28] P.A.M. Guichon, G.A. Miller, and A.W. Thomas, Phys. Lett. **124B**, 109 (1983).

[29] A.W. Thomas and K. Holinde, Phys. Rev. Lett. **63**, 2025 (1989).
[30] J. Gasser and H. Leutwyler, Ann. Phys. (N.Y.) **158**, 142 (1984).
[31] V. Bernard, N. Kaiser, and U.-G. Meissner, Int. J. Mod. Phys. E **4**, 193 (1995).
[32] J. Gasser, M.E. Sainio, and A. Svarc, Nucl. Phys. **B307**, 779 (1988).
[33] S.D. Bass, Phys. Lett. B **463**, 286 (1999).
[34] M.N. Butler, M.J. Savage, and R.P. Springer, Nucl. Phys. **B399**, 69 (1993).
[35] Y. Kuramashi, M. Fukugita, H. Mino, M. Okawa, and A. Ukawa, Phys. Rev. Lett. **72**, 3448 (1994).
[36] W. Bardeen, A. Duncan, E. Eichten, and H. Thacker, Phys. Rev. D **62**, 114505 (2000).
[37] MILC Collaboration, T. DeGrand and U.M. Heller, Phys. Rev. D **65**, 114501 (2002).
[38] MILC Collaboration, C.W. Bernard *et al.*, Phys. Rev. D **61**, 111502(R) (2000).
[39] R. Sommer, Nucl. Phys. **B411**, 839 (1994).
[40] R.G. Edwards, U.M. Heller, and T.R. Klassen, Nucl. Phys. **B517**, 377 (1998).
[41] D.B. Leinweber, R.M. Woloshyn, and T. Draper, Phys. Rev. D **43**, 1659 (1991).
[42] D.B. Leinweber and T.D. Cohen, Phys. Rev. D **47**, 2147 (1993).
[43] F.E. Close, *An Introduction to Quarks and Partons* (Academic Press, London, 1979).

Young, R.D., Leinweber, D.B., and Thomas, A.W., (2003) Convergence of chiral effective field theory.
Progress in Particle and Nuclear Physics, v. 50 (2), pp. 399-417, 2003

Physical Nucleon Properties from Lattice QCD

D. B. Leinweber, A. W. Thomas, and R. D. Young

Special Research Center for the Subatomic Structure of Matter and Department of Physics, University of Adelaide, Adelaide SA 5005, Australia

(Received 10 March 2003; published 16 June 2004)

We investigate various resummations of the chiral expansion and fit to the extremely accurate lattice QCD data for the mass of the nucleon recently obtained by the CP-PACS group. Using a variety of finite-range regulators, we demonstrate a remarkably robust chiral extrapolation of the nucleon mass. The systematic error associated with the chiral extrapolation alone is estimated to be less than 1%.

DOI: 10.1103/PhysRevLett.92.242002 PACS numbers: 12.39.Fe, 12.38.Aw, 12.38.Gc, 14.20.Dh

Hadronic physics presents fascinating theoretical challenges to the understanding of strongly interacting systems in terms of their fundamental degrees of freedom in QCD, quarks, and gluons. Lattice gauge theory [1] has so far provided the only rigorous method for solving nonperturbative QCD. We will show that recent progress within the field [2] together with advances in effective field theory (EFT) [3] now permit systematically accurate chiral extrapolations of observables, enabling the determination of the physical properties of hadrons from lattice QCD simulations, even though it is not yet feasible to make calculations at the physical quark mass.

It is now possible to make extremely accurate lattice QCD calculations of the masses of hadrons, such as the nucleon, with dynamical fermions. Indeed the CP-PACS group has just reported data with a precision of order 1% [2]. However, such precise evaluations are limited to quark masses an order of magnitude larger than those found in nature. In order to compare with experiment, which is after all one of the main aims in the field, it is therefore necessary to extrapolate in quark mass. Such an extrapolation is complicated by the unavoidable nonanalytic behavior in quark mass, which arises from Goldstone boson loops in QCD with dynamically broken chiral symmetry [4].

Early work motivated by the important role of Goldstone bosons led to the construction of chiral quark models [5], which incorporated this nonanalytic behavior. An alternative, systematic approach, designed to avoid reference to a model, involved the construction of an effective field theory to describe QCD at low energy [6]. The application to baryons has developed to the point where chiral perturbation theory (χPT) is now understood as a rigorous approach near the chiral limit [7,8].

Because it is defined as an expansion in momenta and masses about the chiral limit, χPT provides an attractive approach to the problem of quark mass extrapolation for lattice QCD. The advantages of formulating χPT with a finite-range regulator (FRR), as opposed to the commonly implemented dimensional regularization (DR), have been demonstrated by Donoghue *et al.* [9]. Early implementations of a FRR to evaluate chiral loop integrals in χPT suggested that, in the context of the extrapolation of lattice data from relatively large quark masses, FRR provides a more reliable procedure [10,11]. There has been considerable debate on whether current lattice data are within the scope of dimensionally regularized χPT or whether the form of the FRR chosen introduces significant model dependence [12]. However, this issue has now been addressed in a recent detailed study of numerous regularization schemes in χPT, both dimensional and FRR [3]. This study quantified the applicable range of the EFT and established that all of the FRR considered provided equivalent results over the range $m_\pi^2 \lesssim 0.8$ GeV^2.

Here we demonstrate that by adopting the FRR formulation of χPT one can improve its convergence properties to the point where the chiral extrapolation to the physical quark mass can be carried out with a systematic uncertainty of less than 1%. Given this remarkable result, the current errors on extrapolated quantities are dominated by the statistical errors arising from the large extrapolation distance—the lightest simulated pion mass being typically $m_\pi^2 \simeq 0.27$ GeV^2, in comparison with the physical value, 0.02 GeV^2.

In the usual formulation of effective field theory, the nucleon mass as a function of the pion mass (given that $m_\pi^2 \propto m_q$ [13]) has the formal expansion

$$M_N = a_0 + a_2 m_\pi^2 + a_4 m_\pi^4 + a_6 m_\pi^6 + \cdots + \sigma_{NN}^\pi + \sigma_{N\Delta}^\pi + \sigma_{\rm tad}^\pi. \quad (1)$$

In principle, the coefficients, a_n, can be expressed in terms of the parameters of the underlying effective Lagrangian to a given order of chiral perturbation theory. In practice, for current applications to lattice QCD, the parameters must be determined by fitting to the lattice results themselves. The additional terms, σ_{NN}^π, $\sigma_{N\Delta}^\pi$, and $\sigma_{\rm tad}^\pi$, are loop corrections involving the (Goldstone) pion, which yield the leading (LNA) and next-to-leading nonanalytic (NLNA) behavior of M_N. As these terms involve the coupling constants in the chiral limit, which are essentially model independent [14], the only additional complication they add is that the ultraviolet behavior of the loop integrals must be regulated in some way.

Traditionally, one uses dimensional regularization, which (after infinite renormalization of a_0 and a_2) leaves only the nonanalytic terms, $c_{\rm LNA} m_\pi^3$ and $c_{\rm NLNA} m_\pi^4 \times \ln(m_\pi/\mu)$, respectively. (Note that the coefficient $c_{\rm LNA}$ is the sum of contributions from the $N \to \Delta\pi$ and tadpole diagrams.) Within dimensional regularization, one then arrives at a truncated power series for the chiral expansion,

$$M_N = c_0 + c_2 m_\pi^2 + c_{\rm LNA} m_\pi^3 + c_4 m_\pi^4 + c_{\rm NLNA} m_\pi^4 \ln\frac{m_\pi}{\mu} + c_6 m_\pi^6 + \cdots, \quad (2)$$

where the bare parameters, a_i, have been replaced by the finite, renormalized coefficients, c_i. Through the chiral logarithm, one has an additional mass scale, μ, but the dependence on this is eliminated by matching c_4 to "data" (in this case, lattice QCD). We work to fourth order in the chiral expansion and include the next analytic term to compensate short-distance physics contained in the NLNA loop integrals, as suggested in Ref. [9]. Provided the series expansion in Eq. (2) is convergent over the range of values of m_π where the lattice data exist, one can then use Eq. (2) to evaluate M_N at the physical pion mass. Unfortunately, there is considerable evidence that this series is not sufficiently convergent [3,12,15–17].

In line with the implicit μ dependence of the coefficients in the familiar dimensionally regulated χPT, the systematic FRR expansion of the nucleon mass is

$$M_N = a_0^\Lambda + a_2^\Lambda m_\pi^2 + a_4^\Lambda m_\pi^4 + a_6^\Lambda m_\pi^6 + \sigma_{NN}^\pi(m_\pi, \Lambda) + \sigma_{N\Delta}^\pi(m_\pi, \Lambda) + \sigma_{\rm tad}^\pi(m_\pi, \Lambda), \quad (3)$$

where the dependence on the *shape* of the regulator is implicit. The dependence on the value of Λ and the choice of regulator are eliminated, to the order of the series expansion, by fitting the coefficients, a_n^Λ, to lattice QCD data. The clear indication of success in eliminating model dependence, and hence having found a suitable regularization method, is that the higher order coefficients (a_i^Λ, $i \geq 4$) should be small and that the renormalized coefficients, c_i, and the result of the extrapolation should be insensitive to the choice of ultraviolet regulator.

The key feature of finite-range regularization is the presence of an additional adjustable regulator parameter which provides an opportunity to suppress short-distance physics from the loop integrals of effective field theory. This short-distance physics is otherwise treated incorrectly, as the effective fields are not realized in QCD at short distances. As emphasized in Eq. (3) by the superscripts Λ, the unrenormalized coefficients of the analytic terms of the FRR expansion are regulator-parameter dependent. The large m_π behavior of the loop integrals and the residual expansion (the sum of the a_i^Λ terms) are remarkably different. Whereas the residual expansion will encounter a power divergence, the FRR loop integrals will tend to zero as a power of Λ/m_π as m_π becomes large. Thus, Λ provides an opportunity to govern the convergence properties of the residual expansion and thus the FRR chiral expansion. Since hadron masses are observed to be smooth, almost linear functions of m_π^2 for quark masses near and beyond the strange quark mass [18], it should be possible to find values for the regulator-range parameter, Λ, such that the coefficients a_4^Λ and higher are truly small. In this case, the convergence properties of the residual expansion and the loop expansion are excellent and their truncation benign [19].

In order to investigate the model dependence associated with the truncations of the chiral expansions, several regulators are considered. We evaluate the loop integrals in the heavy baryon limit

$$\sigma_{BB'}^\pi = -\frac{3}{16\pi^2 f_\pi^2} G_{BB'} \int_0^\infty dk \frac{k^4 u^2(k)}{\omega(k)[\omega_{BB'} + \omega(k)]}, \quad (4)$$

$$\sigma_{\rm tad}^\pi = -\frac{3}{16\pi^2 f_\pi^2} c_2 m_\pi^2 \left\{ \int_0^\infty dk \left(\frac{2k^2 u^2(k)}{\sqrt{k^2 + m_\pi^2}} \right) - t_0 \right\}, \quad (5)$$

taking $u(k)$ to be either a sharp cutoff, a dipole, a monopole, or finally a Gaussian. These regulators have very different shapes, with the only common feature being that they suppress the integrand for momenta greater than Λ. In Eq. (4) we have $G_{NN} = g_A^2$ (with $g_A = 1.26$) and $G_{N\Delta} = 16 g_A^2/9$ (to reproduce the empirical width of the Δ resonance). In addition, $\omega(k) = \sqrt{k^2 + m_\pi^2}$, $\omega_{NN} = 0$, and $\omega_{N\Delta} = 292$ MeV, the physical Δ-N mass splitting. In Eq. (5) t_0, defined such that the term in braces vanishes at $m_\pi = 0$, is a local counter term introduced in FRR to ensure a linear relation for the renormalization of c_2.

In addition, we also consider the case where Eq. (2) is modified to maintain the correct branch-point (BP) structure at $m_\pi = \omega_{N\Delta}$ [20], in particular,

$$\sigma_{N\Delta}^\pi = -\frac{3}{16\pi^2 f_\pi^2} G_{N\Delta} \left\{ \frac{1}{4}(2\Delta^3 - 3m^2\Delta) \log\left(\frac{m^2}{\mu^2}\right) - \frac{1}{2}(\Delta^2 - m^2)^{3/2} \times \log\left(\frac{\Delta - \sqrt{\Delta^2 - m^2}}{\Delta + \sqrt{\Delta^2 - m^2}} \right) \right\}. \quad (6)$$

One can now compare the expansion about the chiral limit for these six different regularization schemes in order to assess their rate of convergence. It turns out that all the FRR expansions precisely describe the dimensional regularization expansion over the range $m_\pi^2 \in (0, 0.7)$ GeV^2. Furthermore, the smooth, FRR formulations are consistent with each other, for the renormalized chiral coefficients, $c_{0,2,4}$, to an extraordinarily precise level [3]. This ensures a systematically accurate extrapolation to the regime of physical quark masses.

For this study we use recent precision nucleon mass data obtained in lattice QCD by CP-PACS [2]. Simulations are performed using the mean-field improved clover fermion action with the Iwasaki gluon

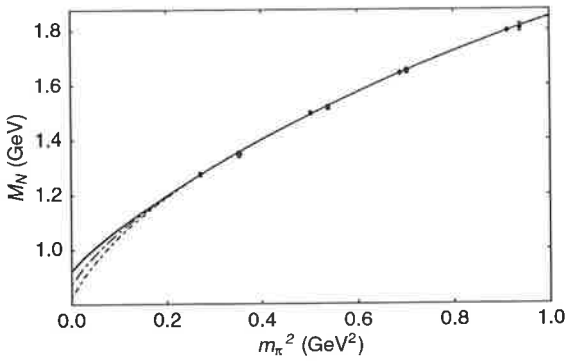

FIG. 1. Fits to lattice data for various ultraviolet regulators. The sharp cutoff, monopole, dipole, and Gaussian cases are depicted by solid lines, *indistinguishable* on this plot. The dimensional regularized forms are illustrated by the dash-dotted curves, with the correct branch point corresponding to the higher curve. Lattice data are from Ref. [2].

action, known to provide small scaling violations. We choose the largest volumes at the two smallest lattice spacings [21] such that the results are good approximations to the continuum theory. These data are used to determine the unknown parameters, a_0–a_6, in Eq. (3) for each choice of regularization. Only in the naive, dimensionally regulated form, i.e., without the $N \to \Delta\pi$ branch structure of Eq. (6), do the a_i coincide with the c_i of Eq. (2). It is only the extreme accuracy of the data which makes the determination of as many as four parameters possible.

Figure 1 shows the resulting fits to the lattice data over the range $m_\pi^2 \in (0, 1.0)\,\mathrm{GeV}^2$, with the corresponding parameters given in Table I. It is remarkable that all four curves based on FRR are indistinguishable on this plot. Furthermore, we see from Table I that the coefficient of m_π^4 in all of those cases is quite small—an order of magnitude smaller than the dimensionally regularized forms. Similarly, the FRR coefficients of m_π^6 are again much smaller than their DR counterparts. This indicates that the residual series, involving a_i, is converging when the chiral loops are evaluated with a FRR.

TABLE I. Bare, unrenormalized, parameters extracted from the fits to lattice data displayed in Fig. 1. All quantities are in units of appropriate powers of GeV and $\mu = 1$ GeV in Eq. (2). Dim. stands for dimensional and BP for the branch-point form defined in Eq. (6).

Regulator	a_0	a_2	a_4	a_6	Λ	χ^2/dof
Dim. regulator	0.827	3.58	3.63	−0.711	⋯	0.43
Dim. regulator (BP)	0.792	4.15	8.92	0.384	⋯	0.41
Sharp Cutoff	1.06	1.47	−0.554	0.116	0.4	0.40
Monopole	1.74	1.64	−0.485	0.085	0.5	0.40
Dipole	1.30	1.54	−0.492	0.089	0.8	0.40
Gaussian	1.17	1.48	−0.504	0.095	0.6	0.40

TABLE II. Renormalized expansion coefficients in the chiral limit obtained from various regulator fits to lattice data. (All quantities are in units of appropriate powers of GeV.) Errors are statistical in origin arising from lattice data. Deviations in the central values indicate systematic errors associated with the chiral extrapolation.

Regulator	c_0	c_2	c_4
Dim. regulator	0.827(120)	3.58(50)	3.6(15)
Dim. regulator (BP)	0.875(120)	3.14(50)	7.2(15)
Sharp cutoff	0.923(130)	2.61(66)	15.3(16)
Monopole	0.923(130)	2.45(67)	20.5(30)
Dipole	0.922(130)	2.49(67)	18.9(29)
Gaussian	0.923(130)	2.48(67)	18.3(29)

As explained by Donoghue *et al.* [9], one can combine the order $m_\pi^{0,2,4,\ldots}$ terms from the self-energies with the "bare" expansion parameters, $a_{0,2,4,\ldots}$, to obtain physically meaningful renormalized coefficients. These are shown in Table II, in comparison with the corresponding DR coefficients found using Eq. (2). Details of this renormalization procedure are given in Ref. [3]. The degree of consistency between the best-fit values found using all choices of FRR is remarkably good. On the other hand, DR significantly underestimates c_4. We can understand the problem very simply; it is not possible to accurately reproduce the necessary $1/m_\pi^2$ behavior of the chiral loops (for $m_\pi > \Lambda$) with a third order polynomial in m_π^2.

It is clear that the use of an EFT with a FRR enables one to make an accurate extrapolation of the nucleon mass as a function of the quark mass. Although minimal deviation is seen between the best-fit curves, we need to determine how well these curves are in fact constrained by the statistical uncertainties of the lattice data. As all data points are statistically independent, the one-sigma deviation from the best-fit curve is defined by the region for $(\chi^2 - \chi^2_{\mathrm{min}})/\mathrm{dof} < 1$. We use a standard χ^2 measure, weighted by the squared error of the simulated data point, and χ^2_{min} corresponds to the optimum fit to the data.

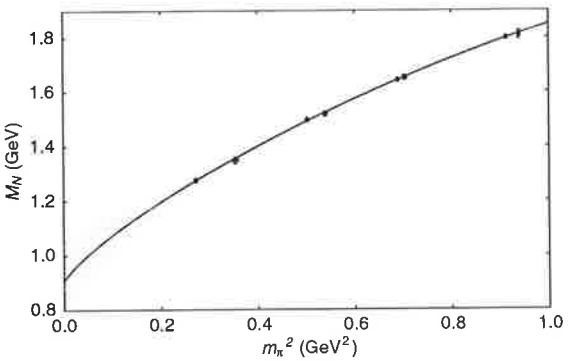

FIG. 2. Error analysis for the extraction of the nucleon mass using a dipole regulator. The shaded region corresponds to the region allowed within the present statistical errors.

TABLE III. The nucleon mass, m_N (GeV), and the sigma commutator, σ_N (MeV), extrapolated to the physical pion mass obtained in a NLNA (fourth order) chiral expansion. Convergence of the expansion is indicated by the nucleon mass obtained in an analysis where we retain only the LNA (third order) behavior.

	LNA	NLNA	
Regulator	m_N	m_N	σ_N
Dim. regulator	0.784	0.884 ± 0.103	50.3 ± 10.0
Dim. regulator (BP)	0.784	0.923 ± 0.103	42.7 ± 10.0
Sharp cutoff	0.968	0.961 ± 0.116	34.0 ± 13.0
Monopole	0.964	0.960 ± 0.116	33.0 ± 13.0
Dipole	0.963	0.959 ± 0.116	33.3 ± 13.0
Gaussian	0.966	0.960 ± 0.116	33.2 ± 13.0

We show the one-sigma variation from the best-fit dipole curve by the shaded region in Fig. 2. The primary source of the large error band is the large extrapolation distance. It is clear that a simulated point at a pion mass, $m_\pi^2 \sim 0.1$ GeV^2, would greatly reduce the statistical error in the extrapolation. The extrapolated values for the nucleon mass are shown in Table III [25]. It is especially interesting to observe the very small difference between the physical nucleon masses obtained with each FRR when we go from LNA to NLNA, i.e., when the effect of the Δ is included. (The change is typically a few MeV for a FRR but more than 100 MeV for DR.) Once again the convergence properties of the FRR expansion are remarkable.

To summarize, we have shown that the extremely precise dynamical simulation data from CP-PACS permit one to determine four parameters in the chiral extrapolation formulas, Eqs. (2) and (3). Whereas the former (involving dimensional regularization) does not appear to be convergent over the required mass range, the improved convergence properties of the finite-range regularized expansion yield an excellent description of the data over the full mass range, regardless of the functional form chosen for the vertex regulator. Table III summarizes the resulting values of the physical nucleon mass and sigma commutator. The systematic error in the chiral extrapolation, based upon a smooth FRR, is less than 1% for the nucleon mass and within 2% for the sigma commutator. We note also that the systematic uncertainty in the determination of the low energy constant, c_0, is less than 1%, while for c_2 it is at the level of a few percent. With the issue of chiral extrapolation addressed, there is an urgent need for high precision lattice QCD simulations at $m_\pi^2 \sim 0.1$ GeV^2 in order to reduce the present statistical error on the extrapolation. Such simulations should be feasible with the new generation of computers dedicated to lattice QCD currently under construction.

We thank M. Birse, J. McGovern, and S.V. Wright for helpful conversations. This work was supported by the Australian Research Council.

[1] K. G. Wilson, Phys. Rev. D **10**, 2445 (1974).
[2] CP-PACS, A. Ali Khan *et al.*, Phys. Rev. D **65**, 054505 (2002).
[3] R. D. Young, D. B. Leinweber, and A.W. Thomas, Prog. Part. Nucl. Phys. **50**, 399 (2003).
[4] H. Pagels, Phys. Rep. **16**, 219 (1975).
[5] A.W. Thomas, Adv. Nucl. Phys. **13**, 1 (1984); S. Theberge, G. A. Miller, and A.W. Thomas, Can. J. Phys. **60**, 59 (1982).
[6] S. Weinberg, Physica (Amsterdam) **96A**, 327 (1979).
[7] J. Gasser, M. E. Sainio, and A. Svarc, Nucl. Phys. **B307**, 779 (1988).
[8] V. Bernard, N. Kaiser, and U.-G. Meissner, Int. J. Mod. Phys. E **4**, 193 (1995).
[9] J. F. Donoghue, B. R. Holstein, and B. Borasoy, Phys. Rev. D **59**, 036002 (1999).
[10] D. B. Leinweber, A.W. Thomas, K. Tsushima, and S.V. Wright, Phys. Rev. D **61**, 074502 (2000).
[11] R. D. Young *et al.*, Phys. Rev. D **66**, 094507 (2002).
[12] C. Bernard *et al.*, Nucl. Phys. (Proc. Suppl.) **B119**, 170 (2003).
[13] M. Gell-Mann, R. J. Oakes, and B. Renner, Phys. Rev. **175**, 2195 (1968).
[14] L.-F. Li and H. Pagels, Phys. Rev. Lett. **26**, 1204 (1971).
[15] A.W. Thomas, Nucl. Phys. (Proc. Suppl.) **B119**, 50 (2003).
[16] S.V. Wright, Ph.D. thesis, University of Adelaide, 2002.
[17] T. Hatsuda, Phys. Rev. Lett. **65**, 543 (1990).
[18] W. Detmold *et al.*, Pramana **57**, 251 (2001).
[19] Note that Λ is not selected to approximate the higher order terms of the chiral expansion. These terms simply sum to zero in the region of large quark mass, and the details of exactly how each of the terms enter the sum are largely irrelevant.
[20] M. K. Banerjee and J. Milana, Phys. Rev. D **54**, 5804 (1996).
[21] We employ the UKQCD method [22] to set the physical scale, for each quark mass, via the Sommer scale $r_0 = 0.5$ fm [23,24].
[22] UKQCD, C. R. Allton *et al.*, Phys. Rev. D **60**, 034507 (1999).
[23] R. Sommer, Nucl. Phys. **B411**, 839 (1994).
[24] R. G. Edwards, U. M. Heller, and T. R. Klassen, Nucl. Phys. **B517**, 377 (1998).
[25] Our study has focused on the systematic errors associated with chiral extrapolation, while those arising from finite lattice spacing and volume remain to be quantified.

PHYSICAL REVIEW D 69, 115006 (2004)

Limits on variations of the quark masses, QCD scale, and fine structure constant

V. V. Flambaum
Institute for Advanced Study, Einstein Drive, Princeton, New Jersey 08540, USA
and School of Physics, The University of New South Wales, Sydney NSW 2052, Australia

D. B. Leinweber, A. W. Thomas, and R. D. Young
Special Research Centre for the Subatomic Structure of Matter and Department of Physics, University of Adelaide, Adelaide SA 5005, Australia

(Received 10 February 2004; published 2 June 2004)

We perform calculations of the dependence of nuclear magnetic moments on quark masses and obtain limits on the variation of the fine structure constant α and (m_q/Λ_{QCD}) from recent measurements of hydrogen hyperfine (21 cm) and molecular rotational transitions in quasar absorption systems, atomic clock experiments with hyperfine transitions in H, Rb, Cs, Yb^+, Hg^+, and optical transition in Hg^+. Experiments with Cd^+, deuterium/hydrogen, molecular SF_6, and Zeeman transitions in $^3He/Xe$ are also discussed.

DOI: 10.1103/PhysRevD.69.115006 PACS number(s): 06.20.Jr, 06.30.Ft, 12.10.Dm

I. INTRODUCTION

Interest in the temporal and spatial variation of major constants of physics has been recently revived by astronomical data which seem to suggest a variation of the electromagnetic constant $\alpha=e^2/\hbar c$ at the 10^{-5} level for the time scale 10 billion years, see Ref. [1] (a discussion of other limits can be found in the review [2] and references therein). However, an independent experimental confirmation is needed.

The hypothetical unification of all interactions implies that the variation of the electromagnetic interaction constant α should be accompanied by the variation of masses and the strong interaction constant. Specific predictions need a model. For example, the grand unification model discussed in Ref. [3] predicts that the quantum chromodynamic (QCD) scale Λ_{QCD} (defined as the position of the Landau pole in the logarithm for the running strong coupling constant) is modified as follows: $\delta\Lambda_{QCD}/\Lambda_{QCD}\approx 34\ \delta\alpha/\alpha$. The variation of quark and electron masses in this model is given by $\delta m/m \sim 70\ \delta\alpha/\alpha$. This gives an estimate for the variation of the dimensionless ratio

$$\frac{\delta(m/\Lambda_{QCD})}{(m/\Lambda_{QCD})}\sim 35\frac{\delta\alpha}{\alpha}. \tag{1}$$

This result is strongly model dependent (for example, the coefficient may be an order of magnitude smaller and even of opposite sign [4]). However, the large coefficients in these expressions are generic for grand unification models, in which modifications come from high-energy scales: they appear because the running strong-coupling constant and Higgs constants (related to mass) run faster than α. This means that if these models are correct the variation of masses and the strong interaction scale may be easier to detect than the variation of α.

One can only measure the variation of dimensionless quantities and therefore we want to extract from the measurements the variation of the dimensionless ratio m_q/Λ_{QCD}–where m_q is the quark mass (with the dependence on the renormalization point removed). A number of limits on the variation of m_q/Λ_{QCD} have been obtained recently from consideration of big bang nucleosynthesis, quasar absorption spectra, and the Oklo natural nuclear reactor, which was active about 1.8 billion years ago [5–8] (see also Refs. [9–13]). Below we consider the limits on various combinations of the quark masses and the fine structure constant which follow from quasar absorption radio spectra and laboratory atomic clock comparisons. Laboratory limits with a time base of the order 1 yr are especially sensitive to oscillatory variations of fundamental constants. A number of relevant measurements have been performed already and even larger numbers have been started or are planned. The increase in precision is happening very fast.

It has been pointed out by Karshenboim [14] that measurements of ratios of hyperfine structure intervals in different atoms are sensitive to any variation of nuclear magnetic moments. First rough estimates of the dependence of nuclear magnetic moments on m_q/Λ_{QCD} and limits on the variation of this ratio with time were obtained in Ref. [5]. Using H, Cs, and Hg^+ measurements [15,16], we obtained a limit on the variation of m_q/Λ_{QCD} of about 5×10^{-13} per year. Below we calculate the dependence of nuclear magnetic moments on m_q/Λ_{QCD} and obtain the limits from recent atomic clock experiments with hyperfine transitions in H, Rb, Cs, Yb^+, Hg^+, and the optical transition in Hg^+. It is convenient to assume that the strong interaction scale Λ_{QCD} does not vary, so we will speak about the variation of masses (this means that we measure masses in units of Λ_{QCD}). We shall restore the explicit appearance of Λ_{QCD} in the final answers.

The hyperfine structure constant can be presented in the following form:

$$A=\text{const}\times\left(\frac{m_e e^4}{\hbar^2}\right)[\alpha^2 F_{rel}(Z\alpha)]\left(\mu\frac{m_e}{m_p}\right). \tag{2}$$

The factor in the first set of brackets is an atomic unit of energy. The second "electromagnetic" set of brackets determines the dependence on α. An approximate expression for

the relativistic correction factor (Casimir factor) for an s-wave electron is the following:

$$F_{rel}=\frac{3}{\gamma(4\gamma^2-1)}, \tag{3}$$

where $\gamma=\sqrt{1-(Z\alpha)^2}$ and Z is the nuclear charge. Variation of α leads to the following variation of F_{rel} [15]:

$$\frac{\delta F_{rel}}{F_{rel}}=K\frac{\delta\alpha}{\alpha}, \tag{4}$$

$$K=\frac{(Z\alpha)^2(12\gamma^2-1)}{\gamma^2(4\gamma^2-1)}. \tag{5}$$

More accurate numerical many-body calculations [17] of the dependence of the hyperfine structure on α have shown that the coefficient K is slightly larger than that given by this formula. For Cs ($Z=55$) $K=0.83$ (instead of 0.74), for Rb $K=0.34$ (instead of 0.29), and finally for Hg^+ $K=2.28$ (instead of 2.18).

The last set of brackets in Eq. (2) contains the dimensionless nuclear magnetic moment μ [i.e., the nuclear magnetic moment $M=\mu(e\hbar/2m_pc)$], electron mass m_e and proton mass m_p. We may also include a small correction arising from the finite nuclear size. However, its contribution is insignificant.

Recent experiments measured the time dependence of the ratios of the hyperfine structure intervals of $^{199}Hg^+$ and H [15], ^{133}Cs and ^{87}Rb [18], and the ratio of the optical frequency in Hg^+ to the hyperfine frequency of ^{133}Cs [20]. In the ratio of two hyperfine structure constants for different atoms' time dependence may appear from the ratio of the factors F_{rel} (depending on α) as well as from the ratio of nuclear magnetic moments (depending on m_q/Λ_{QCD}). Magnetic moments in a single-particle approximation (one unpaired nucleon) are

$$\mu=[g_s+(2j-1)g_l]/2 \tag{6}$$

for $j=l+1/2$,

$$\mu=\frac{j}{2(j+1)}[-g_s+(2j+3)g_l] \tag{7}$$

for $j=l-1/2$. Here the orbital g factors are $g_l=1$ for a valence proton and $g_l=0$ for a valence neutron. The present values of the spin g factors g_s are $g_p=5.586$ for protons and $g_n=-3.826$ for neutrons. They depend on m_q/Λ_{QCD}. The light quark masses are only about 1% of the nucleon mass [$m_q=(m_u+m_d)/2\approx 5$ MeV] and the nucleon magnetic moment remains finite in the chiral limit, $m_u=m_d=0$. Therefore one might think that the corrections to g_s arising from the finite quark masses would be very small. However, through the mechanism of spontaneous chiral symmetry breaking, which leads to contributions to hadron properties from Goldstone boson loops, one may expect some enhancement of the effect of quark masses [19]. The natural framework for discussing such corrections is chiral perturbation theory and we discuss these chiral corrections next.

II. CHIRAL PERTURBATION THEORY RESULTS FOR NUCLEON MAGNETIC MOMENTS AND MASSES

In recent years there has been tremendous progress in the calculation of hadron properties using lattice QCD. Moore's Law, in combination with sophisticated algorithms, means that one can now make extremely accurate calculations for light quark masses (m_q) larger than 50 MeV. However, in order to compare with experimental data, it is still necessary to extrapolate quite a long way as a function of quark mass. This extrapolation is rendered nontrivial by the spontaneous breaking of chiral symmetry in QCD, which leads to Goldstone boson loops and, as a direct consequence, nonanalytic behavior as a function of quark mass [21,22]. Fortunately the most important nonanalytic contributions are model independent, providing a powerful constraint on the extrapolation procedure.

In the past few years the behavior of hadron properties as a function of quark mass has been studied over a much wider range than one needs for the present purpose [22–28]. One can therefore apply the successful extrapolation formulas developed in the context of lattice QCD with considerable confidence.

The key qualitative feature learned from the study of lattice data is that Goldstone boson loops are strongly suppressed once the Compton wavelength of the boson is smaller than the source. Inspection of lattice data for a range of observables, from masses to charge radii and magnetic moments, reveals that the relevant mass scale for this transition is $m_q\sim 50$ MeV—i.e., $m_\pi\sim 400$–500 MeV [22,29]. The challenge of chiral extrapolation is therefore to incorporate the correct, model independent nonanalytic behavior dictated by chiral symmetry while ensuring excellent convergence properties of the chiral expansion in the large mass region, as well as maintaining the model independence of the results of the extrapolation. Considerable study of this problem has established that the use of a finite range regulator (FRR) fulfills all of these requirements [30–32]. Indeed, in the case of the mass of the nucleon, it has been shown that the extrapolation from $m_\pi^2\sim 0.25$ GeV^2 to the physical pion mass—a change of m_q by a factor of 10—can be carried out with a systematic error less than 1% [31]. In the following we apply this same method to calculate the change in the nucleon mass, corresponding to quark mass changes at the level of 0.1% or less, as required in the present context.

A. Variation of the nucleon mass with quark mass

The expansion for the mass of the nucleon given in Refs. [31,32] is

$$M_N=a_0+a_2m_\pi^2+a_4m_\pi^4+a_6m_\pi^6+\sigma_{N\pi}+\sigma_{\Delta\pi}+\sigma_{\rm tad}, \tag{8}$$

where the chiral loops which given rise, respectively, to the leading and next-to-leading nonanalytic (LNA and NLNA) behavior are

$$\sigma_{N\pi} = -\frac{3}{32\pi f_\pi^2} g_A^2 I_M(m_\pi, \Delta_{NN}, \Lambda), \tag{9}$$

$$\sigma_{\Delta\pi} = -\frac{3}{32\pi f_\pi^2}\frac{32}{25} g_A^2 I_M(m_\pi, \Delta_{N\Delta}, \Lambda), \tag{10}$$

$$\sigma_{\rm tad} = -\frac{3}{16\pi^2 f_\pi^2} c_2 m_\pi^2 I_T(m_\pi, \Lambda), \tag{11}$$

and the relevant integrals are defined (in heavy baryon approximation) as

$$I_M(m_P, \Delta_{BB'}, \Lambda) = \frac{2}{\pi}\int_0^\infty dk \frac{k^4 u^2(k,\Lambda)}{\omega_k(\Delta_{BB'} + \omega_k)}, \tag{12}$$

$$I_T(m_\pi, \Lambda) = \int_0^\infty dk \left(\frac{2k^2 u^2(k)}{\sqrt{k^2 + m_\pi^2}}\right) - t_0, \tag{13}$$

with $\omega_k = \sqrt{k^2 + m_P^2}$ and $\Delta_{BB'}$ the relevant baryon mass difference (i.e., $M_{B'} - M_B$). We take the Δ–N mass splitting, $\Delta = M_\Delta - M_N$, to have its physical value (0.292 GeV), while $g_A = 1.26$. The regulator function $u(k,\Lambda)$ is taken to be a dipole with mass $\Lambda = 0.8$ GeV. In Eq. (13) t_0, defined such that I_T vanishes at $m_\pi = 0$, is a local counter term introduced in FRR to ensure a linear relation for the renormalization of c_2.

The model independence of the expansion given in Eq. (8) is ensured by fitting the unknown coefficients to the physical nucleon mass and lattice data from the CP-PACS Collaboration [33], yielding $a_0 = 1.22$, $a_2 = 1.76$, $a_4 = -0.829$, $a_6 = 0.260$ (with all parameters expressed in the appropriate powers of GeV). With these parameters fixed one can evaluate the rate of change of the mass of the nucleon with quark or pion mass at the physical pion mass:

$$m_q \frac{\partial}{\partial m_q} M_N = m_\pi^2 \frac{\partial}{\partial m_\pi^2} M_N = 0.035 \text{ GeV}, \tag{14}$$

a quantity commonly known as the pion-nucleon sigma commutator. Using Eq. (14) one finds the relationship (in terms of dimensionless quantities)

$$\frac{\delta M_N}{M_N} = \frac{m_\pi^2}{M_N}\frac{\partial M_N}{\partial m_\pi^2}\frac{\delta m_q}{m_q} \tag{15}$$

$$= 0.037 \frac{\delta m_q}{m_q}. \tag{16}$$

The extension of this procedure to the effect of a variation in the strange quark mass is similar, but one must include the variation arising from η-nucleon loops, as well as kaon loops with intermediate Σ or Λ baryons,

$$\sigma_{N\Sigma}^K + \sigma_{N\Lambda}^K + \sigma_{NN}^\eta. \tag{17}$$

These contributions can be expressed as

$$\sigma_{BB'}^P = -\frac{3}{32\pi f_\pi^2} G_{BB'}^P I_M(m_P, \Delta_{BB'}, \Lambda) \tag{18}$$

with $G_{BB'}^P$ the associated coupling squared. Once again we select the dipole regulator:

$$u(k,\Lambda) = \left(\frac{\Lambda^2}{\Lambda^2 + k^2}\right)^2. \tag{19}$$

For the relevant diagrams, $N \to \Sigma K$, $N \to \Lambda K$, and $N \to N\eta$, we have

$$G_{N\Sigma}^K = \frac{1}{3}(D-F)^2,$$

$$G_{N\Lambda}^K = \frac{1}{9}(3F+D)^2,$$

$$G_{NN}^\eta = \frac{1}{9}(3F-D)^2, \tag{20}$$

where we take $F = 0.50$ and $D = 0.76$. We use the Gell-Mann–Oakes–Renner relation in the SU(2) chiral limit to relate the variation of the kaon mass in the chiral SU(2) limit, $\tilde{m}_K = \sqrt{\mu_K^2 - \frac{1}{2}\mu_\pi^2} = 0.484$ GeV (with $\mu_{\pi\{K\}}$, the physical pion{kaon} mass), to the variation of the strange quark mass ($\delta\tilde{m}_K^2/\tilde{m}_K^2 = \delta m_s/m_s$). Hence the variation of the nucleon mass with strange quark mass is given by

$$\frac{\delta M_N}{M_N} = \left\{\frac{\tilde{m}_K^2}{M_N}\frac{\partial}{\partial \tilde{m}_K^2}(\sigma_{N\Sigma}^K + \sigma_{N\Lambda}^K + \sigma_{NN}^\eta)\right\}\frac{\delta m_s}{m_s}. \tag{21}$$

Using the dipole regulator mass, $\Lambda = 0.8$ GeV, Eq. (21) leads to the result

$$\frac{\delta M_N}{M_N} = 0.011 \frac{\delta m_s}{m_s}. \tag{22}$$

B. Variation of proton and neutron magnetic moments with quark mass

The treatment of the mass dependence of the nucleon magnetic moments is very similar to that for the masses. Once again the loops which give rise to the LNA and NLNA behavior are evaluated with a FRR, while the smooth, analytic variation with quark mass is parametrized by fitting relevant lattice data with a finite number of adjustable constants.

For the lattice data we use the CSSM Lattice Collaboration results [34] of nucleon three-point functions. Results are obtained using established techniques in the extraction of form factor data [35]. Similar calculations have also been recently reported by the QCDSF Collaboration [28]. We use the two heaviest simulation results, $m_\pi^2 \sim 0.6$–0.7 GeV^2 [34]. These simulations were performed with the FLIC fermion action [36] on a $20^3 \times 40$ lattice at $a = 0.128$ fm.

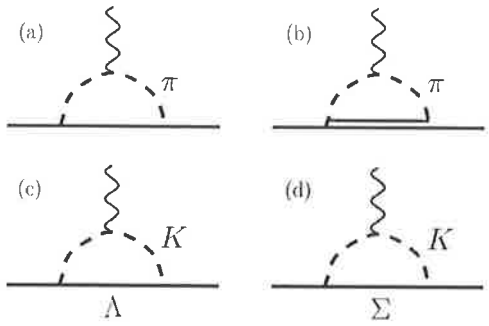

FIG. 1. Chiral corrections to the nucleon magnetic moments included in the present work.

In the magnetic moment case the formulas are a little more complicated, so we leave the details for the Appendix. Suffice it to say here that the relevant processes are shown in Fig. 1. Again we use a dipole form for the regulator with $\Lambda = 0.8$ GeV.

Having parametrized the neutron and proton magnetic moments as a function of m_π, the fractional change versus m_q or m_s is given by

$$\frac{\delta\mu}{\mu} = \left\{ \frac{m_\pi^2}{\mu} \frac{\partial\mu}{\partial m_\pi^2} \right\} \frac{\delta m_q}{m_q}, \tag{23}$$

$$\frac{\delta\mu}{\mu} = \left\{ \frac{\tilde{m}_K^2}{\mu} \frac{\partial\mu}{\partial \tilde{m}_K^2} \right\} \frac{\delta m_s}{m_s}. \tag{24}$$

The numerical results may then be summarized as

$$\frac{\delta\mu_p}{\mu_p} = -0.087\frac{\delta m_q}{m_q}, \tag{25}$$

$$\frac{\delta\mu_p}{\mu_p} = -0.013\frac{\delta m_s}{m_s}, \tag{26}$$

$$\frac{\delta\mu_n}{\mu_n} = -0.118\frac{\delta m_q}{m_q}, \tag{27}$$

$$\frac{\delta\mu_n}{\mu_n} = 0.0013\frac{\delta m_s}{m_s}, \tag{28}$$

$$\frac{\delta(\mu_p/\mu_n)}{(\mu_p/\mu_n)} = 0.031\frac{\delta m_q}{m_q}, \tag{29}$$

$$\frac{\delta(\mu_p/\mu_n)}{(\mu_p/\mu_n)} = -0.015\frac{\delta m_s}{m_s}. \tag{30}$$

III. DEPENDENCE OF ATOMIC TRANSITION FREQUENCIES ON FUNDAMENTAL CONSTANTS

Using the results of the previous section we can now use Eqs. (6), (7) to study the variation of nuclear magnetic moments. For all even Z nuclei with valence neutron (^{199}Hg, ^{171}Yb, ^{111}Cd, etc.) we obtain $\delta\mu/\mu = \delta g_n/g_n$. For ^{133}Cs we have a valence proton with $j = 7/2$, $l = 4$, and

$$\frac{\delta\mu}{\mu} = 0.110\frac{\delta m_q}{m_q} + 0.017\frac{\delta m_s}{m_s}. \tag{31}$$

For ^{87}Rb we have valence proton with $j = 3/2$, $l = 1$, and

$$\frac{\delta\mu}{\mu} = -0.064\frac{\delta m_q}{m_q} - 0.010\frac{\delta m_s}{m_s}. \tag{32}$$

As an intermediate result it is convenient to present the dependence of the ratio of the hyperfine constant A to the atomic unit of energy $E = m_e e^4/\hbar^2$ (or the energy of the $1s$-$2s$ transition in hydrogen, which is equal to $3/8E$) on a variation of the fundamental constants. We introduce a parameter V defined by the relation

$$\frac{\delta V}{V} \equiv \frac{\delta(A/E)}{A/E}. \tag{33}$$

We start from the hyperfine structure of ^{133}Cs which is used as a frequency standard. Using Eqs. (2), (31) we obtain

$$V(^{133}\mathrm{Cs}) = \alpha^{2.83}\left(\frac{m_q}{\Lambda_{QCD}}\right)^{0.110}\left(\frac{m_s}{\Lambda_{QCD}}\right)^{0.017}\frac{m_e}{m_p}. \tag{34}$$

The factor m_e/m_p will cancel out in the ratio of hyperfine transition frequencies. However, it will survive in comparison between hyperfine and optical or molecular transitions (see below). According to Eqs. (16) and (22) the relative variation of the electron to proton mass ratio can be described by the parameter

$$X(m_e/m_p) = \left(\frac{m_q}{\Lambda_{QCD}}\right)^{-0.037}\left(\frac{m_s}{\Lambda_{QCD}}\right)^{-0.011}\frac{m_e}{\Lambda_{QCD}} \tag{35}$$

which can be substituted into Eq. (34) instead of m_e/m_p. This gives an expression which is convenient to use for comparison with optical and molecular vibrational or rotational transitions

$$V(^{133}\mathrm{Cs}) = \alpha^{2.83}\left(\frac{m_q}{\Lambda_{QCD}}\right)^{0.073}\left(\frac{m_s}{\Lambda_{QCD}}\right)^{0.006}\frac{m_e}{\Lambda_{QCD}}. \tag{36}$$

The dependence on the strange quark mass is relatively weak. Therefore it may be convenient to assume that the relative variation of the strange quark mass is the same as the relative variation of the light quark masses (this assumption is motivated by the Higgs mechanism of mass generation) and to use an approximate expression $V(^{133}\mathrm{Cs}) \approx \alpha^{2.83}(m_q/\Lambda_{QCD})^{0.13}(m_e/m_p)$.

For hyperfine transition frequencies in other atoms we obtain

$$V(^{87}\mathrm{Rb}) = \alpha^{2.34}\left(\frac{m_q}{\Lambda_{QCD}}\right)^{-0.064}\left(\frac{m_s}{\Lambda_{QCD}}\right)^{-0.010}\frac{m_e}{m_p}, \tag{37}$$

$$V(^{1}\mathrm{H}) = \alpha^{2}\left(\frac{m_q}{\Lambda_{QCD}}\right)^{-0.087}\left(\frac{m_s}{\Lambda_{QCD}}\right)^{-0.013}\frac{m_e}{m_p}, \tag{38}$$

$$V(^2\mathrm{H})=\alpha^2\left(\frac{m_q}{\Lambda_{QCD}}\right)^{-0.018}\left(\frac{m_s}{\Lambda_{QCD}}\right)^{-0.045}\frac{m_e}{m_p}, \quad (39)$$

$$V(^{199}\mathrm{Hg}^+)=\alpha^{4.3}\left(\frac{m_q}{\Lambda_{QCD}}\right)^{-0.118}\left(\frac{m_s}{\Lambda_{QCD}}\right)^{0.0013}\frac{m_e}{m_p}, \quad (40)$$

$$V(^{171}\mathrm{Yb}^+)=\alpha^{3.5}\left(\frac{m_q}{\Lambda_{QCD}}\right)^{-0.118}\left(\frac{m_s}{\Lambda_{QCD}}\right)^{0.0013}\frac{m_e}{m_p}, \quad (41)$$

$$V(^{111}\mathrm{Cd}^+)=\alpha^{2.6}\left(\frac{m_q}{\Lambda_{QCD}}\right)^{-0.118}\left(\frac{m_s}{\Lambda_{QCD}}\right)^{0.0013}\frac{m_e}{m_p}. \quad (42)$$

Note that the hyperfine frequencies of all even-Z atoms where the nuclear magnetic moment is determined by a valence neutron have the same dependence on quark masses.

IV. LIMITS ON VARIATION OF FUNDAMENTAL CONSTANTS

Now we can use these results to place limits on the possible variation of the fundamental constants from particular measurements. Let us start from the measurements of quasar absorption spectra. Comparison of the atomic H 21 cm (hyperfine) transition with molecular rotational transitions [9] gave limits for the variation of $Y_g\equiv\alpha^2 g_p$. In Refs. [5,37] it was suggested that one might use these limits to estimate the variation of m_q/Λ_{QCD}. According to Eqs. (25) and (26) the relative variation of Y_g can be replaced by the relative variation of Y ($\delta Y/Y=\delta Y_g/Y_g$),

$$Y=\alpha^2\left(\frac{m_q}{\Lambda_{QCD}}\right)^{-0.087}\left(\frac{m_s}{\Lambda_{QCD}}\right)^{-0.013}. \quad (43)$$

Then the measurements in Ref. [9] lead to the following limits on the variation of Y: $\delta Y/Y=(-0.20\pm0.44)10^{-5}$ for redshift $z=0.2467$ and $\delta Y/Y=(-0.16\pm0.54)10^{-5}$ for $z=0.6847$.

The second limit corresponds to roughly $t=6$ billion years ago. There is also a limit on the variation of $X_m\equiv\alpha^2 g_p m_e/m_p$ obtained in Ref. [10]. This limit was interpreted as a limit on the variation of α or m_e/m_p. The relative variation of X_m can be replaced by the relative variation of

$$X=\alpha^2\left(\frac{m_q}{\Lambda_{QCD}}\right)^{-0.124}\left(\frac{m_s}{\Lambda_{QCD}}\right)^{-0.024}\frac{m_e}{\Lambda_{QCD}}. \quad (44)$$

The dependence on quark masses appears from both the proton g factor and the proton mass. The measurement in Ref. [10] leads to the following limit on the variation of X: $\delta X/X=(0.7\pm1.1)10^{-5}$ for $z=1.8$.

Now let us discuss the limits obtained from the laboratory measurements of the time dependence of hyperfine structure intervals. The dependence of the ratio of frequencies $A(^{133}\mathrm{Cs})/A(^{87}\mathrm{Rb})$ can be presented in the following form:

$$X(\mathrm{Cs/Rb})=\frac{V(\mathrm{Cs})}{V(\mathrm{Rb})}=\alpha^{0.49}[m_q/\Lambda_{QCD}]^{0.174}[m_s/\Lambda_{QCD}]^{0.027} \quad (45)$$

and the result of the measurement in Ref. [18] may be presented as a limit on variation of the parameter X:

$$\frac{1}{X(\mathrm{Cs/Rb})}\frac{dX(\mathrm{Cs/Rb})}{dt}=(0.2\pm7)\times10^{-16}/\mathrm{yr}. \quad (46)$$

Note that if the relation (1) were correct, the variation of $X(\mathrm{Cs/Rb})$ would be dominated by the variation of $[m_q/\Lambda_{QCD}]$. The relation (1) would give $X(\mathrm{Cs/Rb})\propto\alpha^8$.

For $A(^{133}\mathrm{Cs})/A(\mathrm{H})$ we have

$$X(\mathrm{Cs/H})=\frac{V(\mathrm{Cs})}{V(\mathrm{H})}=\alpha^{0.83}[m_q/\Lambda_{QCD}]^{0.196}[m_s/\Lambda_{QCD}]^{0.030} \quad (47)$$

and the result of the measurements in Ref. [16] may be presented as

$$\left|\frac{1}{X(\mathrm{Cs/H})}\frac{dX(\mathrm{Cs/H})}{dt}\right|<5.5\times10^{-14}/\mathrm{yr}. \quad (48)$$

For $A(^{199}\mathrm{Hg})/A(\mathrm{H})$ we have

$$X(\mathrm{Hg/H})=\frac{V(\mathrm{Hg})}{V(\mathrm{H})}\approx\alpha^{2.3}[m_q/\Lambda_{QCD}]^{-0.031}[m_s/\Lambda_{QCD}]^{0.015}. \quad (49)$$

The result of the measurement in Ref. [15] may be presented as

$$\left|\frac{1}{X(\mathrm{Hg/H})}\frac{dX(\mathrm{Hg/H})}{dt}\right|<8\times10^{-14}/\mathrm{yr}. \quad (50)$$

Note that because the dependence on masses and the strong interaction scale is very weak here, this experiment may be interpreted as a limit on the variation of α.

In Ref. [14] a limit was obtained on the variation of the ratio of hyperfine transition frequencies $^{171}\mathrm{Yb}^+/^{133}\mathrm{Cs}$ (this limit is based on the measurements of Ref. [38]). Using Eqs. (34), (41) we can present the result as a limit on $X(\mathrm{Yb/Cs})=\alpha^{0.7}[m_q/\Lambda_{QCD}]^{-0.228}[m_s/\Lambda_{QCD}]^{-0.015}$:

$$\frac{1}{X(\mathrm{Yb/Cs})}\frac{dX(\mathrm{Yb/Cs})}{dt}\approx-1(2)\times10^{-13}/\mathrm{yr}. \quad (51)$$

The optical clock transition energy $E(\mathrm{Hg})$ ($\lambda=282$ nm) in the Hg^+ ion can be presented in the following form:

$$E(\mathrm{Hg})=\mathrm{const}\times\left(\frac{m_e e^4}{\hbar^2}\right)F_{rel}(Z\alpha). \quad (52)$$

Numerical calculation of the relative variation of $E(\mathrm{Hg})$ has given [17]

$$\frac{\delta E(\mathrm{Hg})}{E(\mathrm{Hg})}=-3.2\frac{\delta\alpha}{\alpha}. \quad (53)$$

This corresponds to $V(\mathrm{Hg\ Opt})=\alpha^{-3.2}$. Variation of the ratio of the Cs hyperfine splitting $A(\mathrm{Cs})$ to this optical transition energy is described by $X(\mathrm{Opt})=V(\mathrm{Cs})/V(\mathrm{Hg\ Opt})$:

$$X(\mathrm{Opt}) = \alpha^6 \left(\frac{m_q}{\Lambda_{QCD}}\right)^{0.073} \left(\frac{m_s}{\Lambda_{QCD}}\right)^{0.006} \left(\frac{m_e}{\Lambda_{QCD}}\right). \quad (54)$$

Here we used Eq. (36) for $V(\mathrm{Cs})$. The work of Ref. [20] gives the limit on variation of this parameter:

$$\left|\frac{1}{X(\mathrm{Opt})}\frac{dX(\mathrm{Opt})}{dt}\right| < 7\times 10^{-15}/\mathrm{yr}. \quad (55)$$

Molecular vibrational transitions frequencies are proportional to $(m_e/m_p)^{1/2}$. Based on Eq. (35) we may describe the relative variation of vibrational frequencies by the parameter

$$V(\mathrm{vib}) = \left(\frac{m_q}{\Lambda_{QCD}}\right)^{-0.018} \left(\frac{m_s}{\Lambda_{QCD}}\right)^{-0.005} \left(\frac{m_e}{\Lambda_{QCD}}\right)^{0.5}. \quad (56)$$

Comparison of the Cs hyperfine standard with SF_6 molecular vibration frequencies was discussed in Ref. [39]. In this case $X(\mathrm{Cs/Vib}) = \alpha^{2.8}[m_e/\Lambda_{QCD}]^{0.5}[m_q/\Lambda_{QCD}]^{0.091}(m_s/\Lambda_{QCD})^{0.011}$.

The measurements of hyperfine constant ratios in different isotopes of the same atom depends on the ratio of magnetic moments and is therefore sensitive to m_q/Λ_{QCD}. For example, it would be interesting to measure the rate of change for hydrogen/deuterium ratio where $X(\mathrm{H/D}) = [m_q/\Lambda_{QCD}]^{-0.068}[m_s/\Lambda_{QCD}]^{0.032}$.

Walsworth has suggested that one might measure the ratio of the Zeeman transition frequencies in noble gases in order to explore the time dependence of the ratio of nuclear magnetic moments. Consider, for example ^{129}Xe/^{3}He. For ^{3}He the magnetic moment is very close to that of neutron. For other noble gases the nuclear magnetic moment is also given by the valence neutron, however, there are significant many-body corrections. For ^{129}Xe the valence neutron is in an $s_{1/2}$ state, which corresponds to the single-particle value of the nuclear magnetic moment, $\mu = \mu_n = -1.913$. The measured value is $\mu = -0.778$. The magnetic moment of the nucleus changes most efficiently through the spin-spin interaction, because the valence neutron transfers a part of its spin, $\langle s_z \rangle$, to the core protons and the proton magnetic moment is large and has the opposite sign. In this approximation $\mu = (1-b)\mu_n + b\mu_p$. This gives $b = 0.24$ and the ratio of magnetic moments $Y \equiv \mu(^{129}\mathrm{Xe})/\mu(^3\mathrm{He}) \approx 0.76 + 0.24 g_p/g_n$. Using Eqs. (25)–(28) we obtain an estimate for the relative variation of $\mu(^{129}\mathrm{Xe})/\mu(^3\mathrm{He})$, which can be presented as variation of $X = [m_q/\Lambda_{QCD}]^{-0.027}[m_s/\Lambda_{QCD}]^{0.012}$. Here again $\delta Y/Y = \delta X/X$.

Note that the accuracy of the results presented in this paper depends strongly on the fundamental constant under study. The accuracy for the dependence on α is a few percent. The accuracy for m_q/Λ_{QCD} is about 30%—being limited mainly by the accuracy of the single-particle approximation for nuclear magnetic moments. (For comparison, the estimated systematic error associated with the calculation of the effect of the quark mass variation is less than 10%.) Finally, we stress that the relation (1) between the variation of α and m/Λ_{QCD} has been used solely for purposes of illustration.

TABLE I. Chiral coefficients for various diagrams contributing to proton and neutron magnetic moments. We use SU(6) symmetry to relate the meson couplings to the $\pi N\Delta$ vertex, $\mathcal{C} = -2D$.

α	$\beta^p_{\mu\alpha}$	$\beta^n_{\mu\alpha}$
(a)	$-(F+D)^2$	$(F+D)^2$
(b)	$-\frac{2}{9}\mathcal{C}^2$	$\frac{2}{9}\mathcal{C}^2$
(c)	$-\frac{1}{6}(D+3F)^2$	0
(d)	$-\frac{1}{2}(D-F)^2$	$-(D-F)^2$

ACKNOWLEDGMENT

V.F. is grateful to C. Chardonnet, S. Karshenboim, and R. Walsworth for valuable discussions and to the Institute for Advanced Study and the Monell Foundation for hospitality and support. This work was supported by the Australian Research Council.

APPENDIX MAGNETIC MOMENTS

As explained in the text, we explicitly include the processes shown in Fig. 1, which give rise to the leading and next-to-leading nonanalytic behavior as a function of quark mass.

We describe the quark mass dependence of the magnetic moments as

$$\mu = \frac{\alpha_0}{1+\alpha_2 m_\pi^2} + M^{\mathrm{L}}, \quad (A1)$$

where M^{L} denotes the chiral loop corrections given by

$$M^{\mathrm{L}} = \chi_{\mu(a)} I_\mu(m_\pi, 0, \Lambda) + \chi_{\mu(b)} I_\mu(m_\pi, \Delta_{N\Delta}, \Lambda) + \chi_{\mu(c)} I_\mu(m_K, \Delta_{N\Lambda}, \Lambda) + \chi_{\mu(d)} I_\mu(m_K, \Delta_{N\Sigma}, \Lambda). \quad (A2)$$

The chiral coefficients of the loop integrals $\chi_{\mu\alpha}$ are given by

$$\chi_{\mu\alpha} = \beta_{\mu\alpha} \frac{M_N}{8\pi f_\pi^2} \quad (A3)$$

and are summarized in Table I [40–42]. Note that the required analytic terms in the chiral expansion to this order have been placed in a Padé approximant designed to reproduce the Dirac moment behavior of the nucleon at moderate quark mass.

The corresponding loop integral is given by

$$I_\mu(m, \Delta, \Lambda) = -\frac{4}{3\pi}\int_0^\infty dk \frac{(\Delta + 2\omega_k) k^4 u^2(k, \Lambda)}{2\omega_k^3 (\Delta + \omega_k)^2}, \quad (A4)$$

where the various terms have been defined in Sec. II. We note that in the limit where the mass splitting vanishes this integral is normalized such that the leading nonanalytic contribution is m.

With the coefficients of the loop integrals defined, we only require determination of the parameters α_0 and α_2 in Eq. (A1) to constrain the variation with quark mass. We note also that this form assumes no analytic dependence on the strange quark mass, beyond what is implicitly included in the loop diagrams (c,d). We determine $\alpha_{0,2}$ for both the proton and neutron by fitting the physical magnetic moment as well as the lattice QCD data. We fit only to the two heaviest simulation results of the CSSM Lattice Collaboration [34], $m_\pi^2 \sim 0.6$–0.7 GeV^2. These simulations were performed with the FLIC fermion action [36] on a $20^3 \times 40$ lattice at $a = 0.128$ fm. We select the heaviest two data points, where the effects of quenching are anticipated to be small [43,44].

The best fits to the physical values and the lattice data give

$$\alpha_0^p = 2.17\ \mu_N,\ \alpha_2^p = 0.817\ \text{GeV}^{-2}, \tag{A5}$$

$$\alpha_0^n = -1.33\ \mu_N,\ \alpha_2^n = 0.758\ \text{GeV}^{-2}. \tag{A6}$$

Upon renormalization of the loop diagrams, the resultant magnetic moments in the SU(2) chiral limit are given by

$$\mu_0^p = 3.48\ \mu_N,\ \text{and}\ \mu_0^n = -2.58\ \mu_N. \tag{A7}$$

We now take derivatives of Eq. (A1) at the physical pion mass to determine the variation with quark mass. In particular, we have

$$\frac{\delta\mu}{\mu} = \left\{ \frac{m_\pi^2}{\mu} \frac{d\mu}{d m_\pi^2} \right\} \frac{\delta m_q}{m_q}, \tag{A8}$$

$$\frac{\delta\mu}{\mu} = \left\{ \frac{\tilde{m}_K^2}{\mu} \frac{d\mu}{d\tilde{m}_K^2} \right\} \frac{\delta m_s}{m_s}. \tag{A9}$$

This yields the results shown in the text.

[1] J.K. Webb *et al.*, Phys. Rev. Lett. **82**, 884 (1999); **87**, 091301 (2001); M.T. Murphy, J.K. Webb, and V.V. Flambaum, Mon. Not. R. Astron. Soc. **345**, 609 (2003).

[2] J-P. Uzan, Rev. Mod. Phys. **75**, 403 (2003).

[3] P. Langacker, G. Segre, and M.J. Strassler, Phys. Lett. B **528**, 121 (2002); see also X. Calmet and H. Fritzsch, Eur. Phys. J. C **24**, 639 (2002); W.J. Marciano, Phys. Rev. Lett. **52**, 489 (1984).

[4] T. Dent, hep-ph/0305026.

[5] V.V. Flambaum and E.V. Shuryak, Phys. Rev. D **65**, 103503 (2002).

[6] K.A. Olive *et al.*, Phys. Rev. D **66**, 045022 (2002).

[7] V.F. Dmitriev and V.V. Flambaum, Phys. Rev. D **67**, 063513 (2003).

[8] V.V. Flambaum and E.V. Shuryak, Phys. Rev. D **67**, 083507 (2003).

[9] M.T. Murphy *et al.*, Mon. Not. R. Astron. Soc. **327**, 1244 (2001).

[10] L.L. Cowie and A. Songalia, Astrophys. J. **453**, 596 (1995).

[11] A.I. Shlyakhter, Nature (London) **264**, 340 (1976); T. Damour and F.J. Dyson, Nucl. Phys. **B480**, 37 (1996); Y. Fujii *et al.*, *ibid.* **B573**, 377 (2000).

[12] H. Oberhummer, R. Pichler, and A. Csoto, nucl-th/9810057.

[13] S.R. Beane and M.J. Savage, Nucl. Phys. **A713**, 148 (2003).

[14] S.G. Karshenboim, Can. J. Phys. **78**, 639 (2000).

[15] J.D. Prestage, R.L. Tjoelker, and L. Maleki, Phys. Rev. Lett. **74**, 3511 (1995).

[16] N. A. Demidov *et al.*, in *Proceedings of the 6th European Frequency and Time Forum, Noordwijk, the Netherlands*, 1992 (European Space Agency, Noordwijk, 1992), pp. 409–414; L. A. Breakiron, in *Proceedings of the 25th Annual Precise Time Interval Applications and Planning Meeting*, NASA Conference Publication No. 3267 [U.S. Naval Observatory Time Service Department (TSS1), Washington, DC, 1993], pp. 401–412.

[17] V.A. Dzuba, V.V. Flambaum, and J.K. Webb, Phys. Rev. A **59**, 230 (1999); V. A. Dzuba (private communication).

[18] H. Marion *et al.*, Phys. Rev. Lett. **90**, 150801 (2003).

[19] D.B. Leinweber, A.W. Thomas, and R.D. Young, Phys. Rev. Lett. **86**, 5011 (2001).

[20] S. Bize *et al.*, Phys. Rev. Lett. **90**, 150802 (2003).

[21] C. Bernard, S. Hashimoto, D.B. Leinweber, P. Lepage, E. Pallante, S.R. Sharpe, and H. Wittig, Nucl. Phys. B, Proc. Suppl. **119**, 170 (2003).

[22] A.W. Thomas, Nucl. Phys. B, Proc. Suppl. **119**, 50 (2003).

[23] D.B. Leinweber, A.W. Thomas, K. Tsushima, and S.V. Wright, Phys. Rev. D **61**, 074502 (2000).

[24] D.B. Leinweber, D.H. Lu, and A.W. Thomas, Phys. Rev. D **60**, 034014 (1999).

[25] T.R. Hemmert, M. Procura, and W. Weise, Nucl. Phys. **A721**, 938 (2003).

[26] T.R. Hemmert, M. Procura, and W. Weise, hep-lat/0301005.

[27] V. Bernard, T.R. Hemmert, and U.G. Meissner, Nucl. Phys. **A732**, 149 (2004).

[28] QCDSF Collaboration, M. Gockeler *et al.*, hep-lat/0303019.

[29] W. Detmold, D.B. Leinweber, W. Melnitchouk, A.W. Thomas, and S.V. Wright, Pramana, J. Phys. **57**, 251 (2001).

[30] J.F. Donoghue, B.R. Holstein, and B. Borasoy, Phys. Rev. D **59**, 036002 (1999).

[31] D.B. Leinweber, A.W. Thomas, and R.D. Young, Phys. Rev. Lett. (to be published).

[32] R.D. Young, D.B. Leinweber, and A.W. Thomas, Prog. Part. Nucl. Phys. **50**, 399 (2003).

[33] CP-PACS Collaboration, A. Ali Khan *et al.*, Phys. Rev. D **65**, 054505 (2002); **67**, 059901(E) (2003).

[34] J.M. Zanotti, D.B. Leinweber, A.G. Williams, and J.B. Zhang, Nucl. Phys. B (Proc. Suppl.) **129**, 287 (2004).

[35] D.B. Leinweber, R.M. Woloshyn, and T. Draper, Phys. Rev. D **43**, 1659 (1991).

[36] CSSM Lattice Collaboration, J.M. Zanotti *et al.*, Phys. Rev. D **65**, 074507 (2002).

[37] V.F. Dmitriev and V.V. Flambaum, Phys. Rev. D **67**, 063513 (2003).
[38] Chr. Tamm, D. Schnier, and A. Bauch, Appl. Phys. B: Lasers Opt. **60**, 19 (1995); P.T.H. Fisk, M.J. Sellar, M.A. Lawn, and C. Coles, IEEE Trans. Ultrason. Ferroelectr. Freq. Control **44**, 344 (1997); P.T.H. Fisk, Rep. Prog. Phys. **60**, 761 (1997).
[39] C. Chardonnet, Talk at ICOLS 03, Palm Cove, July (2003).
[40] S. Theberge, G.A. Miller, and A.W. Thomas, Can. J. Phys. **60**, 59 (1982); A.W. Thomas, Adv. Nucl. Phys. **13**, 1 (1984).
[41] E. Jenkins, M.E. Luke, A.V. Manohar, and M.J. Savage, Phys. Lett. B **302**, 482 (1993); **388**, 866(E) (1996).
[42] D.B. Leinweber, Phys. Rev. D **69**, 014005 (2004).
[43] R.D. Young, D.B. Leinweber, A.W. Thomas, and S.V. Wright, Phys. Rev. D **66**, 094507 (2002).
[44] R.D. Young, D.B. Leinweber, and A.W. Thomas, Nucl. Phys. B (Proc. Suppl.) **128**, 227 (2004).

PHYSICAL REVIEW D 71, 014001 (2005)

Leading quenching effects in the proton magnetic moment

R. D. Young,[1] D. B. Leinweber,[1] and A. W. Thomas[1,2]

[1]*Special Research Centre for the Subatomic Structure of Matter, and Department of Physics and Mathematical Physics, University of Adelaide, Adelaide SA 5005, Australia*

[2]*Jefferson Laboratory, 12000 Jefferson Avenue, Newport News, Virginia 23606, USA*

(Received 22 June 2004; published 3 January 2005)

We present the first investigation of the extrapolation of quenched nucleon magnetic moments in quenched chiral effective field theory. We utilize established techniques in finite-range regularization and incorporate finite-volume corrections to the relevant loop integrals. Finally, the contributions of dynamical sea quarks to the proton moment are estimated using a recently discovered phenomenological link between quenched and physical QCD.

DOI: 10.1103/PhysRevD.71.014001 PACS numbers: 12.39.Fe, 12.38.Gc

I. INTRODUCTION

Describing the quark content of nucleon structure in terms of QCD is a fundamental aim of modern nuclear physics. As an inherently nonperturbative theory, the most rigorous approach to low-energy phenomena in QCD is by numerical simulations in lattice gauge theory. Although restricted at present to the regime of quark masses exceeding those realized in nature, recent advances in effective field theory (EFT) have made it possible to accurately extract the physical nucleon mass from QCD [1].

These advances and breakthroughs in chiral effective field theory (χEFT) have their origin in the study of a range of hadron properties in QCD, including nucleon magnetic moments and charge radii [2–5], the nucleon sigma commutator [1,6,7], moments of structure functions [8–10] and the ρ-meson mass [11].

With the most detailed studies being on the extrapolation of the nucleon mass, it has been shown that the use of finite-range regularization (FRR) enables the most systematically accurate connection of effective field theory and lattice simulation results [1,12,13]. Mathematically equivalent to dimensional regularization (DR) to any finite order, FRR chiral effective field theory provides a resummation of the chiral expansion with vastly improved convergence properties. Central to FRR is the presence of a finite energy scale which may be used to optimize the convergence properties of the truncated expansion. The success of FRR-EFT is highlighted by the observation that the higher-order terms of the traditional dimensionally regulated expansion, although individually large, must sum to zero to describe lattice QCD results.

Here FRR-χEFT is applied to nucleon magnetic moments calculated in lattice QCD. In particular, we investigate the modifications required for the extrapolation of quenched simulation results. Issues with the formulation of EFT on a finite volume are also discussed. We consider the modifications to chiral-loop integrals on a finite volume and perform a fixed-volume extrapolation.

We extend a phenomenological link between quenched and dynamical baryon masses [14] to the case of magnetic moments to estimate the artifacts associated with the quenched approximation. We find that the full-QCD corrections of the quenched magnetic moments are small over a wide range of quark mass.

Finally, the convergence properties of a truncated Taylor-series expansion of the FRR results in powers of m_π are investigated. We illustrate how any moderate truncation of the series expansion is unable to connect with current lattice simulation results. The inclusion of higher-order chiral-loop corrections associated with the Δ baryon are also considered and found to be small.

II. MAGNETIC MOMENTS—QUARK MASS DEPENDENCE

In a general construction of an effective field theory for low-energy QCD, the expansion of the nucleon's magnetic moment about the chiral limit can be written as

$$\mu_B = a_0^B + a_2^B m_\pi^2 + a_4^B m_\pi^4 + \cdots \chi_{B\pi} I_\pi + \cdots. \quad (1)$$

The term $\chi_{B\pi} I_\pi$ denotes the leading nonanalytic (LNA) chiral correction to the baryon magnetic moment of Fig. 1. Coefficients of low-order nonanalytic contributions to nucleon properties are determined model-independently and are known to high precision phenomenologically [15]. For example, the LNA coefficient to the proton magnetic moment is given by

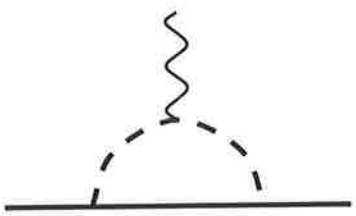

FIG. 1. Diagram providing the leading nonanalytic contribution of pions (dashed curve) to the nucleon (solid line) magnetic moment.

$$\chi_{p\pi} = -\frac{g_A^2 M_N}{8\pi f_\pi^2}. \quad (2)$$

Any extrapolation of lattice QCD simulations must incorporate this knowledge of QCD.

The analytic terms are unconstrained by chiral symmetry, and hence must be determined empirically. Lattice QCD provides an *ab initio* framework to determine these parameters from QCD.

The expression, Eq. (1), is analogous to the chiral expansion of the nucleon mass described in Refs. [1,12]. The regulator dependence of the integrals is implicit. To define the expansion one must define a regularization and renormalization scheme to remove ultraviolet divergences.

In the textbook approach to elementary field theory one commonly uses dimensional regularization to renormalize the theory. In this case, only the residue of the pion pole becomes apparent and the loop contribution is therefore given by

$$\chi_B I_\pi^{\rm DR} \to \chi_B m_\pi, \quad (3)$$

and the linear divergence of the integral is absorbed into an infinite renormalization of a_0.

Alternatively, ultraviolet divergences can be removed by suppressing loop integrals above a finite energy scale. The first systematic study of finite-range regularization in χPT was performed by Donoghue *et al.* [16]. The development of FRR-χPT in the context of lattice QCD [1,11,13,14,17] has found remarkably improved convergence properties of the chiral expansion, providing access to a much wider range of range of quark mass than the naively regularized theory [12]. FRR is therefore best suited to the problem of chiral extrapolation, where the systematic error in the extrapolation of modern lattice simulations is of order 1% [1].

Using FRR, the loop integral, I_π, in the heavy-baryon limit can be expressed as

$$I_\pi = -\frac{4}{3\pi}\int dk \frac{k^4 u^2(k)}{\omega_k^4}, \quad (4)$$

where $\omega_k = \sqrt{k^2 + m_\pi^2}$ and $u(k)$ is the ultraviolet regulator.

Expansion of the loop contributions as a power series enables one to obtain the renormalized chiral expansion parameters, where each of the analytic terms in Eq. (1) are renormalized by a finite amount [12,16]. For example, using a dipole regulator, $u(k) = (1 + k^2/\Lambda^2)^{-2}$, Eq. (4) becomes

$$I_\pi^{\rm DIP} = -\frac{\Lambda^5(m_\pi + 5\Lambda)}{24(m_\pi + \Lambda)^5}, \quad (5)$$

and the Taylor expansion provides

$$I_\pi^{\rm DIP} = -\frac{5}{24}\Lambda + m_\pi - \frac{35}{12\Lambda}m_\pi^2 + \cdots. \quad (6)$$

Therefore, precisely the same LNA contribution is recovered,

$$\chi_{B\pi} I_\pi^{\rm DIP(LNA)} = \chi_{B\pi} m_\pi, \quad (7)$$

with a finite renormalization of all other terms in the series. By varying Λ, strength in the loop integral may be moved to the residual analytic expansion and vice versa. As the moderately large m_π behavior of the loop integral and the residual expansion are radically different, varying Λ provides an opportunity to optimize the convergence properties of the truncated chiral expansion.

We show the mathematical equivalence of the renormalization prescriptions to a given order. The renormalized expansion in dimensional regularization is

$$\mu_B = c_0^B + \chi_{B\pi} m_\pi + c_2^B m_\pi^2 + \cdots, \quad (8)$$

and these renormalized coefficients are recovered from the FRR expansion via

$$c_0^B = a_0^B - \chi_{B\pi}\frac{5}{24}\Lambda, \qquad c_2^B = a_2^B - \chi_{B\pi}\frac{35}{12\Lambda}, \quad (9)$$

where the second terms compensate the Λ dependence of a_i^B.

In summary, in working to leading order in the chiral expansion with a dipole FRR, the quark mass dependence of nucleon magnetic moments in QCD is

$$\mu_B = a_0^B + a_2^B m_\pi^2 + a_4^B m_\pi^4 - \chi_{B\pi}\frac{\Lambda^5(m_\pi + 5\Lambda)}{24(m_\pi + \Lambda)^5}. \quad (10)$$

The inclusion of an m_π^4 term here is in anticipation of adding next-to-leading nonanalytic terms in the following.

III. QUENCHED CONSIDERATIONS

Here we address the necessary modifications to the chiral effective field theory for the quenched approximation. Vacuum fluctuations of $q\bar{q}$ pairs are absent in quenched simulations. As a result, the structure of the low-energy effective field theory is modified. Meson loop diagrams are restricted to only those where the loop is comprised of valence quarks having their origin in the interpolating fields of the baryon correlation function. This has the effect of modifying the effective π–N coupling constants [18,19] and the corresponding factors χ_B are changed accordingly.

To summarize, the LNA contributions to nucleon magnetic moments in both quenched and dynamical QCD, we use the standard notation and define

$$\chi_{B\pi} = \frac{M_N}{8\pi f_\pi^2}\beta_B^\pi, \quad (11)$$

and provide the coefficients, β_B^π, in Table I [18,19]. We use $f_\pi = 93$ MeV, $D = 0.76$ and $F = 0.50$ ($g_A = D + F$).

A peculiar feature of the quenched theory is the appearance of the flavor-singlet η' meson as a light degree of

freedom. In the absence of vacuum quark loops the η' behaves as a Goldstone boson [20,21] and must therefore be incorporated in the low-energy effective field theory.

The η' carries no charge and therefore does not make a direct contribution to the magnetic moment of the nucleon. The leading enhancement of the moment comes from η' dressing of the current insertion as in Fig. 2. Being a flavor singlet, the η' can propagate through a pure gluonic state. This corresponds to a double-hairpin in the quark-flow diagram. The vertex correction to the magnetic moment induced by this loop produces more singular nonanalytic behavior in the chiral limit than the physical theory.

The double-hairpin diagram has a logarithmic divergence near the chiral limit. This is a pathological feature of the quenched approximation, where the magnetic moment tends to infinity near the chiral limit. Physically this is not possible as angular momentum quantization ensures that the induced magnetic field of the meson-loop remains finite, even in the chiral limit [22].

The double-hairpin vertex correction diagram has been calculated in the graded-symmetry approach to QχPT by Savage in Ref. [18], and provides the term

$$\chi_{\eta'}^{(\mathrm{Q})}\mu_B^{(\mathrm{Q})\mathrm{tree}} I_{\eta'}, \tag{12}$$

with coefficient

$$\chi_{\eta'}^{(\mathrm{Q})} = \frac{m_0^2(3F-D)^2}{12\pi^2 f_\pi^2}. \tag{13}$$

The superscript (Q) denotes a quenched quantity. The coefficient m_0^2 is associated with the double-hairpin vertex in the η' propagator. This parameter is related to the physical η' mass [20,21] and we choose a value $m_0^2 = 0.42$ GeV. The loop integral in the heavy-baryon limit is given by

$$I_{\eta'} = -\int dk \frac{k^4 u^2(k)}{\omega_k^5}. \tag{14}$$

The normalization of the integral is such that the LNA contribution to this loop is $\log m_\pi$.

We also highlight that this contribution is proportional to the tree-level moment, $\mu_B^{(\mathrm{Q})\mathrm{tree}}$ [18]. Because of the logarithmic divergence one cannot simply define this to be the renormalized moment in the chiral limit. This necessarily means that one cannot remove the scale dependence of the coefficient of this chiral log using standard methods. We remove the scale dependence by replacing the tree-level coefficient by the renormalized magnetic moment at each quark mass $\mu_B^{(\mathrm{Q})\mathrm{tree}} = \mu_B^{(\mathrm{Q})}$. This approximation will be accurate provided $\chi_{\eta'}^{(\mathrm{Q})}\mu_B^{(\mathrm{Q})\mathrm{tree}} I_{\eta'}$ makes only small contributions for $m_\pi > m_\pi^{\mathrm{phys}}$.

TABLE I. Coefficients of the leading pion-loop contributions to nucleon magnetic moments in QCD and QQCD.

Baryon	β_B^{π}	$\beta_B^{\pi(\mathrm{Q})}$
p	$-(F+D)^2$	$-\frac{4}{3}D^2$
n	$(F+D)^2$	$\frac{4}{3}D^2$

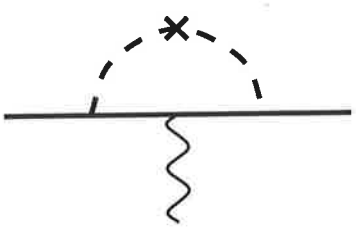

FIG. 2. Double-hairpin η' vertex correction to nucleon magnetic moment.

In Fig. 3 we show the value of the loop contributions for varying pion mass. The corrections from the η' are quite small in the region of interest.

Our expansion in the quenched approximation, analogous to Eq. (1), is given by

$$\mu_B^{(\mathrm{Q})} = a_0^{B(\mathrm{Q})} + a_2^{B(\mathrm{Q})} m_\pi^2 + a_4^{B(\mathrm{Q})} m_\pi^4 + \chi_{B\pi}^{(\mathrm{Q})} I_\pi + \chi_{B\eta'}^{(\mathrm{Q})}\mu_B^{(\mathrm{Q})} I_{\eta'}, \tag{15}$$

and is used to determine the parameters $a_i^{B(\mathrm{Q})}$. The total magnetic moment at arbitrary m_π is then given by

$$\mu_B^{(\mathrm{Q})} = \{a_0^{B(\mathrm{Q})} + a_2^{B(\mathrm{Q})} m_\pi^2 + a_4^{B(\mathrm{Q})} m_\pi^4 + \chi_{B\pi}^{(\mathrm{Q})} I_\pi\} \times (1 - \chi_{B\eta'}^{(\mathrm{Q})} I_{\eta'})^{-1}. \tag{16}$$

We note that at this point the decuplet contributions have been suppressed as their contributions are higher order in the chiral expansion, when one accounts for the octet-decuplet mass splitting realized in the (quenched) chiral limit [14].

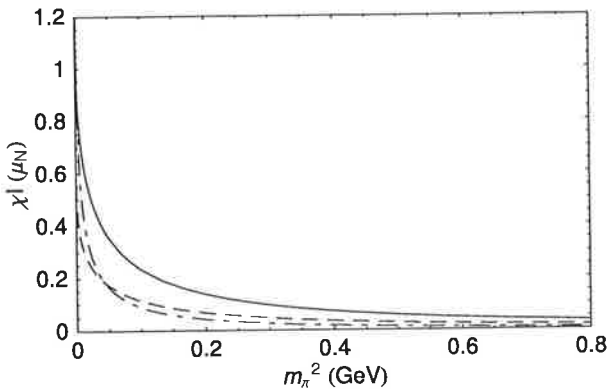

FIG. 3. Loop corrections, in units of μ_N, evaluated with a dipole FRR with $\Lambda = 0.8$ GeV. The dashed and solid curves are the pion-loop corrections of Fig. 1 in quenched and physical QCD, respectively. The dash-dotted curve is the η' vertex correction of quenched QCD, where the physical magnetic moment is used to define the renormalized coupling.

IV. EXTRAPOLATION OF LATTICE MAGNETIC MOMENTS

With the expansion of the low-energy EFT determined, one needs to fix the values of the unconstrained terms empirically. Lattice QCD provides information on the quark mass dependence of hadronic properties and hence enables the determination of these free parameters. If the data analyzed is within the applicable range of the effective field theory then, upon fixing these low-energy constants, one has an accurate extrapolation to the physical regime.

The electromagnetic form factors of the nucleon have recently been studied in simulations of quenched lattice QCD [23–25]. Early simulations of nucleon three-point functions have been performed by Leinweber *et al.* in Ref. [26]. Direct lattice calculations of the nucleon's strangeness form factor have also been carried out in Refs. [27,28].

In this study we choose to analyze only the most recently performed simulations using improved quark actions. Results by Gockeler *et al.* [23] have been obtained using the nonperturbatively improved clover fermion action [29]. We also consider recent form factor simulations by Zanotti *et al.* [24,25] using the fat-link irrelevant clover (FLIC) quark action [30]. For the purposes of this investigation, we select the six most accurate data points from the FLIC data set. The precision of the FLIC fermion results reflects the use of improved unbiased estimation techniques [26], improved actions and high statistics. It has been demonstrated that FRR-χEFT is applicable up to $m_\pi^2 = 0.8$ GeV^2 [12] and hence we also choose to truncate our data set at this scale of pion mass.

All previous chiral extrapolations of lattice electromagnetic structure have been based on χPT under the assumption that quenching effects are minimal [2–5,17,23,31–33]. Here we present the first comprehensive analysis of quenched lattice magnetic moments using QχPT for baryon form factors. Brief reports on preliminary QχPT extrapolations have recently been presented in Refs. [34–36].

In Fig. 4 we show fits to quenched lattice data of the proton magnetic moment using Eqs. (15) and (16). In anticipation of estimating unquenching corrections we have adopted the preferred value of $\Lambda = 0.8$ GeV [14]. The logarithmic divergence of μ_p in the chiral limit is evident.

Figure 5 illustrates the dependence of the extrapolated result, evaluated at the physical pion mass, on the choice of regulator parameter Λ. The vertical axis has been fixed to that of Fig. 4 in order to display the relevant scale. The variation in the quenched proton moment is similar to the statistical uncertainty of the FLIC simulation result at the lightest quark mass considered. Further reduction of the Λ sensitivity could be obtained by considering higher-order terms of the chiral expansion.

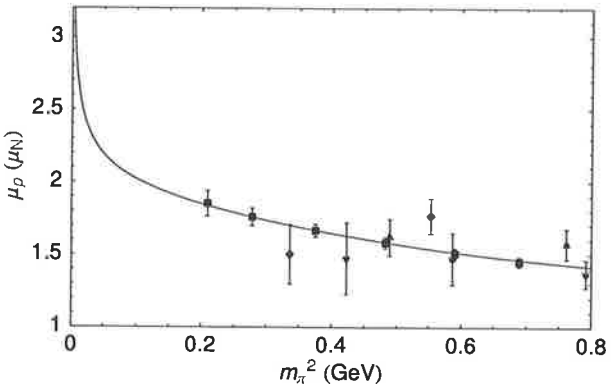

FIG. 4. Fit of Eq. (15) to quenched lattice data. The solid squares (■) illustrate the FLIC fermion results [24,25] and the open symbols describe nonperturbatively improved clover results [23], at $\beta = 6.0$ (▽), $\beta = 6.2$ (△) and $\beta = 6.4$ (◇).

V. EXTRAPOLATION ON A FINITE VOLUME

The previous section assumed the lattice QCD results provide an accurate representation of the results to be realized in the infinite-volume limit. However, results obtained on a lattice of finite spatial extent will differ from those in the infinite-volume limit, particularly in the chiral regime where the pion Compton wavelength can approach the lattice length. Here we extend the formalism of FRR to incorporate finite-volume effects.

The leading-order finite-volume effect in the chiral expansion lies in terms analytic in the small expansion parameter, $1/L$, where L is the length of the cubic volume [37]. Finite-volume corrections also enter through the modification of loop integrals. The requirement that Green's functions are periodic [37] restricts momentum components to the values

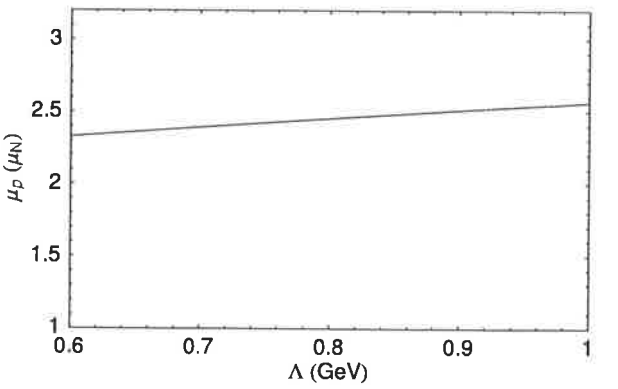

FIG. 5. The dependence of the extrapolated magnetic moment determined at the physical pion mass on the dipole regulator parameter Λ. Variation in the quenched proton moment is similar to the statistical uncertainty of the FLIC simulation result at the lightest quark mass considered.

$$k_i = \frac{2\pi n_i}{L}, \qquad n_i = 0, \pm 1, \pm 2, \ldots. \tag{17}$$

For the p-wave loop contribution of Fig. 1, where strength in the integrand vanishes for $k = 0$ as in Eq. (4), the dominant effect of discretizing the momenta is to introduce a threshold effect [11,14]. Strength in the integrand is not sampled until one component of k reaches $2\pi/L$. Since chiral physics is dominated by the infrared behavior of loop integrals, the nonanalytic terms of the chiral expansion exhibit substantial threshold effects.

To obtain a complete description of the quark mass and volume dependence of hadron properties, one must have an expansion in both m_q and $1/L$ [37]. Without data at varying lattice volumes it is impossible to determine the expansion coefficients of the $1/L$ contributions. Recent calculations have also considered the finite-volume corrections arising from the modification of the leading loop integrals to discretized momentum sums [38,39]. Impressive results for a phenomenological description of the volume dependence of hadron masses have also recently been reported [40].

In the absence of lattice QCD results for magnetic moments from a variety of lattice volumes, it is not possible to rigorously constrain the complete volume-dependent expansion. However, it is possible to precisely describe the impact of the finite volume on the quark mass dependence of magnetic moments on a single, fixed lattice volume.

Evaluating the loop integrals on a finite volume in FRR is a rather simple extension. One simply replaces the continuum integral by the discrete momentum sum over available momenta on a given volume. We formulate the finite-volume corrections in the continuum theory and therefore continue the momentum sum to infinity. This allows the features of finite-range regularization to carry over to the finite volume case. For example, Eq. (4) becomes

$$I_\pi = -\frac{4}{3\pi}\int dk \frac{k^4 u^2(k)}{\omega_k^4} = -\frac{1}{3\pi^2}\int d^3k \frac{k^2 u^2(k)}{\omega_k^4}$$
$$\rightarrow -\frac{1}{3\pi^2}\left(\frac{2\pi}{L}\right)^3 \sum_{\vec{k}} \frac{k^2 u^2(k)}{\omega_k^4}. \tag{18}$$

The discretized momenta on a cube are given by $\vec{k} = k_{\min}\vec{\mathbf{n}}$ for $\vec{\mathbf{n}} \in \mathbb{Z}^3$, with the minimum nontrivial momentum given by $k_{\min} = 2\pi/L$. We note that in obtaining the infinite volume form of Eq. (4) the angular dependence of the three-dimensional integral has been performed analytically. In general, with an angular dependent integrand, one must take caution in the naive conversion to a spherically symmetric sum as shown in Eq. (18). For the integrals used in this paper, we have verified that the spherically symmetric and angular dependent summations are equivalent.

Simulations performed with standard Wilson actions have large $\mathcal{O}(a)$ errors that can be accounted for in the effective field theory. One can introduce new local operators into the chiral Lagrangian reflecting $\mathcal{O}(a)$ terms associated with lattice discretization effects and explicit chiral symmetry breaking [41–43]. However, there has been tremendous success in removing $\mathcal{O}(a)$ errors and suppressing $\mathcal{O}(a^2)$ errors in lattice simulation results through the development of nonperturbatively improved actions [30,44,45]. These actions display excellent scaling properties [46–48], providing near continuum results at finite lattice spacing. In particular, the FLIC fermion simulations, dominating the chiral fits here, are performed using an $\mathcal{O}(a^2)$–mean-field improved Luscher-Weisz plaquette plus rectangle gauge action [49] and the nonperturbatively $\mathcal{O}(a)$-improved FLIC fermion action [30,46]. Hence these lattice results already represent an excellent approximation to the continuum limit.

Figure 6 illustrates the fit of Eq. (15) with the π and η' loop integrals modified as described in Eq. (18) for the finite volume. The physical volume of the FLIC lattice is $V = (2.56\ \text{fm})^3$. The chiral properties of the finite-volume extrapolation are qualitatively different from the infinite-volume curve of Fig. 4. In Fig. 7 we show the regulator parameter dependence on the finite-volume extrapolated magnetic moment for Λ in the range 0.6–1.0 GeV. The variation of the extrapolated moment is suppressed relative to the infinite-volume case, changing by $0.1\mu_N$. This systematic uncertainty is smaller than the statistical uncertainty of the lightest quark mass considered here, and could be suppressed further through the introduction of higher-order terms in the chiral expansion or through the introduction of precise lattice QCD results at light quark masses.

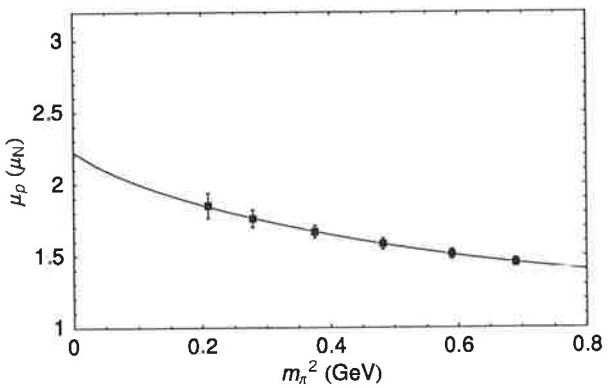

FIG. 6. Finite-volume FRR-EFT fit to FLIC fermion results for fixed volume. Here the dipole-vertex regulator parameter is fixed to $\Lambda = 0.8$ GeV.

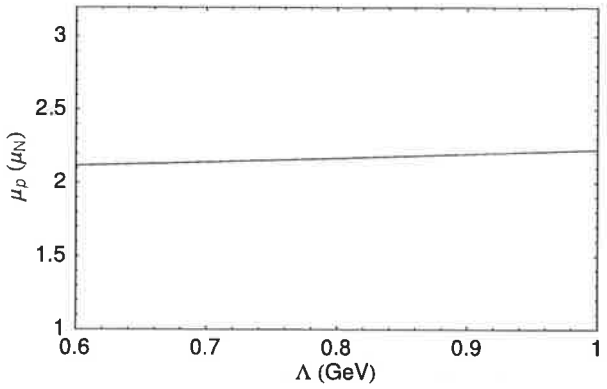

FIG. 7. The extrapolated magnetic moment on a finite volume, $V = (2.56\ \text{fm})^3$, for varying regulator parameter Λ.

VI. ESTIMATING EFFECTS OF DYNAMICAL SEA QUARKS

In a study of baryon masses in quenched and 2 + 1-flavor QCD it has been found that the short-distance physics of the analytic terms in the residual expansion of FRR-EFT are found to be very similar when the chiral-loop effects are evaluated with an appropriate FRR [14]. By identifying the short-distance behavior in quenched QCD (QQCD), one need only restore the chiral-loop effects of QCD to obtain an improved estimate of the physical magnetic moment.

In making such an identification it is essential to have a consistent method for setting the scale in both quenched and dynamical QCD. In particular, one must ensure that the procedure is insensitive to chiral physics. The QCD Sommer scale [50], based on the static quark potential, is insensitive to light quark physics and provides an ideal procedure for the scale determination.

The identification of this phenomenological link between quenched and dynamical simulations has been applied to FLIC fermion calculations of baryon masses [34,36]. Upon replacing the chiral loops of QQCD by their QCD counterparts the nucleon and delta are found to be in good agreement with experiment.

By applying the same principle to the calculation of magnetic moments in quenched QCD one can obtain improved estimates of the physical magnetic moment. The fit parameters, $a_i^{B(\mathrm{Q})}$, are determined by fitting finite-volume quenched lattice QCD using Eq. (15) with discretized momenta and a dipole regulator of 0.8 GeV. The estimate of the quenching effects is obtained under the assumption that the bare residual expansion parameters are unchanged in infinite-volume QCD when $\Lambda = 0.8$ GeV. That is, the full-QCD result can be described by Eq. (10) with the identification $a_i^{B(\mathrm{Q})} = a_i^B$. By fitting with finite-volume FRR-EFT both quenching and finite-volume corrections are incorporated in the final estimate. We show the infinite-volume QCD estimate of the proton magnetic moment by the dashed curve in Fig. 8.

In a similar manner, the infinite-volume limit of QQCD is estimated by fitting the parameters $a_i^{B(\mathrm{Q})}$ of Eq. (15) using finite-volume discretized momenta and a dipole regulator of 0.8 GeV in the loop integrals. The correction is estimated by Eq. (16) calculated with infinite-volume continuous momenta in the loop integrals. Figure 8 illustrates that the finite-volume corrections are negligible in the regime of the lattice QCD simulation results.

We emphasize that this result is a phenomenological estimate, as the size of the correction is Λ dependent. However, an important feature of this approach is that the largest finite-volume corrections lie in the chiral limit as they should. Ultimately, one would like to combine the improved convergence properties of FRR-EFT with the small $1/L$ expansion such that accurate and model-independent determinations of finite-volume effects can be made.

The primary feature of Fig. 8 is that, although the quenched and physical theory have quite different chiral structure, the observable effects are rather small. In particular, the logarithmic divergence is likely to only become apparent well below the physical pion mass. Within the current formalism of lattice QCD it seems such an observation would be a formidable task, particularly given the large lattice volume required to reveal the η' contribution.

The results here, based on the leading chiral corrections, indicate that proton magnetic moments evaluated in quenched simulations give a good approximation to the true theory. The enhancement from the η'-loop compensates for the reduction in the standard pion-loop from QCD to QQCD. The similarity in the effective curvature was also highlighted by Savage [18].

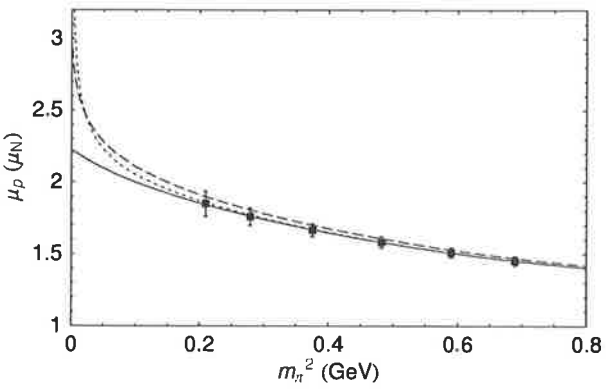

FIG. 8. Correcting the finite-volume quenched approximation to the infinite-volume limit of full-QCD. The solid curve is the finite-volume quenched fit to the data as in Fig. 4. The dotted curve provides an estimate of the infinite-volume limit magnetic moment in the quenched approximation. The dashed curve shows estimates of the proton magnetic moment in full-QCD as described in the text.

VII. SERIES TRUNCATION AND HIGHER ORDER EFFECTS

It is interesting to explore the convergence properties of the series expansion truncated to various order in m_π. The convergence of the truncated series can be investigated by studying the Taylor-series expansion of the FRR dipole regularized form, Eq. (10), which describes lattice results very well. Observing the behavior of the series expansion provides valuable insight into the dynamics of different truncation schemes. Similar studies of a truncation of the chiral-loop corrections to the nucleon mass evaluated with a FRR have been performed in Refs. [51–53].

In Fig. 9 we show the Taylor-series expansion of Eq. (10) truncated at various powers of m_π. This plot demonstrates that the quark mass expansion of the magnetic moment is very sensitive to the truncation of the chiral series. Reproduction of the dipole FRR result at just $m_\pi \sim 300$ MeV requires all terms to order m_π^{10}. If one wishes to reach the quark mass scale of modern lattice QCD simulations many more powers in m_π are required. In fact, the lightest displayed FLIC quark mass requires terms to m_π^{26}, similarly the lightest QCDSF point needs m_π^{50}.

We caution that the Taylor expansion of the FRR result is not equivalent to performing a DR calculation. As we work to leading order in the chiral expansion, only the terms to m_π of the Taylor expansion are guaranteed to be equivalent to the DR expansion. The Taylor series cannot reproduce the correct nonanalytic structures that will appear at higher order in the quark mass expansion.

Standard usage of DR to some chiral order would not lead to the parameter values that are extracted from the expansion of the FRR result. Fitting the low-order chiral expansion based on DR [4,23] to lattice data is enabled by a shift in the low-energy expansion parameters. The fact the expansion parameters differ between the DR and FRR results indicates that the fits are dependent on higher-order terms of the chiral expansion. This signifies that the chiral expansion is not sufficiently convergent in the domain of quark masses presently accessible in lattice QCD, for a regulator independent determination of the low-energy parameters.

This problem might have been anticipated by the fact that at moderately large quark masses the Dirac moment of the nucleon would be revealed

$$\mu_p = \frac{e\hbar}{2M_N}. \tag{19}$$

Knowing that in this regime the nucleon mass grows linearly with m_π^2, the moment would require an expansion in inverse powers of m_π^2 to describe the data [2,3].

We also investigate some of the effects of including higher-order terms in the FRR extrapolation of lattice data. The leading contribution from the delta baryon, shown in Fig. 10, is also incorporated into the fit. Equation (15) becomes

$$\mu_B^{(Q)} = a_0^{B(Q)} + a_2^{B(Q)} m_\pi^2 + a_4^{B(Q)} m_\pi^4 + \chi_{B\eta'}^{(Q)} \mu_B^{(Q)} I_{\eta'} + \chi_{B\pi}^{(Q)} I_\pi + \chi_{B\pi}^{\Delta(Q)} I_\Delta \pi, \tag{20}$$

where, analogous to Eq. (11), the corresponding couplings are given by

$$\chi_{B\pi}^{\Delta} = \frac{M_N}{8\pi f_\pi^2} \beta_{B\Delta}^{\pi}, \tag{21}$$

and Table II. The loop integral is also modified by the fact that the intermediate baryon propagator is nondegenerate with the external state. With the mass splitting given by Δ,

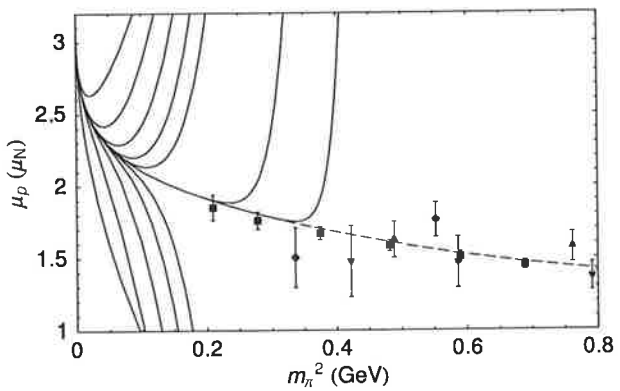

FIG. 9. Truncations of the Taylor expansion of the full-QCD expression of the magnetic moment, Eq. (10), to various orders in m_π. The leftmost curves display a succession of truncations from m_π up to m_π^{10}. To reach convergence at the lightest FLIC data point considered here one requires terms up to m_π^{26}, while for QCDSF terms to m_π^{50} are necessary. The dashed curve displays the full-QCD expression as displayed in Fig. 8.

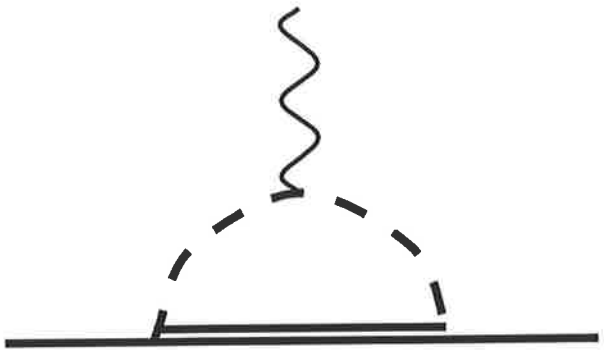

FIG. 10. Leading pion-loop contribution to nucleon magnetic moment from the Δ resonance.

TABLE II. Coefficients of the leading decuplet, pion-loop contributions to nucleon magnetic moments in QCD and QQCD [18], $C = -2D$.

Baryon	$\beta^{\pi}_{B\Delta}$	$\beta^{\pi(\mathrm{Q})}_{B\Delta}$
p	$-\frac{2}{9}C^2$	$-\frac{1}{6}C^2$
n	$\frac{2}{9}C^2$	$\frac{1}{6}C^2$

Eq. (4) becomes

$$I_\pi = -\frac{4}{3\pi}\int dk \frac{(\Delta + 2\omega_k)k^4 u^2(k)}{2\omega_k^3(\Delta + \omega_k)^2}. \qquad (22)$$

Given that the finite-volume corrections are negligible in the regime where the lattice QCD results lie, we illustrate the role of the Δ in FRR-EFT by taking the lattice results as an accurate representation of the infinite-volume limit and evaluate the loop integrals of Eq. (20) in the infinite-volume limit.

The fit of Eq. (20) to lattice results is shown by the dotted curve of Fig. 11. The comparison with the leading-order result (solid curve) shows that the effect of the decuplet on the extrapolation result is negligible. The new nonanalytic behavior introduced by an explicit inclusion of the Δ was already approximated well by the analytic terms in the expansion at leading order. Although the extrapolation shows little sensitivity to the inclusion of the Δ, it will be necessary to explicitly include this degree of freedom if one is to extract the low-energy constants to this order.

With regard to the estimation of full-QCD corrections, the inclusion of the decuplet is again a small effect. With the Δ, the QCD estimate of the proton magnetic moment at the physical quark mass is increased by $0.05\mu_N$ from the leading-order result. Although small for the proton, the inclusion of such contributions is found to be important for other baryons of the octet in the extraction of the strangeness magnetic moment of the proton [54,55].

Finally, the prediction of the physical proton magnetic moment obtained by including the Δ contributions and compensating for the finite lattice volume is $2.54(30)\mu_N$, where the uncertainty is statistical in origin. This result agrees well with the experimental value of $2.79\mu_N$.

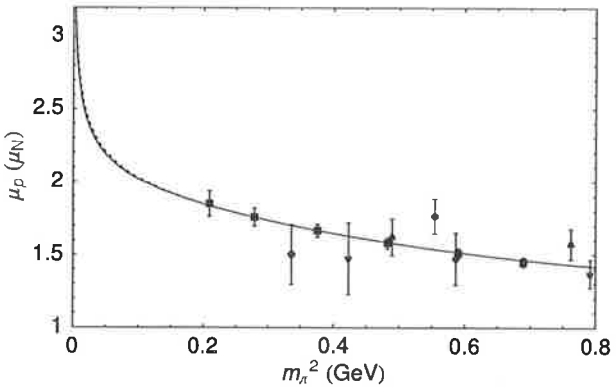

FIG. 11. The role of Δ contributions in the extrapolation of the proton magnetic moment. The solid curve displays the leading-order QQCD extrapolation of Eq. (16), without explicit decuplet contributions, as seen in Fig. 4. If Eq. (16) is extended to include the pion contributions with decuplet baryons in Eq. (20), one obtains the dotted curve.

VIII. CONCLUSIONS

Quenched and physical magnetic moments are in good agreement over a large range of pion mass. Although pion effects alone are decreased in QQCD, the new behavior introduced by the η' acts to suppress any difference.

We have demonstrated that the magnetic moments are extremely sensitive to the truncation of the chiral series. The domain where the chiral expansion can be formulated, truly independent of regulator, is likely to be a rather narrow window near the chiral limit. It is clear that there must be a transition between the rapid chiral variation and the smoothly varying lattice data at a scale around $m_\pi^2 \sim 0.1\ \mathrm{GeV}^2$. FRR-EFT provides an effective resummation of the chiral expansion that ensures that the slow variation of magnetic moments observed in lattice QCD arises naturally.

Finally, by estimating finite-volume and quenching effects through the leading one-loop contributions of the finite-range regularized meson cloud, we obtain an excellent value for the physical magnetic moment of the proton. Combined with the previous success in describing the difference between quenched and full-QCD nucleon and Δ masses [14], these results strengthen the argument that artifacts of the quenched approximation can be accurately corrected using phenomenological methods. Ultimately, lattice QCD simulations incorporating light dynamical-quark degrees of freedom on a variety of lattice volumes are required to achieve the goal of an *ab initio* determination of nucleon properties.

ACKNOWLEDGMENTS

We would like to thank Ian Cloet, Emily Hackett-Jones, and Stewart Wright for helpful discussions. This work was supported by the Australian Research Council and by DOE Contract No. DE-AC05-84ER40150, under which SURA operates Jefferson Laboratory.

[1] D. B. Leinweber, A. W. Thomas, and R. D. Young, Phys. Rev. Lett. **92**, 242002 (2004).
[2] D. B. Leinweber, D. H. Lu, and A. W. Thomas, Phys. Rev. D **60**, 034014 (1999).
[3] E. J. Hackett-Jones, D. B. Leinweber, and A. W. Thomas, Phys. Lett. B **489**, 143 (2000).
[4] T. R. Hemmert and W. Weise, Eur. Phys. J. A **15**, 487 (2002).
[5] E. J. Hackett-Jones, D. B. Leinweber, and A. W. Thomas, Phys. Lett. B **494**, 89 (2000).
[6] D. B. Leinweber, A. W. Thomas, and S. V. Wright, Phys. Lett. B **482**, 109 (2000).
[7] M. Procura, T. R. Hemmert, and W. Weise, Phys. Rev. D **69**, 034505 (2004).
[8] W. Detmold *et al.*, Phys. Rev. Lett. **87**, 172001 (2001).
[9] W. Detmold, W. Melnitchouk, and A. W. Thomas, Phys. Rev. D **66**, 054501 (2002).
[10] T. R. Hemmert, M. Procura, and W. Weise, Phys. Rev. D **68**, 075009 (2003).
[11] D. B. Leinweber, A. W. Thomas, K. Tsushima, and S. V. Wright, Phys. Rev. D **64**, 094502 (2001).
[12] R. D. Young, D. B. Leinweber, and A. W. Thomas, Prog. Part. Nucl. Phys. **50**, 399 (2003).
[13] D. B. Leinweber, A. W. Thomas, K. Tsushima, and S. V. Wright, Phys. Rev. D **61**, 074502 (2000).
[14] R. D. Young, D. B. Leinweber, A. W. Thomas, and S. V. Wright, Phys. Rev. D **66**, 094507 (2002).
[15] L. F. Li and H. Pagels, Phys. Rev. Lett. **26**, 1204 (1971).
[16] J. F. Donoghue, B. R. Holstein, and B. Borasoy, Phys. Rev. D **59**, 036002 (1999).
[17] I. C. Cloet, D. B. Leinweber, and A. W. Thomas, Phys. Lett. B **563**, 157 (2003).
[18] M. J. Savage, Nucl. Phys. **A700**, 359 (2002).
[19] D. B. Leinweber, Phys. Rev. D **69**, 014005 (2004).
[20] S. R. Sharpe, Phys. Rev. D **46**, 3146 (1992).
[21] C. W. Bernard and M. F. L. Golterman, Phys. Rev. D **46**, 853 (1992).
[22] D. B. Leinweber, A. W. Thomas, and R. D. Young, Phys. Rev. Lett. **86**, 5011 (2001).
[23] QCDSF Collaboration, M. Gockeler *et al.*, hep-lat/0303019.
[24] J. M. Zanotti *et al.*, Nucl. Phys. Proc. Suppl. **128**, 233 (2004).
[25] J. M. Zanotti, D. B. Leinweber, A. G. Williams, and J. B. Zhang, Nucl. Phys. Proc. Suppl. **129**, 287 (2004).
[26] D. B. Leinweber, R. M. Woloshyn, and T. Draper, Phys. Rev. D **43**, 1659 (1991).
[27] S. J. Dong, K. F. Liu, and A. G. Williams, Phys. Rev. D **58**, 074504 (1998); Kentucky Field Theory Collaboration, N. Mathur and S. J. Dong, Nucl. Phys. Proc. Suppl. **94**, 311 (2001).
[28] R. Lewis, W. Wilcox, and R. M. Woloshyn, Phys. Rev. D **67**, 013003 (2003).
[29] M. Luscher *et al.*, Nucl. Phys. **B491**, 323 (1997).
[30] CSSM Lattice Collaboration, J. M. Zanotti *et al.*, Phys. Rev. D **65**, 074507 (2002).
[31] D. B. Leinweber and A. W. Thomas, Phys. Rev. D **62**, 074505 (2000).
[32] J. D. Ashley, D. B. Leinweber, A. W. Thomas, and R. D. Young, Eur. Phys. J. A **19**, 9 (2004).
[33] V. V. Flambaum, D. B. Leinweber, A. W. Thomas, and R. D. Young, Phys. Rev. D **69**, 115006 (2004).
[34] R. D. Young, D. B. Leinweber, and A. W. Thomas, Nucl. Phys. Proc. Suppl. **128**, 227 (2004).
[35] R. D. Young, D. B. Leinweber, and A. W. Thomas, Nucl. Phys. Proc. Suppl. **129**, 290 (2004).
[36] D. B. Leinweber *et al.*, Nucl. Phys. **A737**, 177 (2004).
[37] J. Gasser and H. Leutwyler, Nucl. Phys. **B307**, 763 (1988).
[38] QCDSF-UKQCD Collaboration, A. Ali Khan *et al.*, Nucl. Phys. **B689**, 175 (2004).
[39] S. R. Beane, Phys. Rev. D **70**, 034507 (2004).
[40] B. Orth, T. Lippert, and K. Schilling, Nucl. Phys. Proc. Suppl. **129**, 173 (2004).
[41] G. Rupak and N. Shoresh, Phys. Rev. D **66**, 054503 (2002).
[42] O. Bar, G. Rupak, and N. Shoresh, Phys. Rev. D **67**, 114505 (2003).
[43] S. Aoki, Phys. Rev. D **68**, 054508 (2003).
[44] M. Luscher, S. Sint, R. Sommer, and P. Weisz, Nucl. Phys. **B478**, 365 (1996).
[45] R. Narayanan and H. Neuberger, Phys. Lett. B **302**, 62 (1993); Nucl. Phys. **B412**, 574 (1994); Phys. Rev. Lett. **71**, 3251 (1993); Nucl. Phys. **B443**, 305 (1995).
[46] J. M. Zanotti, B. G. Lasscock, D. B. Leinweber, and A. G. Williams, hep-lat/0405015 [Phys. Rev. Lett. (to be published)].
[47] R. G. Edwards, U. M. Heller, and T. R. Klassen, Phys. Rev. Lett. **80**, 3448 (1998).
[48] S. J. Dong, F. X. Lee, K. F. Liu, and J. B. Zhang, Phys. Rev. Lett. **85**, 5051 (2000).
[49] M. Luscher and P. Weisz, Commun. Math. Phys. **97**, 59 (1985); **98**, 433(E) (1985).
[50] R. G. Edwards, U. M. Heller, and T. R. Klassen, Nucl. Phys. **B517**, 377 (1998).
[51] R. E. Stuckey and M. C. Birse, J. Phys. G **23**, 29 (1997).
[52] S. V. Wright, Ph.D. thesis, University of Adelaide, 2002.
[53] C. Bernard *et al.*, Nucl. Phys. Proc. Suppl. **119**, 170 (2003).
[54] D. B. Leinweber *et al.*, Nucl. Phys. Proc. Suppl. **128**, 132 (2004).
[55] D. B. Leinweber *et al.*, hep-lat/0406002.

Precise Determination of the Strangeness Magnetic Moment of the Nucleon

D. B. Leinweber,[1] S. Boinepalli,[1] I. C. Cloet,[1] A. W. Thomas,[2] A. G. Williams,[1] R. D. Young,[1] J. M. Zanotti,[3] and J. B. Zhang[1]

[1]*Special Research Centre for the Subatomic Structure of Matter and Department of Physics, University of Adelaide, Adelaide SA 5005, Australia*

[2]*Jefferson Laboratory, 12000 Jefferson Avenue, Newport News, Virginia 23606, USA*

[3]*John von Neumann-Institut für Computing NIC, Deutsches Elektronen-Synchrotron DESY, D-15738 Zeuthen, Germany*

(Received 8 June 2004; published 3 June 2005)

By combining the constraints of charge symmetry with new chiral extrapolation techniques and recent low mass quenched lattice-QCD simulations of the individual quark contributions to the magnetic moments of the nucleon octet, we obtain a precise determination of the strange magnetic moment of the proton. The result, namely, $G_M^s = (-0.046 \pm 0.019)\mu_N$ is consistent with the latest experimental measurements but an order of magnitude more precise. This poses a tremendous challenge for future experiments.

DOI: 10.1103/PhysRevLett.94.212001 PACS numbers: 12.39.Fe, 12.38.Gc, 13.40.Em, 14.20.Dh

There is currently enormous interest in the determination of the strangeness content of the nucleon. It is crucial to our understanding of QCD to determine precisely the role played by heavier, nonvalence flavors. On the experimental side new results on strangeness in the nucleon have been reported recently from Jefferson Laboratory (JLab) (HAPPEX) [1] and MIT-Bates (SAMPLE) [2]. In the near future we can expect even more precise results from the A4 experiment at Mainz as well as G0 and HAPPEX2 at JLab. By contrast, the theoretical situation is somewhat confused, with the predictions of various quark models covering an enormous range. Direct calculations within lattice QCD have not yet helped to clarify the situation, with values for G_M^s ranging from -0.28 ± 0.10 [3] to $+0.05 \pm 0.06$ [4].

We take a different approach, exploiting the advances in lattice QCD which have enabled quenched QCD (QQCD) simulations of magnetic moments at pion masses as low as 0.3–0.4 GeV [5–8], as well as the development of new chiral extrapolation techniques [9,10]. Using these techniques we determine, in full QCD, the ratios of the valence u quark contribution to the magnetic moment of the physical proton to that in the Σ^+ and of the valence u quark in the physical neutron to that in the Ξ^0. From these ratios, the experimental values of the octet moments and charge symmetry we deduce a new theoretical value for G_M^s which is precise: setting a tremendous challenge for the next generation of parity violation experiments.

As illustrated in Fig. 1, the three-point function required to extract a magnetic moment in lattice QCD involves two topologically distinct processes. (Of course, in full QCD these diagrams incorporate an arbitrary number of gluons and quark loops.) The left-hand diagram illustrates the connected insertion of the current to one of the "valence" quarks of the baryon. In the right-hand diagram the external field couples to a quark loop. The latter process, where the loop involves an s quark, is entirely responsible for G_M^s.

Under the assumption of charge symmetry [11], the magnetic moments of the octet baryons satisfy [12]

$$\begin{aligned} p &= e_u u^p + e_d d^p + O_N; & n &= e_d u^p + e_u d^p + O_N, \\ \Sigma^+ &= e_u u^\Sigma + e_s s^\Sigma + O_\Sigma; & \Sigma^- &= e_d u^\Sigma + e_s s^\Sigma + O_\Sigma, \\ \Xi^0 &= e_s s^\Xi + e_u u^\Xi + O_\Xi; & \Xi^- &= e_s s^\Xi + e_d u^\Xi + O_\Xi. \end{aligned} \tag{1}$$

Here, p and Ξ^- are the physical magnetic moments of the proton and Ξ^-, and similarly for the other baryons. The valence u quark sector magnetic moment in the proton, corresponding to the left-hand side of Fig. 1, is denoted u^p. Charge symmetry has been used to replace the d quark contribution in the neutron by u^p, d in the Σ^- by u in the Σ^+ (u^Σ), and so on. The labels on quark magnetic moments allow for the environment sensitivity implicit in the three-point function [12,13]. That is, the naive expectations of the constituent quark model, namely $u^p/u^\Sigma = u^n/u^\Xi = 1$, may not be satisfied. The total contribution from quark loops, O_N, contains sea-quark-loop contributions (right-hand side of Fig. 1) from u, d, and s quarks. By definition

$$O_N = \frac{2}{3}{}^l G_M^u - \frac{1}{3}{}^l G_M^d - \frac{1}{3}{}^l G_M^s, \tag{2}$$

$$= \frac{{}^l G_M^s}{3}\left(\frac{1 - {}^l R_d^s}{{}^l R_d^s}\right), \tag{3}$$

where the ratio of s to d quark *loops*, ${}^l R_d^s \equiv {}^l G_M^s / {}^l G_M^d$, is expected to lie in the range (0,1). In deriving Eq. (3), we

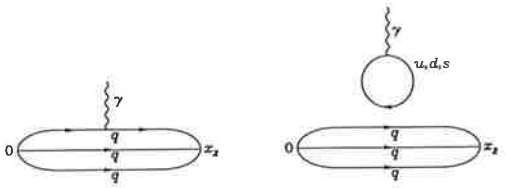

FIG. 1. Diagrams illustrating the two topologically different insertions of the current within the framework of lattice QCD.

have used charge symmetry to set ${}^lG^u_M = {}^lG^d_M$. Since the chiral coefficients for the d and s loops in the right-hand side of Fig. 1 are identical, the main difference comes from the mass of the K compared with that of the π.

With a little algebra O_N, and hence $G^s_M(\equiv {}^lG^s_M)$, may be isolated from Eqs. (1) and (3)

$$G^s_M = \left(\frac{{}^lR^s_d}{1-{}^lR^s_d}\right)\left[2p + n - \frac{u^p}{u^\Sigma}(\Sigma^+ - \Sigma^-)\right], \quad (4)$$

$$G^s_M = \left(\frac{{}^lR^s_d}{1-{}^lR^s_d}\right)\left[p + 2n - \frac{u^n}{u^\Xi}(\Xi^0 - \Xi^-)\right]. \quad (5)$$

Incorporating the experimentally measured baryon moments [14], Eqs. (4) and (5) become

$$G^s_M = \left(\frac{{}^lR^s_d}{1-{}^lR^s_d}\right)\left[3.673 - \frac{u^p}{u^\Sigma}(3.618)\right]\mu_N, \quad (6)$$

$$G^s_M = \left(\frac{{}^lR^s_d}{1-{}^lR^s_d}\right)\left[-1.033 - \frac{u^n}{u^\Xi}(-0.599)\right]\mu_N. \quad (7)$$

These expressions for G^s_M are exact consequences of QCD, under the assumption of charge symmetry.

Equating (6) and (7) provides a linear relationship between u^p/u^Σ and u^n/u^Ξ, which must be satisfied within QCD under the assumption of charge symmetry. Figure 2 displays this relationship. Since this line does not pass through the point (1.0,1.0), corresponding to the simple quark model assumption of universality, there must be an environment effect exceeding 12% in both ratios or approaching 20% or more in at least one of the ratios. A positive value for $G^s_M(0)$ would require an environment sensitivity exceeding 70% in the u^n/u^Ξ ratio.

The numerical simulations of the electromagnetic form factors presented here are carried out using the fat link irrelevant clover (FLIC) fermion action [5,6] in which

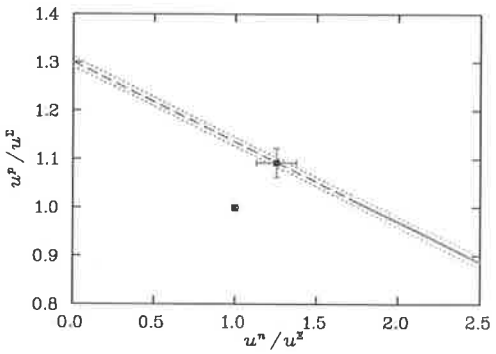

FIG. 2 (color online). The constraint [dashed line $G^s_M(0) < 0$, solid line $G^s_M(0) > 0$] on the ratios u^p/u^Σ and u^n/u^Ξ implied by charge symmetry and experimental moments. Experimental uncertainties are indicated by the dotted bounds. The assumption of environment independent quark moments is indicated by the crossed square. Our final result (chiral corrected extrapolation of lattice results) is illustrated by the filled square on the charge symmetry line.

the irrelevant operators, introduced to remove fermion doublers and lattice spacing artifacts, are constructed with APE smeared links [15]. Perturbative renormalizations are small for smeared links and the mean-field improved coefficients used here are sufficient to remove $\mathcal{O}(a)$ errors from the lattice fermion action [16].

The $\mathcal{O}(a)$-improved conserved vector current [17] is used. Nonperturbative improvement is achieved via the FLIC procedure, where the terms of the Noether current having their origin in the irrelevant operators of the fermion action are constructed with mean-field improved APE smeared links. The results presented here are obtained using established techniques [18] from a sample of 400 $20^3 \times 40$ mean-field $\mathcal{O}(a^2)$-improved Luscher-Weisz [19] gauge field configurations having a lattice spacing of 0.128 fm, determined by the Sommer scale $r_0 = 0.49$ fm.

One of the major challenges in connecting lattice calculations of hadronic properties with the physical world [20] is that currently accessible quark masses are much larger than the physical values. Our present analysis has been made possible by a significant breakthrough in the regularization of the chiral loop contributions to hadron observables [9,10,21]. Through the process of regulating loop integrals via a finite-range regulator (FRR) [9,22], the chiral expansion is effectively resummed to produce an expansion with vastly improved convergence properties. In particular, we extrapolate FLIC fermion calculations of the valence quark contributions to baryon moments (u^p, u^n, u^Σ, u^Ξ) to the physical mass regime. We select the dipole-vertex FRR with $\Lambda = 0.8$ GeV, which yields the best simultaneous description of both quenched and dynamical simulation results [23].

Separation of the valence and sea-quark-loop contributions to the meson cloud of full QCD hadrons is a nontrivial task. We use the diagrammatic method for evaluating the quenched chiral coefficients of leading nonanalytic (LNA) terms in heavy-baryon quenched chiral perturbation theory (QχPT) [24,25]. The valence contributions (key to this analysis) are obtained by removing the direct-current coupling to sea-quark loops from the total contributions. Upon further removal of "indirect sea-quark-loop" contributions, where a valence quark forms a meson composed with a sea-quark loop, one obtains the "quenched valence" contributions, the conventional view of the quenched approximation.

Figure 3 displays the diagrams providing the leading contributions to the chiral expansion of baryon magnetic moments (upper diagrams) and their associated quark flows in QQCD. The associated chiral expansion for the proton magnetic moment μ_p is

$$\mu_p = a_0^\Lambda + \mu_p \chi_{\eta'} I_{\eta'}(m_\pi, \Lambda) + \chi_{\pi B} I_B(m_\pi, \Lambda) + \chi_{KB} I_B(m_K, \Lambda) + a_2^\Lambda m_\pi^2 + a_4^\Lambda m_\pi^4, \quad (8)$$

where the repeated index B sums over allowed baryon octet and decuplet intermediate states. Loop integrals denoted by I are defined by

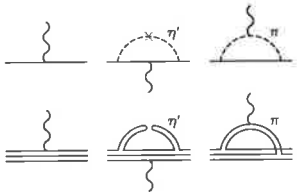

FIG. 3 (color online). Diagrams providing the leading contributions to the chiral expansion of baryon magnetic moments (upper diagrams) and their associated quark flows (lower diagrams) in QQCD.

$$I_B(m,\Lambda) = -\frac{2}{3\pi} \times \int dk \frac{\left(2\sqrt{k^2+m^2}+\Delta_{BN}\right)k^4 u^2(k,\Lambda)}{(k^2+m^2)^{3/2}\left(\sqrt{k^2+m^2}+\Delta_{BN}\right)^2}, \quad (9)$$

$$I_{\eta'}(m_\pi,\Lambda) = -\int_0^\infty dk \frac{k^4}{(k^2+m_\pi^2)^{5/2}} u^2(k,\Lambda), \quad (10)$$

where Δ_{BN} is the relevant baryon mass splitting and $u(k,\Lambda)$ is the dipole-vertex regulator. The coefficients χ denote the known model-independent coefficients of the LNA term for π and K mesons [25,26]. We take $m_K^2 = m_K^{(0)2} + \frac{1}{2}m_\pi^2$, and use the physical values to define $m_K^{(0)}$. The m_π^4 term in Eq. (8) allows for some curvature associated with the Dirac moment of the baryon, which should go as $1/m_\pi^2$ for moderately large quark masses.

Figure 4 illustrates a fit of FRR QχPT to the FLIC fermion lattice results (solid curve), where only the discrete momenta allowed in the finite volume of the lattice are summed in performing the loop integral. The long-dashed curve that also runs through the lattice results corresponds to replacing the discrete sum by the infinite-volume, continuous momentum integral. For all but the lightest quark mass, finite-volume effects are negligible.

The coefficients of the residual expansion, a_0^Λ, a_2^Λ, a_4^Λ, show excellent signs of convergence. For example, the fit to u^Σ yields values 1.48(7), $-0.90(23)$, and 0.42(19) in appropriate powers of GeV, respectively. Incorporating baryon mass splittings into the kaon loop contributions is essential, e.g., the contribution of $\Sigma \to NK$ is almost doubled when the $\Sigma - N$ mass splitting is included.

Figure 5 illustrates the considerations in correcting the quenched u quark contribution to yield the valence u quark contribution in full QCD. The removal of quenched η' contributions and the appropriate adjustment of π and K loop coefficients [24–26] provides the dot-dashed curve of Fig. 4. This is our best estimate of the valence u quark contribution (connected insertion) to the proton magnetic moment of full QCD. Finally, the disconnected insertion of the current is included to estimate the total contribution of the u quark sector to the proton magnetic moment [24–26]

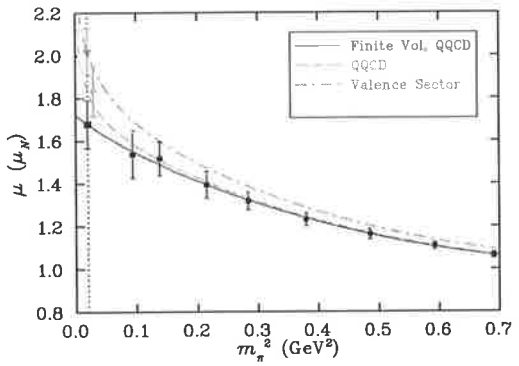

FIG. 4 (color online). The contribution of a single u quark (with unit charge) to the magnetic moment of the proton. Lattice simulation results (square symbols for $m_\pi^2 > 0.05$ GeV) are extrapolated to the physical point (vertical dashed line) in finite-volume QQCD as well as infinite-volume QQCD, valence, and full QCD; see text for details. Extrapolated values at the physical pion mass (vertical dashed line) are offset for clarity.

(fine dash-dotted curve in Fig. 4). Figure 6 displays similar results for the Σ^+.

From these chiral extrapolations, we estimate the ratios of the valence (connected) u quark contributions, u^p/u^Σ and u^n/u^Ξ. The final results

$$\frac{u^p}{u^\Sigma} = 1.092 \pm 0.030, \qquad \frac{u^n}{u^\Xi} = 1.254 \pm 0.124, \quad (11)$$

are plotted in Fig. 2. The precision of these results follows from the use of correlated ratios of moments which act to reduce uncertainties associated with the lattice spacing, the regulator mass, and statistical fluctuations [27]. This result leaves no doubt that G_M^s is negative. The fact that this point lies exactly on the constraint curve is highly nontrivial, and provides a robust check of the validity of the analysis techniques presented here.

As a further check, in Fig. 7 we compare the lattice-QCD predictions of the baryon magnetic moments constructed from chirally corrected extrapolations of the individual quark sectors. The results display an unprecedented level of agreement with experiment. We note that the

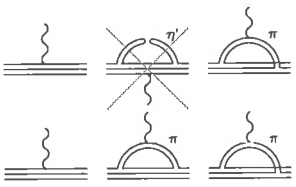

FIG. 5 (color online). Correcting QχPT (upper) to the valence sector of full QCD (lower diagrams). We remove quenched negative-metric η' contributions and adjust the chiral coefficients of π and K loops to account for the coupling of a valence quark to the photon in a meson made from a sea-quark loop. Coupling to the antiquark in the bottom-right diagram is also included in the valence contribution of full QCD.

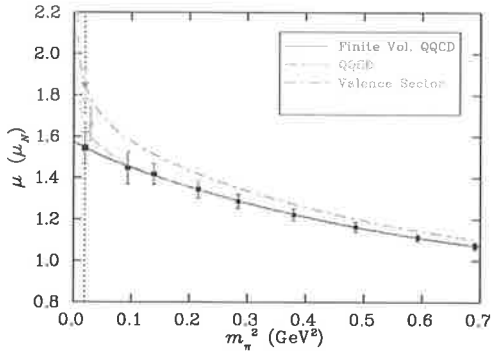

FIG. 6 (color online). The contribution of a single u quark (with unit charge) to the magnetic moment of the Σ^+. Curves and symbols are as for Fig. 4.

experimental constraints on u^{Σ} and u^{Ξ} emphasized by Wong [28] are both satisfied precisely.

While G_M^s is most certainly negative, it remains to set the magnitude. This requires an estimate of the strange to light sea-quark-loop contributions, ${}^lR_d^s$. Earlier estimates of ${}^lR_d^s$ were based on the constituent quark model. A more reliable approach is to estimate the loops using the same successful model invoked to correct the quenched results to full QCD [10,23], as illustrated in Fig. 7. Allowing the dipole mass parameter to vary between 0.6 and 1.0 GeV provides ${}^lR_d^s = G_M^s/G_M^d = 0.139 \pm 0.042$. A complete analysis of the errors associated with the determination of G_M^s using Eqs. (4), (5), and (11) is reported in Ref. [27]. The uncertainty is dominated by the statistical errors included in Eq. (11) and the uncertainty just noted for ${}^lR_d^s$. The final result for the strangeness magnetic moment of the nucleon is

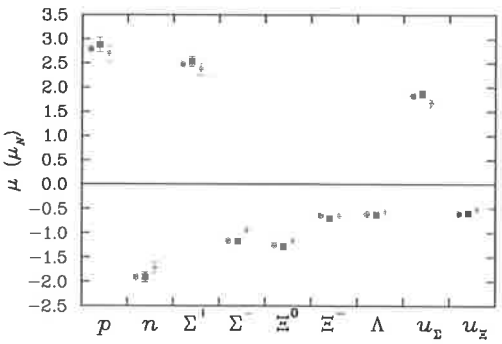

FIG. 7 (color online). The 1 standard deviation agreement between the FRRχPT corrected lattice simulation results (■) and the experimentally measured baryon magnetic moments (●). Quenched (◆) and finite-volume quenched (⊠) results are also illustrated.

$$G_M^s = (-0.046 \pm 0.019)\mu_N. \quad (12)$$

This precise value sets a tremendous challenge for the next generation of parity violation experiments.

We thank the Australian Partnership for Advanced Computing (APAC) for generous grants of supercomputer time which have enabled this project. This work is supported by the Australian Research Council and by DOE Contract No. DE-AC05-84ER40150, under which SURA operates Jefferson Laboratory.

[1] K. A. Aniol *et al.* (HAPPEX Collaboration), Phys. Lett. B **509**, 211 (2001).
[2] D. T. Spayde *et al.* (SAMPLE Collaboration), Phys. Lett. B **583**, 79 (2004).
[3] N. Mathur and S. J. Dong, Nucl. Phys. B Proc. Suppl. **94**, 311 (2001); S. J. Dong *et al.*, Phys. Rev. D **58**, 074504 (1998).
[4] R. Lewis, W. Wilcox, and R. M. Woloshyn, Phys. Rev. D **67**, 013003 (2003).
[5] J. M. Zanotti *et al.* (CSSM Lattice Collaboration), Phys. Rev. D **65**, 074507 (2002).
[6] D. B. Leinweber *et al.*, Eur. Phys. J. A **18**, 247 (2003).
[7] J. M. Zanotti, B. Lasscock, D. B. Leinweber, and A. G. Williams, Phys. Rev. D **71**, 034510 (2005)..
[8] J. M. Zanotti, S. Boinepalli, W. Kamleh, D. B. Leinweber, and A. G. Williams, Phys. Lett. B **616**, 196 (2005)..
[9] R. D. Young, D. B. Leinweber, and A. W. Thomas, Prog. Part. Nucl. Phys. **50**, 399 (2003).
[10] R. D. Young, D. B. Leinweber, and A. W. Thomas, Phys. Rev. D **71**, 014001 (2005).
[11] G. A. Miller *et al.*, Phys. Rep. **194**, 1 (1990).
[12] D. B. Leinweber, Phys. Rev. D **53**, 5115 (1996).
[13] D. B. Leinweber and A. W. Thomas, Phys. Rev. D **62**, 074505 (2000).
[14] K. Hagiwara *et al.* (Particle Data Group), Phys. Rev. D **66**, 010001 (2002).
[15] M. Falcioni *et al.*, Nucl. Phys. **B251**, 624 (1985).
[16] S. O. Bilson-Thompson *et al.*, Ann. Phys. (N.Y.) **304**, 1 (2003).
[17] G. Martinelli *et al.*, Nucl. Phys. **B358**, 212 (1991).
[18] D. B. Leinweber *et al.*, Phys. Rev. D **43**, 1659 (1991).
[19] M. Luscher and P. Weisz, Commun. Math. Phys. **97**, 59 (1985); **98**, 433 (1985).
[20] T. D. Cohen and D. B. Leinweber, Comments Nucl. Part. Phys. **21**, 137 (1993); A. W. Thomas, Aust. J. Phys. **44**, 173 (1991).
[21] D. B. Leinweber, A. W. Thomas, and R. D. Young, Phys. Rev. Lett. **92**, 242002 (2004).
[22] J. F. Donoghue *et al.*, Phys. Rev. D **59**, 036002 (1999).
[23] R. D. Young *et al.*, Phys. Rev. D **66**, 094507 (2002).
[24] D. B. Leinweber, Nucl. Phys. B Proc. Suppl. **109A**, 45 (2002).
[25] D. B. Leinweber, Phys. Rev. D **69**, 014005 (2004).
[26] M. J. Savage, Nucl. Phys. **A700**, 359 (2002).
[27] D. B. Leinweber *et al.*, Eur. Phys. J. A **24S2**, 79 (2005).
[28] C. W. Wong, hep-lat/0103021.